High frequency dynamic response of marine risers with application to flow-induced vibration

by

Enrique C. Gonzalez
B.S. Civil Engineering 1984 Federal University of Rio de Janeiro
M.S. Structural Engineering 1990 Federal University of Rio de Janeiro

Submitted to the Department of Ocean Engineering in partial fulfillment of the requirements for the degree of

DOCTOR OF PHILOSOPHY in OCEAN ENGINEERING
at the
MASSACHUSETTS INSTITUTE OF TECHNOLOGY

FEBRUARY 2001

Signature of Author: Signature Redacted
Department of Ocean Engineering
December 13, 2000

Certified by: Signature Redacted
J. Kim Vandiver
Professor of Ocean Engineering
Thesis Supervisor

Accepted by: .....
Professor Nicholas Patrikalakis
Kawasaki Professor of Engineering
Chairman, Departmental Committee on Graduate Studies

High frequency dynamic response of marine risers with application to flow-induced vibration

by
Enrique C. Gonzalez
Submitted to the Department of Ocean Engineering on December 13, 2000
in partial fulfillment of the requirements for the degree of
Doctor of Philosophy in Ocean Engineering

ABSTRACT

Vortex-Induced Vibration (VIV) of risers is the object of substantial research due to its importance in reducing the fatigue life of risers. The problems associated with VIV increase in difficulty and importance as the industry works in deeper water. This dissertation is directed at two topics relevant to VIV research: the development of better structural dynamic models of risers and the acquisition and analysis of model test data and full scale data with the purpose of deepening our understanding of VIV on real oil production systems.

Two new beam elements (one straight and one curved) are developed in the context of the Wave-Based Finite Element Method. Beam curvature, tension variation, rotary inertia, shear deformation and the influence of soil are taken into account. The new elements are tested against less efficient conventional FEM's. Comparison of natural frequencies and mode shapes of steel catenary risers show good agreement.

Three different experiments are analyzed and some interesting VIV properties are observed. The first experiment employed a model over 1200 feet long. The test dealt with three different configurations, which included a lazywave and a catenary riser. Several types of motion are applied on the top end of the riser while accelerations and bending moments are measured at different points on the riser. The second experiment is a smaller scale test performed on a catenary riser subjected to out-of plane, top-end displacements. Many cases of resonance were verified. In the last experiment, a full-scale steel catenary riser from the Petrobras P-18 production facility was instrumented to measure, among other things, bending moments near the touch down point and on the top of the riser and accelerations at three different points along the riser. Some preliminary results are presented based on the analysis of these measurements.

Thesis Supervisor: J. Kim Vandiver
Title: Professor of Ocean Engineering

Acknowledgments

First of all, I wish to thank my wife, Raquel, and my sons, Felipe and Nicholas, for all the support, encouragement and joy they provided me during all these years here in MIT. They came with me so that I could accomplish my dream and during these years I went through many ups and downs, perhaps more downs than ups, and they were always by my side helping me to continue.

I wish to thank my supervisor, prof. J. Kim Vandiver for guiding me through this research. The numerous fruitful discussions and the encouragement during these years of study are highly appreciated.

I am also very grateful not only to Petrobras for the financial support but also to many people in the company who supported me from the beginning to the end. They are too numerous to be mentioned by the names. However, there are some that I think I should highlight, such as Dr. Alvaro Maia and Dr. Marcio Mourelle.

I wish to thank to all members of my thesis committee for the ideas and suggestions given to my defense.

I wish to thank Yongming Cheng for the comments, suggestions and ideas he provided me during my study.

I wish to thank all the people at the laboratory in Technological Research Institute (IPT), especially Paulo Parra, for the help provided during the tests with the steel catenary riser model. I could not forget the help provided by Dr. Antonio C. Fernandes for the ideas and suggestions given during these tests.

Especial thanks go to Dr. Marcos Donato. He also graduated from MIT 3 years ago and provided extremely valuable help for me and my family when we arrived at MIT. His help and interest during all these years are very appreciated too.

I wish to thank Karl Burr for the interesting discussions we had and for the help and encouragement provided, especially in this final stage of my study.

I am also very grateful to my mother, Elvira, and mother-in-law, Leyla, for all the help, interest and cheering provided during these years of research.

Contents

List of Figures

Nomenclature

u_i	generic displacement (linear or angular) on the degree of freedom i
f_i	generic force (force or bending moment) on the degree of freedom i
ω	wave frequency
w	transverse displacement
v	longitudinal displacement
E	Young's modulus
I	Moment of inertia
s	Distance measured along the beam longitudinal axis
$\overline{T}$	Static tension
c	Damping coefficient of soil
k	Spring stiffness of soil
γ	Wavenumber
A	Cross sectional area
ρ	Mass density
q	External distributed load per unit length
t	Time
$[K]$	Dynamic stiffness matrix for the whole structure
$[K_t]$	Dynamic stiffness matrix for a discontinuity element
$[K_e]$	Complete dynamic stiffness matrix for the (straight or curved) beam element
$[K_{ea}]$	Dynamic stiffness matrix for the (straight or curved) beam element with axial motion only
$[K_{et}]$	Dynamic stiffness matrix for the (straight or curved) beam element with transverse motion only
$[K_{ei}]$	Dynamic stiffness matrix for the straight semi-infinite beam element
$[K_{ij}]$	Stiffness submatrix relating node i to node j

$\vec{F}_{et}$	Nodal force vector of a beam element considering transverse motion only
$\vec{U}_{et}$	Nodal displacement vector of a beam element considering transverse motion only
w_0	Wave amplitude
ψ	Rotation of the beam cross-section due to bending
ϕ	Rotation of the beam cross-section due to shear force
α	Rotation of the tangent to the neutral axis of the beam (straight or curved)
T	Dynamic tension
M	Dynamic bending moment
Q	Dynamic shear force
G	Shear modulus
κ	Adjustment coefficient for shear deformation
R	Static radius of curvature
m_a	transverse added mass of a cylinder
m_t	total transverse mass (structural plus added mass)
H_d	Hydrodynamic diameter
D	Diameter of the line
f_S	vortex shedding frequency
V	velocity magnitude of the flow
P	Period
S_t	Strouhal number
KC	Keulegan-Carpenter number

Chapter 1

Introduction

1.1 Motivation

The discoveries of oil fields in deeper and deeper water have caused the offshore industry to look for technically feasible and cost-effective solutions that allow the exploration of these fields. One of the most important components of offshore development is the riser as it transfers fluids from the subsea units to floating platforms and vice versa. Furthermore, the dynamic behavior of risers becomes even more important as exploratory drilling and production operations move into deeper water.

Flexible risers have been used widely by all oil companies in their offshore activities but these risers have limitations in diameter, especially as we go to deeper and deeper waters. The significant use of these flexible pipes caused the companies to look for alternatives to this component since it represents a significant amount of the total cost of a production unit. In some cases, a floating unit can have up to eighty flexible risers connected to it. Hence, there is a need for a new technology to face the increasing demand for large diameter risers. The steel catenary riser (SCR) alternative started to be investigated in detail not only to compete with the expensive flexible riser, so far the typical solution for semi-submersible production platforms, but also to guarantee the feasibility of potential deeper oil fields under exploration. One of the aspects of this investigation is the vibration of a steel catenary riser when subjected to the environmental loads.

Risers are subjected to environmental forces from different sources like currents, waves and the wave-induced motion of the floating vessel. Typical periods are in the range of 6 to 20 seconds. Another important force appears when a riser is subjected to a current. The alternate shedding of vortices in the near wake causes the appearance of transverse oscillating lift forces that will act on the riser. Consequently, it will vibrate in a direction perpendicular to the ambient flow. These

vibrations are referred to as Vortex-Induced Vibration (VIV) and they are typically smaller than two cylinder diameters, with periods of the order of 1 second or smaller. Although VIV does not produce large oscillation amplitudes when compared to the motions caused by waves and vessels, there are two reasons that make it an important issue to study: the effect on the fatigue life of the riser and the amplification of the drag coefficient from a nominal value of 1.2 (for Reynolds numbers below 3×10^5) up to a value of 3.0 or even higher. Consequently, an increase in the in-line displacements of the risers will be verified.

One interesting aspect is that VIV can also occur even in still water if the riser is moving, due to the motion of the vessel to which it is attached. In this case the riser will feel an oscillatory current induced by its motion and the Keulegan-Carpenter (KC) number plays an important role in this phenomenon.

Hence, developing the technology for estimating vortex-induced vibration (VIV) response is a critical need for fatigue design of drilling and production risers. The need for a complimentary analysis and design capabilities has been recognized since the 60's. Since then, vortex-induced vibration of slender cylinders has become one of the most extensively researched topics in the hydrodynamics and structural engineering literature. However, the complexity of the problem does not lend itself to standard analytical or numerical solutions. Current research in the prediction of vortex-induced vibration of risers has focused attention on many different areas, such as the physics of the fluid-structure interaction, the development of more adequate structural dynamic models and the acquisition and analysis of full-scale data with the purpose of calibrating response prediction codes used to design a riser. The present dissertation will focus on the last two areas.

We will apply the wave-based finite element method (WBFEM) to develop both straight and curved beam elements that can be used in the dynamic analysis of risers. It will be shown in the present dissertation that as frequency increases, the propagating wavelength decreases. Thus, if a conventional finite element model is used to study a marine riser, it is necessary to decrease the element length to represent its dynamic behavior well. A large number of elements will be required. The WBFEM allows the study of the dynamic behavior of a riser in a wide range of excitation frequencies with the same mesh of finite elements without losing accuracy since the method uses the solutions of the governing dynamic equations of the beam element to obtain its dynamic stiffness matrix. Hence, since it is a high frequency dynamic model, it is suitable for

VIV problems. The model is linear but at such small amplitudes of vibration (between 1 and 2 diameters as a maximum value) caused by VIV, most structural non-linearities are quite weak. Another important characteristic of this method is the possibility of representing propagating decaying waves. As higher and higher modes are excited by VIV, the chance of propagating waves instead of standing waves occurring increases. The WBFEM is capable of representing this characteristic through the use of complex modulus of the elasticity of the material because the imaginary part will account for the damping effects.

In the experiments presented in this dissertation, we present data from measurements taken from small scale to full scale risers. The intention is to gain some insights related to the VIV threshold and resonance phenomena and compare the displacement and stress measurements with the predictions of numerical codes. The main idea here is to better understand what is needed to improve the models used in the numerical codes to design a riser subjected to VIV. The full scale measurements are particularly interesting because they can provide information for real risers at full scale Reynolds number and mode shapes.

1.2 Background

The mechanics of risers have been the object of substantial research due to their importance in offshore activities. Because of their complexity, many numerical methods have been developed to analyze marine risers such as the Transfer Matrix Method (TMM), the Dynamic Stiffness Method (DSM) and the Finite Element Method (FEM).

Li Li [27] developed a transfer matrix model to solve string/lump system linear dynamics. This treatment allowed for systematic and analytical formulations for free vibration, Green's function, wave propagation and forced vibration problems. He also studied the effects of finite-sized lumps on wave propagation.

Clough and Penzien [10] presented the DSM applied to a flexural beam element with constant properties and also considering axial effects. It is based on the exact solution of the dynamic equilibrium equation. In the end, the coefficients of the dynamic stiffness matrix are dependent on the input frequency.

Mark Hayner [17] applied the Wave-based Finite Element Method to study wave propagation on in-vacuo cylindrical shells with discontinuities. He wanted to better understand the shell-

plate interaction, which plays an important role in the acoustic scattering and radiation processes from submarine hulls.

Kim [24] employed the WKB asymptotic method to analyze a long slender beam and in the end obtained some closed forms asymptotically.

Triantafyllou [46], using the WKB method, obtained a general asymptotic solution to the linear dynamics of a taut inclined cable. Through this solution, he studied the cable hybrid modes, which are a mixture of taut wire and inelastic chain dynamics.

Tjavaras [44] studied the mechanisms of the dynamic response characteristic of highly extensible cables through the Finite Difference Method.

Experiments with circular cylinders in the laboratory have been done for at least 30 years and much insight into the VIV problem has been gained through these experiments. More recently, Gopalkrishnan [14] focused attention on the measurement, through forced-oscillation experiments in a towing tank, of the vortex-induced lift and drag forces acting on circular cylinders undergoing sinusoidal and amplitude-modulated oscillations. In the end, he derived lift, drag and added mass coefficients for circular cylinders.

M. Venugopal [50] proposed a new damping model based on measurements on a flexible cylinder covering a wide range of cross flow and in line reduced velocities.

More recently, A. H. Techet [43] performed visualization studies of the flow behind an oscillating tapered cylinder at Reynolds numbers from 400 to 1500. In addition, forces were measured at both ends of a rigid tapered cylinder performing transverse oscillations within an oncoming flow.

Vandiver [11, 48] introduced many new insights into vertical risers subjected to VIV by examining acceleration and stress measurements from cylinders, both in the laboratory and in the offshore ocean.

1.3 Overview of the dissertation

The material presented in this dissertation is organized in seven chapters. The introductory material with the motivation and overview of the dissertation are presented in the first chapter. The content of each of the following chapters is briefly summarized below.

In Chapter 2, we study the use of WBFEM to develop two types of straight beam elements, one with constant properties and the other with slowly varying tension. For both types, we divide the element in two categories: considering or neglecting the effects of rotary inertia. Since the wave dispersion plays a very important role in the beam dynamic, we study the propagation of waves for different conditions of a beam element.

In Chapter 3 we apply the same method for a curved beam element to include the effect of curvature in the propagation of waves on risers. Since it is the beginning of a new development we started by working with constant radius of curvature elements. Again, we develop two types of beam elements: one with constant properties and the other with slowly varying tension. We also take into account transverse distributed loads acting on both curved and straight beam elements in the context of the WBFEM. In the end, we present several examples showing the influence of the curvature on the wave dispersion relation and some simple applications of the elements developed up to this point to the dynamic analysis of beams. These results are compared to theoretical values.

Chapter 4 is dedicated to the analysis of measured data from two different experiments. One is the model used by Petrobras to represent the steel catenary riser that is installed in the platform P18. The other is the large scale models of 3 different configurations tested in a lake in the USA. All of them are related to the use of steel catenary risers as an important component of offshore exploration. This alternative is becoming attractive for the reasons explained before. All the experiments described in this chapter deal with the imposition of harmonic motion on the top end of the model and the corresponding measurements of quantities related to the model response.

In Chapter 5, we give examples about the applications of the beam elements developed in the context of the wave-based finite element method to the riser dynamic analysis. The risers considered here are the following: straight, steel catenary, lazy wave and CVAR. Natural frequencies and mode shapes are calculated and compared to the same quantities calculated by a computer program that uses FEM.

In chapter 6, we describe the monitoring program of a full scale steel catenary riser installed in platform P18. This program was developed by Petrobras to reduce the uncertainties related to the design criteria of SCR and to calibrate computer codes used in the design of risers. It encompasses measurements of environmental conditions (basically ocean currents, waves and

wind), forces and bending moments near the touch down point and at the top end, and accelerations at some points along the riser. Some preliminary results are shown and analyzed and some conclusions are drawn. Because of confidentiality of the data involved in this project, we have to show only a piece of it.

Chapter 7 presents the principal conclusions drawn in this research. We also point out the major benefits and shortcomings that need to be addressed and suggest some areas that need further research.

Due to the increasing interest in steel marine risers in different configurations, as was explained in Section 1.1, in this dissertation we are mainly going to focus on this type of riser.

Chapter 2

Straight Beam Element

2.1 Introduction

In this chapter, we study the application of the Wave Based Finite Element Method (WBFEM) to obtain the dynamic stiffness matrix of a straight beam segment. Two types of element are considered here: one with constant tension distribution over the element and another with slowly varying tension distribution, where the WKB method is used to find a solution for the differential equation of dynamic equilibrium. Some other aspects are considered, like the calculation of wave reflection and the formulation of a semi-infinite beam element. At the end of this chapter, some cases are studied just to clarify the concepts explained in the sections.

2.2 Governing Equations for Beams with Constant Tension

A typical straight beam is shown in Figure 2-1 with its local system of reference for displacements and forces at its ends. Numbers 1 and 2 inside the circles represent both ends of the beam. The beam is made out of a linear elastic material and the effects of shear deformation and rotary inertia are neglected. Besides, it is supported by a visco-elastic foundation, which is represented by an uniform distribution of springs and dampers along the beam. All the material and geometric properties are constant over the length of the element. The beam is also subjected to a constant, static axial tensile force $\overline{T}$. Figure 2-1 also shows the sign convention for both end displacements and forces, which are represented by the vectors $\vec{U}_{el} = \{u_1 \quad u_2 \quad u_3 \quad u_4\}^T$ and

$\bar{F}_{el}=\{f_1 \quad f_2 \quad f_3 \quad f_4\}^T$, respectively. The quantities u_1 and u_3 are the transverse displacements while u_2 and u_4 are the rotations and are defined by the expression $-\partial w/\partial s$ because of the local system of reference. The quantities f_1 and f_3 are the vertical forces while f_2 and f_4 are the bending moments.

Figure 2-1: Straight beam element on visco-elastic foundation with constant tension.

It is important to stress here that throughout this work, in the derivation of all the equations, we are restrained to the linear regime.

The governing equation of the dynamics of a tensioned beam on visco-elastic foundation has been derived before by many investigators (see for instance reference [16]) and so the derivation will not be repeated here. Its final form is

$$EI\frac{\partial^4 w}{\partial s^4}-\bar{T}\frac{\partial^2 w}{\partial s^2}+kw+c\frac{\partial w}{\partial t}+\rho A\frac{\partial^2 w}{\partial t^2}=q(s,t) \tag{2.1}$$

In the derivation of this equation the following relations were used to define bending moment and shear force, respectively

$$M=-EI\frac{\partial^2 w}{\partial s^2} \tag{2.2}$$

and shear force by

$$Q=\frac{\partial M}{\partial s} \qquad \Rightarrow Q=-EI\frac{\partial^3 w}{\partial s^3} \tag{2.3}$$

Equations (2.2) and (2.3) were adapted to the local system of reference adopted (see Figure 2-1). For the free vibration condition we have $q(s,t)=0$. Thus, the equation of motion becomes

$$EI\frac{\partial^4 w}{\partial s^4}-\bar{T}\frac{\partial^2 w}{\partial s^2}+kw+c\frac{\partial w}{\partial t}+\rho A\frac{\partial^2 w}{\partial t^2}=0 \qquad (2.4)$$

A harmonic solution of the form

$$w(s,t)=w_0\exp(i(\gamma s-\omega t)) \qquad (2.5)$$

can be assumed, where w_0 is the amplitude of the motion. Then we substitute (2.5) into equation (2.4). After canceling the common terms, we obtain the equation that relates the wavenumber γ to the wave frequency ω for given beam material properties and geometry, known as the dispersion relation for the beam:

$$EI\gamma^4+\bar{T}\gamma^2+k-ic\omega+\rho A\omega^2=0 \qquad (2.6)$$

The four roots of this equation are

$$\begin{aligned}
\gamma_1&=\sqrt{-\frac{\bar{T}}{2EI}+\sqrt{\left(\frac{\bar{T}}{2EI}\right)^2+\frac{\rho A\omega^2-k+ic\omega}{EI}}}\\
\gamma_2&=-\gamma_1\\
\gamma_3&=\sqrt{-\frac{\bar{T}}{2EI}-\sqrt{\left(\frac{\bar{T}}{2EI}\right)^2+\frac{\rho A\omega^2-k+ic\omega}{EI}}}\\
\gamma_4&=-\gamma_3
\end{aligned} \qquad (2.7)$$

These four roots represent four different wavenumbers of waves propagating along the beam. The wavenumber γ_i is a complex quantity, with spatial decay corresponding to the imaginary part and spatial oscillation corresponding to the real part. Depending on the range of frequencies we are working with we can have only evanescent waves (γ_i is purely imaginary) or

propagating waves (γ_i is purely real). Another characteristic is that there are two waves propagating and/or decaying to the right and two to the left.

Based on equations (2.7), the general solution for the transverse displacement at any position along the beam axis can be described in terms of these four waves as

$$w(s,t) = w_{01}\exp(i(\gamma_1 s - \omega t)) + w_{02}\exp(i(\gamma_2 s - \omega t)) + w_{03}\exp(i(\gamma_3 s - \omega t)) + w_{04}\exp(i(\gamma_4 s - \omega t)) \tag{2.8}$$

Note that equation (2.8) is exact to within the assumptions that allowed the derivation of the governing differential equation (2.1).

Throughout this work, it is assumed a steady state time dependence of $\exp(-i\omega t)$ for all variables. This assumption is hereafter implied. This term will only appear when it becomes necessary for the understanding of the text. Therefore, we can rewrite equation (2.8) above as

$$w(s) = w_{01}\exp(i\gamma_1 s) + w_{02}\exp(i\gamma_2 s) + w_{03}\exp(i\gamma_3 s) + w_{04}\exp(i\gamma_4 s) \tag{2.9}$$

The only unknowns are the wave amplitudes, which depend on the boundary conditions and the loads applied. Equation (2.9) will be the basis for the construction of the dynamic stiffness matrix of the beam element shown in Figure 2-1 through the use of the WBFEM.

As we will see later when we study the reflection coefficients, there will be advantages in sorting the waves in equation (2.9) so that γ_1 and γ_2 correspond to right-going (i.e., the real part of γ_i is positive) or right-decaying (i.e., γ_i is pure positive imaginary) waves while γ_3 and γ_4 correspond to the left-going (i.e., the real part of γ_i is negative) or left-decaying (i.e., γ_i is pure negative imaginary) waves. This sorting is implied from now on in this work.

2.3 Dynamic Stiffness Matrix

To obtain the dynamic stiffness matrix we start by determining the nodal displacements u_i and forces f_i, located at the ends of the beam element of Figure 2-1. This is easily accomplished

once we know the expression that defines the transverse displacement field along the beam element, $w(s)$, as shown in equation (2.9). We have

$$
\begin{aligned}
u_1 &= w(s=0) \\
u_2 &= -\frac{\partial w}{\partial s}(s=0) \\
u_3 &= w(s=L) \\
u_4 &= -\frac{\partial w}{\partial s}(s=L) \\
f_1 &= EI\frac{\partial^3 w}{\partial s^3} - \bar{T}\frac{\partial w}{\partial s}(s=0) \\
f_2 &= EI\frac{\partial^2 w}{\partial s^2}(s=0) \\
f_3 &= -EI\frac{\partial^3 w}{\partial s^3} + \bar{T}\frac{\partial w}{\partial s}(s=L) \\
f_4 &= -EI\frac{\partial^2 w}{\partial s^2}(s=L)
\end{aligned}
\tag{2.10}
$$

Note that f_1 and f_3 had contributions from the shear force plus the axial tension $\bar{T}$. The expressions for f_1 and f_2 (i.e., at $s=0$) had to be reversed in sign in order to make them consistent with the convention of positive directions, as shown in Figure 2-1.

Substituting the expression (2.9) into (2.10) above, we obtain the following expressions for the nodal displacements:

$$u_1 = w_{01} + w_{02} + w_{03} + w_{04}$$

$$u_2 = -i\gamma_1 w_{01} - i\gamma_2 w_{02} - i\gamma_3 w_{03} - i\gamma_4 w_{04}$$

$$u_3 = w_{01}\exp(i\gamma_1 L) + w_{02}\exp(i\gamma_2 L) + w_{03}\exp(i\gamma_3 L) + w_{04}\exp(i\gamma_4 L)$$

$$u_4 = -i\gamma_1 w_{01}\exp(i\gamma_1 L) - i\gamma_2 w_{02}\exp(i\gamma_2 L) - i\gamma_3 w_{03}\exp(i\gamma_3 L) - i\gamma_4 w_{04}\exp(i\gamma_4 L)$$

In matrix form we can write the last four equations as

$$\vec{U}_{el} = [D]\cdot\vec{W} \tag{2.11}$$

where $\vec{W} = \{w_{01}\, w_{02}\, w_{03}\, w_{04}\}^T$ is the vector of wave amplitudes. As for the end forces we get

$$f_1 = -EI(iw_{01}\gamma_1^3 + iw_{02}\gamma_2^3 + iw_{03}\gamma_3^3 + iw_{04}\gamma_4^3) - \overline{T}(iw_{01}\gamma_1 + iw_{02}\gamma_2 + iw_{03}\gamma_3 + iw_{04}\gamma_4)$$

$$f_2 = -EI(w_{01}\gamma_1^2 + w_{02}\gamma_2^2 + w_{03}\gamma_3^2 + w_{04}\gamma_4^2$$

$$f_3 = EI(iw_{01}\gamma_1^3 \exp(i\gamma_1 L) + iw_{02}\gamma_2^3 \exp(i\gamma_2 L) + iw_{03}\gamma_3^3 \exp(i\gamma_3 L) + iw_{04}\gamma_4^3 \exp(i\gamma_4 L)$$
$$+ \overline{T}(iw_{01}\gamma_1 \exp(i\gamma_1 L) + iw_{02}\gamma_2 \exp(i\gamma_2 L) + iw_{03}\gamma_3 \exp(i\gamma_3 L) + iw_{04}\gamma_4 \exp(i\gamma_4 L))$$

$$f_4 = EI(w_{01}\gamma_1^2 \exp(-i\gamma_1 L) + w_{02}\gamma_2^2 \exp(-i\gamma_2 L) + w_{03}\gamma_3^2 \exp(-i\gamma_3 L) + iw_{04}\gamma_4^2 \exp(-i\gamma_4 L)$$

The equations above can be written in matrix form as

$$\vec{F}_{el} = [C] \cdot \vec{W} \tag{2.12}$$

The components of the 4×4 matrices $[C]$ and $[D]$ are the terms that multiply w_{01}, w_{02}, w_{03} and w_{04} in the equations above. They are known as the force-amplitude matrix and displacement-amplitude matrix, respectively, and they are shown below.

$$[D] = \begin{bmatrix} 1 & 1 & 1 & 1 \\ -i\gamma_1 & -i\gamma_2 & -i\gamma_3 & -i\gamma_4 \\ \exp(i\gamma_1 L) & \exp(i\gamma_2 L) & \exp(i\gamma_3 L) & \exp(i\gamma_4 L) \\ -i\gamma_1 \exp(i\gamma_1 L) & -i\gamma_2 \exp(i\gamma_2 L) & -i\gamma_3 \exp(i\gamma_3 L) & -i\gamma_4 \exp(i\gamma_4 L) \end{bmatrix}$$

$$[C] = EI \begin{bmatrix} -i\gamma_1^3 & -i\gamma_2^3 & -i\gamma_3^3 & -i\gamma_4^3 \\ -\gamma_1^2 & -\gamma_2^2 & -\gamma_3^2 & -\gamma_4^2 \\ i\gamma_1^3 \exp(i\gamma_1 L) & i\gamma_2^3 \exp(i\gamma_2 L) & i\gamma_3^3 \exp(i\gamma_3 L) & i\gamma_4^3 \exp(i\gamma_4 L) \\ \gamma_1^2 \exp(i\gamma_1 L) & \gamma_2^2 \exp(i\gamma_2 L) & \gamma_3^2 \exp(i\gamma_3 L) & \gamma_4^3 \exp(i\gamma_4 L) \end{bmatrix} +$$

$$\overline{T} \begin{bmatrix} -i\gamma_1 & -i\gamma_2 & -i\gamma_3 & -i\gamma_4 \\ 0 & 0 & 0 & 0 \\ i\gamma_1 \exp(i\gamma_1 L) & i\gamma_2 \exp(i\gamma_2 L) & i\gamma_3 \exp(i\gamma_3 L) & i\gamma_4 \exp(i\gamma_4 L) \\ 0 & 0 & 0 & 0 \end{bmatrix}$$

As expected, the force and displacement matrices are functions of beam material, geometric properties and frequency. From equation (2.11) we get

$$\vec{W} = [D]^{-1} \cdot \vec{U}_{et} \tag{2.13}$$

After substitution of (2.13) into (2.12) we obtain

$$\vec{F}_{et} = [C] \cdot [D]^{-1} \cdot \vec{U}_{et} \Rightarrow \qquad \vec{F}_{et} = [K_{et}] \cdot \vec{U}_{et}$$

where $[K_{et}]$ is the dynamic stiffness matrix of the beam element shown in Figure 2-1, considering only transverse motion. Notice that the vector of wave amplitudes disappears when we relate nodal forces to the corresponding nodal displacements.

Because of the complexity of the terms involved in the formation of the matrices $[D]$ and $[C]$ above, sometimes the analytical form of the stiffness matrix components becomes very long and difficult to be obtained symbolically, as we will see in the next sections. Thus, in the present work they were calculated through the numerical implementation of the operation

$$[K_S] = [C] \cdot [D]^{-1} \tag{2.14}$$

In specific cases, however, the analytical expression of the dynamic stiffness matrix can be obtained. Let's suppose we have a tensioned beam were the wavelengths are given by $\gamma_1 = -\gamma_2 = \gamma_p$, real roots corresponding to propagating waves and $\gamma_3 = -\gamma_4 = -i\gamma_e$, pure imaginary roots corresponding to evanescent waves. In this case, the stiffness matrix is given by

$$K = \frac{EI}{b}\begin{bmatrix} k_{11} & k_{12} & k_{13} & k_{14} \\ k_{12} & k_{22} & k_{23} & k_{24} \\ k_{13} & k_{23} & k_{33} & k_{34} \\ k_{14} & k_{24} & k_{34} & k_{44} \end{bmatrix}$$

where

$$b = 8\gamma_p\gamma_e + 4(\gamma_e^2 - \gamma_p^2)\sinh(\gamma_e L)\sin(\gamma_p L) - 8\gamma_p\gamma_e \cosh(\gamma_e L)\cos(\gamma_p L)$$

$$k_{11} = 4(\gamma_p^3\gamma_e + \gamma_p\gamma_e^3)(\gamma_e \sinh(\gamma_e L)\cos(\gamma_p L) + \gamma_p \cosh(\gamma_e L)\sin(\gamma_p L))$$

$$k_{12} = -8\gamma_e^4 \sinh(\gamma_e L)\sin(\gamma_p L) + 4(\gamma_p\gamma_e^3 - \gamma_p^3\gamma_e)\cosh(\gamma_e L)\cos(\gamma_p L) + (\gamma_p^3\gamma_e - \gamma_p\gamma_e^3)$$

$$k_{13} = 4\left(\gamma_p^3\gamma_e - \gamma_p\gamma_e^3\right)\left(\gamma_e \sinh(\gamma_e L) + \gamma_p \sin(\gamma_p L)\right)$$

$$k_{14} = 4\left(\gamma_p\gamma_e^3 + \gamma_p^3\gamma_e\right)\cos(\gamma_p L) - 4\left(\gamma_p\gamma_e^3 + \gamma_p^3\gamma_e\right)\cosh(\gamma_e L)$$

$$k_{22} = -4\left(\gamma_p^2 + \gamma_e^2\right)\left(\gamma_p \sinh(\gamma_e L)\cos(\gamma_p L) - \gamma_e \cosh(\gamma_e L)\sin(\gamma_p L)\right)$$

$$k_{23} = -k_{14}$$

$$k_{24} = 4\left(\gamma_p^2 + \gamma_e^2\right)\left(\gamma_p \sinh(\gamma_e L) - \gamma_e \sin(\gamma_p L)\right)$$

$$k_{33} = k_{11}$$

$$k_{34} = -k_{12}$$

$$k_{44} = k_{22}$$

We see that the stiffness matrix will be symmetric and pure real. Positive values denote spring-like behavior while negative values denote mass-like behavior. Dissipative effects may be included by letting the modulus of elasticity, E, be complex. This will result in a complex dynamic stiffness matrix which elements have negative imaginary parts.

From this point on the stiffness matrix given by equation (2.14) may be used in the same way as any conventional FEM stiffness matrix [see reference [2]]. In general, an element is part of a global system of elements representing a structure subjected to a combination of external loads. The local stiffness matrix of each element, $[K_{el}]$, is taken from the local to the global system of reference and used to assemble the global stiffness matrix, $[K]$, of the whole structure. We can follow a similar procedure for the element force vector and form the equation $[K]\vec{U} = \vec{F}$, which is solved for the nodal displacements $\vec{U}$. Having determined these displacements, the wave amplitudes for each element can be obtained through equation (2.11), i.e., $\vec{W} = [D]^{-1}\vec{U}_{el}$, where $\vec{U}_{el}$ corresponds to a specific element of the structure and it is taken from the vector $\vec{U}$.

2.4 Semi-Infinite Length Beam Element

The use of the WBFEM makes it possible to obtain the dynamic stiffness matrix of a straight element that extends from a known point $(s=0)$ to positive infinity. This type of element will be useful for the study of reflection of waves travelling along risers. The best way to obtain the stiffness matrix of this element is to start by rewriting equation (2.11) as

$$\begin{Bmatrix} \vec{U}_1 \\ \vec{U}_2 \end{Bmatrix} = \begin{bmatrix} [D_{11}] & [D_{12}] \\ [D_{21}] & [D_{22}] \end{bmatrix} \begin{Bmatrix} \vec{W}_r \\ \vec{W}_l \end{Bmatrix} \tag{2.15}$$

and (2.12) as

$$\begin{Bmatrix} \vec{F}_1 \\ \vec{F}_2 \end{Bmatrix} = \begin{bmatrix} [C_{11}] & [C_{12}] \\ [C_{21}] & [C_{22}] \end{bmatrix} \begin{Bmatrix} \vec{W}_r \\ \vec{W}_l \end{Bmatrix} \tag{2.16}$$

where the subscripts '1' and '2' refer to nodes 1 and 2 of the finite element shown in Figure 2-1 while 'r' and 'l' represent right-going or right-decaying waves and left-going or left-decaying waves, respectively. The subscript 'et' was omitted in this section to avoid difficulties to understanding other subscripts. However, it is important to emphasize that in this section we are working only with the element itself and considering only transverse motion. Vectors $\vec{U}_1$, $\vec{U}_2$, $\vec{F}_1$, $\vec{F}_2$, $\vec{W}_r$ and $\vec{W}_l$ have dimensions 2 by 1. The matrices $[D_{ij}]$ and $[C_{ij}]$ have dimensions 2 by 2 and they are sub-matrices of $[D]$ and $[C]$, respectively. According to this convention, $\vec{W}_r$ is the vector of the amplitudes of the right-going waves and $\vec{W}_l$ is the vector of the amplitudes of the left-going waves. $\vec{F}_1$ is the vector of forces that act upon node 1 and $\vec{F}_2$ is the vector of forces that act upon node 2.

Therefore, in order to make this beam element semi-infinite, we imagine that node 2 moves to positive infinity (see Figure 2-1) and that only right-going waves are present (which means that $\vec{W}_l = \vec{0}$). Then equations (2.15) and (2.16) can be redefined as

$$\left.\begin{aligned} \vec{U}_1 &= [D_{11}] \cdot \vec{W}_r \\ \vec{F}_1 &= [C_{11}] \cdot \vec{W}_r \end{aligned}\right\} \Rightarrow \vec{F}_1 = [C_{11}] \cdot [D_{11}]^{-1} \cdot \vec{U}_1 \Rightarrow \vec{F}_1 = [K_{et}] \cdot \vec{U}_1$$

where $[K_{ei}]=[C_{11}]\cdot[D_{11}]^{-1}$ is the dynamic stiffness matrix for the semi-infinite beam studied here. We can imagine now a propagating wave going in the direction of the end located in the infinite with wavelength $\gamma_1=\gamma_p$ and a evanescent wave, decaying in the same direction, with wavelength $\gamma_2=-i\gamma_e$. Substituting these values in the expression given above for $[K_{ei}]$, we will have

$$[K_{ei}]=\frac{EI}{\gamma_p^2+\gamma_e^2}\begin{bmatrix}-\left(\gamma_p^4\gamma_e+\gamma_p^2\gamma_e^3\right)-i\left(\gamma_e^4\gamma_p+\gamma_e^2\gamma_p^3\right) & i\left(\gamma_p^3\gamma_e+\gamma_p\gamma_e^3\right)\\ i\left(\gamma_p^3\gamma_e+\gamma_p\gamma_e^3\right) & \left(\gamma_p^2\gamma_e+\gamma_e^3\right)-i\left(\gamma_p^3+\gamma_e^2\gamma_p\right)\end{bmatrix}$$

It is interesting to note that, even though we are dealing with an elastic system, there will be dissipation due to radiation, as indicated by the imaginary parts of the stiffness matrix elements. This is caused by the fact that there are only right-going waves taking away with them the energy from the system.

2.5 Effects of Shear and Rotary Inertia

It was pointed out in the development of the governing equation for thin beams that two major assumptions were made: both the effects of shear deformation and rotary inertia were neglected. The basic assumption in excluding shear deformations was that a normal to the neutral axis of the beam remains straight during deformation and that its angular rotation is equal to the slope of the beam neutral axis (see section 2.2).

To take the effect of shear deformation into account in a beam bending analysis, we continue with the assumption that a plane section originally normal to the neutral axis remains plane but not normal to the neutral axis.

The study of wave propagation on beams under these assumptions showed that infinite phase velocities were predicted for high frequencies. This point will be exemplified later in this chapter. Hence, there are at least two cases where the consideration of both effects can have a significant influence:

1. If the cross-sectional dimensions are not small compared to the length of the beam.
2. When we are working with high frequencies.

To address this problem, in the next section we consider both effects in the wave propagation of beams.

2.5.1 Governing Equations

We consider here an element of beam lying on an elastic foundation (no dampers are considered here) and subjected to shear force, bending moment and a constant tension as shown in Figure 2-2. The displacement of the neutral plane of the beam is still measured by w and the slope of the longitudinal axis is still given by $\partial w / ds$. Now, a new independent variable ψ is introduced in order to measure the slope of the cross section due only to bending (see Figure 2-2). The slope of the longitudinal (neutral) axis is given by the following relationship

$$\frac{\partial w}{\partial s} = -(\psi + \phi) \tag{2.17}$$

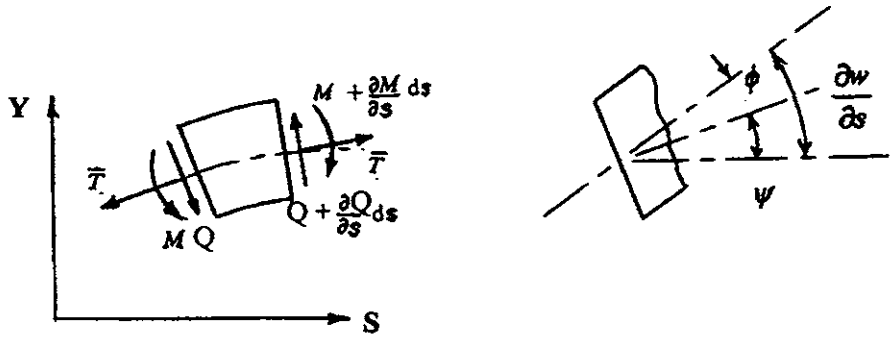

Figure 2-2: Differential element from a straight beam taking into account the effect of shear deformation

where ϕ is a constant shearing strain across the section of the beam. Since the real shearing stress and strain vary over the beam section, the shearing strain ϕ in equation (2.17) is an equivalent constant strain on a corresponding shear area A_S, defined by $A_S = \kappa A$, where κ is a adjustment coefficient that will depend on the shape of the cross section.

Another assumption is that the relationship between bending moment and curvature is expressed by

$$M = EI\frac{\partial \psi}{\partial s} \tag{2.18}$$

Now the shear force at any cross section is not determined through the knowledge of the bending moment as we did in equation (2.3). It is defined by

$$Q = -\tau A_S = -(G\phi)(\kappa A) = GA\kappa\left(\frac{\partial w}{\partial s} + \psi\right) \tag{2.19}$$

It is also noteworthy that we are still using the same system of reference as shown in Figure 2-1. Writing the equation of motion in the vertical direction for the element shown in Figure 2-2 we get

$$-Q + \left(Q + \frac{\partial Q}{\partial s}ds\right) + \overline{T}\alpha - \overline{T}\left(\alpha + \frac{\partial \alpha}{\partial s}ds\right) - kwds = \rho A ds\frac{\partial^2 w}{\partial t^2}$$

where $\alpha = -\dfrac{\partial w}{\partial s}$ is the rotation of the longitudinal axis.

After neglecting higher order effects and canceling opposite terms, the equation above can be reduced to the following

$$\frac{\partial Q}{\partial s} + \overline{T}\frac{\partial^2 w}{\partial s^2} - kw = \rho A\frac{\partial^2 w}{\partial t^2} \tag{2.20}$$

Writing the equation of motion about the axis of rotation and proceeding in the same way we did for the vertical direction we get

$$\frac{\partial M}{\partial s} - Q = \rho I\frac{\partial^2 \psi}{\partial t^2} \tag{2.21}$$

(a more detailed derivation of the equations of motion can be seen in the reference [16]). Substituting equations (2.18) and (2.19) into the two governing equations (2.20) and (2.21) gives

$$\begin{cases} GA\kappa\left(\dfrac{\partial^2 w}{\partial s^2}+\dfrac{\partial \psi}{\partial s}\right)+\overline{T}\dfrac{\partial^2 w}{\partial s^2}-kw=\rho A\dfrac{\partial^2 w}{\partial t^2} \\ -GA\kappa\left(\dfrac{\partial\ w}{\partial s}+\psi\right)+EI\dfrac{\partial^2 \psi}{\partial s^2}=\rho I\dfrac{\partial^2 \psi}{\partial t^2} \end{cases} \tag{2.22}$$

2.5.2 Dynamic Stiffness Matrix

To calculate the dynamic stiffness matrix of a straight beam element based on equations (2.22) we use the same procedure that was used before for the beam with no consideration of the effects of rotary inertia and shear deformation. In other words, we assume a harmonic solution of the form $w = w_0 \exp(i(\gamma s - \omega t))$ and $\psi = \psi_0 \exp(i(\gamma s - \omega t))$ and plug them into the governing equations (2.22) above. It gives

$$\begin{cases} GA\kappa\left(-w_0\gamma^2+i\gamma\psi_0\right)+\overline{T}\left(-w_0\gamma^2\right)-kw_0=\rho A\left(-w_0\omega^2\right) \\ -GA\kappa\left(i\gamma w_0+\psi_0\right)-EI\gamma^2\psi_0=-\rho I\omega^2\psi \end{cases} \tag{2.23}$$

The system of equations (2.23) can be rearranged and written in matrix form as

$$\begin{bmatrix} GA\kappa\gamma^2+\overline{T}\gamma^2+k-\rho A\omega^2 & -GA\kappa i\gamma \\ -iGA\kappa\gamma & -GA\kappa-EI\gamma^2+\rho I\omega^2 \end{bmatrix}\begin{Bmatrix} w_0 \\ \psi_0 \end{Bmatrix}=\begin{Bmatrix} 0 \\ 0 \end{Bmatrix} \tag{2.24}$$

It can be seen that equations (2.24) are satisfied by the trivial solution $w_0 = \psi_0 = 0$, which implies that there is no wave propagation. For a nontrivial solution, the determinant of the coefficients of w_0 and ψ_0 must be zero. After doing it and rearranging the terms we get:

$$\begin{aligned} &\gamma^4 EI\left(-GA\kappa-\overline{T}\right)+\gamma^2\left(GA\kappa\rho I\omega^2-\overline{T}GA\kappa+\overline{T}\rho I\omega^2-EIk+\rho AEI\omega^2\right) \\ &\quad+\rho Ik\omega^2-GA\kappa k+\rho A^2\omega^2 G\kappa-\rho A\omega^4 I=0 \end{aligned} \tag{2.25}$$

We can see that this equation has four roots. If we rewrite equation 2.25 as $l\gamma^4+m\gamma^2+n=0$, where

$$
\begin{aligned}
l &= -EI(GA\kappa - \overline{T}) \\
m &= GA\kappa\rho I\omega^2 - \overline{T}GA\kappa + \overline{T}\rho I\omega^2 - EIk + \rho EAI\omega^2 \\
n &= \rho Ik\omega^2 - GA\kappa k + \rho A^2\omega^2 G\kappa - \rho AI\omega^4
\end{aligned}
\tag{2.26}
$$

we can use the well known expressions for these four roots

$$
\begin{aligned}
\gamma_{1,2} &= \pm\frac{\sqrt{-2l\left(m - \sqrt{m^2 - 4\ln}\right)}}{2l} \\
\gamma_{3,4} &= \pm\frac{\sqrt{-2l\left(m + \sqrt{m^2 - 4\ln}\right)}}{2l}
\end{aligned}
\tag{2.27}
$$

Equations (2.24) are not independent of each other because we equated the determinant of coefficients to zero. From the bottom equation we obtain the following amplitude ratio

$$
\left(\frac{\psi_0}{w_0}\right)_j = i\frac{GA\kappa\gamma_j}{\rho I\omega^2 - GA\kappa - EI\gamma_j} = P_j, \quad j = 1,2,3,4 \tag{2.28}
$$

In equation (2.28) the symbol 'j' represents any one of the four waves traveling along the beam. Equation (2.28) shows that there is a relationship between the amplitude of vertical displacement and the amplitude of the rotation due to bending moment. Thus, the general solution for the system of equations (2.22), omitting the term $\exp(-i\omega t)$, is

$$
\begin{aligned}
w &= w_{01}\exp(i\gamma_1 s) + w_{02}\exp(i\gamma_2 s) + w_{03}\exp(i\gamma_3 s) + w_{04}\exp(i\gamma_4 s) \\
\psi &= \psi_{01}\exp(i\gamma_1 s) + \psi_{02}\exp(i\gamma_2 s) + \psi_{03}\exp(i\gamma_3 s) + \psi_{04}\exp(i\gamma_4 s)
\end{aligned}
\tag{2.29}
$$

where the amplitudes w_{0i} and ψ_{0i} are related by expression (2.29) and the wavenumbers γ_i are given by equations (2.26) and (2.27).

With this knowledge we can proceed using the WBFEM as was done before in section 2.3. The end conditions for displacements and forces are the following

$$
\begin{aligned}
u_1 &= w(s=0) \\
u_2 &= \psi(s=0) \\
u_3 &= w(s=L)
\end{aligned}
$$

$$u_4 = \psi(s = L)$$

$$f_1 = -GA\kappa(\frac{\partial w}{\partial s} + \psi) - \bar{T}\frac{\partial w}{\partial s}(s = 0) \tag{2.30}$$

$$f_2 = -EI\frac{\partial \psi}{\partial s}(s = 0)$$

$$f_3 = GA\kappa(\frac{\partial w}{\partial s} + \psi) + \bar{T}\frac{\partial w}{\partial s}(s = L)$$

$$f_4 = EI\frac{\partial \psi}{\partial s}(s = L)$$

Substituting equations (2.29) into (2.30) we get the following matrix relations

$$\vec{U}_{et} = [D]\cdot\vec{W} \quad \text{and} \quad \vec{F}_{et} = [C]\cdot\vec{W}$$

where

$$[D] = \begin{bmatrix} 1 & 1 & 1 & 1 \\ P_1 & P_2 & P_3 & P_4 \\ \exp(i\gamma_1 L) & \exp(i\gamma_2 L) & \exp(i\gamma_3 L) & \exp(i\gamma_4 L) \\ P_1\exp(i\gamma_1 L) & P_2\exp(i\gamma_2 L) & P_3\exp(i\gamma_3 L) & P_4\exp(i\gamma_4 L) \end{bmatrix}$$

$$[C] = \begin{bmatrix} -GA\kappa(i\gamma_1 + P_1) & -GA(i\gamma_2 + P_2) \\ -iEI\gamma_1 P_1 & -iEI\gamma_2 P_2 \\ GA\kappa(i\gamma_1 + P_1)\exp(i\gamma_1 L) & GA(i\gamma_2 + P_2)\exp(i\gamma_2 L) \\ iEI\gamma_1 P_1\exp(i\gamma_1 L) & iEI\gamma_2 P_2\exp(i\gamma_2 L) \end{bmatrix}$$

$$\begin{bmatrix} -GA\kappa(i\gamma_3 + P_3) & -GA(i\gamma_4 + P_4) \\ -iEI\gamma_3 P_3 & -iEI\gamma_4 P_4 \\ GA\kappa(i\gamma_3 + P_3)\exp(i\gamma_3 L) & GA(i\gamma_4 + P_4)\exp(i\gamma_4 L) \\ iEI\gamma_3 P_3\exp(i\gamma_3 L) & iEI\gamma_4 P_4\exp(i\gamma_4 L) \end{bmatrix} +$$

$$\bar{T}\begin{bmatrix} -i\gamma_1 & -i\gamma_2 & -i\gamma_3 & -i\gamma_4 \\ 0 & 0 & 0 & 0 \\ i\gamma_1\exp(i\gamma_1 L) & i\gamma_2\exp(i\gamma_2 L) & i\gamma_3\exp(i\gamma_3 L) & i\gamma_4\exp(i\gamma_4 L) \\ 0 & 0 & 0 & 0 \end{bmatrix}$$

The sign in the first two rows of matrix $[C]$ had to be reversed for the same reason as explained before, in section 2.3. The matrix $[K_{el}]$ is obtained by the expression $[C]\cdot[D]^{-1}$.

2.6 Examples

2.6.1 Wave Dispersion

For the first example, we will study the wave dispersion of a straight beam supported by a visco-elastic foundation and subjected to a constant tension. This beam is also in water, since it is was taken from a steel catenary riser that will be studied in chapter 5. The objective of this example is to study the relationship between the wavelength γ and wave frequency ω according to the wave dispersion. The properties of the beam are $E = 2.067\times10^{11}\ N/m^2$, $A = 0.007426m^2$, $I = 0.2181\times10^{-4}m^4$, $\rho = 10759.6kg/m^3$, $H_d = 0.181m$. We will study different cases of the same beam but with increasing complexity

- *Pure beam element*

Here we study only a beam element without foundation (which means $k = 0$), static tension (i.e., $\overline{T} = 0$) or damping. In this case, the wave dispersion equation is given by

$$EI\gamma^4 + \rho A\omega^2 = 0$$

There are four wavenumber roots at each frequency for this equation and since it is second order in γ^2, two of them are negative values of the two other roots. Hence, there are two pure real roots, $\pm\gamma_p$, corresponding to the propagating waves and two pure imaginary roots, $\pm i\gamma_e$, corresponding to the evanescent waves. Plotting the relation between wavenumber γ_p and frequency, in Hz (obtained by calculating $\frac{\omega}{2\pi}$), for the data given above, we obtain the curve

shown below, in Figure 2-3. It expresses the idea that as the frequency increases, the wavelength decreases.

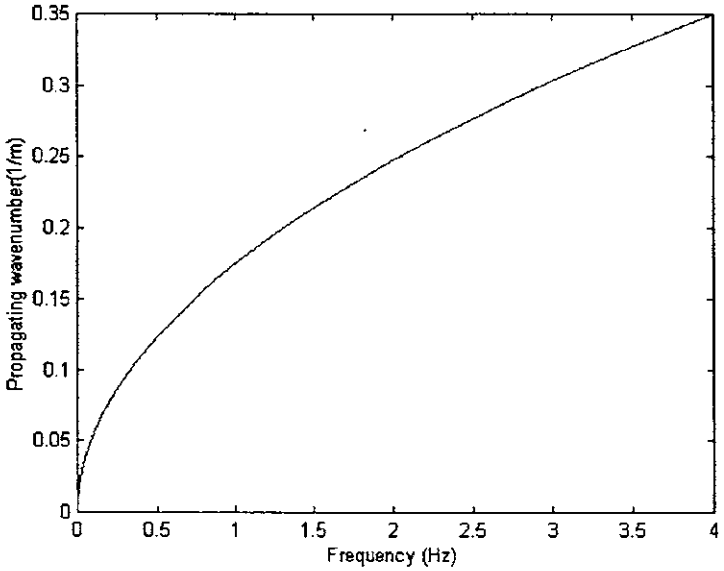

Figure 2-3: Curve of the wave dispersion relation regarding a transverse propagating wave on a beam.

- *The beam on an elastic foundation*

After setting $\overline{T} = c = 0$ and $k = 100kN/m$, the wave dispersion, represented by equation (2.6), becomes

$$EI\gamma^4 + k + \rho A\omega^2 = 0$$

Solving this equation for γ we have

$$\gamma^4 = \omega^2 \frac{\rho A}{EI} - \frac{k}{EI} \tag{2.31}$$

The roots of equation (2.31) are the four wavenumbers are given by equations (2.7). If we pick γ_1 and plot it against frequency ω we obtain the curve shown in Figure 2-4. In this plot, we used frequency in Hz, which is obtained by the ratio $\frac{\omega}{2\pi}$. If we do the same for the other wavenumbers, the result is the plot shown schematically in Figure 2-5.

If we set $\gamma = 0$ in equation (2.31) we will have $\omega^2 = \frac{k}{\rho A}$ which can be considered a cutoff frequency. For frequencies above the cutoff there is either purely harmonic wave propagation or purely evanescent wave. For frequencies below cutoff there is propagating wave (because of the real part of γ) with spatially varying amplitude (because of the imaginary part of γ) and the real part is equal to the imaginary part. It is noteworthy that in this perfectly elastic system we can encounter complex wavenumbers. It also happens for problems associated with energy losses of the system.

For the case considered in the present example, the cutoff frequency is equal to 4.88 Hz (see Figure 2-4 below).

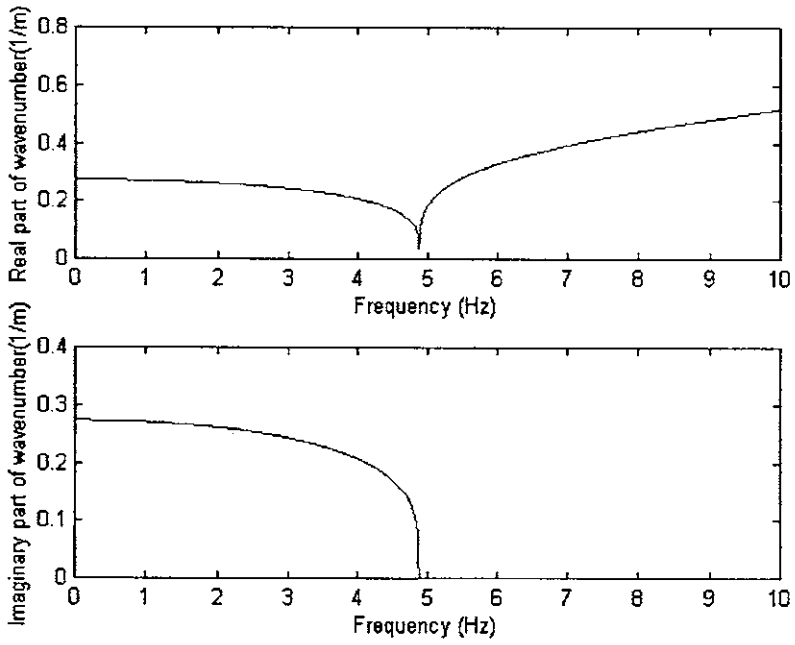

Figure 2-4: Frequency spectrum for one wavenumber of a straight beam element on an elastic foundation.

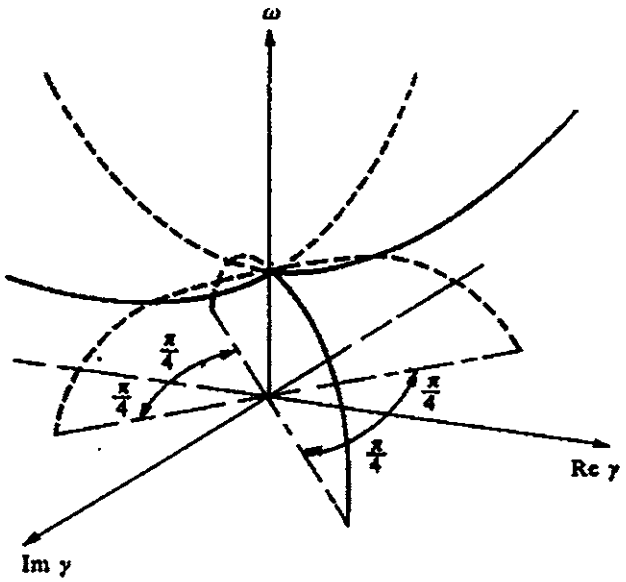

Figure 2-5: Complete frequency spectrum for all four wavenumbers of a straight beam element on an elastic foundation. Reproduced from reference [16].

- *The beam on an elastic foundation and subjected to tension*

Now we set $\overline{T} = 121250N$, $c = 0$ and $k = 100kN/m$. According to equations (2.7) one wavenumber is given by

$$\gamma_1 = \sqrt{-\frac{\overline{T}}{2EI} + \sqrt{\left(\frac{\overline{T}}{2EI}\right)^2 + \frac{\rho A\omega^2 - k}{EI}}}$$

or, rewriting it

$$\gamma_1 = \sqrt{-\frac{\overline{T}}{2EI} + \sqrt{\omega^2 \frac{\rho A}{EI} + \frac{\overline{T}^2 - 4EIk}{4E^2I^2}}} \tag{2.32}$$

In order to have $\gamma_1 = 0$, the frequency, ω, will have to be equal to $\sqrt{\frac{k}{\rho A}}$ again. For frequencies above this cutoff, the wavenumber γ_1 will be real, which means purely propagating wave.

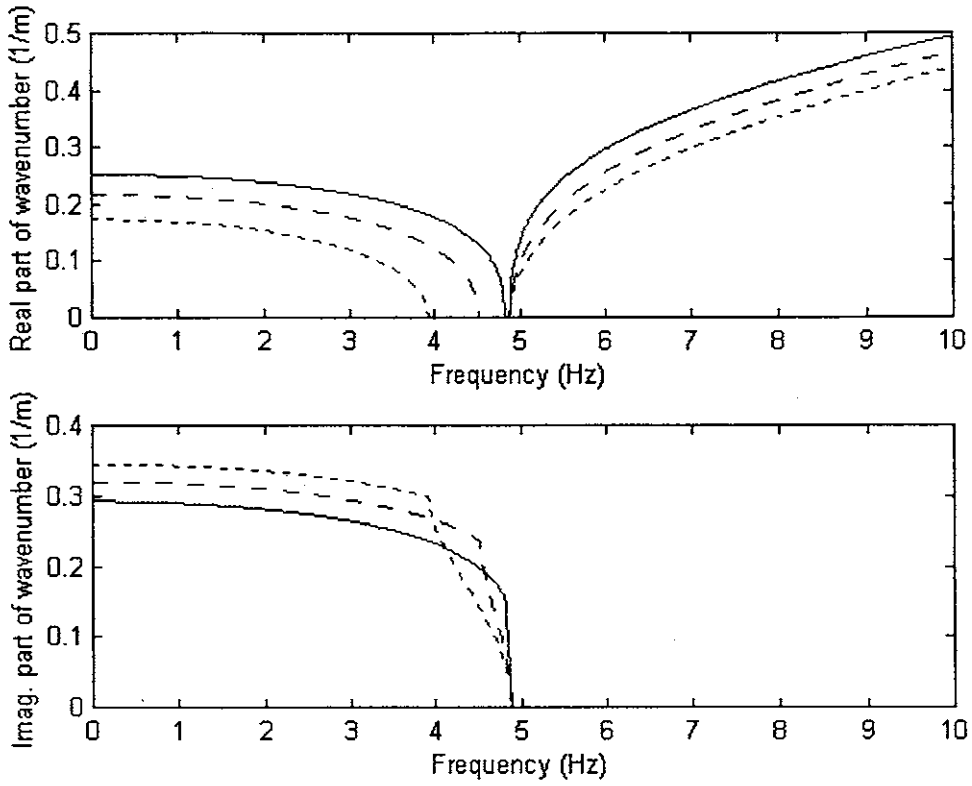

Figure 2-6: Dispersion relation for a straight beam element on elastic foundation subjected to three different static tensions: 800kN for dotted curve, 500kN for dashed curve and 200kN for solid curve.

Another point is that if set $\omega = \sqrt{\frac{k}{\rho A} - \frac{\overline{T}^2}{4EI\rho A}} = \omega_0$, then from (2.32) we will have $\gamma_1^2 = -\frac{\overline{T}}{2EI}$, i.e., it will be purely imaginary. Thus, there are three different ranges of frequencies: above cutoff, between cutoff and ω_0 (there will be only evanescent waves which means no propagating waves occurs) and below ω_0 (there will be propagating waves with amplitude varying in space). Notice that ω_0 will always be smaller than the cutoff frequency, as long as $\overline{T}$ is tensile. The plot for the curve of γ_1 as a function of frequency (in Hz) is shown in Figure 2-6. We can see that the cutoff frequency is not affected by $\overline{T}$ but ω_0 gets closer to the cutoff as $\overline{T}$ decreases. The ultimate stage would be the previous example studied where $\overline{T} = 0$. The

complete plot including the four wavenumbers is not shown because it would be too messy, making the understanding more difficult.

- *The beam on a visco-elastic foundation and subjected to tension*

Finally, we set $\overline{T} = 200000N$, $c = 10Ns/m^2$ and $k = 100kN/m$. Two curves are presented in Figure 2-7 for the dispersion relation, showing the influence of the soil damping c on the wavenumber: curve 1, with $c = 10Ns/m^2$ and curve 2, with $c = 100Ns/m^2$.

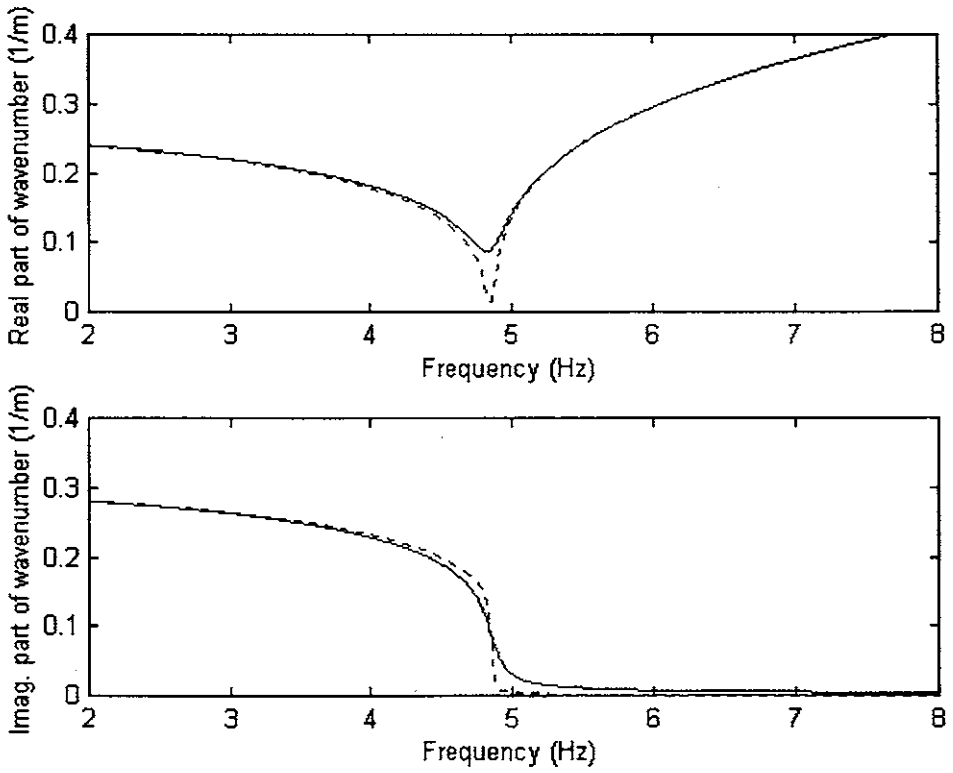

Figure 2-7: Dispersion relation for a straight beam element on visco-elastic foundation subjected to a static tensions of 200kN with two different values of soil damping: $c = 10Ns/m^2$ for dotted curve and $c = 100Ns/m^2$ for solid curve.

2.7 Reflection Coefficients

When a wave is propagating on a beam and encounters a certain kind of discontinuity (a change in mass, cross-section or flexural rigidity, for example) part of it will be reflected and part will continue to travel in the same direction. The situation is represented schematically in the Figure 2-8 where the beam is supposed to extend to plus infinity and the discontinuity to minus infinity. Using the WBFEM, the reflection coefficient (the relationship between the incident wave and the reflected wave) is relatively easy to be obtained. This is because the knowledge of the waves travelling in terms of wave number and direction is available.

First it is assumed that the discontinuity that generates the wave reflection is represented by a dynamic stiffness $[K_t]$. This matrix means that if a displacement vector $\vec{U} = \{u_1 \quad u_2\}^T$ is applied to the end of the discontinuity without the beam, a certain force vector $\vec{F} = \{f_1 \quad f_2\}^T$ will result on the same location. Applying the dynamic equilibrium to the discontinuity shown in Figure 2-8 we have

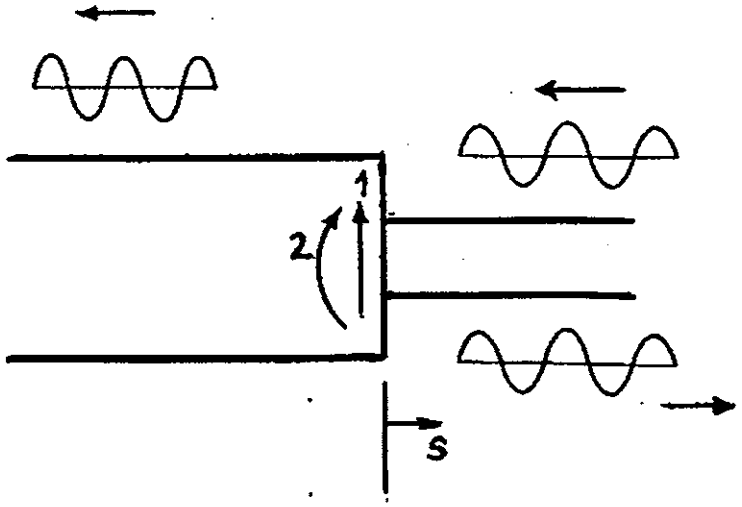

Figure 2-8: Reflection of an incident wave when it encounters a discontinuity on the beam.

$$[K_t]\vec{U}_t = \vec{F}_t \tag{2.33}$$

Looking at equations (2.15) and (2.16) we see that the vector of displacements and forces at the left end of the beam depicted in Figure 2-8 are defined as

$$\begin{aligned} \vec{U}_1 &= [D_{11}]\cdot\vec{W}_r + [D_{12}]\cdot\vec{W}_l \\ \vec{F}_1 &= [C_{11}]\cdot\vec{W}_r + [C_{12}]\cdot\vec{W}_l \end{aligned} \tag{2.34}$$

Now we can impose continuity of displacements and forces between the beam and the discontinuity:

$$\begin{aligned} \vec{U}_t &= \vec{U}_1 \\ \vec{F}_t &= -\vec{F}_1 \end{aligned} \tag{2.35}$$

After substitution of equations (2.34) and (2.35) into (2.33) we get

$$[K_t]\cdot([D_{11}]\cdot\vec{W}_r + [D_{12}]\cdot\vec{W}_l) = -([C_{11}]\cdot\vec{W}_r + [C_{12}]\cdot\vec{W}_l)$$

From the equation above we can obtain the amplitude ratio vector

$$\vec{W}_r = -([K_t]\cdot[D_{11}]+[C_{11}])^{-1}\cdot([K_t]\cdot[D_{12}]+[C_{12}])\cdot\vec{W}_l \tag{2.36}$$

The equation above gives the amplitude of the right-going wave (reflected) per unit amplitude of the left-going wave (incident). To exemplify the use of equation (2.36) in the calculation of the wave reflection, we can imagine a tensioned straight beam like the one shown in Figure 2-8. Let's assume it has two purely propagating wavenumbers, γ_P (rightward) and $-\gamma_P$ (leftward), and two purely attenuated wavenumber, γ_A and $-\gamma_A$. These waves are sorted so that $\gamma_1 = \gamma_P$, $\gamma_2 = -\gamma_A$, $\gamma_3 = -\gamma_P$ and $\gamma_4 = \gamma_A$. If we set $\vec{W}_l = \{1 \quad 0\}^T$, we impose a propagating incident wave of unit amplitude with no amplitude attenuation. Using equation (2.36) we can obtain $\vec{W}_r$ which corresponds to the amplitudes of the reflected waves, both propagating and evanescent. It is in this sense that $\vec{W}_r$ is being called amplitude ratio.

The method explained in this section is general and can be used for straight and curved beam elements. We just have to use the appropriate vectors and matrices in equation (2.36).

2.8 Beams with Slowly Varying Tension

Now the case of a beam element with a slowly varying tension will be studied here. The local system of reference for the end displacements and forces is the same as the one shown in Figure 2-1. It is an attempt to improve the results that can be obtained with the methodology used previously for the constant tension beam. First we will neglect the effect of shear deformation and then we will study the same type of element considering the effect of shear deformation. Although this effect is not important for the range of frequencies we are working with, the procedure adopted in this section is very similar to the one we are going to use for the curved beam with slowly varying tension but a little simpler. Thus, it will not only help in understanding the method applied to the curved beam element (see chapter 3) but also establish the formulation for this type of element and it will be available in case another researcher needs to use it.

2.8.1 Neglecting the Effect of Shear Deformation

In terms of the application of the WBFEM, the procedure used in the previous sections can be adopted for the case of the beam element with slowly varying static tension, $\overline{T}$, once we know the expression for the transverse displacement along it. The main difference is how the solution of the differential equation is obtained. This time it will be approximate as we are going to use the WKB method.

The differential equation of dynamic equilibrium for the free vibration of beam can be rewritten in a more general way as

$$\frac{\partial^2}{\partial s^2}\left(EI\frac{\partial^2 w}{\partial s^2}\right)-\frac{\partial}{\partial s}\left(\overline{T}(s)\frac{\partial w}{\partial s}\right)+\rho A\frac{\partial^2 w}{\partial t^2}=0 \qquad (2.37)$$

The expressions for the bending moment, M , and shear force, V , are given by

$$M = -EI\frac{\partial^2 w}{\partial s^2} \tag{2.38}$$

$$Q = -EI\frac{\partial^3 w}{\partial s^3} \tag{2.39}$$

This time the influence of a visco-elastic foundation will not be taken into consideration because in a riser configuration there is no tension variation on a beam lying on a horizontal foundation. The solution of equation (2.37) can be sought through the formal procedure of the WKB method. We look for a time harmonic solution like $w(s,t) = \hat{w}(s)\exp(-i\omega t)$. After substitution of this expression into (2.38) we get

$$\frac{\partial^2}{\partial s^2}\left(EI\frac{\partial^2 \hat{w}}{\partial s^2}\right) - \frac{\partial}{\partial s}\left(\overline{T}(s)\frac{\partial \hat{w}}{\partial s}\right) - \rho A\,\hat{w}(s)\omega^2 = 0 \tag{2.40}$$

According to WKB method, we can assume that

$$\hat{w}(s) = \exp(i\theta(s))\{w_0(s) + w_1(s) + w_2(s) + \ldots\}$$

where

$$\frac{\partial\theta}{\partial s} = \gamma(s)$$

$$w_0(s) >> w_1(s) >> w_2(s) >> \ldots$$

In the present work, we will consider that

$$\hat{w}(s) = \exp(i\theta(s))w_0(s) \tag{2.41}$$

where $w_0(s)$ is the slowly varying amplitude of the wave. Equation (2.40) can be expanded to the following form

$$\frac{\partial^2 EI}{\partial s^2}\frac{\partial^2 \hat{w}}{\partial s^2} + 2\frac{\partial(EI)}{\partial s}\frac{\partial^3 \hat{w}}{\partial s^3} + EI\frac{\partial^4 \hat{w}}{\partial s^4} - \frac{\partial\overline{T}(s)}{\partial s}\frac{\partial \hat{w}}{\partial s} - \overline{T}(s)\frac{\partial^2 \hat{w}}{\partial s^2} - m_t\,\hat{w}(s)\omega^2 = 0 \tag{2.42}$$

where $m_t = \rho A$.

To substitute equation (2.41) into (2.42), it is important that first we obtain the expressions for the derivatives of $\hat{w}$:

- $\frac{d\hat{w}}{ds} = (\frac{dw_0}{ds} + w_0 i\gamma)\exp(i\theta)$
- $\frac{d^2\hat{w}}{ds^2} = (\frac{d^2w_0}{ds^2} + 2\frac{dw_0}{ds}ik - w_0\gamma^2 + w_0 i\frac{d\gamma}{ds})\exp(i\theta)$
- $\frac{d^3\hat{w}}{ds^3} = (\frac{d^3w_0}{ds^3} + 3\frac{d^2w_0}{ds^2}i\gamma + 3\frac{dw_0}{ds}i\frac{d\gamma}{ds} - 3\frac{dw_0}{ds}\gamma^2)\exp(i\theta)$ (2.43)
- $\frac{d^4\hat{w}}{ds^4} = (\frac{d^4w_0}{ds^4} + \frac{d^3w_0}{ds^3}i\gamma + 3\left(\frac{d^3w_0}{ds^3}\right) + 6i\left(\frac{d^2w_0}{ds^2}\right)\frac{d\gamma}{ds} - 6\left(\frac{d^3w_0}{ds^3}\right)\gamma^2 + 4i\frac{dw_0}{ds}\frac{d^2\gamma}{ds^2} -$

$$18\gamma\frac{dw_0}{ds}\frac{d\gamma}{ds} - 4i\frac{dw_0}{ds}\gamma^3 - 3w_0\left(\frac{d\gamma}{ds}\right)^2 - 3w_0\gamma\frac{d^2\gamma}{ds^2} - 6iw_0\gamma^2\frac{d\gamma}{ds} - w_0\gamma^4 + iw_0\frac{d^3\gamma}{ds^3} -$$

$$w_0\gamma\frac{d^2\gamma}{ds^2})\exp(i\theta)$$

As we are dealing with slowly varying quantities, the order of the first derivative of w_0 is smaller than the order of w_0. Thus, after we substitute equations (2.43) and (2.41) into equation (2.42) we can group the terms with the same order and make the sum of them equal to zero. This way we have an idea of the behavior of the beam element at each order. The terms without any derivatives have the highest order of all in equation (2.42) and they will be grouped first. We are going to examine this procedure in detail.

The first two terms in equation (2.42) contribute nothing to the leading order because bending stiffness is considered constant inside the beam element. Even if they involved slowly varying quantities, they would contribute nothing because they have second and first derivatives of bending stiffness. The third term has a fourth order derivative of $\hat{w}$. If we look at its expression

in (2.44), we see that the only term with leading order is $-w_0\gamma^4$. The fourth term contribute nothing to the leading order either because of the first derivative of $\overline{T}$. The fifth term has a second derivative of $\hat{w}$. Looking at the explicit expression for this derivative in (2.44), we see that the only contributing term is $-w_0\gamma^2$. Finally, the last term contributes because there is no derivatives in it. Therefore, to the leading order, we have:

$$-(EI\gamma^4+\overline{T}\gamma^2+m_t\omega^2)w_0\exp(i\theta)=0 \qquad \Rightarrow \qquad EI\gamma^4+\overline{T}\gamma^2+m_t\omega^2=0 \qquad (2.44)$$

The interesting point here is that, to the leading order, the beam has the same dispersion relation as the uniform beam.

The next-order terms are those that have just the first derivative in their expressions. Following the same procedure that was used for the leading order terms, we get for the next lower order:

$$EI\left(-3i\frac{dw_0}{ds}\gamma^3-3iw_0\gamma^2\frac{d\gamma}{ds}-i\gamma^3\frac{dw_0}{ds}-3iw_0\gamma^2\frac{d\gamma}{ds}\right)-i\frac{d\overline{T}}{ds}w_0\gamma-2iw_0\gamma^3\frac{d(EI)}{ds}$$
$$-\overline{T}\left(2i\gamma\frac{dw_0}{ds}+iw_0\frac{d\gamma}{ds}\right)=0$$

where the common term $\exp(i\theta)$ was left out of the equation. After rearranging, this equation can be rewritten as

$$2\frac{dw_0}{ds}\left(-2EI\gamma^3-\overline{T}\gamma\right)+w_0\left(-6EI\gamma^2\frac{d\gamma}{ds}-2\gamma^3\frac{d(EI)}{ds}-\gamma\frac{d\overline{T}}{ds}-\overline{T}\frac{d\gamma}{ds}\right)=0$$

which is equivalent to

$$\frac{d}{ds}\left(w_0^2(-2\gamma^3EI-\overline{T}\gamma)\right)=0 \qquad \Rightarrow \qquad w_0^2(2\gamma^3EI+\overline{T}\gamma)=C_1^2$$

Hence

$$w_0=\frac{C_1}{\sqrt{2\gamma^3EI+\overline{T}\gamma}} \qquad (2.45)$$

The last equation gives the value of w_0, which is dependent of a constant C_1 to be determined by the boundary conditions.

Thus, the general solution for the differential equation (2.40), up to the order considered here, is

$$\hat{w}(s) = w_{01}\exp(i\theta_1) + w_{02}\exp(i\theta_2) + w_{03}\exp(i\theta_3) + w_{04}\exp(i\theta_4) \tag{2.46}$$

where θ_i is a function of s and is given by $\int_0^s \gamma_i(\xi)d\xi$, γ_i is given by the roots of equation (2.44) and w_{0i} is given by equation (2.45).

Now we can proceed with the calculation of matrices $[C]$, $[D]$ and consequently $[K_{et}]$ by using the WBFEM. Once we know the expression that defines the transverse displacement (see equation 2.46) we need to obtain the vectors of end displacements $\vec{U}_{et}$ and end forces $\vec{F}_{et}$. In order to achieve this goal, we first have to obtain the following quantities:

- At $s = 0$

$$\hat{w} = w_{01}(0) + w_{02}(0) + w_{03}(0) + w_{04}(0)$$

$$\frac{d\hat{w}}{ds} = w_{01}(0)i\gamma_1(0) + w_{02}(0)i\gamma_2(0) + w_{03}(0)i\gamma_3(0) + w_{04}(0)i\gamma_4(0)$$

$$\frac{d^2\hat{w}}{ds^2} = -w_{01}(0)\gamma_1^2(0) - w_{02}(0)\gamma_2^2(0) - w_{03}(0)\gamma_3^2(0) - w_{04}(0)\gamma_4^2(0)$$

$$\frac{d^3\hat{w}}{ds^3} = -iw_{01}(0)\gamma_1^3(0) - iw_{02}(0)\gamma_2^3(0) - iw_{03}(0)\gamma_3^3(0) - iw_{04}(0)\gamma_4^3(0)$$

- At $s = L$

$$\hat{w} = w_{01}(L)\exp\left(i\int_0^l \gamma_1(\xi)d\xi\right) + w_{02}(L)\exp\left(i\int_0^l \gamma_2(\xi)d\xi\right) +$$
$$w_{03}(L)\exp\left(i\int_0^l \gamma_3(\xi)d\xi\right) + w_{04}(L)\exp\left(i\int_0^l \gamma_4(\xi)d\xi\right)$$

$$\frac{d\hat{w}}{ds} = w_{01}(L)i\gamma_1(L)\exp\left(i\int_0^l \gamma_1(\xi)d\xi\right) + w_{02}(L)i\gamma_2(L)\exp\left(i\int_0^l \gamma_2(\xi)d\xi\right) +$$

$$w_{03}(L)i\gamma_3(L)\exp\left(i\int_0^l \gamma_3(\xi)d\xi\right) + w_{04}(L)i\gamma_4(L)\exp\left(i\int_0^l \gamma_4(\xi)d\xi\right)$$

$$\frac{d^2\hat{w}}{ds^2} = -w_{01}(L)i\gamma_1^2(L)\exp\left(i\int_0^l \gamma_1(\xi)d\xi\right) - w_{02}(L)i\gamma_2^2(L)\exp\left(i\int_0^l \gamma_2(\xi)d\xi\right) -$$

$$w_{03}(L)i\gamma_3^2(L)\exp\left(i\int_0^l \gamma_3(\xi)d\xi\right) - w_{04}(L)i\gamma_4^2(L)\exp\left(i\int_0^l \gamma_4(\xi)d\xi\right)$$

$$\frac{d^3\hat{w}}{ds^3} = -iw_{01}(L)i\gamma_1^3(L)\exp\left(i\int_0^l \gamma_1(\xi)d\xi\right) - iw_{02}(L)i\gamma_2^3(L)\exp\left(i\int_0^l \gamma_2(\xi)d\xi\right) -$$

$$iw_{03}(L)i\gamma_3^3(L)\exp\left(i\int_0^l \gamma_3(\xi)d\xi\right) - iw_{04}(L)i\gamma_4^3(L)\exp\left(i\int_0^l \gamma_4(\xi)d\xi\right)$$

To reduce the size of the expressions for the components of matrices $[D]$ and $[C]$, the following designations will be made

$$B_j = \int_0^L \gamma_j(\xi)d\xi \qquad e_j = \frac{C_j}{\sqrt{2\gamma_j{}^3 EI + \bar{\bar{T}}\gamma_j}} \quad j = 1,2,3,4 \tag{2.47}$$

The integral in equation (2.47) is performed numerically.

The end conditions for displacements are:

$$\begin{aligned} u_1 &= \hat{w}(s=0) \\ u_2 &= -\frac{\partial \hat{w}}{\partial s}(s=0) \\ u_3 &= \hat{w}(s=L) \\ u_4 &= -\frac{\partial \hat{w}}{\partial s}(s=L) \end{aligned} \tag{2.48}$$

The end conditions for forces are:

$$f_1 = EI\frac{\partial^3 \hat{w}}{\partial s^3} - \bar{T}\frac{\partial \hat{w}}{\partial s}(s=0)$$

$$f_2 = EI\frac{\partial^2 \hat{w}}{\partial s^2}(s=0)$$

$$f_3 = -EI\frac{\partial^3 \hat{w}}{\partial s^3} + \bar{T}\frac{\partial \hat{w}}{\partial s}(s=L) \qquad (2.49)$$

$$f_4 = -EI\frac{\partial^2 \hat{w}}{\partial s^2}(s=L)$$

Applying equation (2.46) into equations (2.48) and (2.49) and writing the result in matrix form we obtain the expressions for the matrices $[C]$ and $[D]$. Then $[K_{et}]$ is obtained through the expression $[C]\cdot[D]^{-1}$.

$$[D] = \begin{bmatrix} e_1(0) & e_2(0) & e_3(0) & e_4(0) \\ e_1(0)i\gamma_1(0) & e_2(0)i\gamma_2(0) & e_3(0)i\gamma_3(0) & e_4(0)i\gamma_4(0) \\ e_1(L)\exp(iB_1) & e_2(L)\exp(iB_2) & e_3(L)\exp(iB_3) & e_4(L)\exp(iB_4) \\ e_1(0)i\gamma_1(0)\exp(iB_1) & e_2(0)i\gamma_2(0)\exp(iB_2) & e_3(0)i\gamma_3(0)\exp(iB_3) & e_4(0)i\gamma_4(0)\exp(iB_4) \end{bmatrix}$$

$$[C] = EI\begin{bmatrix} -ie_1(0)\gamma_1^3(0) & -ie_2(0)\gamma_2^3(0) \\ -e_1(0)\gamma_1^2(0) & -e_2(0)\gamma_2^2(0) \\ ie_1(L)\gamma_1^3(L)\exp(iB_1) & ie_2(L)\gamma_2^3(L)\exp(iB_2) \\ e_1(L)\gamma_1^2(L)\exp(iB_1) & e_2(L)\gamma_2^2(L)\exp(iB_2) \end{bmatrix}$$

$$\begin{bmatrix} -ie_3(0)\gamma_3^3(0) & -ie_4(0)\gamma_4^3(0) \\ -e_3(0)\gamma_3^2(0) & -e_4(0)\gamma_4^2(0) \\ ie_3(L)\gamma_3^3(L)\exp(iB_3) & ie_4(L)\gamma_4^3(L)\exp(iB_4) \\ e_3(L)\gamma_3^2(L)\exp(iB_3) & e_4(L)\gamma_4^2(L)\exp(iB_4) \end{bmatrix} +$$

$$\bar{T}\begin{bmatrix} -ie_1(0)\gamma_1(0) & -ie_2(0)\gamma_2(0) \\ 0 & 0 \\ ie_1(L)\gamma_1(L)\exp(iB_1) & ie_2(L)\gamma_2(L)\exp(iB_2) \\ 0 & 0 \end{bmatrix}$$

$$\begin{bmatrix} -ie_3(0)\gamma_3(0) & -ie_4(0)\gamma_4(0) \\ 0 & 0 \\ ie_3(L)\gamma_3(L)\exp(iB_3) & ie_4(L)\gamma_4(L)\exp(iB_4) \\ 0 & 0 \end{bmatrix}$$

2.8.2 Considering Shear Deformation Effects

A completely analogous procedure can be followed to consider the effects of shear deformation and rotary inertia for the case of beam element with varying properties (in our case, these properties can be cross-sectional area, moment of inertia and static tension). The only difference is that now we are going to work with two quantities. In the case of curved beam it is going to be three.

Rewriting the governing equations (2.20) and (2.21) in a more general way, taking into account varying properties, we get

$$\begin{aligned} &\frac{\partial Q}{\partial s}+\frac{\partial}{\partial s}\left(\bar{T}\frac{\partial w}{\partial s}\right)-kw-\rho A\frac{\partial^2 w}{\partial t^2}=0 \\ &\frac{\partial M}{\partial s}-Q=\rho I\frac{\partial^2 \psi}{\partial t^2} \end{aligned} \tag{2.50}$$

Substituting the expressions $Q=GA\kappa\left(\frac{\partial w}{\partial s}+\psi\right)$ and $M=EI\frac{\partial \psi}{\partial s}$ into equations (2.50) above and expanding them we get

$$\begin{aligned} &\frac{\partial(GA\kappa)}{\partial s}\left(\frac{\partial w}{\partial s}+\psi\right)+GA\kappa\left(\frac{\partial^2 w}{\partial s^2}+\frac{\partial \psi}{\partial s}\right)+\frac{\partial \bar{T}}{\partial s}\frac{\partial w}{\partial s}+\bar{T}\frac{\partial^2 w}{\partial s^2}-kw-m\frac{\partial^2 w}{\partial t^2}=0 \\ &\frac{\partial(EI)}{\partial s}\frac{\partial \psi}{\partial s}+EI\frac{\partial^2 \psi}{\partial s^2}-GA\kappa\left(\frac{\partial w}{\partial s}+\psi\right)-m\frac{\partial^2 \psi}{\partial t^2}=0 \end{aligned} \tag{2.51}$$

If we assume solutions of the form $w=\hat{w}\exp(-i\omega t)$ and $\psi=\hat{\psi}\exp(-i\omega t)$ and then plug them into the governing equations (2.51) above we get

$$\frac{\partial(GA\kappa)}{\partial s}\left(\frac{\partial \hat{w}}{\partial s}+\hat{\psi}\right)+GA\kappa\left(\frac{\partial^2 \hat{w}}{\partial s^2}+\frac{\partial \hat{\psi}}{\partial s}\right)+\frac{\partial \bar{T}}{\partial s}\frac{\partial \hat{w}}{\partial s}+\bar{T}\frac{\partial^2 \hat{w}}{\partial s^2}-k\hat{w}+m_t\omega^2\hat{w}=0$$

$$\frac{\partial(EI)}{\partial s}\frac{\partial \hat{\psi}}{\partial s}+EI\frac{\partial^2 \hat{\psi}}{\partial s^2}-GA\kappa\left(\frac{\partial \hat{w}}{\partial s}+\hat{\psi}\right)-m_r\omega^2\frac{\partial^2 \hat{\psi}}{\partial t^2}=0 \qquad (2.52)$$

where $m_t=\rho A$ and $m_r=\rho I$.

It is assumed now that the relationships $\hat{w}=w_0\exp(i\theta)$ and $\hat{\psi}=\psi_0\exp(i\theta)$ are valid, as we did in section 2.8.1 (see equation (2.41)). After substitution of these expressions for $\hat{w}$, $\hat{\psi}$ and its corresponding derivatives (see equations (2.43)) into equations (2.52) above, we start to collect the terms with the same order. This procedure was explained in detail before, in section 2.8.1 and will be used here again. Beginning by collecting the terms with the leading order, we get

$$GA\kappa(\psi_0 i\gamma-w_0\gamma^2)-\bar{T}\gamma^2 w_0-kw_0+m_t\omega^2 w_0=0$$
$$-EI\gamma^2\psi_0-GA\kappa(w_0 i\gamma+\psi_0)+m_r\omega^2\psi_0=0$$

These equations are similar to the dispersion relation obtained for the case of beam with constant tension distribution. All the conclusions derived in section 2.5.2 are locally valid here, for instance equation (2.28).

Collecting the next-order terms we get

$$\frac{\partial(GA\kappa)}{\partial s}(w_0 i\gamma+\psi_0)+GA\kappa\left(2\frac{\partial w_0}{\partial s}i\gamma+w_0 i\frac{\partial\gamma}{\partial s}+\frac{\partial\psi_0}{\partial s}\right)+\frac{\partial\bar{T}}{\partial s}w_0 i\gamma+\bar{T}\left(2\frac{\partial w_0}{\partial s}i\gamma+w_0 i\frac{\partial\gamma}{\partial s}\right)=0$$
$$\frac{\partial EI}{\partial s}\psi_0 i\gamma+EI\left(2\frac{\partial\psi_0}{\partial s}i\gamma+\psi_0 i\frac{\partial\gamma}{\partial s}\right)-GA\kappa\frac{\partial w_0}{\partial s}=0$$

Rearranging the equations we get

$$\frac{\partial w_0}{\partial s}i\left(2GA\kappa\gamma+2\bar{T}\gamma\right)+w_0 i\left(\frac{\partial(GA\kappa)}{\partial s}\gamma+GA\kappa\frac{\partial\gamma}{\partial s}+\frac{\partial\bar{T}}{\partial s}\gamma+\bar{T}\frac{\partial\gamma}{\partial s}\right)+\frac{\partial\hat{\psi}}{\partial s}GA\kappa+\psi_0\frac{\partial(GA\kappa)}{\partial s}=0$$

$$\frac{\partial \psi_0}{\partial s} 2EIi\gamma + \psi_0 \left(\frac{\partial EI}{\partial s} i\gamma + EIi \frac{\partial \gamma}{\partial s} \right) - GA\kappa \frac{\partial w_0}{\partial s} = 0$$

Rewriting the equations

$$\frac{\partial}{\partial s}\left(w_0^2 i(GA\kappa\gamma + \bar{T}\gamma)\right) + w_0 \frac{\partial}{\partial s}\left(GA\kappa\psi_0\right) = 0$$

$$\frac{\partial}{\partial s}\left(\psi_0 EIi\gamma\right) - GA\kappa\psi_0 \frac{\partial w_0}{\partial s} = 0$$

Subtracting the second equation from the first one we get

$$\frac{\partial}{\partial s}\left(w_0^2 i(GA\kappa\gamma + \bar{T}\gamma)\right) - \frac{\partial}{\partial s}\left(\psi_0^2 EIi\gamma\right) + \frac{\partial}{\partial s}\left(GA\kappa\psi_0 w_0\right) = 0$$

or

$$\frac{\partial}{\partial s}\left(w_0^2 (GA\kappa\gamma + \bar{T}\gamma)\right) - \frac{\partial}{\partial s}\left(\psi_0^2 EI\gamma\right) - \frac{\partial}{\partial s}\left(iGA\kappa\psi_0 w_0\right) = 0$$

The solution of this equation is simply

$$w_0^2 (GA\kappa i\gamma + \bar{T}\gamma) - \psi_0^2 EI\gamma - iGA\kappa\psi_0 w_0 = C_1^2 \tag{2.53}$$

As we have seen before, there is a relationship between w_0 and ψ_0 (see equation (2.28)). Applying it to equation (2.53) above we get the final expression for w_0

$$w_{0j} = \frac{C_{1,j}}{\sqrt{\left(GA\kappa\gamma_j + \bar{T}\right) - P_j^2 EI\gamma_j - iGA\kappa P_j}} \tag{2.54}$$

and

$$\psi_{0j} = P_j w_{0j} \tag{2.55}$$

with j going from 1 to 4, one value for each wave. Thus, the general solution for the system of equations (2.52) can be written as

$$w(s) = \hat{w}_1 \exp(i\theta_1) + \hat{w}_2 \exp(i\theta_2) + \hat{w}_3 \exp(i\theta_3) + \hat{w}_4 \exp(i\theta_4) \tag{2.56}$$

$$\psi(s) = \hat{\psi}_1 \exp(i\theta_1) + \hat{\psi}_2 \exp(i\theta_2) + \hat{\psi}_3 \exp(i\theta_3) + \hat{\psi}_4 \exp(i\theta_4) \tag{2.57}$$

where θ_i is a function of s and is given by $\int_0^s \gamma_i d\xi$, w_0 is given by equation (2.54) and ψ_0 is given by equation (2.55).

In a similar way to what was done for the constant tension beam, we impose now the end conditions:

- For displacements

$$\begin{aligned} u_1 &= \hat{w}(s=0) \\ u_2 &= \hat{\psi}(s=0) \\ u_3 &= \hat{w}(s=L) \\ u_4 &= \hat{\psi}(s=L) \end{aligned} \tag{2.58}$$

- For forces

$$\begin{aligned} f_1 &= -GA\kappa\left(\frac{\partial \hat{w}}{\partial s} + \hat{\psi}\right) - \bar{T}\frac{\partial \hat{w}}{\partial s}(s=0) \\ f_2 &= -EI\frac{\partial \hat{\psi}}{\partial s}(s=0) \\ f_3 &= GA\kappa\left(\frac{\partial \hat{w}}{\partial s} + \hat{\psi}\right) + \bar{T}\frac{\partial \hat{w}}{\partial s}(s=L) \\ f_4 &= EI\frac{\partial \hat{\psi}}{\partial s}(s=L) \end{aligned} \tag{2.59}$$

From equations (2.56) to (2.59) we can obtain matrices $[C]$ and $[D]$. Matrix $[K]$ is obtained through the operation $[C]\cdot[D]^{-1}$. The final expression is

$$[D]=\begin{bmatrix} e_1(0) & e_2(0) & e_3(0) & e_4(0) \\ e_1(0)P_1 & e_2(0)P_2 & e_3(0)P_3 & e_4(0)P_4 \\ e_1(L)\exp(iB_1) & e_2(L)\exp(iB_2) & e_3(L)\exp(iB_3) & e_4(L)\exp(iB_4) \\ e_1(0)P_1\exp(iB_1) & e_2(0)P_2\exp(iB_2) & e_3(0)P_3\exp(iB_3) & e_4(0)P_4\exp(iB_4) \end{bmatrix}$$

where

$$B_j=\int_0^L \gamma_j(\xi)d\xi \qquad j=1,2,3,4$$

and e_j is now defined as $\dfrac{1}{\sqrt{\left(GA\kappa\gamma_j+\overline{T}\right)-P_j{}^2EI\gamma_j-iGA\kappa P_j}}$, the term that multiplies the constant of integration in equation (2.54).

$$[C]=\begin{bmatrix} -GA\kappa(0)(i\gamma_1+P_1)e_1(0) & -GA\kappa(0)(i\gamma_2+P_2)e_2(0) \\ -EI(0)ie_1(0)\gamma_1(0)P_1 & -EI(0)ie_2(0)\gamma_2(0)P_1 \\ GA\kappa(L)(i\gamma_1+P_1)e_1(L)\exp(iB_1) & GA\kappa(L)(i\gamma_2+P_2)e_2(L)\exp(iB_2) \\ EI(L)ie_1(L)\gamma_1(L)P_1\exp(iB_1) & EI(L)ie_2(L)\gamma_2(L)P_2\exp(iB_2) \end{bmatrix}$$

$$\begin{bmatrix} -GA\kappa(0)(i\gamma_3+P_3)e_3(0) & -GA\kappa(0)(i\gamma_4+P_4)e_4(0) \\ -EI(0)ie_3(0)\gamma_3(0)P_3 & -EI(0)ie_4(0)\gamma_4(0)P_4 \\ GA\kappa(L)(i\gamma_3+P_3)e_3(L)\exp(iB_3) & GA\kappa(L)(i\gamma_4+P_4)e_4(L)\exp(iB_4) \\ EI(L)ie_3(L)\gamma_3(L)P_3\exp(iB_3) & EI(L)ie_4(L)\gamma_4(L)P_4\exp(iB_4) \end{bmatrix}+$$

$$\overline{T}\begin{bmatrix} -ie_1(0)\gamma_1(0) & -ie_2(0)\gamma_2(0) & -ie_3(0)\gamma_3(0) & -ie_4(0)\gamma_4(0) \\ 0 & 0 & 0 & 0 \\ ie_1(L)\gamma_1(L)\exp(iB_1) & ie_2(L)\gamma_2(L)\exp(iB_2) & ie_3(L)\gamma_3(L)\exp(iB_3) & ie_4(L)\gamma_4(L)\exp(iB_4) \\ 0 & 0 & 0 & 0 \end{bmatrix}$$

2.9 Consideration of Added Mass

Most of the cases that will be studied here refers to structures in water. In this case, the governing equations must be changed in order to take into account the added mass due to dynamic resistance of the surrounding water.

The formula for the added mass of a cylinder segment moving perpendicular to its longitudinal axis is given by $m_a = \frac{\pi H_d^2}{4}$,where H_d is the hydrodynamic diameter. Hence, the total mass for transverse translation should be given by $m_t = \rho A + m_a$ and the governing equations of motion in the case of submerged lines are written, in its general form as .

$$\frac{\partial^2}{\partial s^2}\left(EI(s)\frac{\partial^2 w}{\partial s^2}\right) - \frac{\partial}{\partial s}\left(\bar{T}(s)\frac{\partial w}{\partial s}\right) + m_t(s)\frac{\partial^2 w}{\partial t^2} = 0 \qquad (2.60)$$

For the rest of this work the added mass will be considered in the derivations of the equations

.

2.10 Consideration of Structural Damping

For an elastic material, the modulus of elasticity is a pure real number. However, in a marine riser analysis, the hydrodynamic damping causes the propagating wave to dissipate energy as it travels along the line. Consequently, the wave decays with the distance traveled. This condition can be studied in the context of WBFEM through the use of a complex modulus of elasticity, expressed of its real and imaginary parts as

$$E = E_r + iE_i = E_r(1 + i\eta)$$

where the loss factor can be defined as $\eta = \frac{E_i}{E_r}$, a positive real number. In chapter 5, we are going to see some examples showing the use of this damping.

Chapter 3

Curved Beam Elements with Constant Radius

3.1 Introduction

In this chapter we start studying the curved beam element with constant radius of curvature. We develop the formulation of the dynamic stiffness matrix for two cases: one with constant tension distribution over the length of the element and another for the slowly varying tension. Then it is shown how the straight element and the curved one can be combined in order to allow the dynamic analysis of a more complex structure like a marine riser. We also establish a method to consider the response of a structure to a distributed, harmonic load acting on it. Finally, in this chapter, we show how the elements developed here can be useful to determine dynamic properties of a beam and compare the results obtained through WBFEM with the corresponding theory.

3.2 Dynamic Stiffness Matrix Formulation with Constant Tension

A typical segment of circular beam is shown in Figure 3-1 with its local system of reference for displacements and forces at its ends. Numbers 1 and 2 inside the circles represent both ends of the beam. The beam is made out of a linear elastic material and the effects of rotary inertia and shear deformation are neglected because the range of frequencies we are going to work with is much smaller than the one that make the consideration of these effects necessary. Besides, no kind of contact between soil and beam is considered in the present study. All the material and geometric properties are constant over the length of the element. The beam is also subjected to a constant axial tensile force along its longitudinal axis. Figure 3-1 also shows the sign convention for both nodal displacements and forces which are represented by the vectors

$\vec{U} = \{u_1 \quad u_2 \quad u_3 \quad u_4 \quad u_5 \quad u_6\}^T$ and $\vec{F} = \{f_1 \quad f_2 \quad f_3 \quad f_4 \quad f_5 \quad f_6\}^T$, respectively. This time the axial motion is included because it is coupled with the transverse displacements, as we will see. Quantities u_1 and u_4 are the axial displacements, u_2 and u_5 are the transverse displacements while u_3 and u_6 are the rotations of the longitudinal axis. Similarly f_1 and f_4 are the axial forces, f_2 and f_5 are the normal forces while f_3 and f_6 are the bending moments.

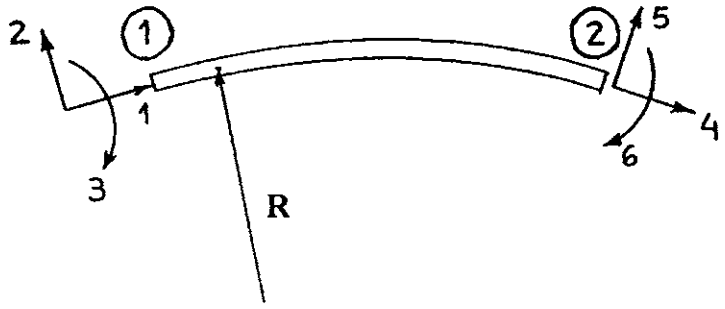

Figure 3-1: Curved beam element with constant radius subjected to constant static tension with all 6 degrees of freedom.

The procedure to obtain the dynamic stiffness matrix of the curved beam element will be analogous to the one used with the straight beam element. Equations like (2.11) and (2.12) will be obtained for the curved beam element. In the case of straight beam, the axial displacement was uncoupled from the transverse displacement and so we could study one independent of the other. However, in a curved beam, the curvature couples both types of displacements and so they have to be studied together.

The equation governing the dynamics of a cable element and a circular beam element have been studied separately by other investigators (see references [15], [16] and [45]). So it will not be repeated here. By combining them we can arrive at the governing equations of a constant tension circular beam, which can be expressed as

$$\frac{\partial^2 M}{\partial s^2} - \overline{T}\frac{\partial \alpha}{\partial s} - \frac{T}{R} = m_t \frac{\partial^2 w}{\partial t^2} \tag{3.1}$$

$$\frac{\partial T}{\partial s} + \frac{1}{R}\frac{\partial M}{\partial s} - \frac{1}{R}\overline{T}\alpha = \rho A \frac{\partial^2 v}{\partial t^2} \tag{3.2}$$

where

$$T = EA\left(\frac{w}{R} + \frac{\partial v}{\partial s}\right) \tag{3.3}$$

$$M = EI\frac{\partial}{\partial s}\left(\frac{v}{R} - \frac{\partial w}{\partial s}\right) \tag{3.4}$$

$$Q = \frac{\partial M}{\partial s} \tag{3.5}$$

$$\alpha = \frac{v}{R} - \frac{\partial w}{\partial s} \tag{3.6}$$

and $m_t = \rho A + m_a$, in order to take into account the added mass, as described in section 2.9. However, its influence is neglected in the longitudinal direction. Substituting equations (3.3) to (3.6) into (3.1) and (3.2) we get

$$EI\frac{\partial^3}{\partial s^3}\left(\frac{v}{R} - \frac{\partial w}{\partial s}\right) - \overline{T}\frac{\partial}{\partial s}\left(\frac{v}{R} - \frac{\partial w}{\partial s}\right) - \frac{EA}{R}\left(\frac{w}{R} + \frac{\partial v}{\partial s}\right) = m_t \frac{\partial^2 w}{\partial t^2} \tag{3.7}$$

$$EA\left(\frac{w}{R} + \frac{\partial v}{\partial s}\right) + \frac{EI}{R}\frac{\partial^2}{\partial s^2}\left(\frac{v}{R} - \frac{\partial w}{\partial s}\right) - \frac{\overline{T}}{R}\left(\frac{v}{R} - \frac{\partial w}{\partial s}\right) = \rho A \frac{\partial^2 v}{\partial t^2} \tag{3.8}$$

Assuming a harmonic solution like $v(s,t) = v_0 \exp(i(\gamma s - \omega t))$ and $w(s,t) = w_0 \exp(i(\gamma s - \omega t))$ for the displacements, where v_0 and w_0 are the constant wave amplitudes, and substituting them into equations (3.7) and (3.8) we end up with

$$-EI\left(\frac{i\gamma^3 v_0}{R} + \gamma^4 w_0\right) - \overline{T}\left(\frac{i\gamma w_0}{R} + \gamma^2 w_0\right) - \frac{EA}{R}\left(\frac{w_0}{R} + i\gamma w_0\right) = -m_t \omega^2 w_0$$

$$EA\left(\frac{i\gamma w_0}{R} - \gamma^2 v_0\right) + \frac{EI}{R}\left(-\frac{\gamma^2 v_0}{R} + i\gamma^3 w_0\right) - \frac{\overline{T}}{R}\left(\frac{v_0}{R} - i\gamma w_0\right) = -\rho A \omega^2 v_0$$

Rewriting the equations above in matrix form we have

$$\begin{bmatrix} -EI\gamma^4 - \bar{T}\gamma^2 - \dfrac{EA}{R^2} + m_t\omega^2 & -\dfrac{iEI\gamma^3}{R} - \dfrac{\bar{T}i\gamma}{R} - \dfrac{EAi\gamma}{R} \\ \dfrac{1}{R}\left(EAi\gamma + iEI\gamma^3 + \bar{T}i\gamma\right) & -EA\gamma^2 - EI\left(\dfrac{\gamma}{R}\right)^2 + \rho A\omega^2 - \dfrac{\bar{T}}{R^2} \end{bmatrix} \begin{Bmatrix} w_0 \\ v_0 \end{Bmatrix} = \begin{Bmatrix} 0 \\ 0 \end{Bmatrix} \tag{3.9}$$

If we set the determinant of the 2 by 2 matrix of coefficients to zero in order to have a solution different than the null vector, we get the following equation:

$$\gamma^6 EIEA + \gamma^4\left(-EI\rho A\omega^2 + \bar{T}EA - \frac{2EIEA}{R^2}\right) + \gamma^2\left(-\bar{T}\rho A\omega^2 + \frac{EIEA}{R^4} - m_t\omega^2\frac{EI}{R^2} - \frac{2\bar{T}EA}{R^2}\right)$$
$$- \frac{EA\rho A\omega^2}{R^2} + \frac{\bar{T}EA}{R^4} + m_t\omega^4\rho A - m_t\omega^2\frac{\bar{T}}{R^2} = 0$$

This equation admits 6 solutions for γ which means that there are six waves along the curved beam. Two of them have positive real parts and two others have negative real parts. Positive real parts correspond to right-going propagating waves while negative values correspond to left-going propagating waves. They represent two wave types which are dominated by longitudinal and transverse beam deflections. Finally there is one positive purely imaginary γ (i. e. spatial decaying to the left) and one negative purely imaginary γ (i. e. spatial decaying to the right). The analytical expressions for these wave numbers were found with the help of Maple software and implemented in a computer routine. Because of their length they were not written here but they are designated as γ_1, γ_2, γ_3, γ_4, γ_5 and γ_6 and, like the case of straight beam, they were sorted so that the first three are right-going or right-decaying waves while the last three are left-going or left-decaying waves. This operation will prove to be very helpful when we study reflection of waves on risers because in this case we can identify the direction the waves are travelling.

Since the equations (3.9) are not independent of each other, if we want to obtain a non-zero displacement, the relation between the wave amplitudes v_0 and w_0 can be obtained from one of them. Choosing the second one we will get the following amplitude ratio:

$$\frac{w_{0j}}{v_{0j}} = \frac{EAR^2\gamma_j^2 + EI\gamma_j^2 - \rho AR^2\omega^2 + \bar{T}}{EAi\gamma_j + iEI\gamma_j^3 + \bar{T}i\gamma_j} = P_j \quad j = 1,\ldots,6 \tag{3.10}$$

Since we have six wavenumbers, the transverse and axial displacements are given respectively by the following expressions

$$w = w_{01}\exp(i\gamma_1 s) + w_{02}\exp(i\gamma_2 s) + w_{03}\exp(i\gamma_3 s) + w_{04}\exp(i\gamma_4 s) + w_{05}\exp(i\gamma_5 s) + w_{06}\exp(i\gamma_6 s) \quad (3.11)$$

$$v = v_{01}\exp(i\gamma_1 s) + v_{02}\exp(i\gamma_2 s) + v_{03}\exp(i\gamma_3 s) + v_{04}\exp(i\gamma_4 s) + v_{05}\exp(i\gamma_5 s) + v_{06}\exp(i\gamma_6 s) \quad (3.12)$$

with the wave amplitudes w_{0j} and v_{0j} related by the equation (3.10).

To determine the dynamic stiffness matrix, we must first obtain matrices $[C]$ and $[D]$. These matrices can be obtained after we have an expression for the displacement field along the beam, defined by expressions (3.11) and (3.12). These matrices will be 6 by 6 this time because there are 6 waves travelling along the beam.

As we know, the displacement-amplitude matrix relates the beam wave amplitudes to the displacements at the element nodes and is formally defined by the relation $[D]\cdot\vec{W} = \vec{U}$. So we can satisfy the displacements (linear and angular) conditions at the ends of the beam element ($s = 0$ and $s = L$) by using equations (3.11) and (3.12):

$$u_1 = v(0)$$

$$u_2 = w(0)$$

$$u_3 = \frac{v(0)}{R} - \frac{\partial w(0)}{\partial s}$$

$$u_4 = v(L)$$

$$u_5 = w(L)$$

$$u_6 = \frac{v(L)}{R} - \frac{\partial w(L)}{\partial s}$$

So matrix $[D]$ is given by

$$[D]=\begin{bmatrix} 1 & 1 & 1 \\ P_1 & P_2 & P_3 \\ \left(\frac{1}{R}-iP_1\gamma_1\right) & \left(\frac{1}{R}-iP_2\gamma_2\right) & \left(\frac{1}{R}-iP_3\gamma_3\right) \\ \exp(i\gamma_1 L) & \exp(i\gamma_2 L) & \exp(i\gamma_3 L) \\ P_1\exp(i\gamma_1 L) & P_2\exp(i\gamma_2 L) & P_3\exp(i\gamma_3 L) \\ \left(\frac{1}{R}-iP_1\gamma_1\right)\exp(i\gamma_1 L) & \left(\frac{1}{R}-iP_2\gamma_2\right)\exp(i\gamma_2 L) & \left(\frac{1}{R}-iP_3\gamma_3\right)\exp(i\gamma_3 L) \end{bmatrix}$$

$$\begin{bmatrix} 1 & 1 & 1 \\ P_4 & P_5 & P_6 \\ \left(\frac{1}{R}-iP_4\gamma_4\right) & \left(\frac{1}{R}-iP_5\gamma_5\right) & \left(\frac{1}{R}-iP_6\gamma_6\right) \\ \exp(i\gamma_4 L) & \exp(i\gamma_5 L) & \exp(i\gamma_6 L) \\ P_4\exp(i\gamma_4 L) & P_5\exp(i\gamma_5 L) & P_6\exp(i\gamma_6 L) \\ \left(\frac{1}{R}-iP_4\gamma_4\right)\exp(i\gamma_4 L) & \left(\frac{1}{R}-iP_5\gamma_5\right)\exp(i\gamma_5 L) & \left(\frac{1}{R}-iP_6\gamma_6\right)\exp(i\gamma_6 L) \end{bmatrix}$$

The force-amplitude matrix relates the beam wave amplitudes to the displacements at the element nodes and is formally defined by the relation $[C]\cdot\vec{W}=\vec{F}$. We can satisfy the force conditions at the ends of the beam element ($s=0$ and $s=L$) by using equations (3.3), (3.4) and (3.5) together with (3.11) and (3.12):

$$f_1 = EA\left(\frac{w(0)}{R}+\frac{\partial v(0)}{\partial s}\right)$$

$$f_2 = EI\frac{\partial^2}{\partial s^2}\left(\frac{v(0)}{R}-\frac{\partial w(0)}{\partial s}\right)-\overline{T}\left(\frac{v(0)}{R}-\frac{\partial w(0)}{\partial s}\right)$$

$$f_3 = EI\frac{\partial}{\partial s}\left(\frac{v(0)}{R}-\frac{\partial w(0)}{\partial s}\right)$$

$$f_4 = EA\left(\frac{w(L)}{R}+\frac{\partial v(L)}{\partial s}\right)$$

$$f_5 = EI\frac{\partial^2}{\partial s^2}\left(\frac{v(L)}{R}-\frac{\partial w(L)}{\partial s}\right)-\overline{T}\left(\frac{v(L)}{R}-\frac{\partial w(L)}{\partial s}\right)$$

$$f_6 = EI\frac{\partial}{\partial s}\left(\frac{v(L)}{R} - \frac{\partial w(L)}{\partial s}\right)$$

In doing so we get the following expression for matrix $[C]$

$$[C] = \begin{bmatrix} -EA\left(\frac{P_1}{R} + i\gamma_1\right) & -EA\left(\frac{P_2}{R} + i\gamma_2\right) \\ EI\left(\frac{\gamma_1^2}{R} - iP_1\gamma_1^3\right) & EI\left(\frac{\gamma_2^2}{R} - iP_2\gamma_2^3\right) \\ -EI\left(\frac{i\gamma_1}{R} + P_1\gamma_1^2\right) & -EI\left(\frac{i\gamma_2}{R} + P_2\gamma_2^2\right) \\ EA\left(\frac{P_1}{R} + i\gamma_1\right)\exp(i\gamma_1 L) & EA\left(\frac{P_2}{R} + i\gamma_2\right)\exp(i\gamma_2 L) \\ -EI\left(\frac{\gamma_1^2}{R} - iP_1\gamma_1^3\right)\exp(i\gamma_1 L) & -EI\left(\frac{\gamma_2^2}{R} - iP_2\gamma_2^3\right)\exp(i\gamma_2 L) \\ EI\left(\frac{i\gamma_1}{R} + P_1\gamma_1^2\right)\exp(i\gamma_1 L) & EI\left(\frac{i\gamma_2}{R} + P_2\gamma_2^2\right)\exp(i\gamma_2 L) \end{bmatrix}$$

$$\begin{bmatrix} -EA\left(\frac{P_3}{R} + i\gamma_3\right) & -EA\left(\frac{P_4}{R} + i\gamma_4\right) \\ EI\left(\frac{\gamma_3^2}{R} - iP_3\gamma_3^3\right) & EI\left(\frac{\gamma_4^2}{R} - iP_4\gamma_4^3\right) \\ -EI\left(\frac{i\gamma_3}{R} + P_3\gamma_3^2\right) & -EI\left(\frac{i\gamma_4}{R} + P_4\gamma_4^2\right) \\ EA\left(\frac{P_3}{R} + i\gamma_3\right)\exp(i\gamma_3 L) & EA\left(\frac{P_4}{R} + i\gamma_4\right)\exp(i\gamma_4 L) \\ -EI\left(\frac{\gamma_3^2}{R} - iP_3\gamma_3^3\right)\exp(i\gamma_3 L) & -EI\left(\frac{\gamma_4^2}{R} - iP_4\gamma_4^3\right)\exp(i\gamma_4 L) \\ EI\left(\frac{i\gamma_3}{R} + P_3\gamma_3^2\right)\exp(i\gamma_3 L) & EI\left(\frac{i\gamma_4}{R} + P_2\gamma_4^2\right)\exp(i\gamma_4 L) \end{bmatrix}$$

$$
\begin{bmatrix}
-EA\left(\frac{P_5}{R}+i\gamma_5\right) & -EA\left(\frac{P_6}{R}+i\gamma_6\right) \\
EI\left(\frac{\gamma_5^2}{R}-iP_5\gamma_5^3\right) & EI\left(\frac{\gamma_6^2}{R}-iP_6\gamma_6^3\right) \\
-EI\left(\frac{i\gamma_5}{R}+P_5\gamma_5^2\right) & -EI\left(\frac{i\gamma_6}{R}+P_6\gamma_6^2\right) \\
EA\left(\frac{P_5}{R}+i\gamma_5\right)\exp(i\gamma_5 L) & EA\left(\frac{P_6}{R}+i\gamma_6\right)\exp(i\gamma_6 L) \\
-EI\left(\frac{\gamma_5^2}{R}-iP_5\gamma_5^3\right)\exp(i\gamma_5 L) & -EI\left(\frac{\gamma_6^2}{R}-iP_6\gamma_6^3\right)\exp(i\gamma_6 L) \\
EI\left(\frac{i\gamma_5}{R}+P_5\gamma_5^2\right)\exp(i\gamma_5 L) & EI\left(\frac{i\gamma_6}{R}+P_6\gamma_6^2\right)\exp(i\gamma_6 L)
\end{bmatrix}+
$$

$$
\overline{T}\begin{bmatrix}
\begin{pmatrix}0\\ \frac{1}{R}-iP_1\gamma_1\\ 0\\ 0\end{pmatrix} & \begin{pmatrix}0\\ \frac{1}{R}-iP_2\gamma_2\\ 0\\ 0\end{pmatrix} & \begin{pmatrix}0\\ \frac{1}{R}-iP_3\gamma_3\\ 0\\ 0\end{pmatrix} \\
\begin{pmatrix}\frac{1}{R}-iP_1\gamma_1\\ 0\\ 0\end{pmatrix}\exp(i\gamma_1 L)) & \begin{pmatrix}\frac{1}{R}-iP_2\gamma_2\\ 0\\ 0\end{pmatrix}\exp(i\gamma_2 L) & \begin{pmatrix}\frac{1}{R}-iP_3\gamma_3\\ 0\\ 0\end{pmatrix}\exp(i\gamma_3 L)
\end{bmatrix}
$$

$$
\begin{bmatrix}
\begin{pmatrix}0\\ \frac{1}{R}-iP_4\gamma_4\\ 0\\ 0\end{pmatrix} & \begin{pmatrix}0\\ \frac{1}{R}-iP_5\gamma_5\\ 0\\ 0\end{pmatrix} & \begin{pmatrix}0\\ \frac{1}{R}-iP_6\gamma_6\\ 0\\ 0\end{pmatrix} \\
\begin{pmatrix}\frac{1}{R}-iP_4\gamma_4\\ 0\\ 0\end{pmatrix}\exp(i\gamma_4 L) & \begin{pmatrix}\frac{1}{R}-iP_5\gamma_5\\ 0\\ 0\end{pmatrix}\exp(i\gamma_5 L) & \begin{pmatrix}\frac{1}{R}-iP_6\gamma_6\\ 0\\ 0\end{pmatrix}\exp(i\gamma_6 L)
\end{bmatrix}
$$

And finally, the stiffness matrix is obtained through the operation $[C]\cdot[D]^{-1}$.

3.3 Dynamic Stiffness Matrix Formulation with Slowly Varying Tension

We are going to study the case of a curved beam with slowly varying static tension, $\overline{T}$, along its longitudinal axis. All other properties are constant on the element including the radius of curvature. The beam element under consideration here is depicted in Figure 3-1 together with the local system of reference for the degrees of freedom. Except for the varying properties mentioned above, the characteristics of the beam studied in the previous section are applicable here. Based on these assumptions the dynamic governing equations are changed to a more general form as

$$\frac{\partial^2 M}{\partial s^2} - \frac{\partial}{\partial s}\left(\overline{T}\alpha\right) - \frac{T}{R} = \rho A \frac{\partial^2 w}{\partial t^2} \tag{3.13}$$

$$\frac{\partial T}{\partial s} + \frac{1}{R}\frac{\partial M}{\partial s} - \frac{1}{R}\overline{T}\alpha = \rho A \frac{\partial^2 v}{\partial t^2} \tag{3.14}$$

where the forces on any section are given by

$$T(s,t) = EA\left(\frac{w(s,t)}{R} + \frac{\partial v(s,t)}{\partial s}\right) \tag{3.15}$$

$$M(s,t) = EI\frac{\partial}{\partial s}\left(\frac{v(s,t)}{R} - \frac{\partial w(s,t)}{\partial s}\right) \tag{3.16}$$

$$Q(s,t) = \frac{\partial M(s,t)}{\partial s} \tag{3.17}$$

and

$$\alpha(s,t) = \frac{v(s,t)}{R} - \frac{\partial w(s,t)}{\partial s} \tag{3.18}$$

Substituting equations (3.15) to (3.18) into (3.13) and (3.14) we get

$$\frac{\partial^2}{\partial s^2}\left(EI\frac{\partial}{\partial s}\left(\frac{v}{R} - \frac{\partial w}{\partial s}\right)\right) - \frac{\partial}{\partial s}\left(\overline{T}\left(\frac{v}{R} - \frac{\partial w}{\partial s}\right)\right) - \frac{EA}{R}\left(\frac{w}{R} + \frac{\partial v}{\partial s}\right) = \rho A \frac{\partial^2 w}{\partial t^2} \tag{3.19}$$

$$\frac{\partial}{\partial s}\left(EA\left(\frac{w}{R}+\frac{\partial v}{\partial s}\right)\right)+\frac{\partial}{\partial s}\left(\frac{EI}{R}\frac{\partial}{\partial s}\left(\frac{v}{R}-\frac{\partial w}{\partial s}\right)\right)-\frac{\overline{T}}{R}\left(\frac{v}{R}-\frac{\partial w}{\partial s}\right)=\rho A\frac{\partial^2 v}{\partial t^2} \tag{3.20}$$

Assuming a harmonic solution of the form $v(s,t)=\hat{v}(s)\exp(-i\omega t)$ and $w(s,t)=\hat{w}(s)\exp(-i\omega t)$ for the displacements and substituting them into equations (3.19) and (3.20) we end up with

$$\frac{\partial^2}{\partial s^2}\left(EI\frac{\partial}{\partial s}\left(\frac{\hat{v}}{R}-\frac{\partial \hat{w}}{\partial s}\right)\right)-\frac{\partial}{\partial s}\left(\overline{T}\left(\frac{\hat{v}}{R}-\frac{\partial \hat{w}}{\partial s}\right)\right)-\frac{EA}{R}\left(\frac{\hat{w}}{R}+\frac{\partial \hat{v}}{\partial s}\right)+m_t\hat{w}\omega^2=0 \tag{3.21}$$

$$\frac{\partial}{\partial s}\left(EA\left(\frac{\hat{w}}{R}+\frac{\partial \hat{v}}{\partial s}\right)\right)+\frac{\partial}{\partial s}\left(\frac{EI}{R}\frac{\partial}{\partial s}\left(\frac{\hat{v}}{R}-\frac{\partial \hat{w}}{\partial s}\right)\right)-\frac{\overline{T}}{R}\left(\frac{\hat{v}}{R}-\frac{\partial \hat{w}}{\partial s}\right)+\rho A\hat{v}\omega^2=0 \tag{3.22}$$

where the term $\exp(-i\omega t)$ was left out of the equation. After working with the derivatives, equations (3.21) and (3.22) can be expanded to

$$\frac{1}{R}\left(\frac{d^2(EI)}{ds^2}\frac{d\hat{v}}{ds}+2\frac{d(EI)}{ds}\frac{d^2\hat{v}}{ds^2}+EI\frac{d^3\hat{v}}{ds^3}\right)-\frac{d^2(EI)}{ds^2}\frac{d^2\hat{w}}{ds^2}-EI\frac{d^4\hat{w}}{ds^4}-2\frac{d(EI)}{ds}\frac{d^3\hat{w}}{ds^3}-$$
$$\frac{1}{R}\frac{d\overline{T}}{ds}\hat{v}-\frac{1}{R}\overline{T}\frac{d\hat{v}}{ds}+\frac{d\overline{T}}{ds}\frac{d\hat{w}}{ds}+\overline{T}\frac{d^2\hat{w}}{ds^2}-\frac{EA\hat{w}}{R^2}-\frac{EA}{R}\frac{d\hat{v}}{ds}+m\hat{w}\omega^2=0 \tag{3.23}$$

$$\frac{d(EA)}{ds}\frac{\hat{w}}{R}+\frac{EA}{R}\frac{d\hat{w}}{ds}+\frac{d(EA)}{ds}\frac{d\hat{v}}{ds}+EA\frac{d^2\hat{v}}{ds^2}+\frac{1}{R^2}\frac{d(EI)}{ds}\frac{d\hat{v}}{ds}+\frac{1}{R^2}EI\frac{d^2\hat{v}}{ds^2}-$$
$$\frac{1}{R}\frac{d(EI)}{ds}\frac{d^2\hat{w}}{ds^2}-\frac{1}{R}EI\frac{d^3\hat{w}}{ds^3}-\frac{\overline{T}}{R^2}\hat{v}+\frac{\overline{T}}{R}\frac{d\hat{w}}{ds}+m\hat{v}\omega^2=0 \tag{3.24}$$

In order to solve this system of equations we resort again to the formal procedure of WKB method, as we did before for the case of straight beam. First we assume that the relations $\hat{w}(s)=\exp(i\theta(s))w_0(s)$ and $\hat{v}(s)=\exp(i\theta(s))v_0(s)$ are valid, where $\theta(s)=\int_0^s\gamma_i(\xi)d\xi$. The expressions for the derivatives of $\hat{v}$ and $\hat{w}$ that appear in the equations (3.23) and (3.24) above have already been calculated in chapter 2 and are shown in equations (2.43). So, if we substitute them into equations (3.23) and (3.24) and start collecting the terms with equivalent order, the

same way we did before for the case of slowly varying static tension on straight beams, we will find:

1. To the leading order (i.e., terms with no derivatives), we get

- $$-i\frac{EI}{R}\gamma^3 v_0 - EIw_0\gamma^4 - i\frac{\overline{T}}{R}v_0\gamma - \overline{T}w_0\gamma^2 - \frac{EA}{R^2}w_0 - i\frac{EA}{R}v_0\gamma + m\omega^2 w_0 = 0$$
- $$i\frac{EA}{R}\gamma w_0 - EAv_0\gamma^2 - \frac{EI}{R^2}v_0\gamma^2 + i\frac{EI}{R}w_0\gamma^3 + \frac{i\overline{T}\gamma}{R}w_0 - \frac{\overline{T}}{R^2}v_0 + m\omega^2 v_0 = 0$$

Notice that, again, we obtain the same dispersion relation that we obtained for the curved beam with constant tension. It means that there will be six wave numbers, which are no longer constant, but a function of s and still slowly varying. With this difference in mind we can use here in this section the same equations for the wavenumbers obtained before.

2. For the next-order terms (i.e., with one first derivative only)

- $$-\frac{2}{R}\frac{d(EI)}{ds}\gamma^2 v_0 - 3\frac{EI}{R}\gamma^2\frac{dv_0}{ds} - 3\frac{EI}{R}v_0\gamma\frac{d\gamma}{ds} + 3iEI\frac{dw_0}{ds}\gamma^3 + 3iEIw_0\gamma^2\frac{d\gamma}{ds} + EIi\gamma^3\frac{dw_0}{ds} + 3iEIw_0\gamma^2\frac{d\gamma}{ds} + 2i\frac{d(EI)}{ds}\gamma^3 w_0 - \frac{1}{R}\frac{d\overline{T}}{ds}v_0 - \frac{\overline{T}}{R}\frac{dv_0}{ds} + i\frac{d\overline{T}}{ds}w_0\gamma + \overline{T}\left(2i\frac{dw_0}{ds}\gamma + iw_0\frac{d\gamma}{ds}\right) - \frac{EA}{R}\frac{dv_0}{ds} = 0$$

- $$\frac{d(EA)}{ds}\frac{w_0}{R} + \frac{EA}{R}\frac{dw_0}{ds} + i\frac{d(EA)}{ds}\gamma w_0 + EA\left(2i\frac{dv_0}{ds}\gamma + iv_0\frac{d\gamma}{ds}\right) + i\frac{1}{R^2}\frac{d(EI)}{ds}v_0\gamma + \frac{EI}{R^2}\left(2i\frac{dv_0}{ds}\gamma + iv_0\frac{d\gamma}{ds}\right) + \frac{1}{R}\frac{d(EI)}{ds}w_0\gamma^2 + 3\frac{EI}{R}\left(\frac{dw_0}{ds}\gamma^2 + w_0\gamma\frac{d\gamma}{ds}\right) + \frac{\overline{T}}{R}\frac{dw_0}{ds} = 0$$

Rearranging both equations

- $$\frac{dv_0}{ds}\frac{1}{R}\left(-EA - \overline{T} - 3EI\gamma^2\right) + \frac{v_0}{R}\left(-2\gamma^2\frac{d(EI)}{ds} - 3EI\gamma\frac{d\gamma}{ds} - \frac{d\overline{T}}{ds}\right) + \frac{dw_0}{ds}\left(4iEI\gamma^3 + 2i\overline{T}\gamma\right) + w_0\left(6iEI\gamma^2\frac{d\gamma}{ds} + 2i\frac{d(EI)}{ds}\gamma^3 + i\frac{d\overline{T}}{ds}\gamma + i\overline{T}\frac{d\gamma}{ds}\right) = 0$$
- $$2\frac{dv_0}{ds}\left(iEA\gamma + i\frac{EI}{R^2}\gamma\right) + v_0\left(i\frac{d(EA)}{ds}\gamma + iEA\frac{d\gamma}{ds} + i\gamma\frac{1}{R^2}\frac{d(EI)}{ds} + i\frac{EI}{R^2}\frac{d\gamma}{ds}\right) +$$

$$\frac{dw_0}{ds}\left(\frac{EA}{R}+\frac{\overline{T}}{R}+3\gamma^2\frac{EI}{R}\right)+w_0\left(\frac{1}{R}\frac{d(EA)}{ds}+\frac{\gamma^2}{R}\frac{d(EI)}{ds}+3\gamma\frac{EI}{R}\frac{d\gamma}{ds}\right)=0$$

Both equations are equivalent to

- $$\frac{dv_0}{ds}w_0\left(-\frac{EA}{R}-\frac{\overline{T}}{R}-3\frac{EI\gamma^2}{R}\right)+v_0w_0\left(-\frac{2}{R}\gamma^2\frac{d(EI)}{ds}-3\frac{EI}{R}\gamma\frac{d\gamma}{ds}-\frac{1}{R}\frac{d\overline{T}}{ds}\right)+\frac{d}{ds}\left(w_0^2(2iEI\gamma^3+\overline{T}i\gamma)\right)=0$$
- $$\frac{dw_0}{ds}v_0\left(\frac{EA}{R}+\frac{\overline{T}}{R}+3\frac{EI\gamma^2}{R}\right)+v_0w_0\left(\frac{1}{R}\frac{d(EA)}{ds}+\frac{\gamma^2}{R}\frac{d(EI)}{ds}+3\gamma\frac{EI}{R}\frac{d\gamma}{ds}\right)+\frac{d}{ds}\left(v_0^2(iEA\gamma+\frac{EI}{R^2}i\gamma)\right)=0$$

Subtracting the first equation from the second one we get

$$\frac{d}{ds}\left(v_0^2(iEA\gamma+\frac{EI}{R^2}i\gamma)\right)-\frac{d}{ds}\left(w_0^2(2iEI\gamma^3+\overline{T}i\gamma)\right)+\frac{d}{ds}\left(\frac{EA}{R}v_0w_0\right)+3\frac{d}{ds}\left(\frac{EI}{R}v_0w_0\gamma^2\right)+\frac{d}{ds}\left(\frac{\overline{T}}{R}v_0w_0\right)=0$$

If we multiply the equation above by $-i$ and then integrate it, we get the following relation

$$v_0^2\left(iEA\gamma+\frac{EI}{R^2}i\gamma\right)-w_0^2(2iEI\gamma^3+\overline{T}i\gamma)-i\frac{v_0w_0}{R}\left(EA+3EI\gamma^2+\overline{T}\right)=C_1^2 \qquad (3.25)$$

where C_1^2 is a constant of integration.

As the equations for the leading order are the same as those for the constant tension curved beam, we conclude that the equation (3.10) is still valid. The only difference is that now P_j is a function of s. Introducing it in the equation (3.25) we get

$$v_0^2\left[\left(iEA\gamma+\frac{EI}{R^2}i\gamma\right)-P^2(2iEI\gamma^3+\overline{T}i\gamma)-i\frac{P}{R}\left(EA+3EI\gamma^2+\overline{T}\right)\right]=C_1^2$$

So, the expression for the amplitude v_0 is

$$v_0(s) = \frac{C_1}{\sqrt{\left(EA\gamma + \frac{EI}{R^2}\gamma\right) - P^2(2EI\gamma^3 + \bar{T}\gamma) - i\frac{P}{R}\left(EA + 3EI\gamma^2 + \bar{T}\right)}} = Q(s)C_1 \tag{3.26}$$

Consequently the expression for the displacements are given by

$$\hat{w}(s,t) = \left(w_{01}(s)\exp\left(i\theta_1(s)\right) + w_{02}(s)\exp\left(i\theta_2(s)\right) + w_{03}(s)\exp\left(i\theta_3(s)\right) + w_{04}(s)\exp\left(i\theta_4(s)\right) + w_{05}(s)\exp\left(i\theta_5(s)\right) + w_{06}(s)\exp\left(i\theta_6(s)\right)\right)\exp(-i\omega t) \tag{3.27}$$

$$\hat{v}(s,t) = \left(v_{01}(s)\exp\left(i\theta_1(s)\right) + v_{02}(s)\exp\left(i\theta_2(s)\right) + v_{03}(s)\exp\left(i\theta_3(s)\right) + v_{04}(s)\exp\left(i\theta_4(s)\right) + v_{05}(s)\exp\left(i\theta_5(s)\right) + v_{06}(s)\exp\left(i\theta_6(s)\right)\right)\exp(-i\omega t) \tag{3.28}$$

where the wave amplitudes w_{0j} and v_{0j} are related by the equation (3.10) and v_{0j} is given by (3.26).

Following the usual procedure, now we have to look at the end conditions for displacements:

$$\begin{aligned} u_1 &= \hat{v}(0) \\ u_2 &= \hat{w}(0) \\ u_3 &= \frac{\hat{v}(0)}{R} - \frac{\partial \hat{w}(0)}{\partial s} \\ u_4 &= \hat{v}(L) \\ u_5 &= \hat{w}(L) \\ u_6 &= \frac{\hat{v}(L)}{R} - \frac{\partial \hat{w}(L)}{\partial s} \end{aligned} \tag{3.29}$$

For the forces we have

$$f_1 = EA\left(\frac{\hat{w}(0)}{R} + \frac{\partial \hat{v}(0)}{\partial s}\right)$$

$$f_2 = EI\frac{\partial^2}{\partial s^2}\left(\frac{\hat{v}(0)}{R} - \frac{\partial \hat{w}(0)}{\partial s}\right) - \bar{T}\left(\frac{\hat{v}(0)}{R} - \frac{\partial \hat{w}(0)}{\partial s}\right)$$

$$f_3 = EI\frac{\partial}{\partial s}\left(\frac{\hat{v}(0)}{R} - \frac{\partial \hat{w}(0)}{\partial s}\right)$$

$$f_4 = EA\left(\frac{\hat{w}(L)}{R} + \frac{\partial \hat{v}(L)}{\partial s}\right) \tag{3.30}$$

$$f_5 = EI\frac{\partial^2}{\partial s^2}\left(\frac{\hat{v}(L)}{R} - \frac{\partial \hat{w}(L)}{\partial s}\right) - \bar{T}\left(\frac{\hat{v}(L)}{R} - \frac{\partial \hat{w}(L)}{\partial s}\right)$$

$$f_6 = EI\frac{\partial}{\partial s}\left(\frac{\hat{v}(L)}{R} - \frac{\partial \hat{w}(L)}{\partial s}\right)$$

The next step is to obtain matrices $[C]$ and $[D]$ substituting equations (3.27) and (3.28) into (3.29) and (3.30). The resultant matrices $[D]$and $[C]$ are, respectively

$$[D] = \begin{bmatrix} Q_1(0) & Q_2(0) \\ P_1(0)Q_1(0) & P_2(0)Q_2(0) \\ \dfrac{Q_1(0)}{R} - iP_1Q_1(0)\gamma_1 & \dfrac{Q_2(0)}{R} - iP_2Q_2(0)\gamma_2 \\ Q_1(L)\exp(iB_1) & Q_2(L)\exp(iB_2) \\ P_1(L)Q_1(L)\exp(iB_1) & P_2(L)Q_2(L)\exp(iB_2) \\ \left(\dfrac{Q_1(L)}{R} - iP_1Q_1(L)\gamma_1\right)\exp(iB_1) & \left(\dfrac{Q_2(L)}{R} - iP_2Q_2(L)\gamma_2\right)\exp(iB_2) \end{bmatrix}$$

$$\begin{matrix} Q_3(0) & Q_4(0) \\ P_3(0)Q_3(0) & P_4(0)Q_4(0) \\ \dfrac{Q_3(0)}{R} - iP_3Q_3(0)\gamma_3 & \dfrac{Q_4(0)}{R} - iP_4Q_4(0)\gamma_4 \\ Q_3(L)\exp(iB_3) & Q_4(L)\exp(iB_4) \\ P_3(L)Q_3(L)\exp(iB_3) & P_4(L)Q_4(L)\exp(iB_4) \\ \left(\dfrac{Q_3(L)}{R} - iP_3Q_3(L)\gamma_3\right)\exp(iB_3) & \left(\dfrac{Q_4(L)}{R} - iP_4Q_4(L)\gamma_4\right)\exp(iB_4) \end{matrix}$$

$$
\begin{bmatrix}
Q_5(0) & Q_6(0) \\
P_5(0)Q_5(0) & P_6(0)Q_6(0) \\
\dfrac{Q_5(0)}{R} - iP_5Q_5(0)\gamma_5 & \dfrac{Q_6(0)}{R} - iP_6Q_6(0)\gamma_6 \\
Q_5(L)\exp(iB_5) & Q_6(L)\exp(iB_6) \\
P_5(L)Q_5(L)\exp(iB_5) & P_6(L)Q_6(L)\exp(iB_6) \\
\left(\dfrac{Q_5(L)}{R} - iP_5Q_5(L)\gamma_5\right)\exp(iB_5) & \left(\dfrac{Q_6(L)}{R} - iP_6Q_6(L)\gamma_6\right)\exp(iB_6)
\end{bmatrix}
$$

$$
[C] = \begin{bmatrix}
-EA\left(P_1\dfrac{Q_1}{R} + i\gamma_1 Q_1\right) & -EA\left(P_2\dfrac{Q_2}{R} + i\gamma Q_2\right) \\
-EI\left(-Q_1\dfrac{\gamma_1^2}{R} + iP_1Q_1\gamma_1^3\right) & -EI\left(-Q_2\dfrac{\gamma_2^2}{R} + iP_2Q_2\gamma_1^3\right) \\
-EI\left(iQ_1\dfrac{\gamma_1}{R} + P_1Q_1\gamma_1^2\right) & -EI\left(iQ_2\dfrac{\gamma_2}{R} + P_2Q_2\gamma_1^2\right) \\
EA\left(P_1\dfrac{Q_1}{R} + i\gamma_1 Q_1\right)\exp(iB_1) & EA\left(P_2\dfrac{Q_2}{R} + i\gamma_2 Q_2\right)\exp(iB_2) \\
EI\left(-Q_1\dfrac{\gamma_1^2}{R} + iP_1Q_1\gamma_1^3\right)\exp(iB_1) & EI\left(-Q_2\dfrac{\gamma_2^2}{R} + iP_2Q_2\gamma_2^3\right)\exp(iB_2) \\
EI\left(iQ_1\dfrac{\gamma_1}{R} + P_1Q_1\gamma_1^2\right)\exp(iB_1) & EI\left(iQ_2\dfrac{\gamma_2}{R} + P_2Q_2\gamma_2^2\right)\exp(iB_2)
\end{bmatrix}
$$

$$
\begin{bmatrix}
-EA\left(P_3\dfrac{Q_3}{R} + i\gamma_3 Q_3\right) & -EA\left(P_4\dfrac{Q_4}{R} + i\gamma Q_4\right) \\
-EI\left(-Q_3\dfrac{\gamma_3^2}{R} + iP_3Q_3\gamma_3^3\right) & -EI\left(-Q_4\dfrac{\gamma_4^2}{R} + iP_4Q_4\gamma_4^3\right) \\
-EI\left(iQ_3\dfrac{\gamma_3}{R} + P_3Q_3\gamma_3^2\right) & -EI\left(iQ_4\dfrac{\gamma_4}{R} + P_4Q_4\gamma_4^2\right) \\
EA\left(P_3\dfrac{Q_3}{R} + i\gamma_3 Q_3\right)\exp(iB_3) & EA\left(P_4\dfrac{Q_4}{R} + i\gamma_4 Q_4\right)\exp(iB_4) \\
EI\left(-Q_3\dfrac{\gamma_3^2}{R} + iP_3Q_3\gamma_3^3\right)\exp(iB_3) & EI\left(-Q_4\dfrac{\gamma_4^2}{R} + iP_4Q_4\gamma_4^3\right)\exp(iB_4) \\
EI\left(iQ_3\dfrac{\gamma_3}{R} + P_3Q_3\gamma_3^2\right)\exp(iB_3) & EI\left(iQ_4\dfrac{\gamma_4}{R} + P_4Q_4\gamma_4^2\right)\exp(iB_4)
\end{bmatrix}
$$

$$
\begin{bmatrix}
-EA\left(P_5\frac{Q_5}{R}+i\gamma_5 Q_5\right) & -EA\left(P_6\frac{Q_6}{R}+i\gamma Q_6\right) \\
-EI\left(-Q_5\frac{\gamma_5^2}{R}+iP_5Q_5\gamma_5^3\right) & -EI\left(-Q_6\frac{\gamma_6^2}{R}+iP_6Q_6\gamma_6^3\right) \\
-EI\left(iQ_5\frac{\gamma_5}{R}+P_5Q_5\gamma_5^2\right) & -EI\left(iQ_6\frac{\gamma_6}{R}+P_6Q_6\gamma_6^2\right) \\
EA\left(P_5\frac{Q_5}{R}+i\gamma_5 Q_5\right)\exp(iB_5) & EA\left(P_6\frac{Q_6}{R}+i\gamma_6 Q_6\right)\exp(iB_6) \\
EI\left(-Q_5\frac{\gamma_5^2}{R}+iP_5Q_5\gamma_5^3\right)\exp(iB_5) & EI\left(-Q_6\frac{\gamma_6^2}{R}+iP_6Q_6\gamma_6^3\right)\exp(iB_6) \\
EI\left(iQ_5\frac{\gamma_5}{R}+P_5Q_5\gamma_5^2\right)\exp(iB_5) & EI\left(iQ_6\frac{\gamma_6}{R}+P_6Q_6\gamma_6^2\right)\exp(iB_6)
\end{bmatrix}+
$$

$$
\overline{T}\begin{bmatrix}
0 & 0 & 0 \\
\frac{Q_1}{R}-i\gamma_1P_1Q_1 & \frac{Q_2}{R}-i\gamma_2P_2Q_2 & \frac{Q_3}{R}-i\gamma_3P_3Q_3 \\
0 & 0 & 0 \\
0 & 0 & 0 \\
-\left(\frac{Q_1}{R}-i\gamma_1P_1Q_1\right)\exp(iB_1) & -\left(\frac{Q_2}{R}-i\gamma_2P_2Q_2\right)\exp(iB_2)_1 & -\left(\frac{Q_3}{R}-i\gamma_3P_3Q_3\right)\exp(iB_3) \\
0 & 0 & 0
\end{bmatrix}
$$

$$
\begin{bmatrix}
0 & 0 & 0 \\
\frac{Q_4}{R}-i\gamma_4P_4Q_4 & \frac{Q_5}{R}-i\gamma_5P_5Q_5 & \frac{Q_6}{R}-i\gamma_6P_6Q_6 \\
0 & 0 & 0 \\
0 & 0 & 0 \\
-\left(\frac{Q_4}{R}-i\gamma_4P_4Q_4\right)\exp(iB_4) & -\left(\frac{Q_5}{R}-i\gamma_5P_5Q_5\right)\exp(iB_5) & -\left(\frac{Q_6}{R}-i\gamma_6P_6Q_6\right)\exp(iB_6) \\
0 & 0 & 0
\end{bmatrix}
$$

where the first three rows are evaluated at $s=0$ and the last three rows are evaluated at $s=L$. The expressions for B_i are those shown in equation (2.49). Finally, dynamic stiffness matrix is obtained from $[C]\cdot[D]^{-1}$.

3.4 Coupling Between Straight and Curved Beam Elements

As we have seen before, the stiffness matrices involving straight beams have dimension 4 by 4 because the axial displacements are uncoupled from the transverse motion. Thus, the governing equations for the transverse motion are independent from the governing equation for the axial displacement up to the first order. So the stiffness matrix of the element does not take into account the axial motion.

In the case of curved beam, the transverse and axial motions become coupled because of the curvature and so the governing equations involve both types of displacements as we saw in sections 3.2 and 3.3. As a consequence, the stiffness matrix of the curved beam element increased its dimension to 6 by 6.

In order to use both types of elements in the same structure (this will be the case in the next sections when we study risers) we will have to match the stiffness matrices of straight and curved beam elements when we assemble the stiffness matrix of the structure. It means that their dimensions will have to be the same.

This problem was solved by adding to the stiffness matrix of the straight beam element the dimensions related to the axial displacement. In order to achieve this goal we will study in this section only the axial motion on a straight beam up to the point we obtain the stiffness matrix of the beam. The beam element is shown in Figure 3-2 with its local system of reference for forces and displacements. Its stiffness matrix will be 2 by 2 since the element has two degrees of freedom. We will also study two cases: beam with constant and slowly varying properties, using the same methodology we used before. Then the stiffness matrix of the beam with axial motion only will be added to the stiffness matrix of the straight beam element with transverse motion only, studied previously in chapter 2.

We will refer to the beam with axial motion only as a rod.

Figure 3-2: Straight beam element with axial motion only.

3.4.1 Longitudinal wave propagation in straight rods with Constant Properties

The use of WBFEM in the study of one-dimensional rod was done before by other investigators (see, for instance, reference [17]) and so it will only be summarized here.

It is known that the linear equation for the axial motion is

$$\frac{\partial T}{\partial s} = \rho A \frac{\partial^2 v}{\partial t^2} \tag{3.31}$$

Writing the axial force as $T = EA\dfrac{\partial v}{\partial s}$ and substituting it in equation (3.31) above we get

$$E\frac{\partial^2 v}{\partial s^2} = \rho \frac{\partial^2 v}{\partial t^2} \tag{3.32}$$

Now we assume a solution of the form $v = v_0 \exp\left(i(\gamma s - \omega t)\right)$ and insert it into the equation (3.32) above to get the wave dispersion relation

$$\gamma^2 = \frac{\rho}{E}\omega^2 \quad \Rightarrow \quad \gamma = \pm\sqrt{\frac{\rho}{E}}\omega \tag{3.33}$$

Using the terminology adopted in the present work, we can say that the roots are $\gamma_1 = \gamma$ and $\gamma_2 = -\gamma$. So the general solution for the governing equation (3.32) is given by

$$v = v_{01}\exp\left(i(\gamma_1 s - wt)\right) + v_{02}\exp\left(i(\gamma_2 s - wt)\right) \tag{3.34}$$

We see that there are two propagating waves travelling along the rod, one to the right and the other to the left with wave number γ given by equation (3.33). Similar to what was done before for the beam, we can obtain the dynamic stiffness matrix of the rod element using the WBFEM. We will omit the term $\exp(-i\omega t)$ as it is implied throughout this work.

The end conditions for displacements are

$$u_1 = v(0) \qquad \text{and} \qquad u_2 = v(L) \tag{3.35}$$

and for forces are

$$f_1 = EA\frac{\partial v}{\partial s}(s=0) \qquad \text{and} \qquad f_2 = EA\frac{\partial v}{\partial s}(s=L) \tag{3.36}$$

After substitution of (3.34) into (3.35) and (3.36) we obtain the matrices $[C]$ and $[D]$

$$[D] = \begin{bmatrix} 1 & 1 \\ \exp(i\gamma_1 L) & \exp(i\gamma_2 L) \end{bmatrix} \qquad [C] = EA\begin{bmatrix} -i\gamma_1 & -i\gamma_2 \\ i\gamma_1 \exp(i\gamma_1 L) & i\gamma_2 \exp(i\gamma_2 L) \end{bmatrix}$$

If we represent the roots given in equation (3.33) by $\gamma_1 = -\gamma_2 = \gamma$ we will have the following stiffness matrix:

$$K = \frac{EA\gamma}{\sin(\gamma L)}\begin{bmatrix} \cos(\gamma L) & -1 \\ -1 & \cos(\gamma L) \end{bmatrix}$$

3.4.2 Longitudinal wave propagation in straight rods with Slowly Varying Properties

In this section we study the same rod depicted in Figure 3-2 but now with slowing varying properties (like cross-section area).

As seen before, the governing equation (written in a more general way) is

$$\frac{\partial}{\partial s}\left(EA\frac{\partial v}{\partial s}\right) = \rho A\frac{\partial^2 v}{\partial t^2} \tag{3.37}$$

As we are looking for time harmonic solution, we assume that $v(s,t) = \hat{v}(s)\exp(-i\omega t)$ and substitute into equation (3.37) to obtain the relation

$$\frac{\partial}{\partial s}\left(EA\frac{\partial \hat{v}}{\partial s}\right)+\rho A\omega^2 \hat{v}=0 \quad \Rightarrow \quad \frac{\partial(EA)}{\partial s}\frac{\partial \hat{v}}{\partial s}+EA\frac{\partial^2 \hat{v}}{\partial s^2}+\rho A\omega^2 \hat{v}=0 \tag{3.38}$$

Again we use the WKB method to find an approximate solution for equation (3.38). We assume again that $\hat{v}(s)=\exp(i\theta(s))v_0(s)$ where $\frac{\partial\theta}{\partial s}=\gamma(s)$. Plugging this expression and its derivatives into (3.38) and collecting the terms with the same order, we get

- To the leading order

$$-EA\gamma^2+\rho A\omega^2=0$$

or

$$\gamma=\pm\sqrt{\frac{\rho}{E}}\omega \tag{3.39}$$

- Next order

$$EA\left(2i\gamma\frac{dv_0}{ds}+iv_0\frac{d\gamma}{ds}\right)+i\gamma v_0\frac{d(EA)}{ds}=0 \tag{3.40}$$

We note that if we multiply equation (3.40) by v_0 we can rewrite it as $\frac{d}{ds}\left(EA\gamma v_0^2\right)=0$. After the integration we get the following result:

$$v_0(s)=\frac{C_1}{\sqrt{EA(s)\gamma(s)}}$$

The axial displacement, which is the solution of equation (3.38), can be written as

$$\hat{v}(s)=\frac{C_1}{\sqrt{EA(s)\gamma_1(s)}}\exp\left(i\int_0^s\gamma_1(\xi)d\xi\right)+\frac{C_2}{\sqrt{EA(s)\gamma_2(s)}}\exp\left(i\int_0^s\gamma_2(\xi)d\xi\right) \tag{3.41}$$

The end conditions for displacements and forces are, respectively

$$u_1=\hat{v}(0) \qquad \text{and} \qquad u_2=\hat{v}(L) \tag{3.42}$$

and for forces are

$$f_1 = EA\frac{\partial \hat{v}}{\partial s}(s=0) \quad \text{and} \quad f_2 = EA\frac{\partial \hat{v}}{\partial s}(s=L) \tag{3.43}$$

The matrices $[D]$ and $[C]$ are

$$[D]=\begin{bmatrix} \dfrac{1}{\sqrt{EA\gamma_1}} & \dfrac{1}{\sqrt{EA\gamma_2}} \\ \dfrac{1}{\sqrt{EA\gamma_1}}\exp\left(i\int_0^L \gamma_1(\xi)d\xi\right) & \dfrac{1}{\sqrt{EA\gamma_2}}\exp\left(i\int_0^L \gamma_2(\xi)d\xi\right) \end{bmatrix}$$

and

$$[C]=\begin{bmatrix} \dfrac{-i\gamma_1}{\sqrt{EA\gamma_1}} & \dfrac{-i\gamma_2}{\sqrt{EA\gamma_2}} \\ \dfrac{i\gamma_1}{\sqrt{EA\gamma_1}}\exp\left(i\int_0^L \gamma_1(\xi)d\xi\right) & \dfrac{i\gamma_2}{\sqrt{EA\gamma_2}}\exp\left(i\int_0^L \gamma_2(\xi)d\xi\right) \end{bmatrix}$$

where the first line is evaluated at $s=0$ and the second one at $s=L$ .Stiffness matrix is obtained from $[C]\cdot[D]^{-1}$.

Once these matrices are known, we can think of a straight beam element with 6 degrees of freedom (represented symbolically by the word 'dof' from now on), 3 per node, like the curved beam element studied in this chapter. This is the approach given to this element from now on, in the present work. The axial displacements at the ends of the element are now represented by the dof numbers 1 and 4 while dof 2, 3, 5 and 6 are related to the transverse motion. In order to obtain the dynamic stiffness matrix of this new straight beam element we just assemble matrices $[K_{ea}]$ and $[K_{et}]$, paying attention to the relationship between the dof numbers and the type of motion. Since axial and transverse motions are uncoupled in the straight beam element, the terms (1,2), (1,3), (1,5), (1,6), (4,2), (4,3), (4,5), (4,6) and those of transposed positions are zero. The resultant dynamic stiffness matrix $[K_e]$ is represented symbolically as

$$[K_e]=\begin{bmatrix} K_{ea}(1,1) & 0 & 0 & K_{ea}(1,2) & 0 & 0 \\ 0 & K_{et}(1,1) & K_{et}(1,2) & 0 & K_{et}(1,3) & K_{et}(1,4) \\ 0 & K_{et}(2,1) & K_{et}(2,2) & 0 & K_{et}(2,3) & K_{et}(2,4) \\ K_{ea}(2,1) & 0 & 0 & K_{ea}(2,2) & 0 & 0 \\ 0 & K_{et}(3,1) & K_{et}(3,2) & 0 & K_{et}(3,3) & K_{et}(3,4) \\ 0 & K_{et}(4,1) & K_{et}(4,2) & 0 & K_{et}(4,3) & K_{et}(4,4) \end{bmatrix}$$

The procedures explained in sections 2.4 and 2.7 for the semi-infinite beam element and reflection coefficients, respectively, are still valid for the element represented by $[K_e]$. The only difference is that the matrices involved in expressions (2.41) and in the definition of $[K_{ei}]$ are 3 by 3.

3.5 Distributed Transverse Load on Beams

In this section, we are going to develop a method to obtain the nodal forces equivalent to a harmonic load distributed along a beam element number n. The ends of this element are identified by node numbers n and $n+1$.

When we employ the FEM method, including WBFEM, all the equations of equilibrium are related to a finite number of degrees of freedom that describes the response of the structure in terms of displacements and forces. That is why the distributed load acting on a beam element must be substituted by a set of equivalent concentrated forces located at the element's degrees of freedom. They are called nodal loads. In the present work, these degrees of freedom are located at the element's ends (see figures 2-1 and 3-1).

Essentially, the procedure adopted in this work to consider the distributed load is similar to the one used in the conventional FEM. The difference is that now it is going to be applied in the context of the wave based approach. The method we are going to develop is outlined in Figure 3-3, where $q(s,t)$ represents an arbitrary distributed load acting on the beam element. This element belongs to a mesh into which the structure to be studied is divided into. The basic steps are described below:

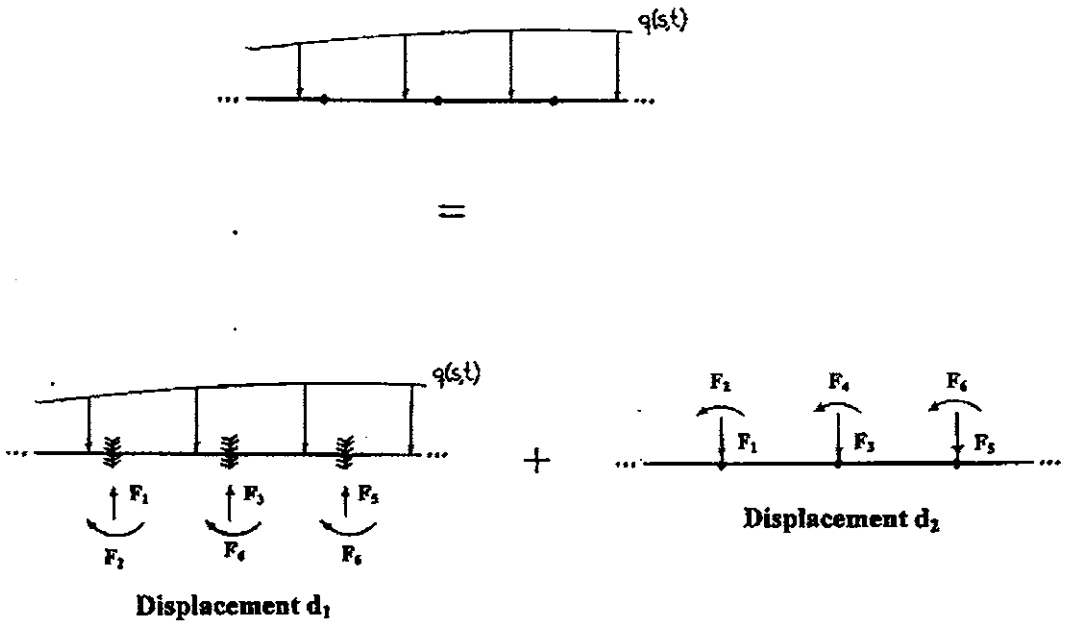

Figure 3-3: Procedure adopted in the FEA to consider distributed load on a beam.

1. We clamp the ends of the beam element n and apply the distributed load q on it. The beam will be subjected to reactions at its ends, represented by the vector force $\vec{F}_{eR}$ and to a displacement field called d_1 along the longitudinal axis.
2. Remove the clamps and substitute the distributed load for the vector force $-\vec{F}_{eR}$ at the ends of the beam element.
3. Compute the element stiffness matrix $[K_e]$
4. Repeat steps 1 and 2 for all other elements of the structure.
5. For each node n we sum the contributions of the corresponding force vectors $-\vec{F}_{eR}$ from elements $n-1$ and n. In the end we will have the nodal force vector $\vec{F}$.
6. Assemble the stiffness matrix of the structure, $[K]$
7. Solve the equation $[K]\vec{U} = \vec{F}$ for the nodal displacements.

8. From the vector $\vec{U}$ we take the vector of displacements at the ends of the beam element n, called $\vec{U}_e$. Then the displacement field along the beam element n is obtained and we call it d_2.
9. The final displacement field of the beam element n is equal to the summation of d_1 and d_2. The forces at the ends of the element n will be given by $[K_e]\vec{U}_e - \vec{F}_{eR}$.

We will study now the parts of the procedure above that had to be adapted to the wave based approach.

3.5.1 Reactions at the clamped ends

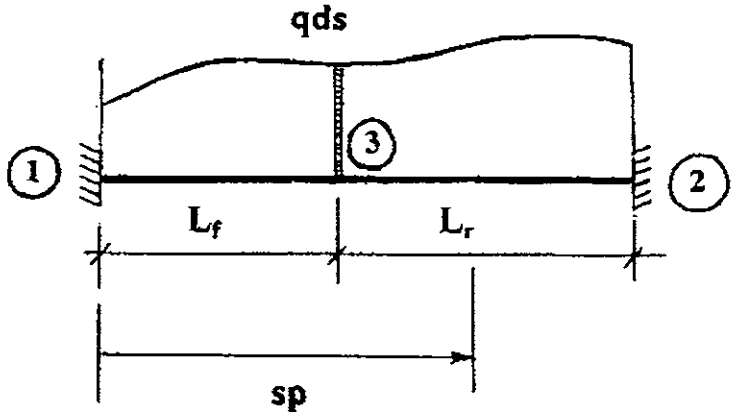

Figure 3-4: Picture showing the parameters considered in the calculation of the displacement at S_P location.

The purpose here is to obtain the reaction forces $\vec{F}_R$ at the ends of a beam element due to any arbitrary distributed load q. In this calculation we are working in the local system of reference of the element under consideration.

We start by focusing our attention on an infinitesimal part of the load qds at the location $s = L_f$, as shown in Figure 3-4. The formulation given here can be applied to both straight and curved

beam element with length L. Now we can divide this element into two new sub-elements. One going from node 1 to node 3 located at $s = L_f$ with length L_f and stiffness matrix defined by

$$\begin{bmatrix} [K_{11}^l] & [K_{13}^l] \\ [K_{31}^l] & [K_{33}^l] \end{bmatrix}$$

where $[K_{ij}^l]$ is a submatrix with dimensions 3 by 3 relating unit displacements at node i to the corresponding concentrated forces at node j. The second element goes from node 3 to node 2 with length L_r and the stiffness matrix is given by

$$\begin{bmatrix} [K_{33}^r] & [K_{32}^r] \\ [K_{23}^r] & [K_{22}^r] \end{bmatrix}$$

Node 3 can be regarded as a new and temporary node that is used just to help us to obtain $\vec{F}_R$. Notice that $L = L_l + L_r$. Each node has three degrees of freedom. At this point we can regard qds as a concentrated force acting on node 3. Based on this assumptions, the equation of dynamic equilibrium of this element, due only to the infinitesimal load qds, can be written in matrix form as

$$\begin{bmatrix} [K_{11}^l] & [K_{13}^l] & [0] \\ [K_{31}^l] & [K_{33}^l]+[K_{33}^r] & [K_{32}^r] \\ [0] & [K_{23}^r] & [K_{22}^r] \end{bmatrix} \begin{Bmatrix} d\vec{U}_1 \\ d\vec{U}_3 \\ d\vec{U}_2 \end{Bmatrix} = \begin{Bmatrix} d\vec{F}_1 \\ d\vec{F}_3 \\ d\vec{F}_2 \end{Bmatrix} \tag{3.44}$$

where

$$d\vec{U}_1 = \{0 \quad 0 \quad 0\}^T,\ d\vec{U}_3 = \{dv \quad dw \quad d\beta\}^T,\ d\vec{U}_2 = \{0 \quad 0 \quad 0\}^T$$

(which represent the infinitesimal displacements at nodes 1, 3 and 2, respectively, due only to qds) and

$$d\vec{F}_1 = \{dR_1 \quad dR_2 \quad dR_3\},\ d\vec{F}_3 = \{0 \quad qds \quad 0\},\ d\vec{F}_2 = \{dR_4 \quad dR_5 \quad dR_6\}$$

(they represent the infinitesimal reactions at node 1, the forces at node 3 and the reactions at node 2, respectively, due to *qds* only).

In the equations above the superscript 'l' means the left sub-element and 'r' means the right sub-element. The subscripts '1', '2' and '3' represent nodes 1, 2 and 3 on the beam, respectively. From the middle equation we have the following relation

$$\left(\left[K_{33}^{l}\right]+\left[K_{33}^{r}\right]\right)d\vec{U}_3 = d\vec{F}_3 \tag{3.45}$$

Equation (3.45) can be solved for the displacements without difficulty:

$$d\vec{U}_3 = \left(\left[K_{33}^{l}\right]+\left[K_{33}^{r}\right]\right)^{-1} d\vec{F}_3 \tag{3.46}$$

Note that vector $d\vec{U}_3$ is a function of the distributed load q. Once this vector is known, the infinitesimal reactions can be obtained by the following equations, extracted from the first and third lines of equation (3.44):

$$d\vec{F}_1 = \left[K_{13}^{l}\right]d\vec{U}_3 \qquad \text{and} \qquad d\vec{F}_2 = \left[K_{23}^{r}\right]d\vec{U}_3$$

So, as a final step, the total reactions can be calculated as the integral of $d\vec{F}_1$ and $d\vec{F}_2$ with s varying from 0 to the length L of the beam element.

3.5.2 Displacement at a location s_P

Now we are going to focus on obtaining the displacement fields, d_1 and d_2 along the beam element shown in Figure 3-4, as explained in steps one and eight in the beginning of section 3.5.

1 – Displacement d_1

It is desired to know the value of the transverse displacement at the location s_P of the beam element. This calculation is a continuation of section 3.5.1, which means that the conditions depicted in Figure 3-4 are still valid and so are all the results obtained in section 3.5.1. In order to determine the transverse displacement d_1 at a specific location s_P we can resort to equation

(3.44) again. We start by calculating the incremental displacement $d(d_1)$ at location s_P due to an infinitesimal load qds. We have to consider three situations:

1. $s_P > L_f$

   In this case location s_P is between nodes 3 and 2. We can focus on the right beam sub-element with length L_r and adopt the same methodology used in section 3.5.1. The infinitesimal displacements and reactions due to qds on node 3 are given, respectively, by

$$d\vec{U}_3 = \{dv \quad dw \quad d\beta\}^T \text{ and } d\vec{F}_3 = \{dR_v \quad dR_w \quad dR_\beta\}$$

   At the same time, on node 2 the infinitesimal displacements and reaction forces are given, respectively, by

$$d\vec{U}_2 = \{0 \quad 0 \quad 0\}^T \quad \text{and} \quad d\vec{F}_2 = \{dR_4 \quad dR_5 \quad dR_6\}$$

   All these quantities are already known from the calculations from section 3.5.1. If we regard location s_P as a new temporary node inside the right beam sub-element, similarly to what was done before, in section 3.5.1, the infinitesimal displacements and concentrated forces acting on this node are given, respectively, by

$$d\vec{U}_{sp} = \{dv_P \quad dw_P \quad d\beta_P\}^T \text{ and } d\vec{F}_{sp} = \{0 \quad 0 \quad 0\}$$

   Therefore, we are ready to apply equation (3.44) to the conditions of this right beam sub-element:

$$\begin{bmatrix} [K^l_{33}] & [K^l_{3sp}] & [0] \\ [K^l_{sp3}] & [K^l_{spsp}]+[K^r_{spsp}] & [K^r_{sp2}] \\ [0] & [K^r_{2sp}] & [K^r_{22}] \end{bmatrix} \begin{Bmatrix} d\vec{U}_3 \\ d\vec{U}_{sp} \\ d\vec{U}_2 \end{Bmatrix} = \begin{Bmatrix} d\vec{F}_3 \\ d\vec{F}_{sp} \\ d\vec{F}_2 \end{Bmatrix}$$

where 'l' stands for the region of sub-element on the left side of location sp, and 'r' stands for the region of sub-element on the right side of location sp.

If we once again get the middle equation from the equation above we will have

$$[K^{l}_{sp3}]d\vec{U}_3 + ([K^{l}_{spsp}]+[K^{r}_{spsp}])d\vec{U}_{sp} = \vec{0} \Rightarrow d\vec{U}_{sp} = -([K^{l}_{spsp}]+[K^{r}_{spsp}])^{-1}[K^{l}_{sp3}]d\vec{U}_3 \qquad (3.47)$$

Now we can integrate equation (3.47) from $s = 0$ to $s = s_P$ along the longitudinal axis of the beam element to get the total displacement at location s_P (which is d_1) due to the distributed load on the left side of $s = s_P$.

To obtain the curvatures, we can focus on the beam sub-element that extends from s_P to node 2 with dynamic stiffness matrix $[K_e]$ and apply the dynamic equation

$$[K_e]\begin{Bmatrix} dv_P \\ dw_p \\ d\beta_P \\ 0 \\ 0 \\ 0 \end{Bmatrix} = \begin{Bmatrix} df_{1P} \\ df_{2P} \\ df_{3P} \\ dR_4 \\ dR_5 \\ dR_6 \end{Bmatrix}$$

The third equation gives increment of the bending moment at location s_P (equal to df_{3P}), since the quantities on the left side of the equation are all known from the previous steps. Thus, the increment in curvature is given by df_{3P}/EI. Then, we integrate this quantity from $s = 0$ up to $s = s_P$.

2. $s_P < L_f$

In this case, location s_P is between nodes 1 and 3. We can focus our attention on the left beam sub-element with length L_f and adopt the same methodology used in item 1 of this section, with the corresponding adaptations. The infinitesimal displacements and reactions due to qds on node 1 are given, respectively, by

$$d\vec{U}_1 = \{0 \quad 0 \quad 0\}^T \quad \text{and} \quad d\vec{F}_1 = \{dR_1 \quad dR_2 \quad dR_3\}^T$$

At the same time, on node 3, the infinitesimal displacements and reaction forces are given, respectively, by

$$d\vec{U}_3 = \{dv \quad dw \quad d\beta\}^T \quad \text{and} \quad d\vec{F}_3 = \{dR_v \quad dR_w \quad dR_\beta\}^T$$

Again, if we regard location s_P as a new temporary node inside the left beam sub-element, similarly to what was done before, in item 1 of the present section, the infinitesimal displacements and concentrated forces acting on this node are given, respectively, by

$$d\vec{U}_{sp} = \{dv_P \quad dw_P \quad d\beta_P\}^T \quad \text{and} \quad d\vec{F}_{sp} = \{0 \quad 0 \quad 0\}$$

Now we can write equation (3.44) for the conditions of this left beam sub-element:

$$\begin{bmatrix} [K^l_{11}] & [K^l_{1sp}] & [0] \\ [K^l_{sp3}] & [K^l_{spsp}]+[K^r_{spsp}] & [K^r_{sp3}] \\ [0] & [K^r_{3sp}] & [K^r_{33}] \end{bmatrix} \begin{Bmatrix} d\vec{U}_1 \\ d\vec{U}_{sp} \\ d\vec{U}_3 \end{Bmatrix} = \begin{Bmatrix} d\vec{F}_1 \\ d\vec{F}_{sp} \\ d\vec{F}_3 \end{Bmatrix}$$

If we get the middle equation from the system above, we will have

$$([K^l_{spsp}]+[K^r_{spsp}])d\vec{U}_{sp} + [K^r_{sp3}]d\vec{U}_3 = \vec{0} \Rightarrow d\vec{U}_{sp} = -([K^l_{spsp}]+[K^r_{spsp}])^{-1}[K^r_{sp3}]d\vec{U}_3 \qquad (3.48)$$

Now we can integrate equation (3.48) from $s = s_P$ to $s = L$ along the longitudinal axis of the beam element to get the total displacement at location s_P(which is d_1) due to the distributed load on the right side of $s = s_P$.

To obtain the curvatures, we can focus on the beam segment that extends from node 1 to location s_P and apply the dynamic equation

$$[K_e]\begin{Bmatrix} 0 \\ 0 \\ 0 \\ dv_P \\ dw_P \\ d\beta_P \end{Bmatrix} = \begin{Bmatrix} dR_1 \\ dR_2 \\ dR_3 \\ df_{4P} \\ df_{5P} \\ df_{6P} \end{Bmatrix}$$

The fifth equation gives the increment of bending moment at location s_P (defined by df_{6P}), since the quantities on the left side of the equation are all known. So, the increment in curvature is given by df_{6P}/EI. Then we integrate this quantity from $s = s_P$ up to $s = L$ along the longitudinal axis of the beam element.

3. $s_P = L_f$

   In this case we already know the displacement at s_P from section 3.5.1. The curvature can be obtained by using the same methodology explained before either using sub-element with length L_f or sub-element with length L_r

For the calculation of d_2, the procedure can be based on the following relations:

$$\vec{U}_e = [D]\vec{W} \quad \Rightarrow \quad \vec{W} = [D]^{-1}\vec{U}_e$$

where vector $\vec{U}_e$ was obtained according to step 8 of the procedure described in the beginning of section 3.5. Knowing the coefficients, we can obtain d_2 through equations (3.27) and (3.28) for the case of curved beam, for example.

3.5.3 An alternative way to calculate reactions at the clamped ends

The method shown in section 3.5.1 had two benefits:

- to calculate the reactions at the clamped ends of the beam element
- to calculate quantities ($d\vec{U}_3$) that will be necessary in the calculation of transverse displacement inside the beam element

However, the calculation of internal displacement does not have to be done for all the elements of the structure. It can even be an option in the analysis if one is interested only the structure response at the nodes. There is a faster way to calculate only the nodal forces equivalent to the distributed load acting on the beam element. This method is well known in the FEM context and it will be summarized below.

Equations 3.11 and 3.12, with the help of equation 3.10, can be written, in matrix form as

$$\vec{u} = \vec{E} \cdot \vec{W}$$

where 2 by 1 vector $\vec{u}$ represents the dynamic transverse and longitudinal displacements along the beam element. The end displacements, $\vec{U}$, are given by $\vec{U} = \vec{D} \cdot \vec{W}$, where $\vec{W}$ is the vector of wave amplitudes. Vector $\vec{W}$ can be expressed by $\vec{W} = \vec{D}^{-1} \cdot \vec{U}$. Substituting this expression in the equation above yields

$$\vec{u} = \vec{E} \cdot \vec{D}^{-1} \cdot \vec{U} \Rightarrow \vec{u} = \vec{N} \cdot \vec{U}$$

where $\vec{N}$ is the interpolation function of the beam element since it relates the internal displacements to the end displacements. Suppose now that we have a distributed load along the element given by a vector $\vec{f} = \{f_l \quad f_t\}$ where f_l and f_t are the longitudinal and transverse components, respectively. It have been proven in the FEM context that the equivalent end forces are given by the expression

$$\vec{F} = \int_0^L \vec{N}^t \cdot \vec{f} \cdot ds$$

Vector $\vec{F}$ is the one we are looking for.

This method was implemented and tested, giving the same vector as the one calculated according to the method explained in section 3.5.1.

3.6 Example

3.6.1 Influence of Curvature

In order to study the effect of curvature on a propagating wavenumber, we will consider here a curved beam element with the same properties of the straight element studied in the section of examples in Chapter 2, but this time, with a radius of curvature and without any soil spring. The static constant tension is $121250N$ and the beam properties are $E=2.067\times10^{11}\ N/m^2$, $A=0.007426m^2$, $I=0.2181\times10^{-4}m^4$, $\rho=10759.6kg/m^3$ and $H_d=0.181m$.

First we are going to focus on the longitudinal wave. Figure 3-5 illustrates graphically the relation between wavenumber and wave frequency governing this type of wave. The solid line corresponds to radius of curvature, R, equal to 400m, the dashed line to $R=500m$ and the dotted line to $R=600m$. It is evident that the curvature has a strong influence on the wavenumber.

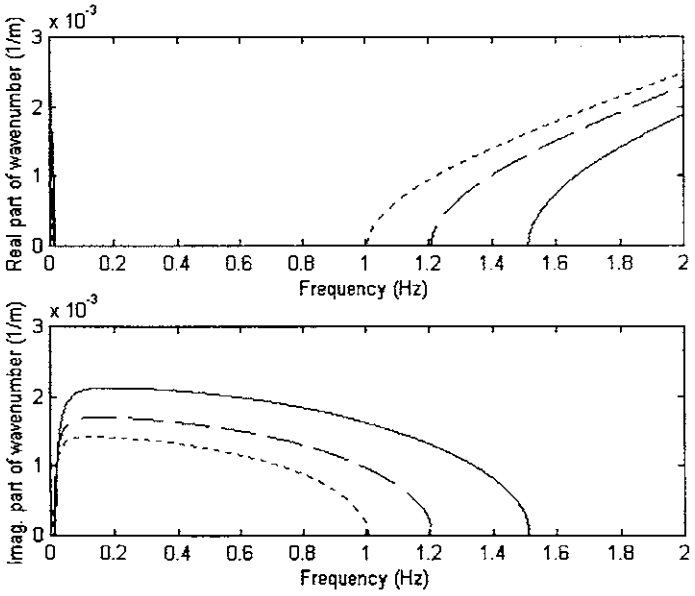

Figure 3-5: Dispersion relation of a curved beam for three different radius of curvature subjected to a static tension equal to $121250N$ concerning longitudinal waves. R=400m corresponds to solid line, R=500m corresponds to dashed line and R=600m corresponds to dotted line.

We can see from Figure 3-5 that the spectrum for wavenumber presents regions of frequencies defining two major types of longitudinal waves. For very low and high frequencies we have purely propagating waves without spatial attenuation. In the intermediate region we have only purely evanescent waves. Both the extension of this intermediate region and the magnitude of the attenuation decrease with increasing radius of curvature. In the limit of radius of curvature very large (i. e., straight beam) the longitudinal wave reduce to that of a rod element.

In Figure 3-6, the relationship between the transverse wavenumbers and frequency are plotted for different radius of curvature of the beam. The dashed curve corresponds to radius equal to 50m, the dashdot curve corresponds to radius of 100m, the dotted line corresponds to radius of 1000m and the solid curve corresponds to the straight beam with the same characteristics. Actually, these wavenumbers are the γ_p mentioned in the first example of section 2.6.1. There is no imaginary part.

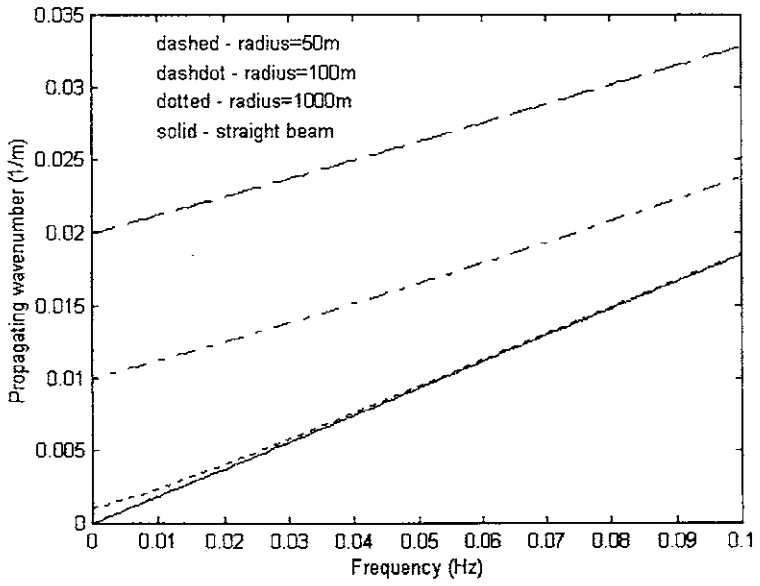

Figure 3-6: Dispersion relation of a curved beam for three different radius of curvature subjected to a static tension equal to $121250N$ concerning transverse waves.

Figure 3-7 shows the same set of curves as those shown in Figure 3-6 for a wider frequency range. As the frequency increases, the curves corresponding to the curved beam get closer to the curve corresponding to the straight beam. It means that there is a frequency above which the

propagating waves do not feel the effect of the curvature because their length is smaller than the radius of curvature. To have an idea about the value of this limit frequency, the difference between the wavenumber of a curved beam and the wavenumber of the straight beam is calculated at each frequency. The following limit frequencies were obtained:

- For a difference equal to 1%

  Radius = 50m ⇒ 1.52Hz ⇒ Ratio wavelength to radius = 0.67

  Radius = 100m ⇒ 0.65Hz ⇒ Ratio wavelength to radius = 0.60

  Radius = 1000m ⇒ 0.06Hz ⇒ Ratio wavelength to radius = 0.54

- For a difference equal to 0.1%

  Radius = 50m ⇒ 9.85Hz ⇒ Ratio wavelength to radius = 0.23

  Radius = 100m ⇒ 3.00Hz ⇒ Ratio wavelength to radius = 0.22

  Radius = 1000m ⇒ 0.21Hz ⇒ Ratio wavelength to radius = 0.16

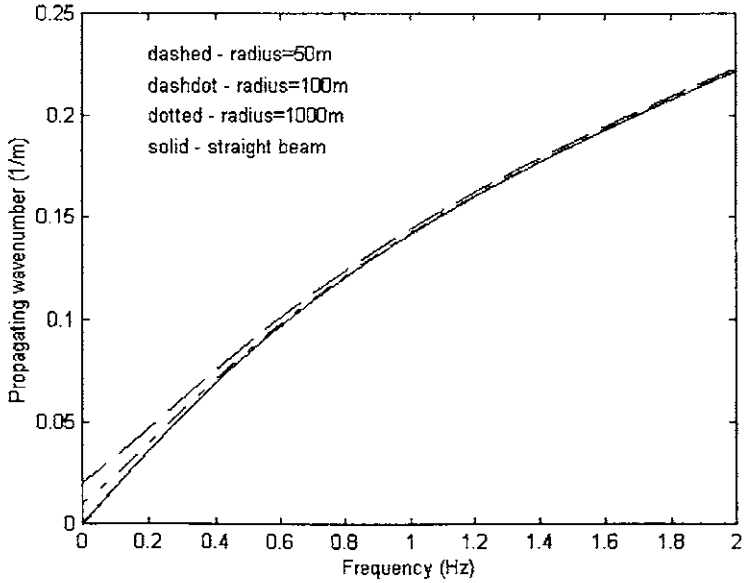

Figure 3-7: Dispersion relation for transverse waves of a curved beam for three different radius of curvature and a straight beam, all of them subjected to a static tension equal to 121250N.

We see that if we are comfortable with 1%, when the wavelength is up to half the beam radius of curvature, the waves will not feel its effect.

3.6.2 Static Values

To test the methodology explained in the previous sections and to have an idea of the capabilities of the WBFEM, we are going to study some simple examples where the static values of displacements, forces and reactions in different structures are calculated by working with the dynamic stiffness matrix at very low frequency (i.e., much smaller than the first natural frequency). For the first two examples, the static values used for comparison are taken from the reference [38].

- The first structure is a straight beam clamped at both ends like the one shown in Figure 3-4. Only one straight element will be used. The data related to it are the following:

  Length: 161m

  Uniform load applied in the whole beam: 0.6462N/m

  Bending Stiffness: 177530kNm2

  Following the methodology explained in section 3.5.1, with a frequency equal to 0.000001Hz, the following quantities were obtained:

  Vertical reaction at one clamped end: 52.023 N

  Bending moment at one clamped end: 1396.0 Nm

  Maximum vertical displacement: 0.00637 m

  Using the expressions contained in the reference [38] mentioned above we get:

  Vertical reaction at one clamped end: 52.023 N

  Bending moment at one clamped end: 1395.95 Nm

  Maximum vertical displacement: 0.00637 m

  We see that the values are equivalent.

  If we now add a constant axial tension on the beam equal to 2459198.25 N, we get the following results by using the dynamic matrices with the same low frequency:

  Vertical reaction at one clamped end: 52.023 N

  Bending moment at one clamped end: 395.33 Nm

  Using the expressions contained in the reference [38] we get:

Vertical reaction at one clamped end: 52.023 N

Bending moment at one clamped end: 395.36 Nm

Again, we see that the results match very well and this fact testify the accuracy of the method.

- The second structure is an arc with the shape of a half of a circumference with its ends clamped. The characteristics of the system are the following:

  Radius of curvature: 3m

  Uniform radial load: 646.2N/m

  Bending Stiffness: 177530kNm2

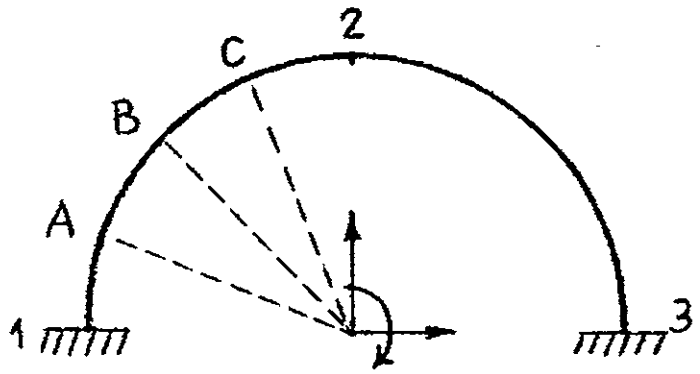

Figure 3-8: Structural arc with clamped ends

We are going to calculate the three reactions at end number 1. Two equal elements were used as shown in Figure 3-8 above. Applying the methodology explained before with a frequency equal to 0.000001 Hz (the first natural frequency of this structure is 33Hz), we obtained:

Horizontal reaction: 47.49 N

Vertical reaction: 1936.2 N

Bending moment: -90.68 Nm

Using the expressions contained in the reference [38] we get:

Horizontal reaction: 47.56 N

Vertical reaction: 1938.6 N

Bending moment: -90.85 Nm

The reaction forces obtained by both methods show good agreement.

Continuing with the same problem, now we are going to test the methodology to calculate the bending moments in 3 points (indicated by A, B and C in Fig. 3-8) equally spaced inside the first curved element, following the procedure explained in section 3.5.2. The bending moments obtained by the WBFEM will be compared by the analytical values obtained by the static equilibrium, since the end reactions at node 1 are already known. The bending moments obtained are shown in the table below.

Point	WBFEM	Analytical
A	-36.24	-36.24
B	10.03	10.06
C	40.98	40.99

Table 3.1: Bending moments in 3 internal points in the curved beam element of the arc shown in Figure 3-8.

The agreement between the results is satisfactory and shows that the methodology works.

- Now we are going to consider an example that, despite its simplicity, will show the importance of representing well the distribution of the radius of curvature along the beam. Suppose we have a horizontal straight beam pinned at both ends with the following characteristics:

  Total length: 1288m

  Bending stiffness: $1.7753\times10^{8}\,Nm^{2}$

  Uniform transverse load magnitude: $0.02585\,N/m$

  If we apply the load at a frequency like 0.000001Hz, we are in fact applying it statically, as we did in the previous examples. For this case, we know that the maximum bending moment will be $qL^{2}/8=5360.46Nm$ while the maximum displacement will be given by $5qL^{4}/(384EI)=5.22m$.

  Modeling this beam with 1 straight beam element length and applying the load at 0.000001Hz we will find $5.22m$ as the maximum displacement and $5360.53Nm$ as the maximum bending moment.

In order to study this straight beam with a curved beam element, we will have to assign it a very large radius of curvature. From the dispersion relation of a straight beam with the properties used in the present example and frequency equal to 0.000001Hz, we obtain the following propagating wavelength: 52450m. According to what was studied in section 3.6.1, the radius of curvature should be at least twice the wavelength so that the wave does not feel its influence. Thus, we choose the radius of curvature equal to 200000m for the curved beam. The distribution of transverse displacement and bending moment along the beam is shown in Figures 3-9 and 3-10, respectively. The maximum values of the curves correspond to 5.22m and 5360.5Nm obtained before.

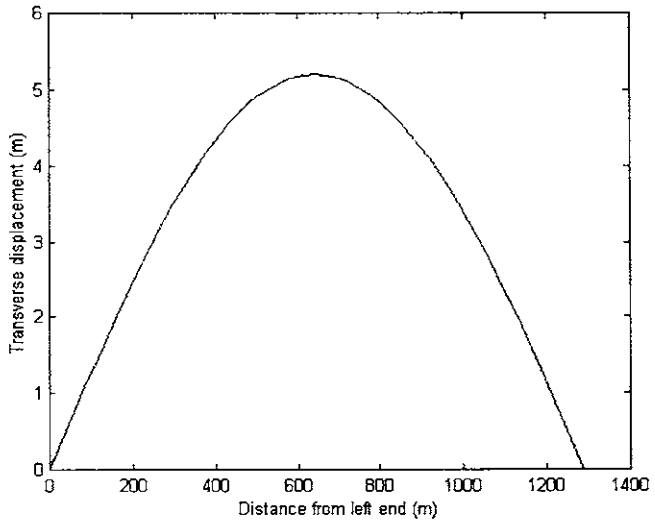

Figure 3-9: Transverse displacement of a straight beam using curved element with 3 different radius of curvature together with the straight element. The origin is the left end

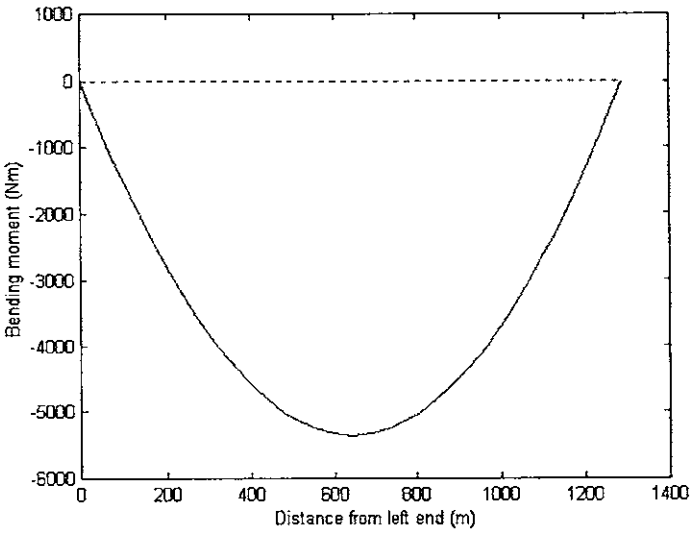

Figure 3-10: Bending moment of a straight beam using curved element with 3 different radius of curvature together with the straight element. The origin is the beam left end.

3.6.3 Dynamic Values

- We are going to study the dynamic response of a simply supported beam to a harmonic concentrated load as shown in Figure 3-11 below,

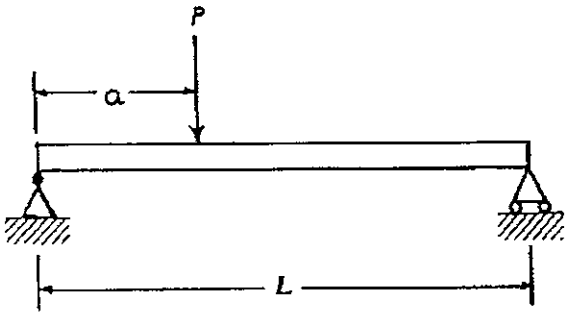

Figure 3-11: Simply supported beam subjected to a concentrated harmonic force

where the position $s = a$ a is the distance between the concentrated force and the left end of the beam (identified here as 'bottom'), p is the force amplitude and ω if the force

frequency, in rad/s. According to reference [36] the transverse displacement is given by the following expression

$$\frac{2p}{\rho AL}\sum_{n=1}^{\infty}\frac{1}{\omega_n^2-\omega^2}\sin\left(\frac{n\pi a}{L}\right)\sin\left(\frac{n\pi s}{L}\right) \tag{3.49}$$

We selected the beam used in the last example of the previous section as the subject of our study. The additional properties of the beam are:

Young's modulus: $2.05\times10^{11}\,N/m^2$

Moment of inertia: $8.66\times10^{-4}\,m^4$

Cross sectional area: $0.104m^2$

Mass per unit length: $0.398kg/m$

Total length: $1288m$

Amplitude p: $100N$

Load frequency: $0.6Hz$

Point of application of concentrated force: $257.6m$ from left end

The beam transverse displacement obtained by the application of formula 3.49 above is shown in Figure 3.12 below. We had to use 25 modes to get convergence in the response.

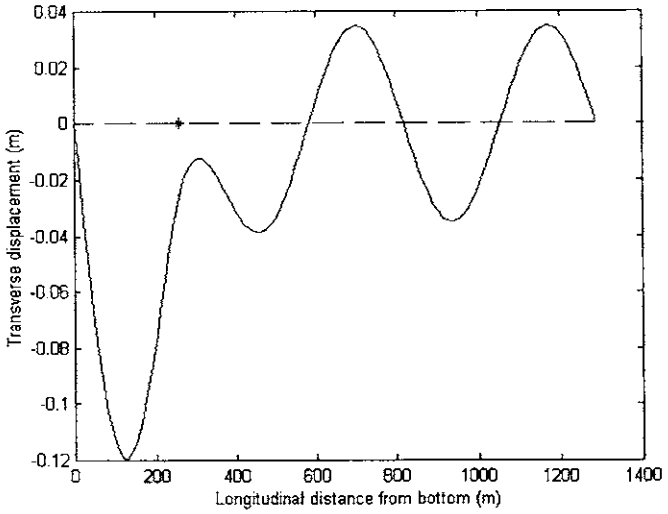

Figure 3-12: Transverse harmonic displacement of the beam depicted in Figure 3.11 caused by a harmonic concentrated load acting on '*'.

In order to test the methodology developed here, we are going to calculate the transverse displacement of the same beam using both the straight and curved beam (with radius of curvature very large) in the context of WBFEM. Only one element will be employed.

First we have to check if we are dealing with the right structure. So, the first 5 natural frequencies (in Hz) are shown in the table 3.2 below. They were obtained through 2 methods: analytical and WBFEM. As we can see they show very good agreement. As we are using 2 decimals, the values presented in the table for each frequency are equal.

Freq. #	WBFEM	Analytical
1	0.02	0.02
2	0.08	0.08
3	0.18	0.18
4	0.32	0.32
5	0.50	0.5

Table 3.2: First five natural frequencies of the straight beam shown in Figure 3-11, calculated by two different methods.

As for the transverse displacement, both types of elements gave the same curve shown in Figure 3-12. Table 3.3 below shows numerical values of transverse displacement amplitude at some values of the relative position s/L along the beam.

The agreement between the results is again very good. The noteworthy point here is the fact that using the WBFEM we did not have to calculate any natural frequency to obtain the structure response.

s/L	Amplitude	
	WBFEM	Analytical
0.1	-0.1193	-0.1193
0.2	-0.0264	-0.0266
0.3	-0.0280	-0.0279
0.4	-0.0293	-0.0293
0.5	0.0253	0.0253
0.6	0.0197	0.0197
0.7	-0.0315	-0.0315
0.8	-0.0103	-0.0103
0.9	0.0346	0.0346

Table 3.3: Transverse displacement of the simply supported beam shown in Figure 3-11 obtained by two different methods: WBFEM and analytically.

- Now we are going to apply a harmonic distributed load on the same beam considered in the previous example, beginning at the left end and finishing at $s = a$. The situation is shown in Figure 3.13 below. The load has constant magnitude equal to p_0. Using the mode superposition method, we find that the expression for the steady-state transverse displacement is given by

$$\frac{2p_0}{\rho A}\sum_{n=1}^{\infty}\frac{1}{\left(\omega_n^2-\omega^2\right)n\pi}\left(1-\cos\left(\frac{n\pi a}{L}\right)\right)sin\left(\frac{n\pi s}{L}\right)sin(\omega t) \tag{3.50}$$

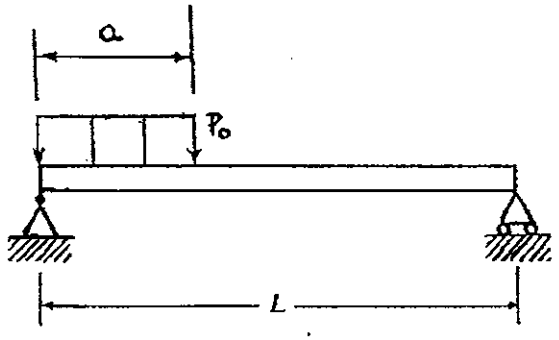

Figure 3-13: Simply supported beam subjected to a constant load from $s = 0$ to $s = 257.6m$

Setting $p_0 = 50N/m$ and $a = 257.6m$, and applying the load at $0.6Hz$, we find the transverse displacement shown in Figure 3.14 below by the solid line.

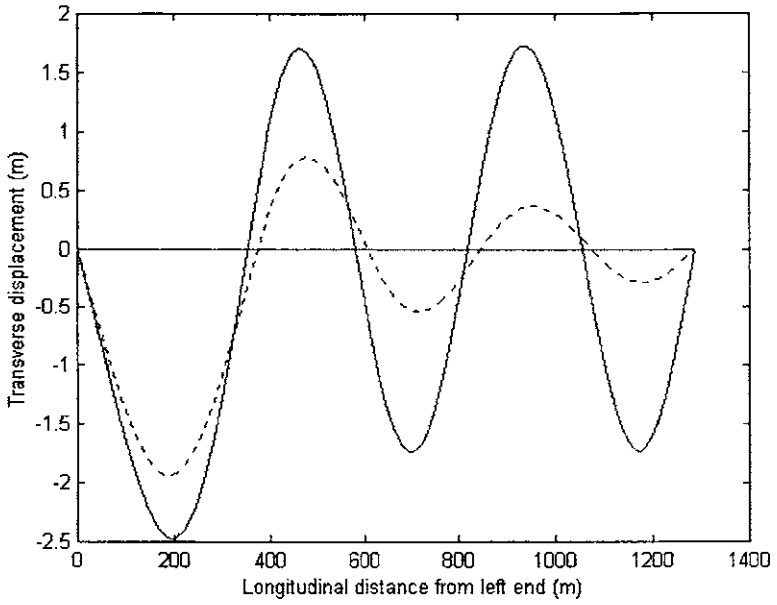

Figure 3-14: Transverse displacement of a simply supported beam for a distributed load with length equal to 'a', measured from the left end. The solid line corresponds to undamped beam and the dotted curve corresponds to a damped beam.

For the sake of comparison, we made the same analysis using one straight beam element developed in chapter 2 to represent the beam. We obtained the same solid curve shown in Figure 3.14. The dotted curve, presented in Figure 3-14, is the transverse displacement of the beam with a complex modulus of elasticity equal to $2.05\times10^{11} - i\cdot 1.2\times10^{11} N/m^2$, to simulate loss of energy, under the same distributed load conditions. Table 3.4 shows the comparison between the transverse displacements obtained by both methods at specific points of the undamped beam.

s/L	Amplitude	
	WBFEM	Analytical
0.1	-2.0290	-2.0445
0.2	-2.0256	-2.0292
0.3	0.7916	0.7879
0.4	1.3481	1.3441
0.5	-1.2735	-1.2701
0.6	-0.9815	-0.9789
0.7	1.5643	1.5601
0.8	0.5135	0.5121
0.9	-1.7179	-1.7133

Table 3.4: Transverse displacement of the simply supported beam shown in Figure 3-13

Then we made the same calculations as before but now using one curved beam element with curvature radius of 500000m and the results were the same as those shown in Figure 3.14 and table 3.4.

- Now we are going to apply a harmonic triangular distributed load on the same beam studied in the previous example. The load is null for $s \le a$ and $s > b$ and increases linearly from 0 to p_0 from $s = a$ to $s = b$. The situation is shown in Figure 3-15.

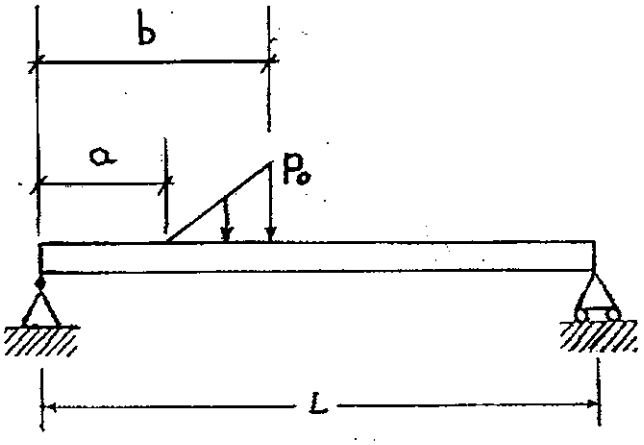

Figure 3-15: Simply supported beam subjected to a constant load from $s = 257.6m$ to $s = 386.4m$

Using the mode superposition method, the steady state transverse displacement is given by the following expression:

$$\frac{2p_0}{\rho AL}\sum_{n=1}^{\infty}\frac{1}{\left(\omega_n^2-\omega^2\right)}\left\{\frac{1}{b-a}\left[\left(\frac{L}{n\pi}\right)\left(a\cos\left(\frac{n\pi a}{L}\right)-b\cos\left(\frac{n\pi b}{L}\right)\right)+\left(\frac{L}{n\pi}\right)^2\cdot\right.\right.$$

$$\left.\left.\left(\sin\left(\frac{n\pi b}{L}\right)-\sin\left(\frac{n\pi a}{L}\right)\right)\right]-\frac{a}{b-a}\left(\frac{L}{n\pi}\right)\left(\cos\left(\frac{n\pi a}{L}\right)-\cos\left(\frac{n\pi b}{L}\right)\right)\right\}\sin\left(\frac{n\pi s}{L}\right)\sin(\omega t)$$

The transverse displacement, expressed by the equation above, is shown by the solid line in Figure 3-16 below. We set $p_0 = 100N/m$, $a = 257.6m$, $b = 386.4m$ and the excitation frequency was 3Hz.

With only one element, we employed both the straight and curved types to calculate the transverse displacement and we obtained the curve represented in Figure 3-16. The region of application of the distributed load is also shown in this figure through the thicker part.

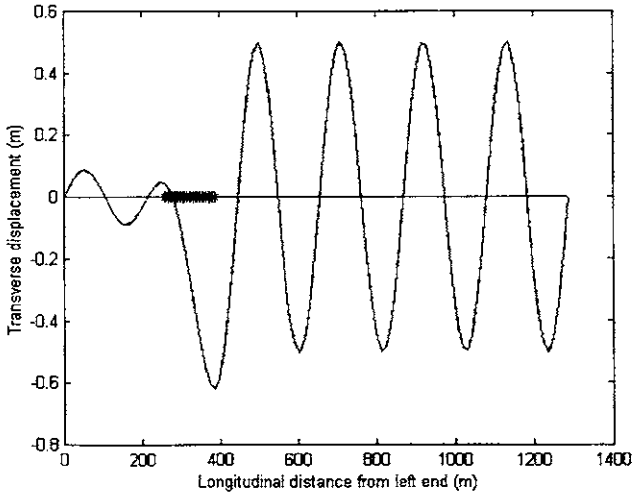

Figure 3-16: Transverse displacement for a triangular distributed load. The solid line is the theoretical response and the dotted line comes from the WBFEM.

- In this example, we are going to calculate the natural frequencies of the arc shown in Figure 3-17 through two ways: one is analytical, taken from reference [8], and another with one curved beam element developed here. Both ends of the arc are pinned.

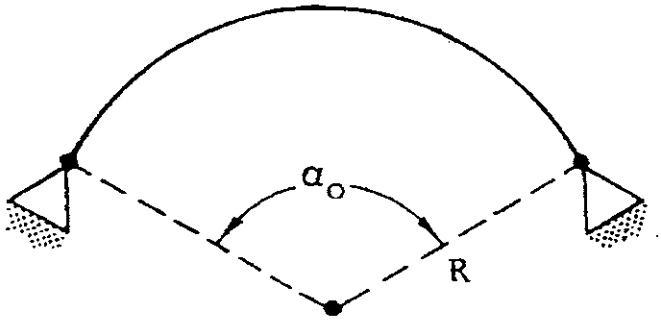

Figure 3-17: Pinned-pinned beam arc

The properties of the arc are the following:

Young's modulus: $2.05\times10^{11} N/m^2$

Moment of inertia: $3.73\times10^{-6} m^4$

Linear mass: $7175.33 kg/m$

Angle of the arc, α_0: $1.6 rad$

Radius of the arc: $3m$

The values for the first seven natural frequencies (in Hz) of the arc are shown in table 3.5 below. They show good agreement between them.

Freq. #	WBFEM	Analytical
1	2.531	2.421
2	5.765	5.705
3	10.986	10.841
4	15.711	16.821
5	18.823	17.433
6	24.440	24.949
7	38.914	39.557

Table 3.5: First seven natural frequencies of the arc shown in Figure 3.15, calculated by two different methods.

Chapter 4

Experiments

4.1 Introduction

In this chapter we will describe some experiments performed with riser models in different configurations. In the first part we are concerned with highly compliant risers. They are large scale models that were tested in a lake with controlled excitations. There is a large amount of data records but in the present work we will focus more on the frequency content issue. Furthermore, there is another doctoral student devoting most of his time to the analysis of the data collected. Then we describe an experiment performed in a towing tank with a steel catenary riser (scr) model in an attempt to have a better understanding of the Keulegan-Carpenter (KC) number threshold. The effect of boundary conditions on propagating waves is also verified experimentally.

4.2 Experiments with HCR Models

In 1998, under the direction of PMB Engineering, SMS performed large scale model tests of 3 different configurations of highly compliant rigid riser model pipes: the Compliant Vertical Access Riser (CVAR), shown in Figure 4-1, the Lazy Wave SCR (LWSCR), shown in Figure 4-2 and the Steel Catenary Riser (SCR), shown in Figure 4-3. These figures are in accordance with the configurations devised by PMB.

These tests were performed in about 800ft of water in Lake Pend Oreille in North Idaho and the goal was to provide greater understanding into the behavior of risers and to compare and verify riser analysis methods and software.

Several vertical amplitudes were applied on top of each riser model at many different frequencies. For each frequency, the steady state response was recorded for riser tension, in-plane and out-of-plane bending moment, in-plane and out-of-plane accelerations, among other quantities. All three riser configurations are pinned at the ends (i. e., no bending restraint) and for the purpose of location, we use a longitudinal coordinate, s, that starts at the bottom end.

The riser models were assembled from 24ft and 12ft joints of 1.5-in.×0.125-in. aluminum pipe and eight instrumented "pup" joints were attached to each configuration in regions of high response as shown in Figures 4-1, 4-2 and 4-3. They measured 2-axis bending and lateral acceleration, twist, tilt and axial tension. The pipe was flooded except for the 2ft instrumented "pup joints" which were left void to protect the instrumentation. The only source of excitation was the harmonic vertical and horizontal motion defined by a pair of amplitude/period and applied to the top end by an actuator on a barge, simulating floating system motions in waves. During the field work some surface current measurements made with wood chips and a stop watch gave a velocity of approximately 15cm/s. With the help of an ADCP it was concluded that the maximum subsurface current was about 5cm/s and that there was no current at depths greater than 100ft. Because of the small values of the measured current and the limited region where it occurs, it is supposed during the data analysis that it is negligible as well as any surface wave. Another point that is worth being mentioned is that during the processing of the data collected the effect of gravity was removed from the accelerometers.

The main data concerning the riser models were the following:

Modulus of elasticity: 10100 ksi

Weight of a 24 foot section with electric cable, in air: 42.887 lbs

Weight of 24' with electric cable, in water: 34.887 lbs

The buoyancy modules material was syntactic foam with a dry unit weight of 28.446 lb/ft, an outside diameter of 4.8025 in. and an inside diameter of 1.75 in. The distribution of these modules obeyed the following rates: 5 modules per 12 ft joint and 10 modules per 24 ft joint length of buoyancy module.

One interesting point in these experiments is the occurrence of intermittent VIV caused by the riser top motion. Although there is no current or wave in the lake, the response of the riser to the top excitation causes the riser to be subjected to an oscillatory flow of lake water. Due to this time-varying in-plane motion, the Strouhal frequency and the transverse vibration frequency

change through each cycle of the motion. As the in-plane velocity varies with respect to time, it would be intuitive to consider the instantaneous velocity normal to the pipe axis to calculate the shedding frequency as

$$f_S = \frac{|V|S_t}{D} \tag{4.1}$$

where $|V|$ is the absolute value of the normal instantaneous velocity of the oscillatory flow. Throughout this work the value assumed for the Strouhal number was 0.18. The modulus sign means that the shedding frequency is kept positive even in the negative cycles of the velocity. Equation (4.1) can be used to estimate the maximum possible vortex shedding frequency by substituting $V_{\max}$ for V.

According to Bearman et al.[1], the problem with equation (4.1) is that it does not take into account the history of the flow in terms of the past velocities. So, he proposed that an estimate of the average expected vortex shedding frequency could be calculated as

$$f_{S,avr} = \frac{|V_{avr}|S_t}{D} \tag{4.2}$$

where $V_{avr=} = \frac{\int_0^t V dt}{t}$. The integral should be calculated for each half cycle of the flow. It means that in order to evaluate the shedding frequency we should use the cumulative average of the instantaneous velocity over each half cycle of the flow so that the flow history is considered.

The absolute amplitude through which the riser moves in response to the top excitation varies along the length but we believe that there is a minimum value above which VIV will occur. A non-dimensional measure of this oscillatory flow is the Keulegan-Carpenter (KC) number, which is defined as

$$KC(s) = \frac{V_{\max}(s)P}{D} \tag{4.3}$$

We can also say that

$$V_{\max}(s) = \omega A(s) = \frac{2\pi}{P} A(s) \quad \Rightarrow \quad KC(s) = 2\pi \frac{A(s)}{D} \tag{4.4}$$

where A is the local displacement amplitude of the riser due to the periodic top motion at the period P. Therefore, one important step in the analysis of intermittent VIV is calculation of the distribution of KC number along the riser and the regions that are above the threshold KC number. The physical interpretation of this cut-off is the fact that for sufficiently small oscillations, the vortices do not have time to enter a lock-in situation, although a vortex or two may be shed without causing the response amplitude to build up to significant levels. As the KC number increases, the phenomenon becomes more steady-state, enabling lock-in to occur. A steady current corresponds to an infinite KC number oscillation as can be verified through equation (4.3).

In the following sections we will study the three configurations separately.

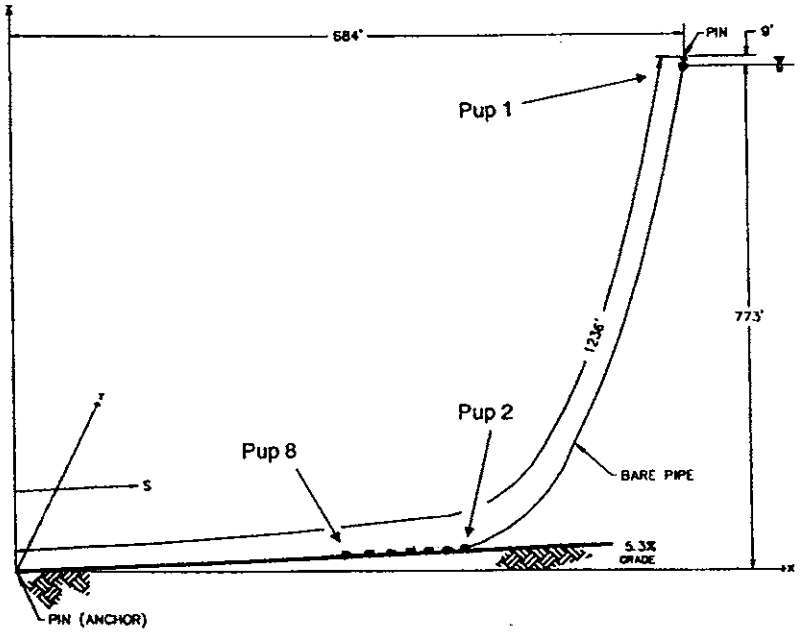

Figure 4-1: Large scale model of a SCR configuration.

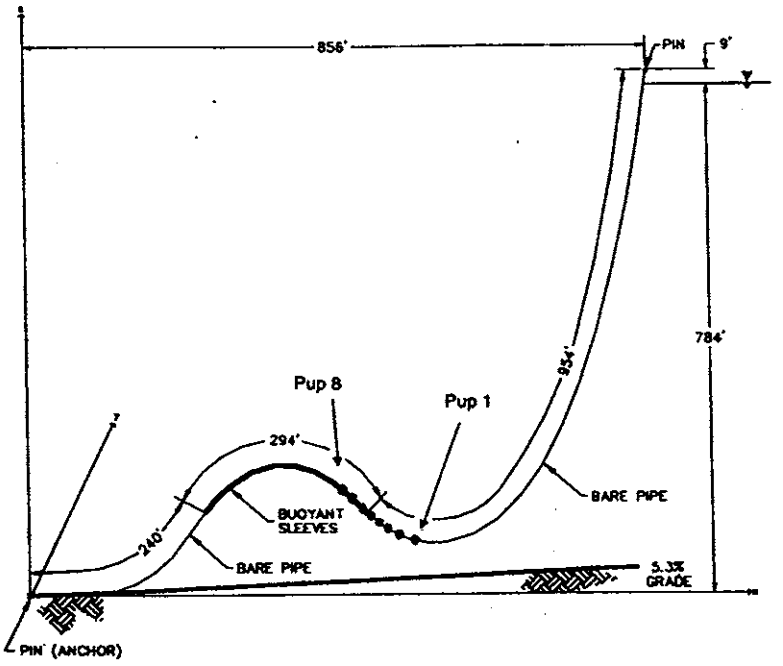

Figure 4-2: Large scale model of a LWSCR configuration.

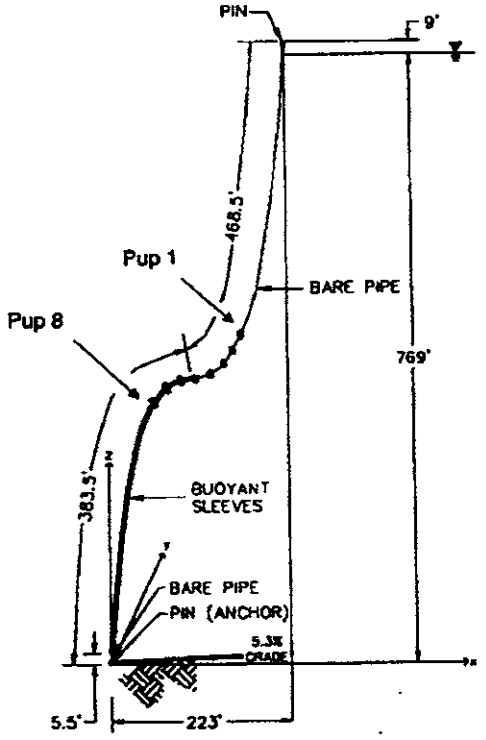

Figure 4-3: Large scale model of a CVAR configuration.

4.2.1 CVAR Configuration

Figure 4-3 shows the geometry of the CVAR. The length of the buoyancy region is 378ft. The pup joints were numbered from 1 to 8 and their locations were, respectively: $s = 453.5ft$, $s = 427.5ft$, $s = 413.5ft$, $s = 399.5ft$, $s = 385.5ft$, $s = 371.5ft$, $s = 357.5ft$ and $s = 331.5ft$. As we can see, three of them are inside the buoyancy region (6, 7 and 8) while the others are outside.

The top motion applied to the CVAR is described below by the combination of the amplitude and period:

- Amplitude of vertical motion (ft): 0.5, 2 and 3
- Period of vertical motion (sec): 3 to 10 sec with increments of 0.5 sec except for 3ft of amplitude which had increments of 1sec.

As a convention, each case is identified by the designation 'cvaranpm' where 'cvar' is the kind of riser, 'an' represents an amplitude equal to 'n' ft and 'pm' a period equal to 'm' sec.

When the riser is subjected to a periodic top motion, its response will cause a relative periodic flow between the riser and the lake water. The magnitude of the flow velocity will be equal to the normal velocity along the riser because there is no current. The distribution of this oscillatory flow velocity along the riser can be estimated with the help of Anflex, a riser FEM program. The riser was modeled with 425 elements of 2ft length each and the motion with 3ft of amplitude and 3s of period was applied to the top node. The amplitude of the normal velocity was obtained for each node and the result is shown in Figure 4-4 by the solid line, together with the magnitude of the normal velocities at the locations of the seven pups represented by 'o'. These velocities were obtained through single integration of the measured accelerations in the plane of the catenary at each pup. Number 7 was defective and is not shown. Figure 4-4 shows good agreement between the Anflex prediction of the absolute value of the normal velocity and the one obtained from the pups, supporting the accuracy of the Anflex model. There is a big drop in the in-plane normal velocity at location $s \approx 415ft$, near pup 5. This feature can be explained by the fact that this pup is located in the inflexion region of the CVAR and so it experienced little in-plane normal velocity.

For this case, the maximum value of KC number was 115.2, and occurred near pup 3 at $s = 415 ft$. The region of maximum normal velocity is just above the buoyant region. Probably this region has a KC number above the threshold value and consequently is subjected to strong vibration. The KC at pup 4 is 99.2 and at pup 2 is 107.3. Using equations 4.1 and 4.2 we can also have an idea of the distribution of the maximum shedding frequency and average shedding frequency for this case. The plot of these distributions are similar to the one shown in Figure 4-4 in shape, except for a multiplication factor. According to equations (4.1) and (4.2), for the maximum shedding frequency, this factor would be $S_t / D = 0.18/0.125 = 1.44$ and for the average shedding frequency it would be $2S_t / \pi D = 0.36/0.393 = 0.92$, both for the outside the buoyant region.

The same type of run was performed for the other excitation cases applied to the CVAR configuration in the lake, as described in the beginning of this section. Linear interpolation was used to obtain the curve shown in Figure 4-5. On the left side it is shown the variation of maximum value of KC number found by running Anflex for each excitation case. All the maximum KC numbers occurred in the middle of the riser model.

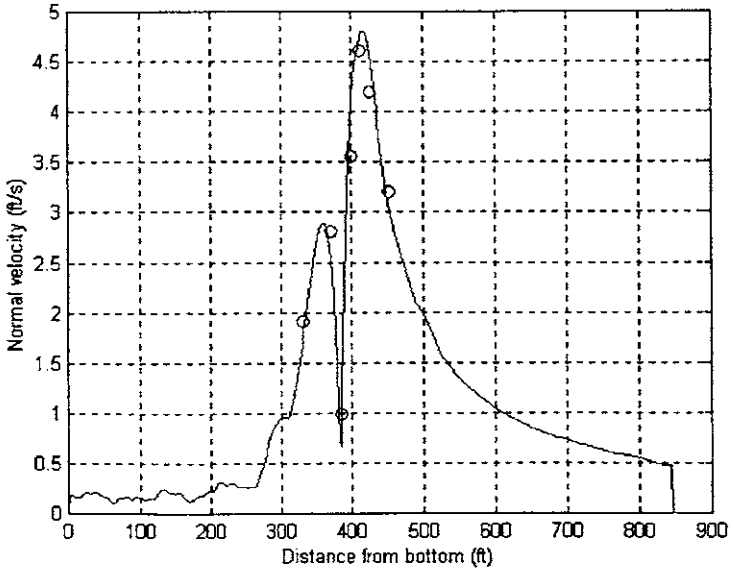

Figure 4-4: Comparison between maximum in-plane normal velocity measured by the pups (indicated by 'o') and normal velocity calculated by Anflex (solid line) for the excitation case cvara3p3.

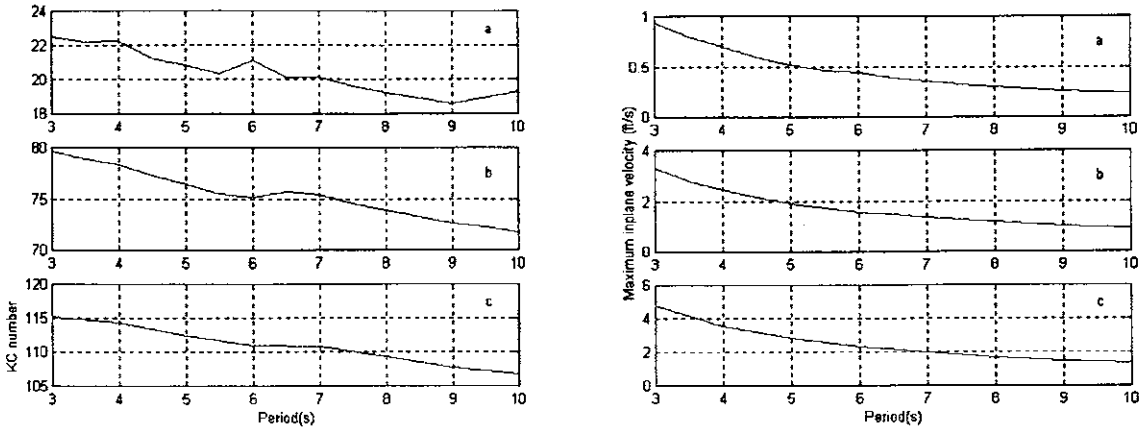

Figure 4-5: Anflex prediction of the variation of maximum KC number (left part) and maximum in-plane velocity (right part) as the period of excitation top motion changes. In the 'a' part the amplitude of motion is 0.5ft, in 'b' part is 2ft and in 'c' part is 3ft.

Using equation (4.3) we can obtain the maximum in-plane velocity corresponding to the maximum KC numbers studied before, for the same excitation cases. Linear interpolation was used between the points. The result is shown on the right side of Figure 4-5 and we can see that the maximum velocity increases as the top motion amplitude or frequency increases too. The shape of each in-plane velocity distribution is very similar to the one shown in Figure 4-4.

In order to determine how the transverse vibration frequency and the Strouhal frequency change within the cycles of the in-plane motion, a spectral analysis of the data within a short window is performed together with a corresponding numerical analysis of the configuration through Anflex. One interesting feature related to this issue and shown by the data, as we will see, is the idea that the maximum riser vibration frequency should be close to the Strouhal frequency when the in-plane normal velocity approaches its peak value. It occurs when the oscillatory in-plane bending moment that was measured by the pup joints approaches the static bending moment (which can be regarded as the mean value of the dynamic in-plane bending moment). Figures 4-6, 4-7 and 4-8 show in the upper part the time history of the in-plane bending moment and in the bottom part the time history of the out-of-plane bending moment. In these figures one can see

that as the in-plane bending moment approaches its mean value there is an increase in the vibration of the out-of-plane bending moment.

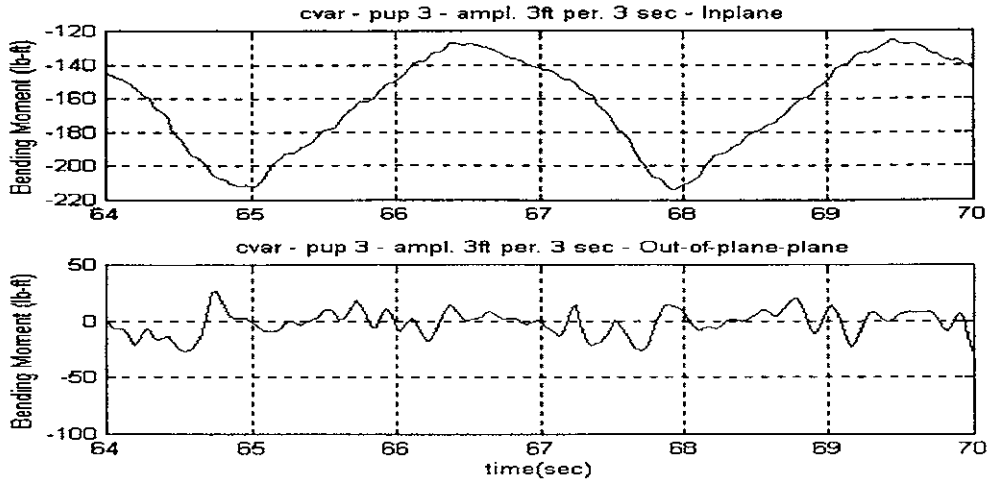

Figure 4-6: Time history of in-plane and out-of-plane bending moment measured by pup 3 for the case cvara3p3.

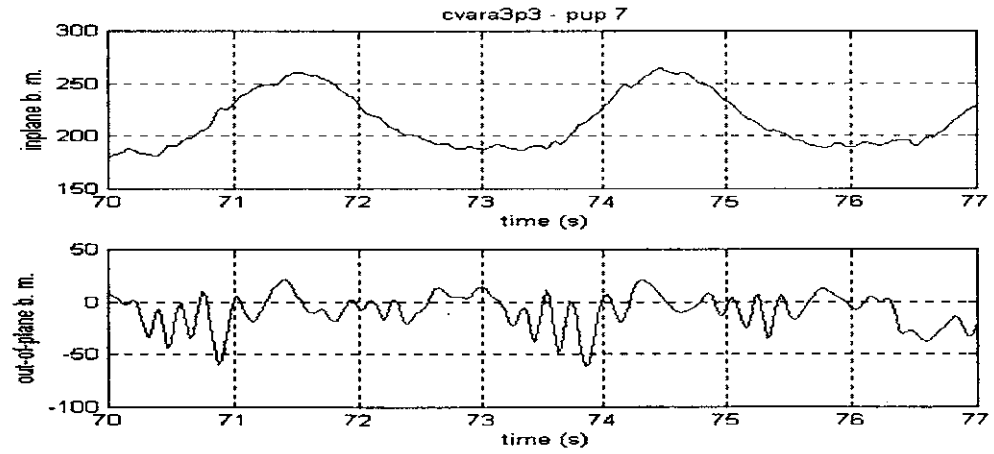

Figure 4-7:Time history of in-plane (upper part) and out-of-plane (bottom part) bending moment (lb-ft) measured by pup 7 for the case cvara3p3.

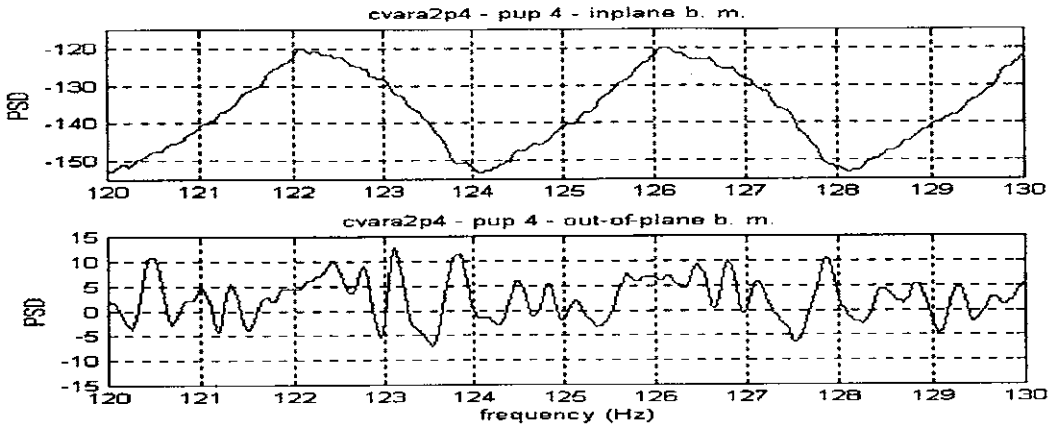

Figure 4-8: Time history of in-plane (upper part) and out-of-plane (bottom part) bending moment (lb-ft) measured by pup 4 for the case cvara2p4.

Figure 4-9 shows the time history of the in-plane bending moment measured by pup 3 for the cvara3p3 case. If compared with the same kind of plot, shown in Figure 4-10 and obtained through Anflex model, we see that both curves are very similar. This fact also supports the accuracy of the model employed. Furthermore, the plot in Figure 4-10 will be used as reference for the study that is ahead.

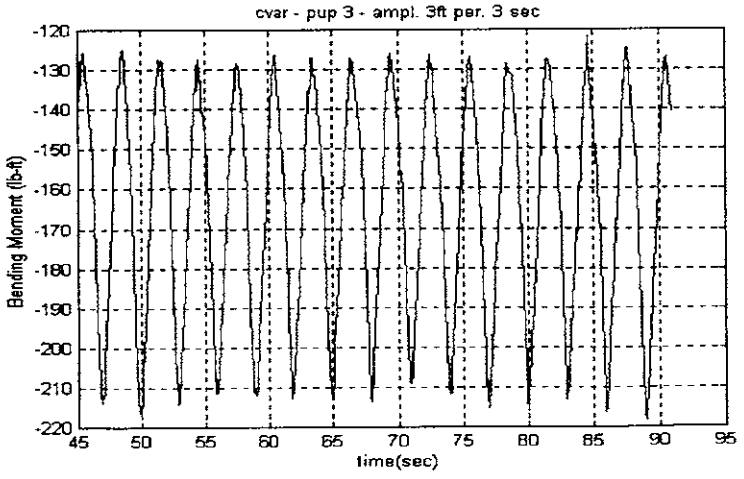

Figure 4-9: Time history of the in-plane bending moment at CVAR pup 3 for vertical top motion with amplitude equal to 3ft and period equal to 3s.

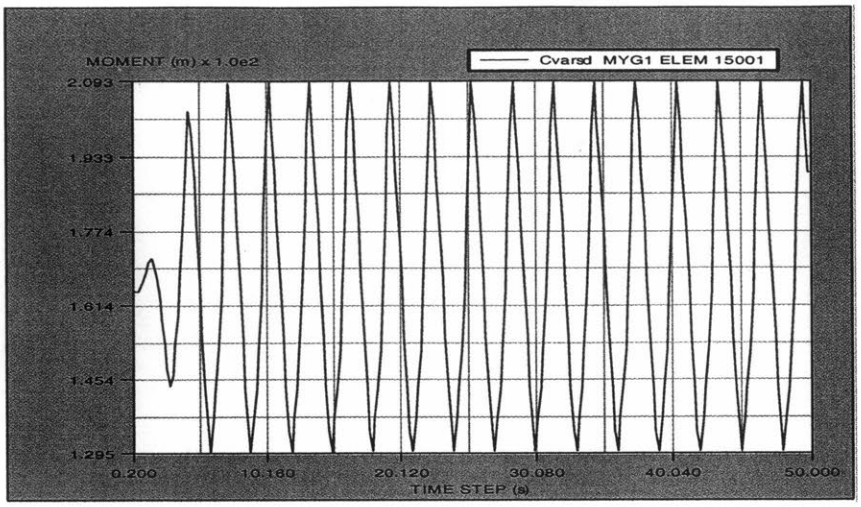

Figure 4-10: Time history of the in-plane bending moment (lb-ft) at a location in the cvara3p3 case for pup 3. This plot was obtained through Anflex.

Now we can focus our attention on the time interval from 65s to 67s (see Figure 4-6) concerning the cvara3p3 case. To have an idea of the frequency content during this period of time, we used the function PMEM from MATLAB and the result is shown in Figure 4-11. It shows that most of the response energy is around the vibration frequency of 6Hz. Looking at the curve shown in Figure 4-9 for the same time interval, we see that it corresponds to a change in the in-plane bending moment from its minimum to its maximum value in a cycle. Now we take an analogous time interval in the plot shown in Figure 4-10 (it was chosen from 45s to 47s) and calculate the instantaneous Strouhal frequency according to equation (4.1) (the result is shown in Figure 4-12). We see that the maximum frequency is around 6Hz, which is very close to the main frequency content for the period studied. The KC number for pup 3 in the cvara3p3 case is around 115.

Now we can do a similar analysis for the cvara3p3 at pup 7. Looking at Figure 4-7, we take the time interval from 73s to 74s to study. Again, through PMEM function we get the frequency content shown in Figure 4-13. The main frequency of vibration is around 3Hz. Calculating the instantaneous Strouhal frequency as explained before, we find the plot shown in Figure 4-14. According to this plot, the maximum Strouhal frequency is never above 1.3Hz. The 3Hz vibration frequency in this pup must come from a propagating wave originated in the input-power region of the riser, probably located near pup 3 . The KC number in this case is 21.6.

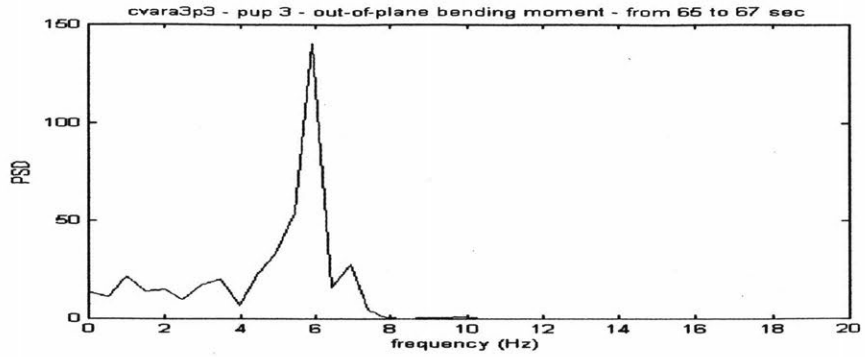

Figure 4-11: Frequency content during the period 65s to 67s of the time history of the out-of-plane bending moment for the cvara3p3 case at pup 3.

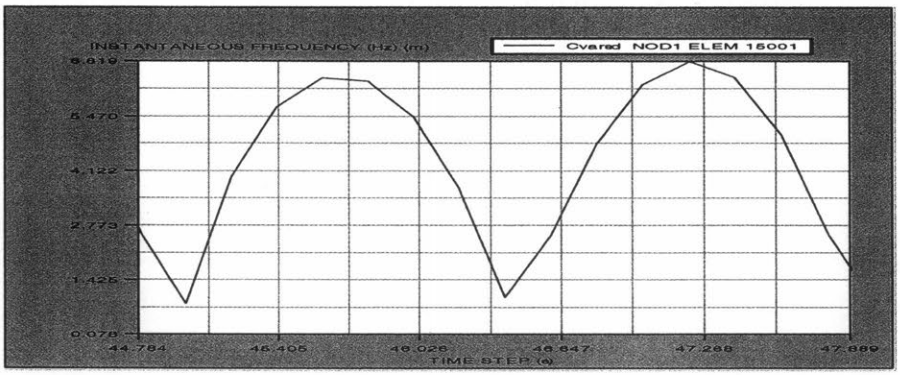

Figure 4-12: Plot of the time history of the instantaneous Strouhal frequency calculated by equation 4.1 from Anflex computed velocities for a time period corresponding to 65s to 67s in Figure 4-6.

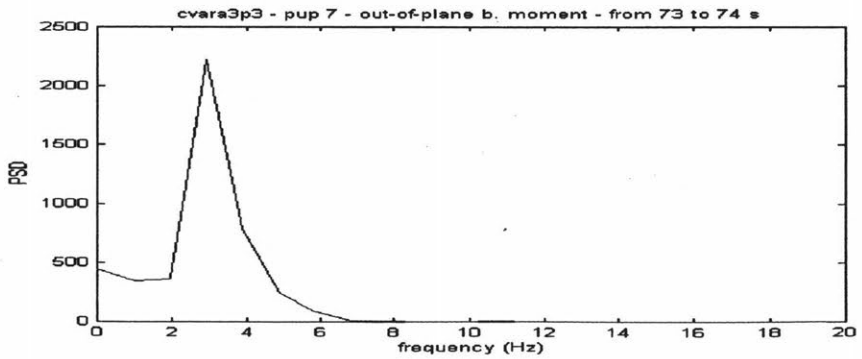

Figure 4-13: Frequency content during the period 73s to 74s of the time history of the out-of-plane bending moment for the cvara3p3 case at pup 7.

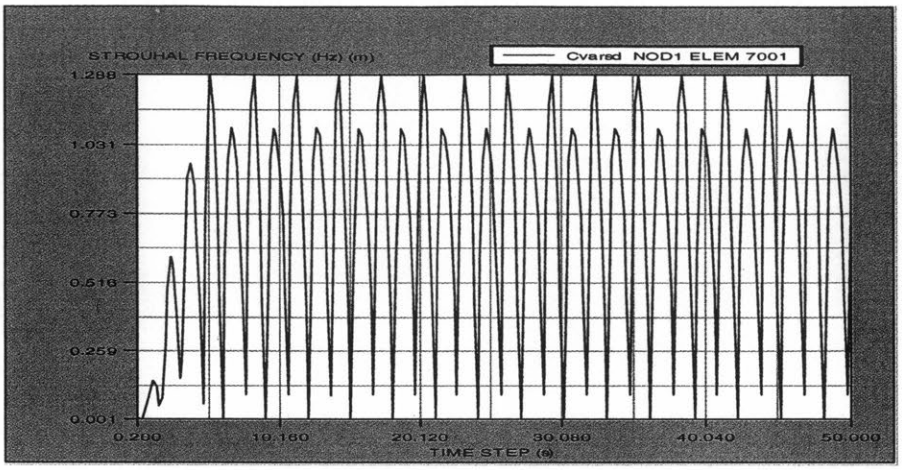

Figure 4-14: Plot of the time history of the instantaneous Strouhal frequency calculated by Anflex for the cvara3p3 case at a location corresponding to pup 7.

As a final example, we take now the cvara2p4 excitation at pup 4 because it is likely that this pup has KC above the threshold value. The procedure does not change. Looking at Figure 4-8, we select the time interval between instants 120.25s and 121.5s to apply the PMEM function. The frequency content is shown in Figure 4-15 and it shows that the response energy is concentrated around 2.4 Hz. The calculation of the instantaneous Strouhal frequency in time gives as a result the plot shown in Figure 4-16. We see that the maximum value is 2.5 Hz.

From the results we have already obtained, we can draw a few conclusions about the CVAR configuration:

1. There is an indication that the bare upper portion of the riser, where the pups 3 and 4 are located, is a power-in region while pup 7 is in a power-out region.
2. The buoyant portion of the riser is subjected to a smaller magnitude of in-plane normal velocity than in the bare portion. This small in-plane motion of the riser's buoyant region keeps it from reaching the KC number threshold necessary to produce VIV power-in.
3. The magnitude of in-plane normal velocity increases as we increase both frequency and/or amplitude of top motion.

To have an idea of the variation of the vibration frequency in time, this frequency was estimated from the time history of the out-of-plane bending moment using the following procedure: two sequential points of zero bending moment were identified. The difference in time between them

was the half period. Thus, the frequency was the inverse of the double of this value. Doing this calculation along the time axis for cvara3p3 at pup 3, we get the time history of the vibration frequency shown in Figure 4-17. This plot confirms that the VIV frequency of vibration oscillates with time. It also confirms the fact that the maximum out-of-plane vibration frequency is near 6 Hz.

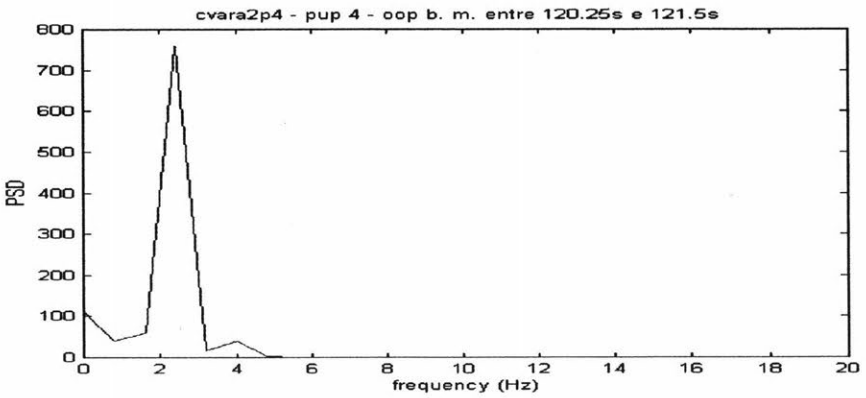

Figure 4-15: Frequency content during the time interval from 120.25s to 121.5s of the time history of the out-of-plane bending moment for the cvara2p4 case at pup 4.

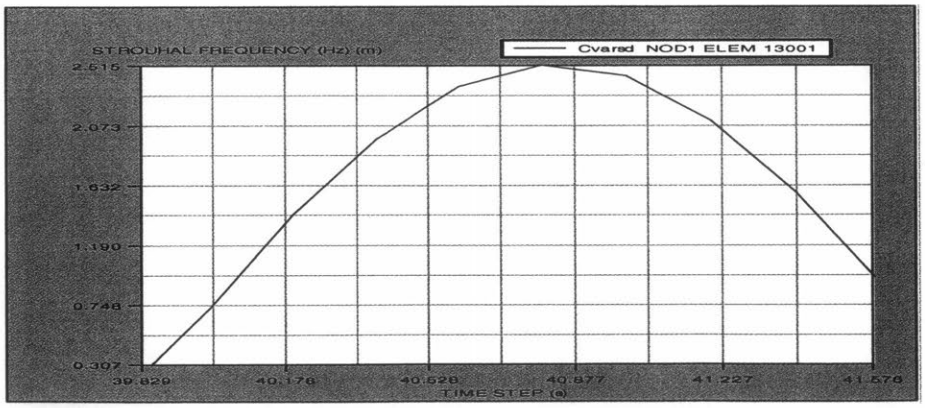

Figure 4-16: Plot of the time history of the instantaneous Strouhal frequency calculated by Anflex for the cvara2p4 case at a location corresponding to pup 4 for a period of time corresponding to 120.25s to 121.5s.

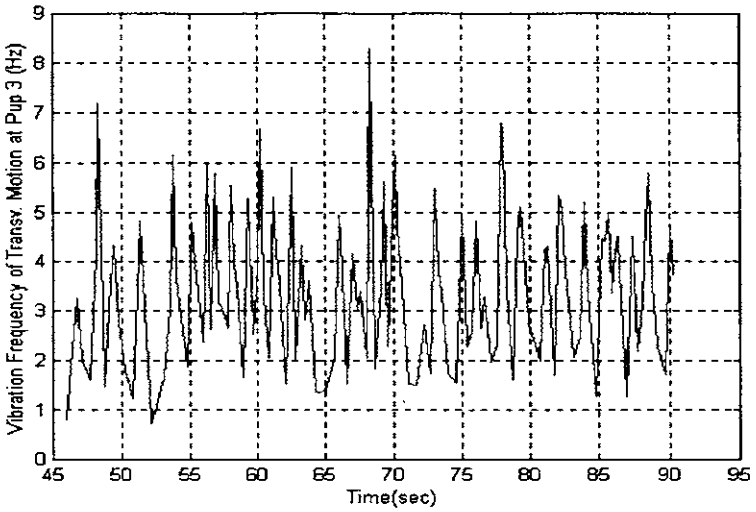

Figure 4-17: Time history of the vibration frequency of the transverse motion estimated from the out-of-plane bending moment time history of pup 3 for the cvara3p3.

Each point in Figure 4-18 corresponds to each case of heave amplitude/input period applied on top of the riser. The horizontal axis represents the KC number based on measured maximum velocity along the riser and the vertical axis represents the ratio out-of-plane vibration amplitude to riser diameter. As we can verify, for pups 1 to 5, which are the most probable to be in the power-in zone, there is a sudden jump in the out-of-plane amplitude when we go from KC below 40 to KC above 80. The conclusion is that there must be some KC threshold between these two limits for the cvar configuration.

Figure 4-19 is an example of the power spectral density (PSD) of the out-of-plane bending moments measured by all the eight pups installed in the riser model for the excitation case with heave amplitude and input period equal to 2 ft and 3 s, respectively. It was used the routine SPECTRUM from MATLAB to perform this calculation. The full length of the data records used in this calculation have been high pass filtered at 5 times the excitation frequency in order to separate the VIV response from the response to the top motion.

Examining the PSD of all the other cases of excitation on top of the riser, some immediate conclusions can be drawn:

- For one single type of excitation, the frequency content varies very little from pup to pup.
- For one single amplitude of motion, if we increase the period of excitation the range of the frequency response above the cutoff decreases.

- For one single period of motion, if we increase the amplitude of the excitation motion the range of the frequency response above the cutoff increases.

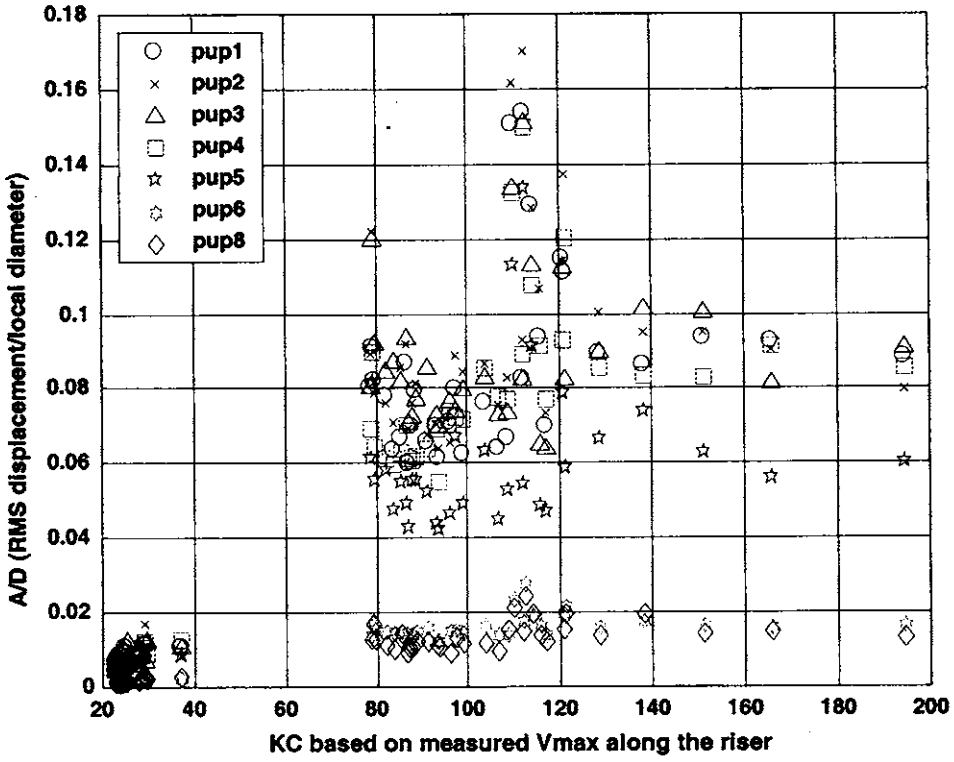

Figure 4-18: Relation between KC number and ratio out-of-plane displacement to riser diameter for each case of excitation applied on top of the cvar configuration.(From Jung Chi-Liao).

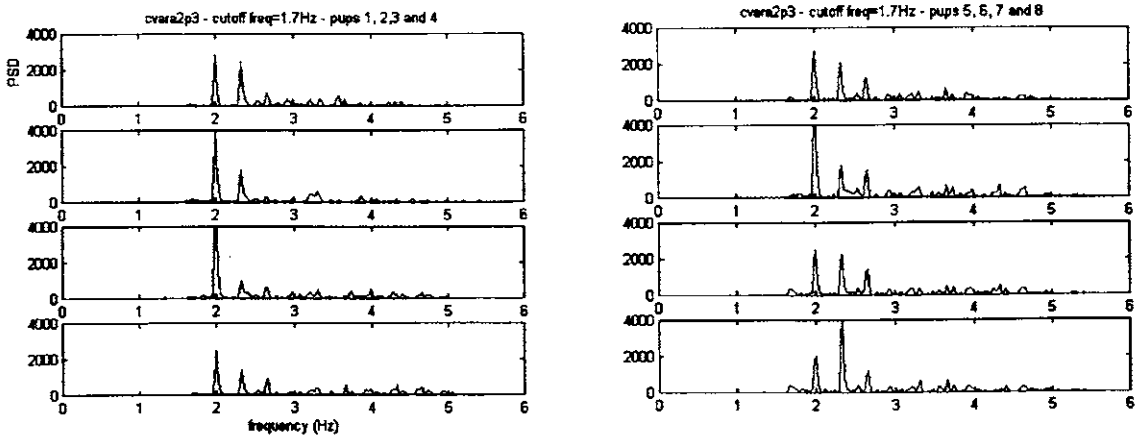

Figure 4-19: Power spectral density of out-of-plane bending moment at all 8 pups for the cvara2p3 case.

4.2.2 LWSCR Configuration

Figure 4-2 shows the geometry of the LWSCR. The length of the buoyancy region is $294\,ft$. The pup joints were numbered from 1 to 8 and their locations were, respectively: $s = 609.5\,ft$, $s = 583.5\,ft$, $s = 569.5\,ft$, $s = 555.5\,ft$, $s = 541.5\,ft$, $s = 527.5\,ft$, $s = 513.5\,ft$ and $s = 487.5\,ft$. Like the CVAR configuration, three of them are inside the buoyancy region (6, 7 and 8) while the others are outside.

The top motion applied to the LWSCR are described below by the combination of the following quantities:

Amplitude of vertical motion (ft): 0.5, 2.5 and 4.

Period of motion (sec): varied from 3s to 10 s with increments of 0.5s. The only exception is for the amplitude 4ft that started with a 3.5 s period.

Each excitation case is identified by the designation 'lwscranpm' where 'lwscr' is the kind of riser, 'an' represents an amplitude equal to 'n' ft and period equal to 'm' sec.

The distribution of normal velocity along the LWSCR configuration was calculated through Anflex and the result for the excitation lwscra4p3.5 is shown in Figure 4-20 by the solid line. Another way to have an idea of this distribution is to single integrate the accelerations measured by the pups installed in the riser model, similarly to what was done before for the CVAR configuration. The values found are represented by 'o' in the Figure 4-20. We see that the distribution given by Anflex can be considered to have a good agreement with the normal velocities measured by the pups, which supports the accuracy of the model. It is noteworthy the fact that the shape of the in-plane normal velocity distribution is similar to the distribution found in the CVAR configuration but it looks like the LWSCR is subjected to smaller magnitudes than in the CVAR. Again, we notice that the main source of excitation comes from the region just above the buoyant length because that is where we have the greatest values of the normal velocity amplitude (and consequently of the KC number above the threshold value).

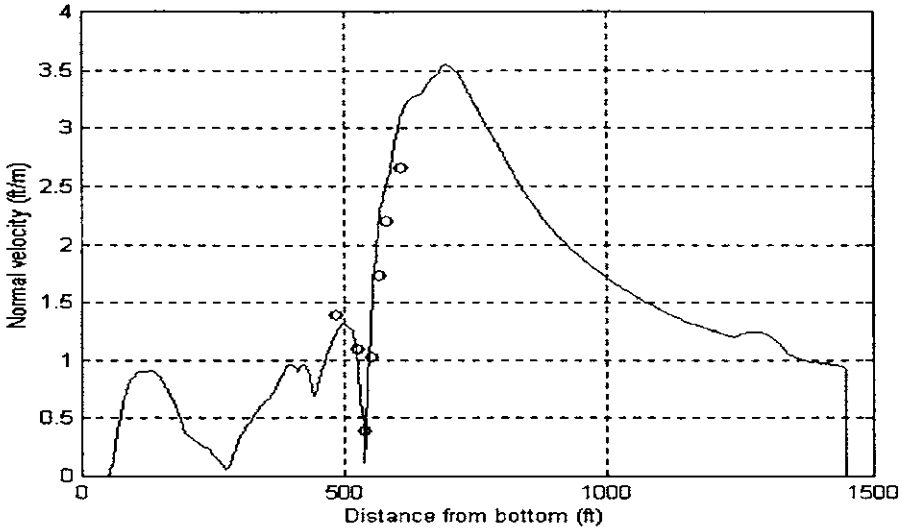

Figure 4-20: Comparison between maximum in-plane normal velocity measured by 7 pups (indicated by 'o') and normal velocity calculated by Anflex (solid line) for the excitation case lwscra4p3.5.

The maximum values of KC number for many excitation cases for the LWSCR riser were all obtained after running Anflex for all the top excitation cases mentioned in the previous page and performed in the lake. Like in the CVAR case, linear interpolation was used to join two consecutive points. The result is shown in the left side of Figure 4-21. If we compare the left side of this figure with the left side of Figure 4-5 for the CVAR riser, we conclude that the LWSCR configuration tends to have smaller KC numbers than the CVAR riser. Another difference is that the location of the maximum KC numbers varied between 0.44 and 0.53 of the riser length. In the CVAR riser it occurred always around 0.5 of the riser length.

Using equation 4.3 we can obtain the corresponding maximum in-plane velocities for the same excitation cases. The result is shown on the right side of Figure 4-21. Again we notice that for one single amplitude of the top motion the maximum velocity decreases as the frequency decreases too.

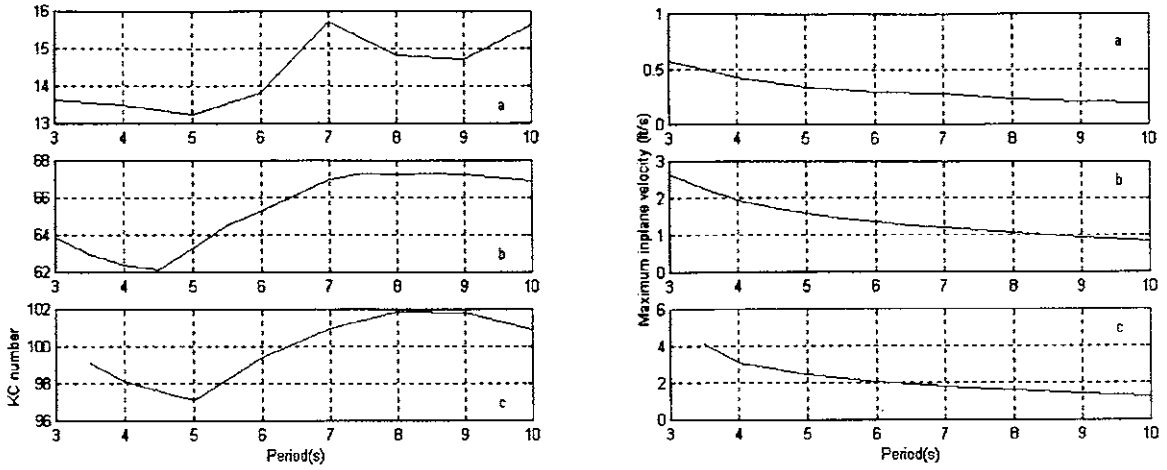

Figure 4-21: Relation between maximum KC number (left side)/maximum in-plane velocity (right side) and the period of excitation on top motion of the riser model. In part 'a' the amplitude was 0.5ft, in part 'b' was 2.5ft and in part 'c' was 4ft.

Figure 4-22 shows the relationship between the rms of the out-of-plane bending moment and the input period for the excitation amplitude of 4ft for each pup number from 1 to 5. This amplitude was chosen because in this case, maximum KC number varies very little as we vary the input period and we can assume it is approximately constant. Hence, Figure 4-22 indicates that the out-of-plane bending moment decreases as the input frequency decreases.

Figure 4-23 shows the root mean square (rms) of the out-of-plane bending moment in pups 1 and 2 for each input frequency with heave amplitudes of 0.5ft and 2.5ft (which correspond to the plots shown on the left part of Figure 4-21a and 4-21b) at all input periods. These two pups were chosen because they are the one that have great chances of being in the input region. The plot shows a jump in the bending moment when the heave amplitude was changed from 0.5ft (maximum KC number around 15) to 2.5ft (maximum KC number around 65). Somewhere between these two values of KC must be the threshold value.

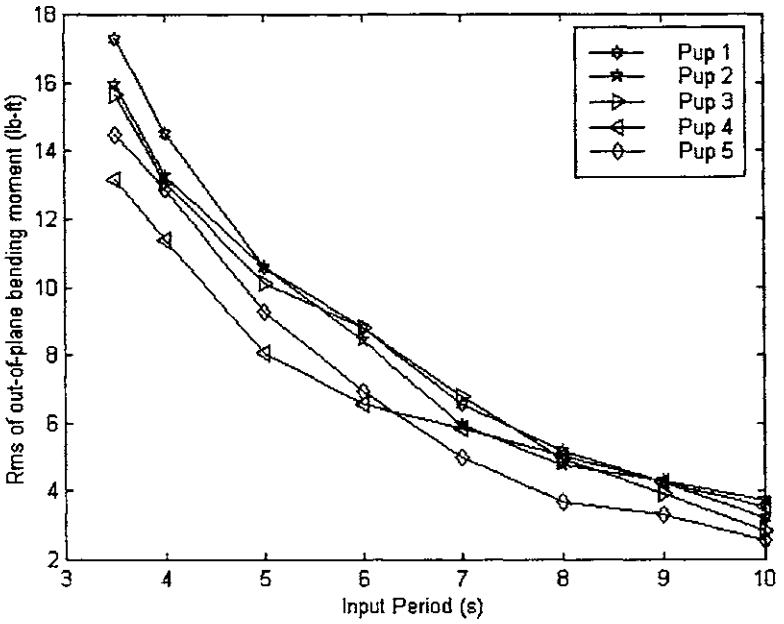

Figure 4-22: Variation of the out-of-plane bending moment as a function of the input period for the first five pups in the lwscr configuration. The heave amplitude is 4ft.

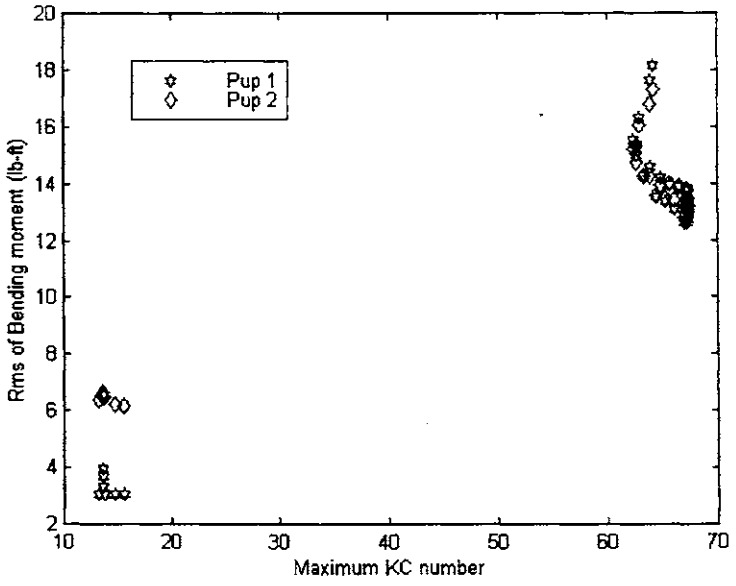

Figure 4-23: Rms of out-of-plane bending moment as a function of maximum KC number in pups 1 and 2 of the lwscr configuration subjected to amplitudes 0.5 ft and 2.5 ft for all periods.

Figure 4-24 shows the power spectral density of the full length of the out-of-plane bending moment records filtered at 5 times the top motion frequency for the excitation case with amplitude of 4ft and period of 3.5s. Examining the plots of power spectral density for the other cases, we see that the LWSCR shows the same trend as CVAR, with the peak vibration frequency increasing with increase in top motion amplitude or frequency and the vibration frequency content not changing so much from one pup to another for the same excitation.

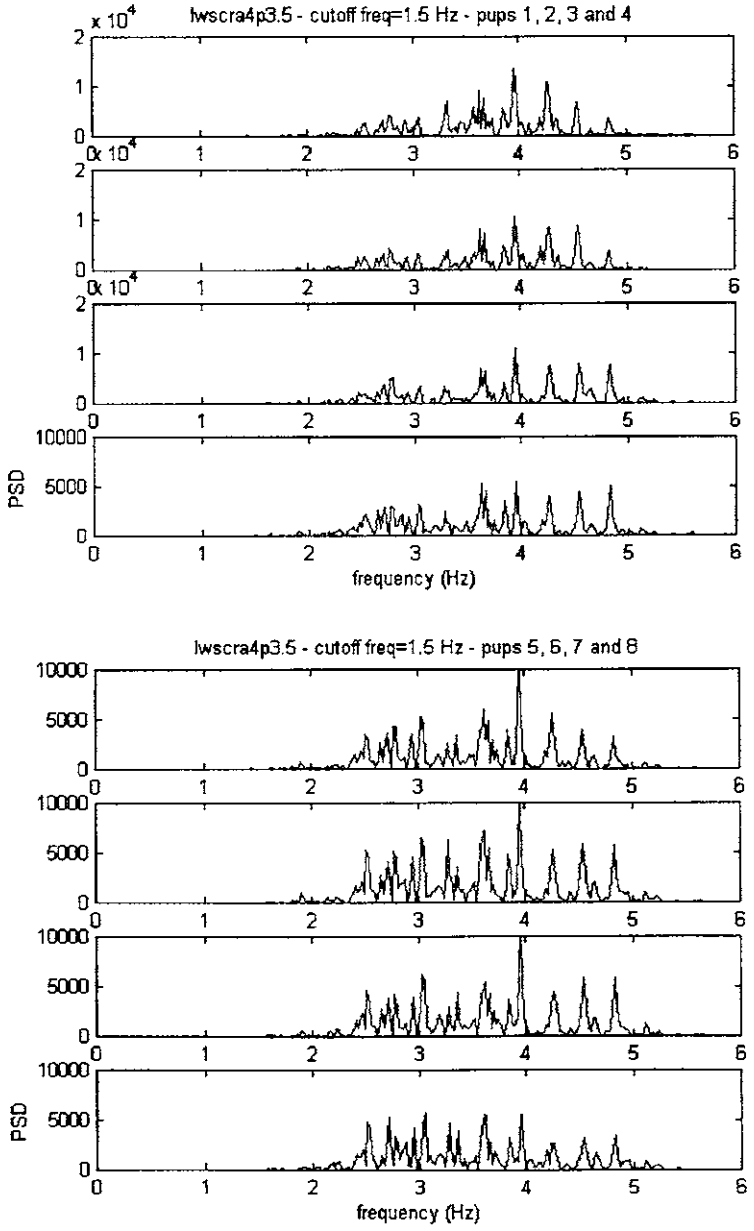

Figure 4-24: Power spectral density of out-of-plane bending moment at all 8 pups for the lwscra4p3.5 case.

4.2.3 SCR Configuration

Figure 4-1 shows the geometry of the SCR. Unlike the CVAR and the LWSCR configurations, there is no buoyant region in the SCR. The pup joints were numbered from 1 to 8 and their locations were, respectively: $s = 1220.5ft$, $s = 378.5ft$, $s = 352.5ft$, $s = 338.5ft$, $s = 324.5ft$, $s = 310.5ft$, $s = 284.5ft$ and $s = 258.5ft$. The only pups that were always above the touch down point were numbers 1 and 2 while pups 3 to 8 were on the bottom, at least in the static equilibrium configuration.

The top motion on the SCR was the most comprehensive of all since it was applied in three different directions: one perpendicular to the catenary plane (amplitudes: 1, 2 and 3.5ft), one horizontal and making 45° with the catenary plane (amplitudes: 2, 3 and 3.5ft) and one vertical (amplitudes: 0.5, 2 and 3ft). In all cases the period of the motion varied between 3 and 10s.

Each excitation case is identified by the designation 'scranpm' where 'scr' is the kind of riser, 'an' represents an amplitude equal to 'n' ft and period equal to 'm' sec. For the horizontal motions, normal to the catenary plane, the first designation is 'hscr'.

The distribution of in-plane normal velocity along the SCR configuration was calculated through Anflex and the result for the vertical excitation scra3p3 is shown in Figure 4-25 by the solid line. Another way to have an idea of this distribution is to single integrate the accelerations measured by the pups installed in the riser model, similarly to what was done before for the CVAR configuration. The values found are represented by 'o' in the Figure 4-25 and they correspond to pups 1 to 5, which had a considerable velocity. We see that the distribution given by Anflex can be considered to have a good agreement with the in-plane normal velocities measured by the pups, which supports the accuracy of the model. The first feature that differs from the distribution for the CVAR and LWSCR is the magnitude of the maximum in-plane normal velocity. It is the highest of all three for a similar excitation. And it means higher Strouhal frequency. The region with these highest values is just above the touch down point. As a consequence, the SCR tends to have the longest region with high normal in-plane velocities. Putting in another way, the SCR would have the longest portion with KC number above the threshold value and consequently the longest power-in region when compared with CVAR and LWSCR configurations.

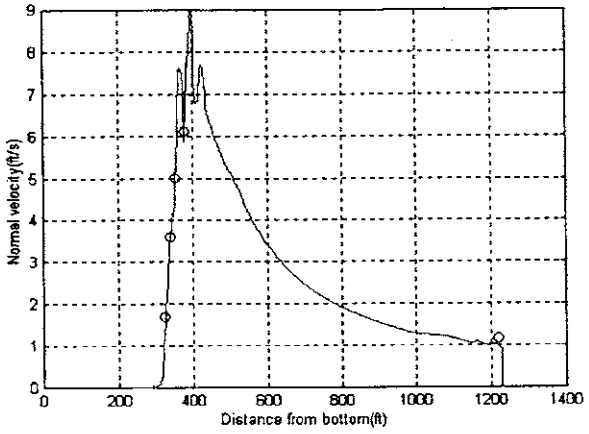

Figure 4-25: Comparison between maximum in-plane normal velocity measured by 5 pups (indicated by 'o') and normal velocity calculated by Anflex (solid line) for the excitation case scra3p3.

Figure 4-26 shows the maximum values of in-plane normal velocity for many vertical excitation cases for the SCR riser. These values were all obtained by running Anflex for all the cases mentioned in the beginning of this section. Linear interpolation was used between two consecutive points. If we compare with the plots shown before in Figures 4-5 and 4-21 for the CVAR and LWSCR risers, respectively, we have the confirmation that the SCR configuration tends to have the highest values. Another difference is that the location of the maximum velocity varied between 0.32 (amplitude of 3ft) and 0.39 (amplitude of 0.5ft) of the riser length.

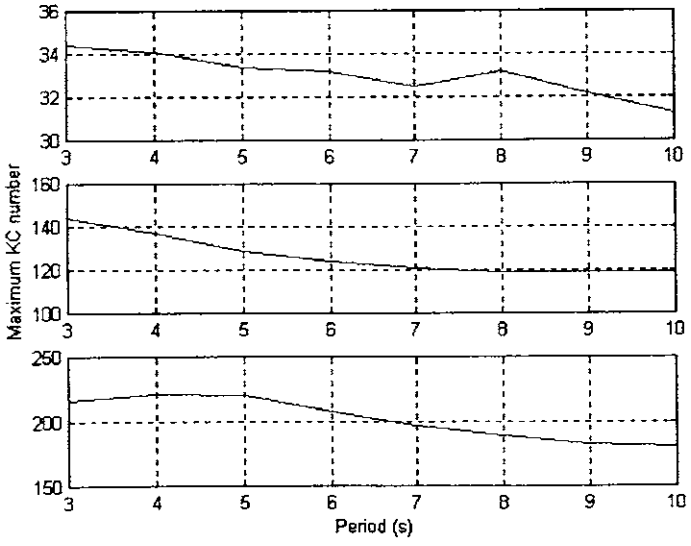

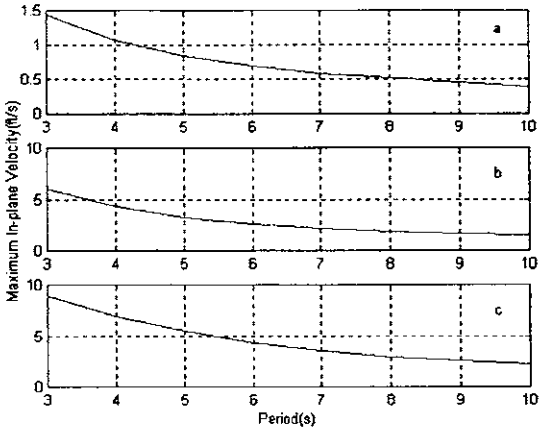

Figure 4-26: Relation between maximum KC number (left side)/maximum in-plane velocity (right side) and the period of excitation on top motion of the riser model. In part 'a' the amplitude was 0.5ft, in part 'b' was 2ft and in part 'c' was 3ft.

Another point is the spectral analysis of the full length of the SCR bending moment records. The power spectral density plots shown in Figures 4-27 to 4-30 refer to the out-of-plane bending moment due to the vertical top motion. The power spectral density shown in Figure 4-31 refers to the in-plane bending moment due to the horizontal top motion. In both cases the series were filtered at 5 times the frequency of the top motion. These plots confirm the conclusion that the range of vibration frequencies increases as the frequency or amplitude of the top motion increases. Furthermore, for the same excitation, we can see that, with respect to the out-of-plane bending moment, pup 1, located next to the top, has a response energy much smaller than pups 2, 3 or 4. Another feature is that this difference in energy seems to decrease as the frequency decreases for a constant amplitude. This can be explained by the hydrodynamic damping that removes energy from the waves generated at pups 2 and 3. As the excitation frequency decreases the magnitude of the velocity decreases too and it causes the hydrodynamic damping to decrease as well. Dynamic buckling can also have a significant influence here since it accounts for a significant part of the response energy in pups 2 and 3.

However this big difference does not happen when the excitation is horizontal. For the vertical top motion, the main excitation for VIV comes from the region close to the touch down point as shown in Figure 4-25. In this case, there will be out-of-plane vibration. For the horizontal top motion perpendicular to the plane of the catenary, the main excitation for VIV comes from the

top region and it will cause in-plane vibration (this type of excitation will be studied in more detail in the next section). Looking at the power spectral density of the in-plane bending moments in Figure 4-31 we see that pups 1, 2 and 3 had a similar level of energy. This probably can be better explained with the help of an example. The amplitude of the horizontal velocity at pup 1 for the hscra2p4 excitation, for instance, is smaller than for the amplitude of the in-plane velocity at pup 2 for the scra2p4, causing the hydrodynamic damping to be smaller in the first case. This fact is confirmed by table 4.1 below. These velocities were obtained through integration of the corresponding measured accelerations. Since the hydrodynamic damping is smaller, the attenuation along the riser will be correspondingly smaller, so the waves generated on top of the riser can travel further in the first case. In addition, dynamic buckling seems to be less significant in the horizontal excitation case.

	In-plane velocity for scra2p4 (in ft/s)	**Out-of-plane velocity for hscra2p4 (in ft/s)**
Pup 1	0.55	0.57
Pup 2	4.26	0.10

Table 4.1: Velocity amplitudes for two top motions on the SCR configuration.

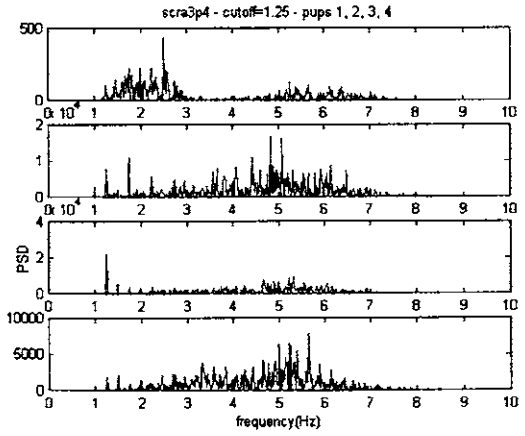

Figure 4-27: Power spectral density of the out-of-plane bending moment at the first four pups for the scra3p4 case.

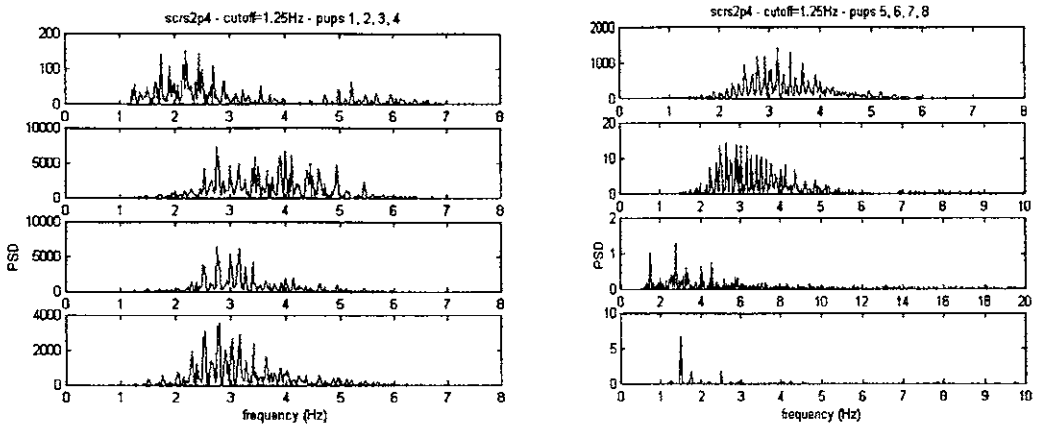

Figure 4-28: Power spectral density of the out-of-plane bending moment at all eight pups for the scra2p4 case.

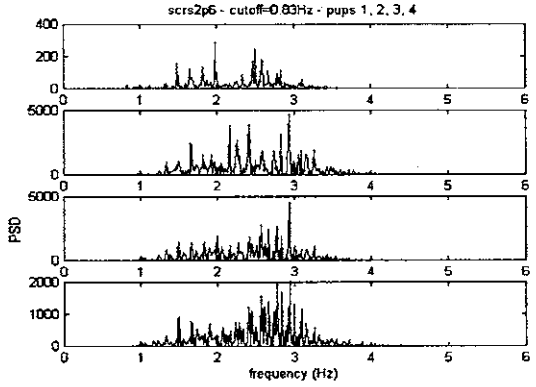

Figure 4-29: Power spectral density of the out-of-plane bending moment at the first four pups for the scra2p6 case.

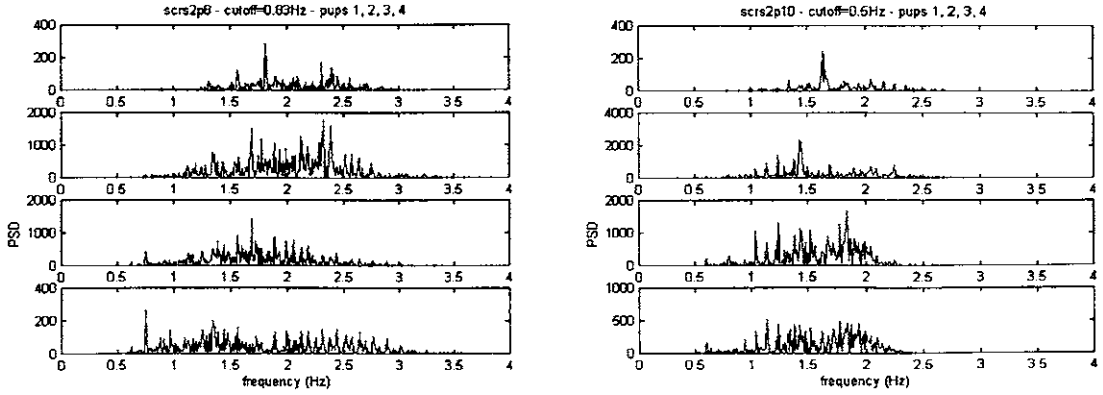

Figure 4-30: Power spectral density of the out-of-plane bending moment at the first four pups for the cases scra2p8 (left) and scra2p10 (right).

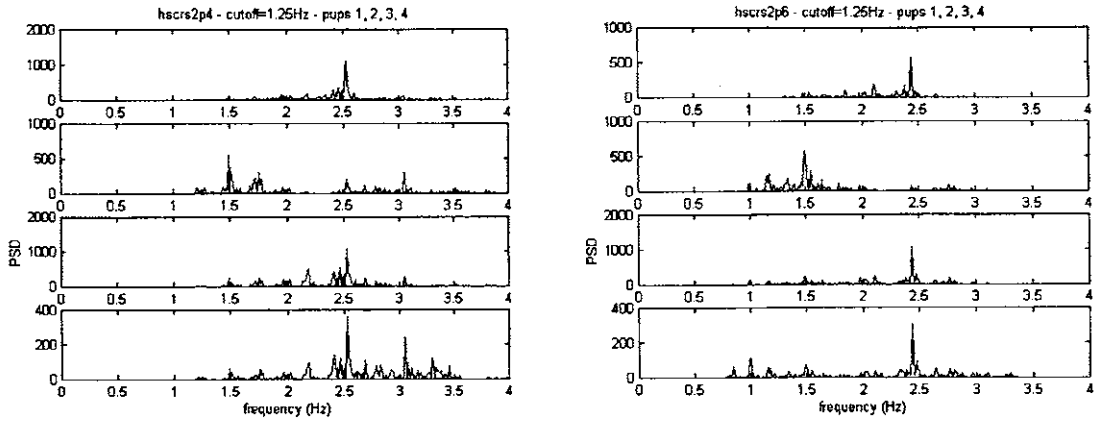

Figure 4-31: Power spectral density of the in-plane bending moment at the first four pups for the cases hscra2p4 (left) and hscra2p6 (right).

An interesting experiment that was performed with the scr model was to apply heave amplitudes of 2 ft and 3 ft using a hard bottom as the foundation. In this case there is only sliding boundary condition with friction and no spring resistance on the bottom. The cutoff frequency can be considered negligible and so all the wave frequencies would be above it, indicating propagation of waves beyond the touch down point. Bending moment time histories measured on pups 2, 3, 4, 5 and 6 can give some insight about the effect of boundary conditions on wave propagation.

Figure 4-32 presents the rms of the out-of-plane bending stresses on pups 2 to 8 for heave amplitude of 2ft while Figure 4-33 refers to the rms of out-of-plane bending stresses on the same pups for heave amplitude of 3 ft. The corresponding out-of-plane bending moment time histories were high-pass filtered at 5 times the input frequency.

Based on the maximum in-plane velocity (see Figure 4-26) for the amplitudes and frequencies of the vertical motion applied on the top end of the riser, an estimate of the propagating wavelength in the out-of-plane direction was made. For the amplitude of 2 ft, the wavelength is 15 ft (for input period of 3 s) and 32 ft (for input period of 10 s). Looking at the plot shown in Figure 4-32 and considering that pups 2 and 8 are 108 ft apart, we conclude that the out-of-plane waves at input period of 3 s penetrate something like 108/15=7.2 wavelengths beyond the tdp. For the waves generated at input period of 10s we see that the waves decay almost everything between pups 2 and 6, which are 60 ft apart. Hence, they penetrate 60/32= 2 wavelength,

approximately, beyond the tdp. The conclusion is that waves at higher frequency penetrate more than at lower frequencies.

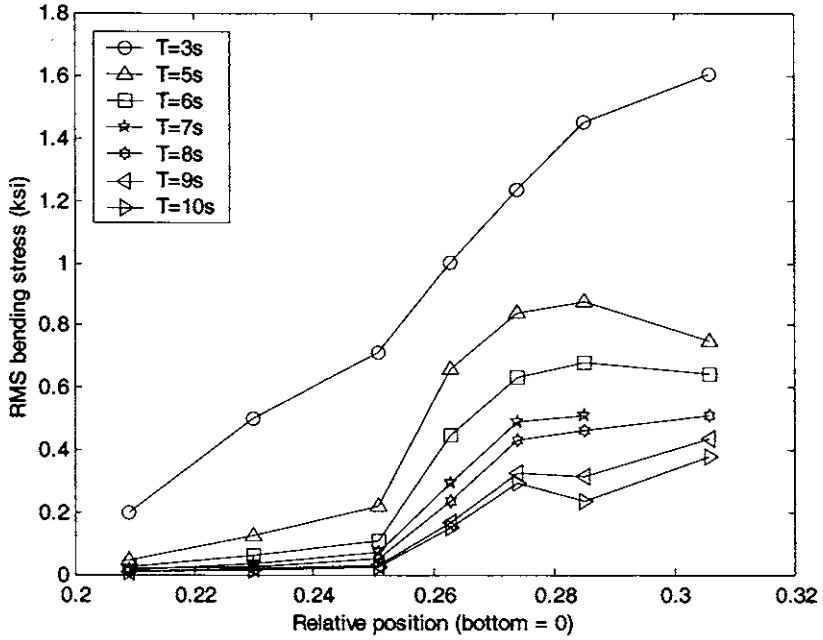

Figure 4-32: Rms of the out-of-plane bending stress for pups 2 to 8 in the scr configuration for heave amplitude of 2ft with hard bottom. T is the input period.

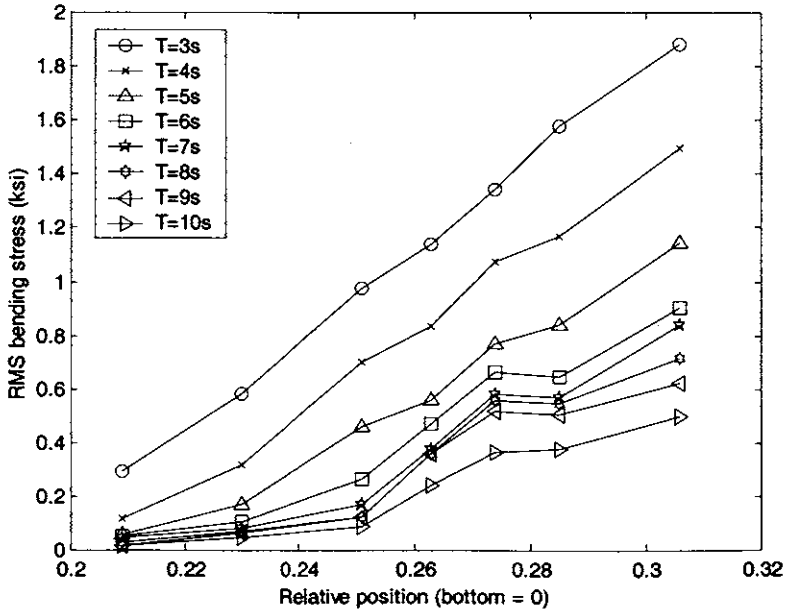

Figure 4-33: Rms of the out-of-plane bending stress for pups 2 to 8 in the scr configuration for heave amplitude of 3ft with hard bottom. T is the input period.

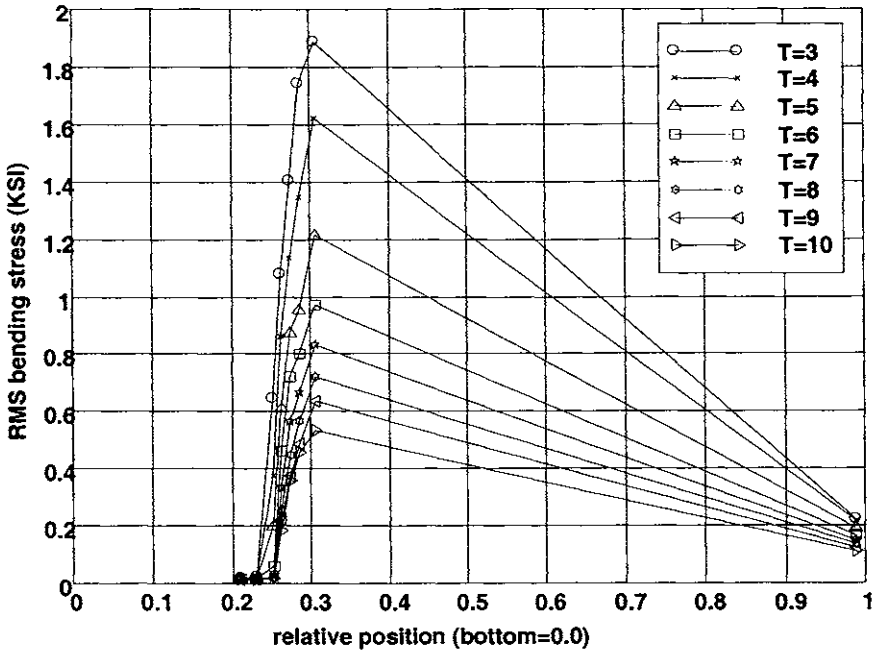

Figure 4-34: Rms of the out-of-plane bending stress for all pups in the scr configuration for heave amplitude of 3ft and in soft soil. T is the input period.

Figure 4-34 presents the rms of the out-of-plane bending moment stresses on all pups, for heave amplitude of 3ft for the soft soil of the lake. The corresponding out-of-plane bending moment time histories were high-pass filtered at 5 times the input frequency. This time is possible that there is lateral resistance due to the soil and in this case a cutoff may exist. However, following the same reasoning as for the hard bottom, we see that the waves with higher frequency tend to penetrate more than at lower frequencies. It is possible there is a cutoff frequency between the 3 second input frequency and the 10 second input frequency case.

4.3 Experiment with a SCR Model

In order to have an alternative assessment of the KC threshold for catenaries in periodic motion, an experiment was conducted with the same model that Petrobras used previously in a project about SCR investigation. The experiment was conducted in the towing tank of the Institute of Technological Research in São Paulo, Brazil and the configuration adopted was the catenary.
The model is composed of a surgical latex tube, a stainless steel cable whose role is to work as the structural element of the model test and lead weights (spheres) in order to provide the mass, as shown schematically in Figure 4-35. Although the latex tube is very soft it also contributes a little to the bending stiffness because of its geometry. It is assumed that the latex tube, the stainless cable and the lead weights do not have relative motion among them, which is a reasonable hypothesis, given the way the model was constructed.

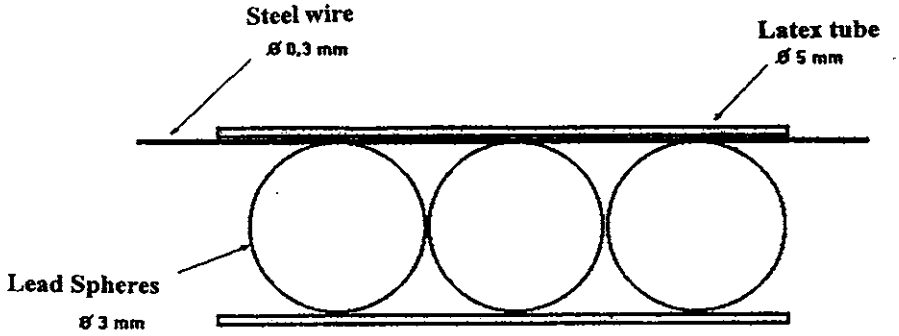

Figure 4-35: Constructive detail of the model.

The main properties of the model are the following:

External diameter: $0.005m$

Internal diameter: $0.003m$

Total length: $7.78m$

Bending stiffness: $1.0\times10^{-4}\,Nm^2$

Axial stiffness: $14622N$

Linear mass: $0.044kg/m$

Vertical projection: $4.1m$

Horizontal projection : $5.7m$

Since the outside diameter was too small to be held by an accelerometer, there was only one point available to measurements: the top end. Therefore, the procedure adopted here was to impose a harmonic motion at the top of the reduced model in the direction perpendicular to the plane of the catenary in order to minimize the influence that buckling near the touch down point might have. The top end of the model was attached to a circular disc. By spinning it we could impose the top motion. There was no other source of load on the model (i. e., no current or wave load was applied). At the same time, the steady state response for the horizontal reaction force on the top node in the plane of the catenary was measured and recorded.

The parametric study had two main quantities of control: each combination of one amplitude with one frequency of top motion defined a case to be studied. In the end, 48 cases were tested in the laboratory. The sampling rate was 25.6 Hz. The values applied to the top node of the scr model are listed below:

Frequencies (Hz): 0.17, 0.20, 0.25, 0.33, 0.50, 0.67

Amplitude (mm): 10, 15, 20, 25, 30, 35, 40, 45

These values were selected after analyzing numerically the model with Anflex for some pairs of amplitude/frequency. A value similar to the corresponding maximum value of KC number given by Anflex was expected to occur in the model during the experiment for the same excitation on top. We intended to limit the KC number range between 10 and 60. For example, Figure 4-36 shows, in the upper part, the curve of the KC number distribution along the model for an imposed horizontal top motion with $0.667Hz$ and amplitude equal to $40mm$, which represents rapid, dynamic conditions. Going downward in the figure, it is shown a plot of the estimate of the maximum possible vortex shedding frequency (see equation 4.1) along the model and the estimate of the average expected vortex shedding frequency (see equation 4.2), respectively. If we assume we are dealing with a sinusoidal varying velocity this average is calculated by multiplying the maximum value by $2/\pi$. Figures 4-36 (right part) and 4-37 show similar plots for the following cases of amplitude/frequency of excitation, respectively: 0.5Hz/20mm and 0.17Hz/10mm (slow, well behaved conditions). For the cases chosen we see that in average the

exciting frequency can go up to approximately $4Hz$. We also see that the maximum magnitude of the velocity occurs on the top and decreases as we follow the line toward the bottom for the rapid dynamic conditions but for the slow dynamic conditions the maximum value can occur in the middle of the line.

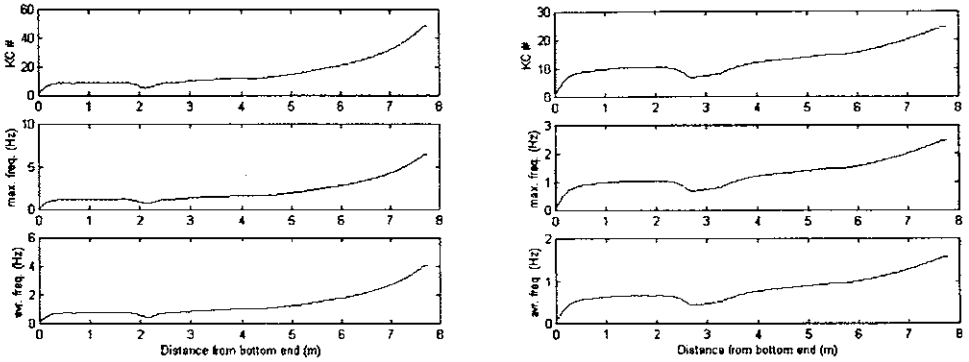

Figure 4-36: Distribution of KC number (top), maximum vortex shedding frequency (middle) and average vortex shedding frequency (bottom) along the model for an imposed motion on top with amplitude 40mm and frequency 0.67 Hz (left side) 20mm and frequency 0.5Hz (right side).

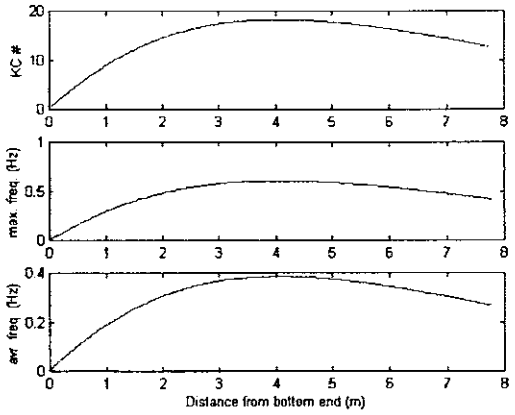

Figure 4-37: Distribution of KC number (top), maximum vortex shedding frequency (middle) and average vortex shedding frequency (bottom) along the model for an imposed motion on top with amplitude 10mm and frequency 0.17Hz.

This model was studied with Anflex in order to obtain an assessment of the natural frequencies. Table 4.2 shows the first ten natural frequencies associated with the in-plane mode shapes only. For the rest of this chapter, we will always be referring to in-plane mode shapes of the model.

Frequency Number	Natural Frequency (Hz)
1	0.543
2	0.860
3	1.201
4	1.507
5	1.832
6	2.136
7	2.455
8	2.760
9	3.076
10	3.380

Table 4.2: First ten natural frequencies of the model

Each case of transverse amplitude/period imposed on the top end of the scr model was applied to the corresponding finite element model through Anflex. Figure 4-38 shows the maximum KC number obtained in this model for each input frequency (in Hz). We see that for the same input frequency, the maximum KC increases with the amplitude and for a fixed amplitude, the maximum KC decreases a little bit for increasing input frequency.

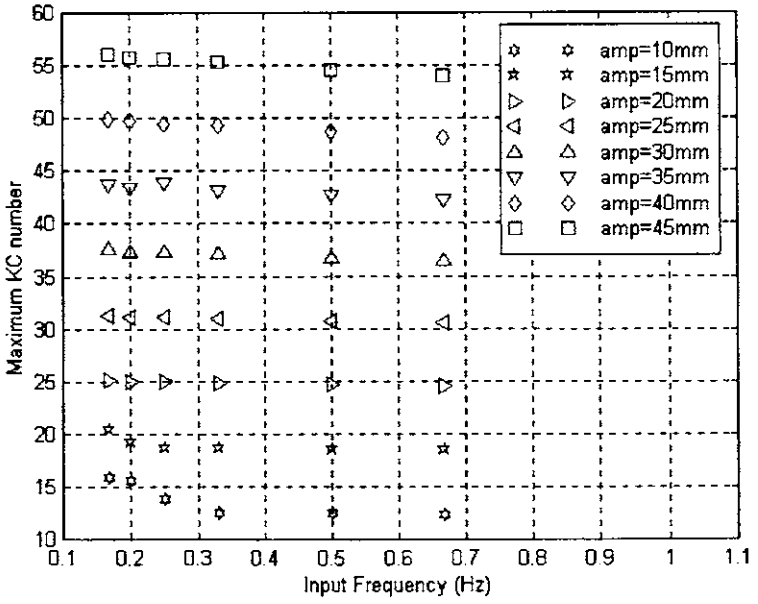

Figure 4-38: Maximum KC number in the scr model obtained by applying the corresponding top motion of each of the 48 cases through Anflex.

To have a better understanding about the frequencies that play an important role in the tests, we made Figure 4-39. The input frequency is in the horizontal axis (in Hz) while the vertical axis represents a general frequency (in Hz) with different origins:

1. Each point represents the average shedding frequency, $f_{S,avr}$, for each of the 48 tests performed with the scr model. . The average shedding frequency can be estimated by the formula $f_{S,avr} = \frac{2}{\pi} KC \cdot St \cdot f_i$, which is a combination of equations 4.2 and 4.3, assuming that the flow is sinusoidal. f_i is the input frequency. The corresponding KC numbers are shown in Figure 4-38. As for the Strouhal number, 0.19 was used. For each input frequency, the average shedding frequency increases with the input amplitude.
2. The inclined lines represent integer multiples of the input frequency, f_m, with m varying from 1 to 7.
3. The horizontal lines represent the natural frequencies, f_n, corresponding to the in-plane mode shapes of the scr model. The first ten values are shown in table 4.2.

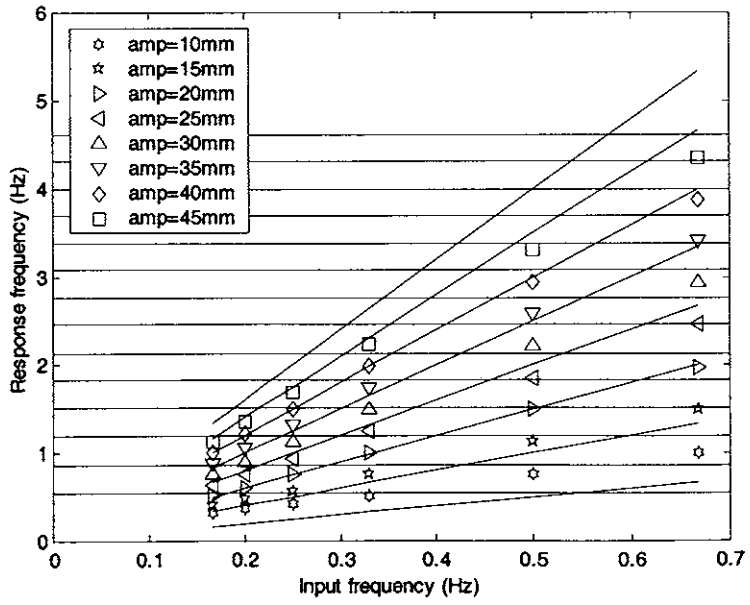

Figure 4-39: Relation among the frequencies involved in each of the 48 cases, marked with specific symbols. The inclined lines are multiples of the input frequency and the horizontal lines are the scr model natural frequencies associated with the in-plane mode shapes.

Figures 4-38 and 4-39 indicate that for the same input frequency, as the KC number increases the model tends to have higher modes excited. Another point indicated by Figure 4-39 is that the first fourteen natural frequencies are the most important for the response of the scr model in the tests. It means that for many of these modes the wave propagation parameter, $n\zeta_n$, is low. This parameter is the product of the mode number and the total modal damping ratio, including the hydrodynamic contribution. It governs the decay of energy in a damped travelling wave. The smaller this parameter becomes the smaller is the decay, which means the easier it is to have standing wave behavior. Hence, one idea that can be assumed, based on these points, is that the threshold KC number has a proportionality nature with the wave parameter. It means that when the lower modes are excited by the oscillatory flow then the threshold KC number is low, like 10 or 15. As higher modes get excited, these threshold values increase too.

Another point is that resonance (amplification of the scr model response) can occur in these tests in many ways. One of them is when the shedding frequency coincides with a natural frequency. Another resonant case might happen when a multiple of the input frequency (higher harmonic) coincides with the shedding frequency.

Looking at figure 4-39 and then going to the spectra we see that, in general, when one of the conditions $f_n = f_{S,avr}$ or $f_m = f_{S,avr}$ or $f_m = f_n = f_{S,avr}$ is satisfied, there is a strong spike in the power spectral density function. Take, for instance, the case with input amplitude/frequency equal to 20/0.5. In Figure 4-39, it corresponds to the condition $f_m = f_n = f_{S,avr} = 1.5Hz$. This frequency is equal to the fourth natural frequency of the scr model and is also equal to the third multiple of the input frequency. If we look at the corresponding spectrum of the transverse reaction force on the top end of the scr model shown in Figure 4-40, we see a strong concentration of energy at $1.5Hz$ too. No filter was applied to this or any other power spectral density shown in this section.

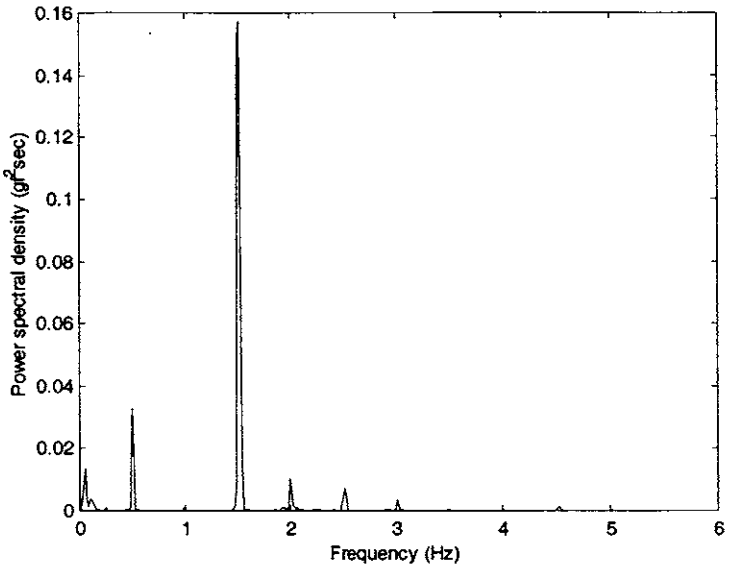

Figure 4-40: Power spectral density of the top reaction in the plane of the catenary for an imposed motion with amplitude of 20 mm and frequency of 0.5 Hz.

Similar behavior of resonance occurs in many other cases. For example:

1. Input amplitude/frequency equal to 40/0.2 happened for $f_m = f_n = f_{S,avr} = 1.2Hz$. This frequency corresponds to the third scr model natural frequency and sixth input frequency multiple. The corresponding spectrum of the top end reaction is shown in Figure 4-41.

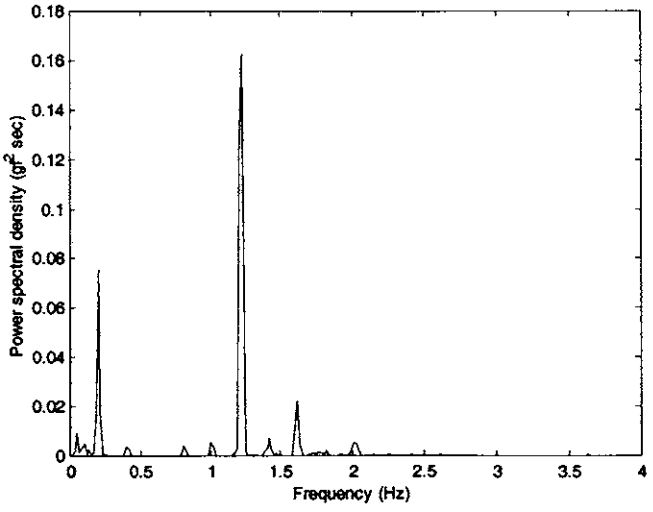

Figure 4-41: Power spectral density of the top reaction in the plane of the catenary for an imposed motion with amplitude of 40 mm and frequency of 0.2 Hz.

2. Input amplitude/frequency equal to 45/0.17 happened for $f_m = f_n = 1.2Hz$. This frequency corresponds to the seventh input frequency multiple. The corresponding spectrum of the top end reaction is shown in Figure 4-42.

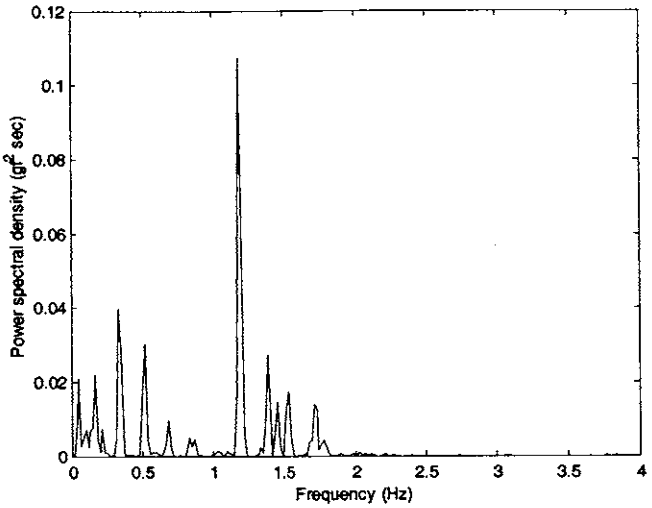

Figure 4-42: Power spectral density of the top reaction in the plane of the catenary for an imposed motion with amplitude of 45 mm and frequency of 0.17 Hz.

3. Input amplitude/frequency equal to 45/0.2 happened for $f_m = f_{S,avr} = 1.4Hz$. This frequency corresponds to the seventh input frequency multiple. The corresponding spectrum of the top end reaction is shown in Figure 4-43.

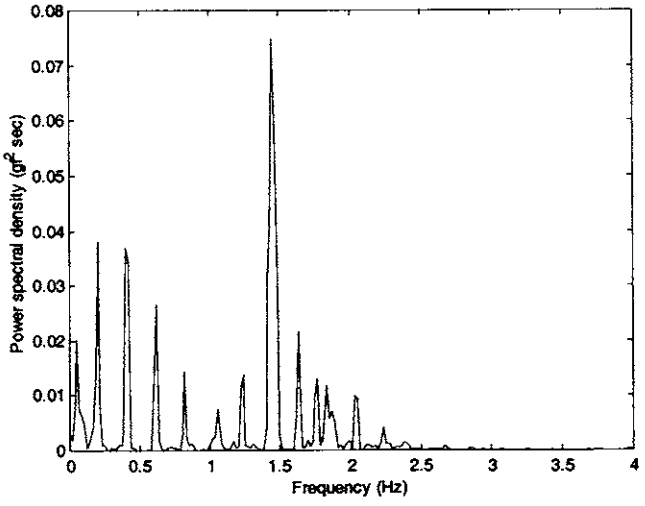

Figure 4-43: Power spectral density of the top reaction in the plane of the catenary for an imposed motion with amplitude of 45 mm and frequency of 0.2 Hz.

Just as a counter example, we can examine the excitation case with amplitude of 30 mm and input frequency of 0.67Hz. The power spectral density of the top reaction force is shown in Figure 4-44 below.

We see that there is a strong contribution in the input frequency. In the higher frequency range, we see that this case corresponds to the point in Figure 4-39 that lies between the frequency numbers 8 (2.76 Hz) and 9 (3.08 Hz) of the model. Figure 4-44 shows that these two frequencies have equivalent contributions in the response of the riser. No resonance occurred. The VIV in this case was small.

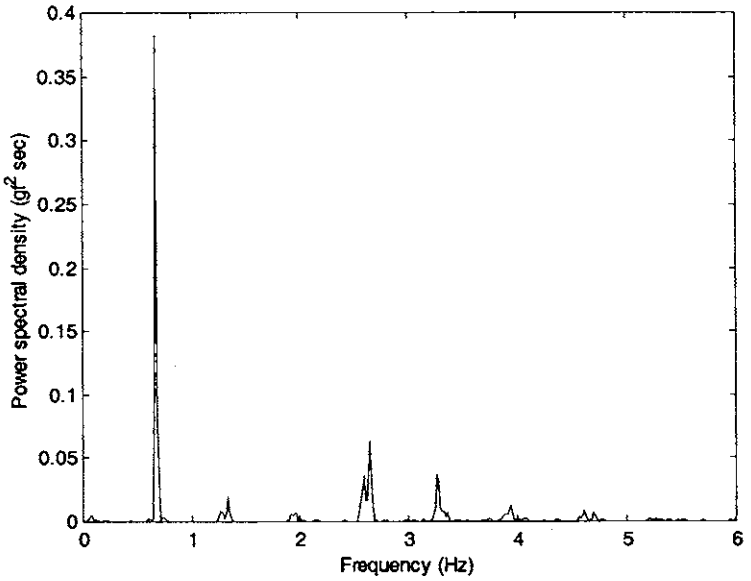

Figure 4-44: Power spectral density of the top reaction in the plane of the catenary for an imposed motion with amplitude of 30 mm and frequency of 0.67 Hz.

Chapter 5

Application of WBFEM to Riser Analysis

5.1 Introduction

In this chapter we will focus our attention on the application of the WBFEM to analyze the behavior of a marine riser in terms of displacements and forces. We will also calculate natural frequencies and mode shapes of some risers and compare them with the values obtained from FEM solution. Four configurations will be studied in the following order: a vertical riser, a SCR, a lazywave and finally a CVAR. Then we will study the wavelength distribution along a riser, how this distribution varies when differences in the riser properties are encountered and the consequences in the calculation of stresses.

5.2 Vertical Riser

As a first example, we will study a pinned-pinned vertical riser with the following properties:

Total length: 1288m

Outside diameter: 0.5334m

Inside diameter: 0.5016m

Hydrodynamic diameter: 1.1303m

Modulus of elasticity: $2.067\times10^{11}\,N/m^2$

Structural mass per unit length in air: $927.4kg/m$

Minimum effective tension: $2350kN$

Tension variation along the riser: $1356.5N/m$

Although this case is simple, it is useful to check the results from the WBFEM for extreme cases. Here we will calculate the natural frequencies of the vertical riser mentioned above through different methods:

1. Using SHEAR7 computer program.
2. Using the straight element with constant tension (developed in chapter 2)
3. Using the straight element with slowly varying tension (developed in chapter 2)
4. Using the curved element with constant tension with a very large radius of curvature (developed in chapter 3) in order to simulate the straight element.
5. Using the curved element with slowly varying tension with a very large radius of curvature (developed in chapter 3) in order to simulate the straight element.

The riser was divided in eight elements of the same length. In methods 2 and 4 the constant tension was calculated as the average value between the elements ends. In methods 4 and 5 the radius of curvature was 10000m for each curved element in order to simulate a straight one. The first ten natural frequencies, in Hz, of the vertical riser described before are listed below in table 5.1 for all 5 methods used.

Freq. No.	Method 1	Method 2	Method 3	Method 4	Method 5
1	0.0157	0.01561	0.01574	0.01561	0.01562
2	0.0314	0.03125	0.03132	0.03125	0.03125
3	0.0471	0.04693	0.04698	0.04696	0.04694
4	0.0628	0.06266	0.06271	0.06266	0.06263
5	0.0787	0.07846	0.07853	0.07851	0.07845
6	0.0946	0.09436	0.09452	0.09437	0.09427
7	0.1106	0.11038	0.11066	0.11046	0.11030
8	0.1268	0.12580	0.12419	0.12580	0.12631
9	0.1430	0.14266	0.14310	0.14278	0.14263
10	0.1594	0.15896	0.15922	0.15896	0.15886

Table 5.1: Natural frequencies of a vertical riser (in Hz) according to different methods.

In practical terms we see that all methods give the same values for the natural frequencies. It is also evident that, as expected, the curved beam element tends to the straight beam element

results when its radius of curvature becomes large enough. This is the correct limiting behavior for the curved element.

5.3 Steel Catenary Riser

For the second example, we consider a single steel catenary riser configuration, like the one shown in Figure 5-1 by the solid line, with the following basic characteristics:

Horizontal projection: $331\,m$

Vertical projection: $192.0\,m$

Water depth: $192.0\,m$

Modulus of elasticity: $2.067\times10^{11}\,N/m^2$

Mass density: $10760\,kg/m^3$

Outside diameter: $0.168m$

Inside diameter: $0.137m$

Hydrodynamic diameter: $0.181\,m$

Soil stiffness: $1\times10^5\,N/m$

Total length: $405m$

Suspended length: 355m

For the time being, the riser extends from the touch down point to the top node and it is subjected to its own weight and buoyancy forces only. The riser is pinned at both ends. The goal is to calculate its natural frequencies. The longitudinal coordinate s has its origin at the bottom node and goes upward toward the top node.

For the calculation of natural frequencies and mode shapes two approaches are considered here: conventional FEM and WBFEM. Then the results are compared. In both approaches, the first step is to obtain the static equilibrium configuration of the catenary which will allow us to know the distribution not only of the tension but also the curvature along the riser. WBFEM can be used for calculation of linear static equilibrium as we have seen before in section 3.6.2 with examples. However the static equilibrium of a catenary calls for a nonlinear solution. So, this

task is accomplished by using a finite element mesh representing the riser and then the conventional FEM procedure to solve the nonlinear equation $[K]\vec{U} = \vec{F}$. In the present work, a computer program named Anflex was used. It can calculate, among other things, natural frequencies and mode shapes which represent the second and final step in the approach with conventional FEM.

As for the second approach, the one using the WBFEM, the next step consists of discretizing the same riser with the straight or curved beam elements studied in previous chapters based on the distribution of properties and forces in the static equilibrium configuration. When using the curved beam elements presented in this work, we have to be careful when discretizing the structure because both types of curved elements present limitations: one has constant tension and constant curvature distribution and the other has constant curvature and slowly varying tension. The solution adopted here was to use an element with a curvature equal to the average of the curvature distribution along the segment it represents. The same approach applies to the tension distribution. Based on this criterion, a mesh is defined so that it represents the distribution of tension and radius of curvature along the riser. With the mesh defined, the dynamic stiffness matrix of the whole riser can be calculated through the assemblage of the element dynamic stiffness matrices, following the traditional FEM techniques. In the FEM model the riser was discretized with 60 elements of the same length while in the WBFEM model we used 36 elements of varying length.

We had to employ both the straight beam element in the region of the riser that is in contact with the sea bottom and the curved beam element between the touch down point and the top node.

Table 5.2 shows the natural frequencies associated with the in-plane mode shapes of the steel catenary riser according to three different methods. As we can see, the values agree very well. If we take the natural frequencies calculated by Anflex as a reference, the difference between natural frequencies using the three methods is less than 1%.

The first and tenth mode shapes are represented by the dashed lines in Figures 5-1 and 5-2, respectively. Figure 5-3 shows the tenth mode calculated Anflex. We see that the modes agree very well too.

Frequency Number	WBFEM Constant Tension	WBFEM S. V. Tension	FEM
1	0.1009	0.1004	0.10191
2	0.1545	0.1543	0.15589
3	0.2168	0.2167	0.21881
4	0.2728	0.2727	0.27527
5	0.3357	0.3355	0.33884
6	0.3957	0.3958	0.39960
7	0.4622	0.4621	0.46676
8	0.5276	0.5276	0.53286
9	0.5989	0.5988	0.60514
10	0.6703	0.6703	0.67742

Table 5.2: The first ten natural frequencies (in Hz) for the steel catenary considering the region laying on the sea bottom.

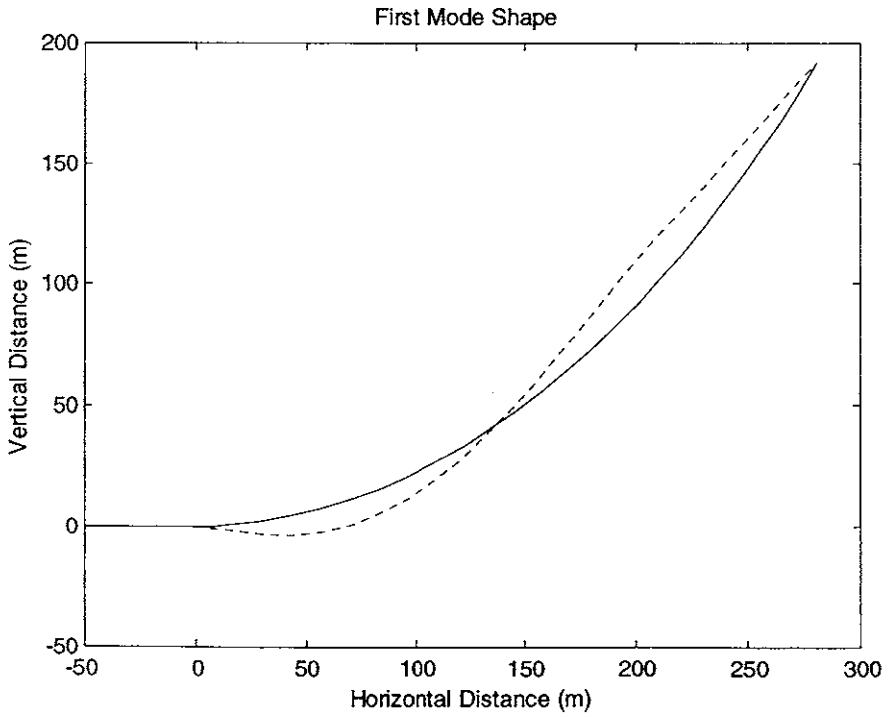

Figure 5-1: Static equilibrium configuration plus the first mode shape calculated through WBFEM. The riser extends from the anchor point to the top node.

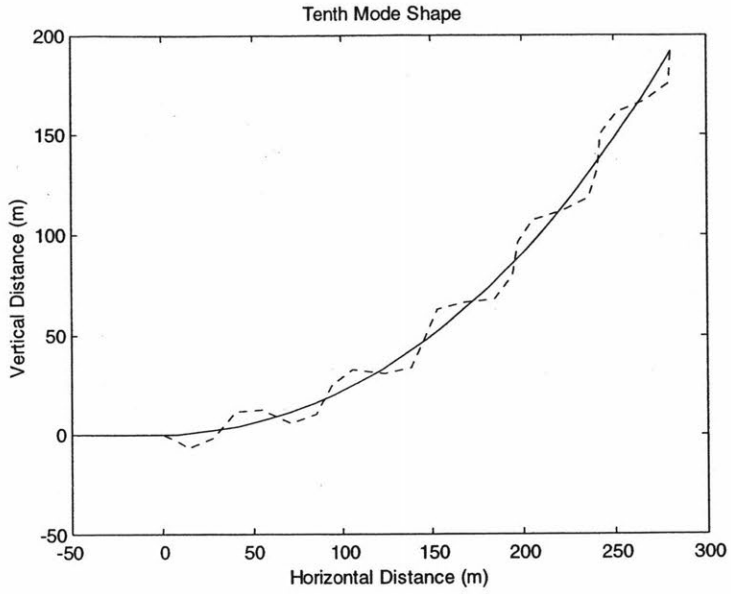

Figure 5-2: Static equilibrium configuration plus the tenth mode shape calculated through WBFEM. The riser extends from the anchor point to the top node.

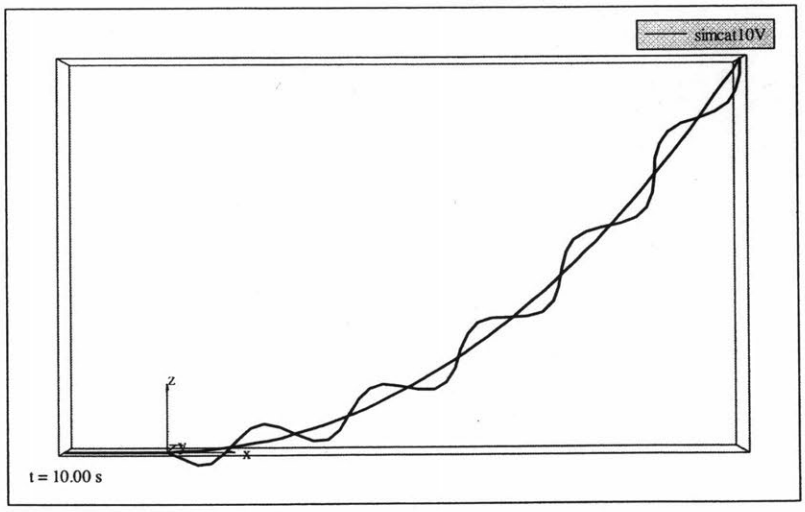

Figure 5-3: Static equilibrium configuration plus the tenth mode shape calculated through traditional FEM. The riser extends from the anchor point to the top node.

Now we apply a distributed load described as follows:

- $q = 0$ for $s \leq 355m$
- q increases linearly from $s = 355m$ to $s = 375m$, from $q = 0$ to $q = 6N/m$
- $q = 6N/m$ from $s = 375m$ to $s = 405m$

In order to introduce damping, a complex value of $2.067\times10^{11} - i\cdot 0.2\times10^{11} N/m^2$ was used for the Young's modulus. The load was applied at two frequencies, 0.67Hz and 2Hz, with the same mesh. Figures 5-4 and 5-5 show the transverse displacement due to the load at these frequencies, respectively.

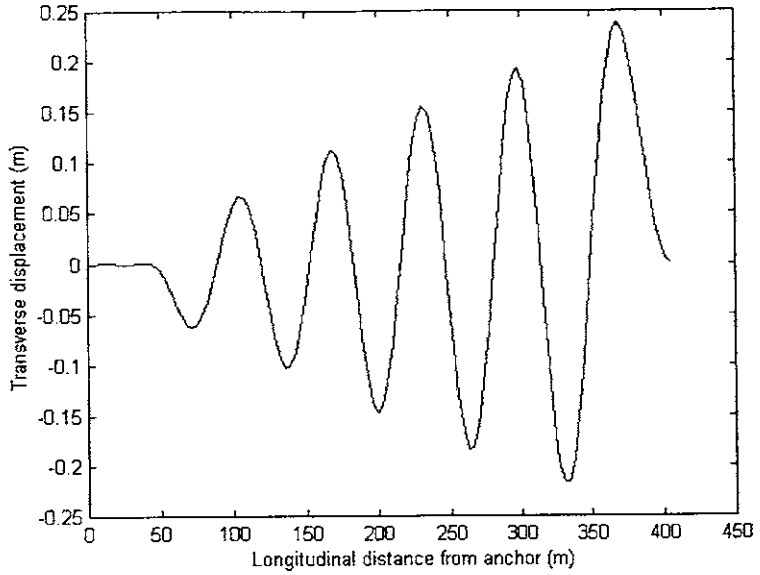

Figure 5-4: Transverse displacement along the scr subjected to a distributed load at 0.67 Hz.

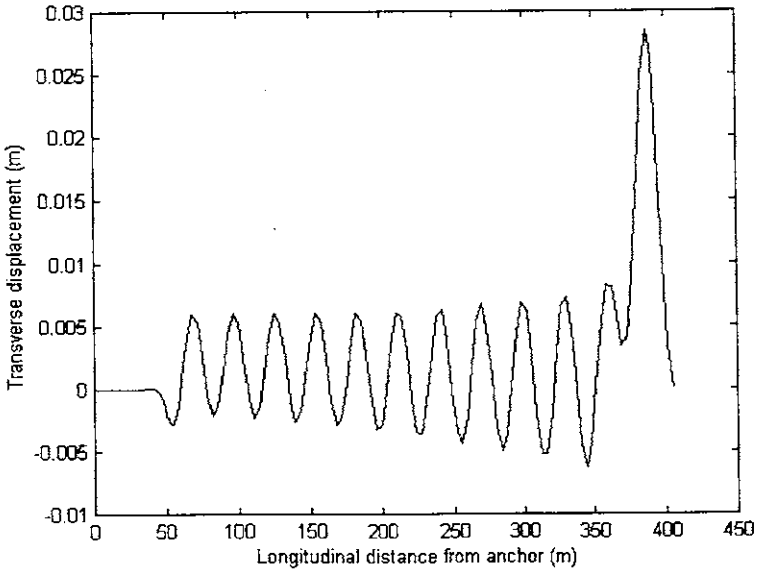

Figure 5-5: Transverse displacement along the scr subjected to a distributed load at 2.0 Hz.

5.4 Lazywave Riser

In this example, we will calculate natural frequencies and mode shapes of the lazy-wave configuration represented in Figure 5-6. The main feature of this configuration is the presence of distributed buoyancy along a region of the riser not far from the bottom causing a hunch in the static configuration of equilibrium. This region represents an increase in the distributed mass for the waves travelling along the riser and so it will cause reflection at both ends. Figure 5-6 shows the configuration of the lazywave under consideration here. The thicker region represents the buoyancy.

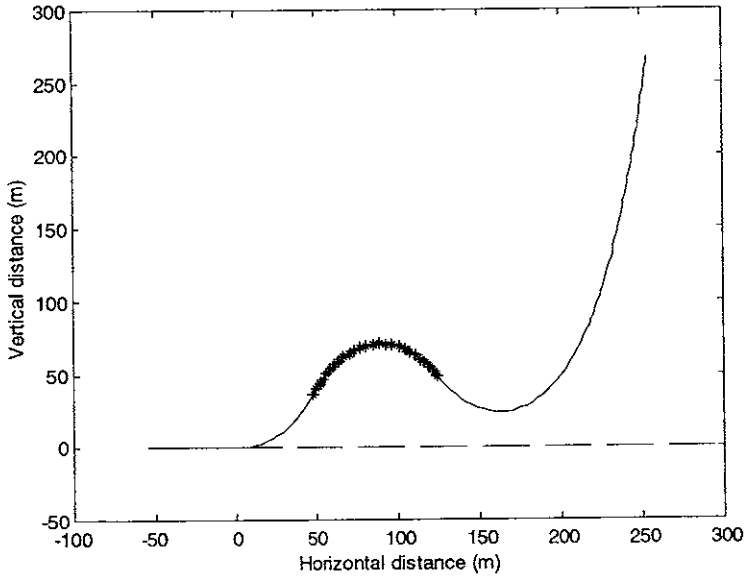

Figure 5-6: Lazywave configuration

The main characteristics of the structural system are

Horizontal projection: $254\,m$

Vertical projection: $267.0\,m$

Length of riser touching the soil: $60\,m$

Water depth: $267.0\,m$

Modulus of elasticity: $8.703\times10^{6}\,kN/m^{2}$

Mass density: $3243\,kg/m^{3}$

Cross-sectional area: $0.0827\,m^2$

Moment of inertia: $0.2849\times10^{-4}\,m^4$

Hydrodynamic diameter outside buoyancy region: $0.49\,m$

Hydrodynamic diameter in the buoyancy region: $0.80\,m$

Length of buoyancy region: $100\,m$

Density of floaters: $2.3\ kN/m$

Buoyancy of floaters: $5.8\ kN/m$

Soil stiffness: $300\ kN/m$

Total length: 540m

Table 5.3 shows a comparison between the natural frequencies obtained from Anflex and from WBFEM. In the first approach, the lazywave was discretized with 136 equally spaced nodes while in the second case it was discretized with 60 nodes at varying distances according to the criteria explained before for the radius of curvature and tension.

In the case of lazywave configuration the difference in terms of natural frequencies is around 5%, greater than the catenary case. This can be explained by the fact that in the catenary configuration the radius of curvature does not vary much along the longitudinal axis of the riser while in the lazy wave configuration we have larger changes of the radius of curvature along the longitudinal axis. It makes the representation of the variation of the radius of curvature along the riser more difficult with the element used in the present work since it has constant radius of curvature. However, the values are not so different and, as we will see next, the mode shapes are very similar. It means that the dynamic behavior of the structural system is reasonably well represented. Besides, as we have seen in chapter 3, as the frequency increases, the propagating waves tend to be independent of the radius of curvature.

Frequency Number	WBFEM Constant Tension	FEM
1	0.0166	0.0166
2	0.0300	0.0314
3	0.0385	0.0425
4	0.0482	0.0483
5	0.0645	0.0652
6	0.0738	0.0771
7	0.0908	0.0970
8	0.1063	0.1122
9	0.1213	0.1281
10	0.1375	0.1452

Table 5.3: First ten natural frequencies (in Hz) of the lazywave configuration according to different methods.

Figures 5-7 and 5-9 show the fifth and tenth mode shapes calculated through the WBFEM while Figures 5-8 and 5-10 show the mode shapes calculated through the traditional FEM. Comparing them we see that there is a good agreement in the mode shapes.

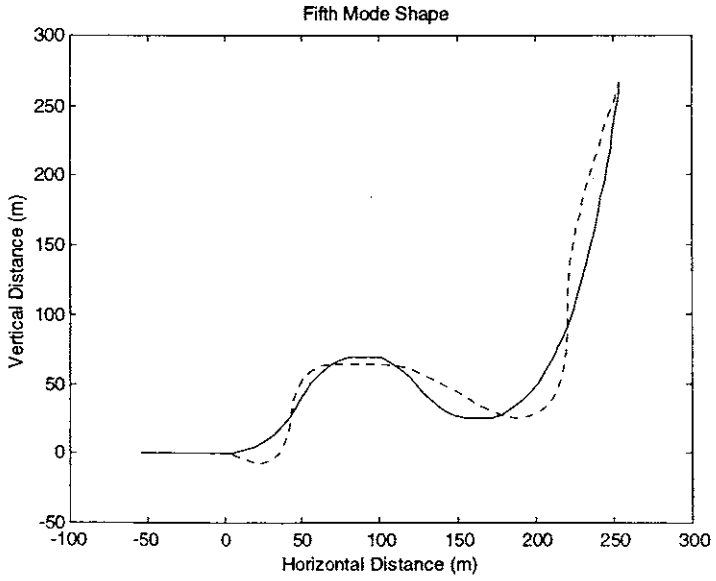

Figure 5-7: The fifth mode shape of the lazy wave configuration considered in this example is represented by the dashed line and it was calculated through WBFEM.

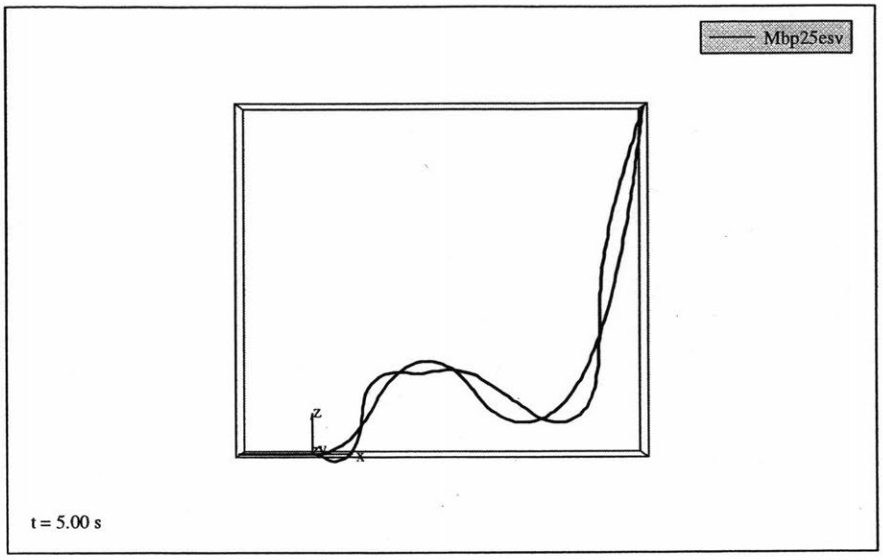

Figure 5-8: The fifth mode shape of the lazy wave configuration calculated through traditional FEM.

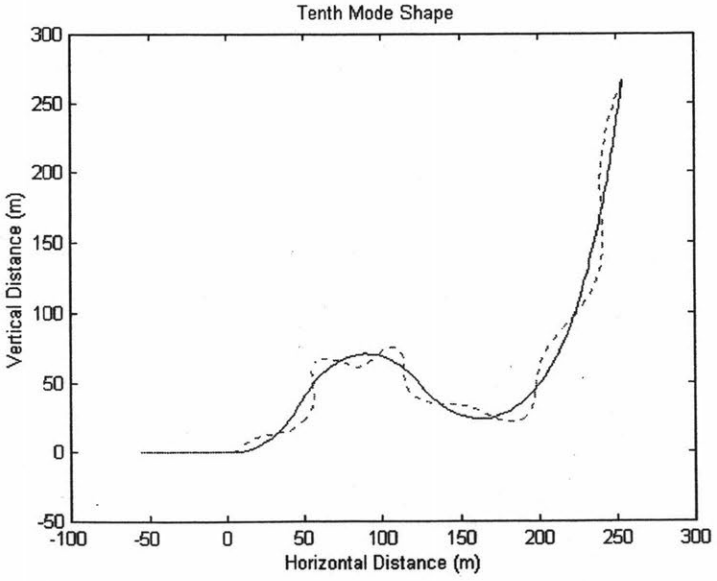

Figure 5-9: The tenth mode shape of the lazy wave configuration considered in this example is represented by the dashed line and it was calculated through WBFEM.

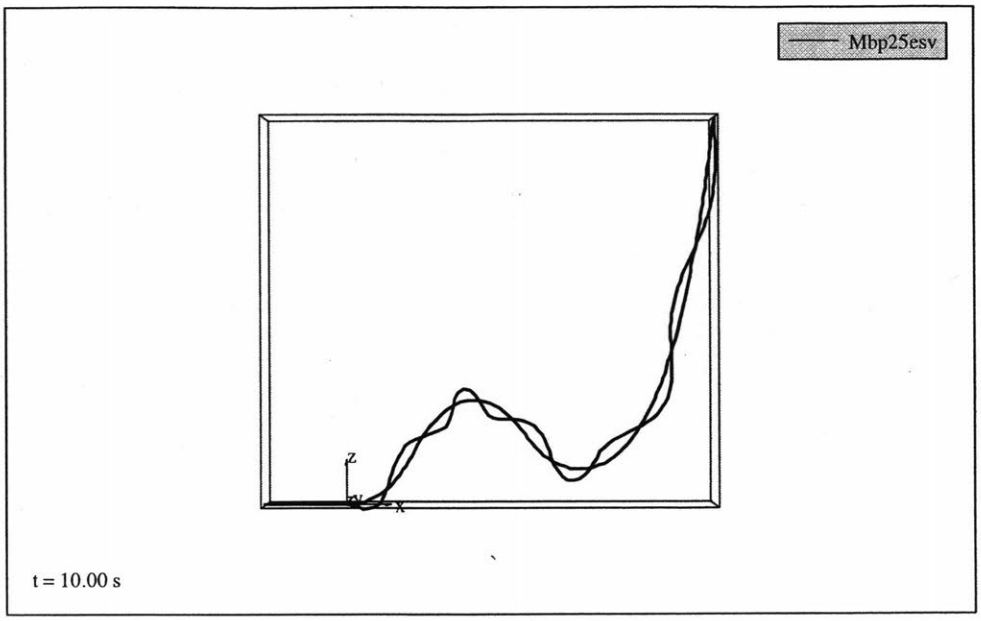

Figure 5-10: The tenth mode shape of the lazy wave configuration calculated through traditional FEM.

5.5 Wavelength on a Riser

Along this work, we have presented the dispersion relation of straight and curved beams for a number of conditions. Equation 2.6 is one example of this relation. Basically, it indicates that the wavelength depends, among other parameters, upon the distribution of mass and tension along the beam longitudinal axis. As we have seen before, in a marine riser it is very likely that a travelling wave will encounter changes in the properties along its longitudinal axis, causing not only the wave to reflect but also its wavelength to change. So, it is interesting to study how the wavelength changes for one constant frequency and the consequences of this change in the behavior of a riser.

The distribution of tension and mass along the longitudinal axis of a riser is defined in the static equilibrium configuration. Figures 5-11 and 5-12 show these distributions for the CVAR configuration discussed in chapter 4, respectively. The increase in the mass corresponds to the buoyant region. We also see that tension has a minimum value near the top end of the buoyant region. Moving away from this point, tension increases.

Using the relation dispersion studied in chapter 3, we get the distribution of wavelength along the CVAR for a specific frequency. Figure 5-13 shows this distribution for 0.5Hz (solid line) and for 1Hz (dashed line). In this figure, it was used the wavelength that corresponds to the propagating transverse waves. Examining these three figures we can draw some important conclusions:

- The wavelength decreases as the frequency increases.
- The wavelength decreases as the tension decreases.
- The wavelength decreases as the mass increases.

The importance of the knowledge of the wavelength is its influence on the fatigue life of the riser. In order to help the understanding of this influence, we can imagine there is a wave travelling downward along the CVAR with unit amplitude always. If, for any reason, the wavelength decreases, as it happens when the wave moves from the bare pipe to the buoyant region, then the curvature will increase and so will the bending stresses. Therefore, in the CVAR case, the buoyant region is more likely to present high dynamic bending stresses and so this region will be very important for the fatigue life. Of course, the final conclusion depends also on the location and magnitude of the dynamic load and on the hydrodynamic damping.

As for a SCR, a critical region is the one near the touch down point since it is the region with the smallest values of axial tension and consequently the curvatures will be the biggest.

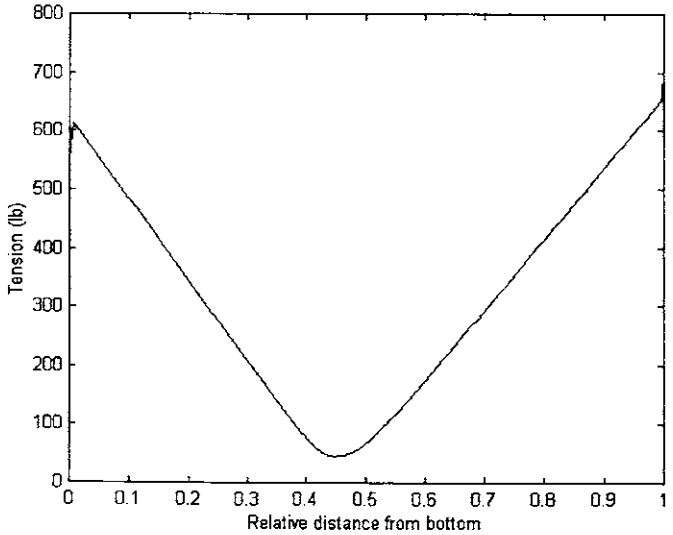

Figure 5-11: Tension distribution along the CVAR configuration

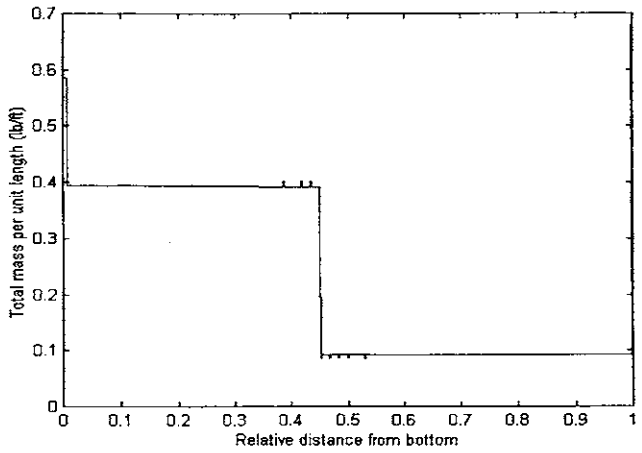

Figure 5-12: Distribution of mass per unit length along the CVAR configuration

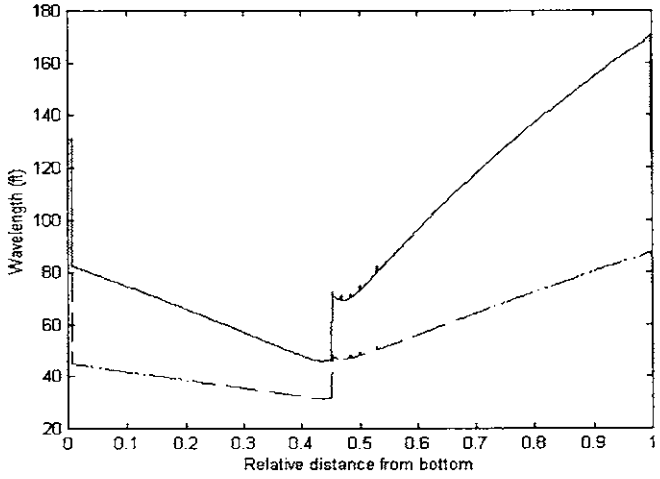

Figure 5-13: Distribution of wavelength along the CVAR for two frequencies: solid curve for 0.5Hz and dashed curve for 1Hz.

5.6 CVAR Configuration

The last structure that we are going to study is the CVAR and we are going to focus our attention to the configuration we studied in chapter 4, which is shown in Figure 4-3.

The natural frequencies can be obtained by following the same procedure adopted previously for the SCR and Lazywave cases: using FEM and WBFEM. In the FEM, the riser is modeled with

425 elements with the same length while in the WBFEM it is modeled with 208 elements where, in the middle region, the element length (about 2 ft) is smaller than the element lengths in the region near the ends (about 14ft). This model was adopted because it is in the middle region where the variation of radius of curvature is sharper. Table 5.4 below shows the result of this calculation for the first ten natural frequencies where 'FEM' stands for the natural frequencies calculated by the program Anflex. All frequencies are given in Hz.

Frequency Number	WBFEM Constant Tension	FEM
1	0.0253	0.0260
2	0.0497	0.0519
3	0.0741	0.0756
4	0.0813	0.0841
5	0.1133	0.1168
6	0.1346	0.1366
7	0.1523	0.1568
8	0.1827	0.1880
9	0.2031	0.2074
10	0.2271	0.2344

Table 5.4: First ten natural frequencies (in Hz) of the CVAR configuration corresponding to the in-plane mode shapes, according to different methods.

The difference in the values is between 2% and 3%.

Chapter 6

Measurements from Full Scale SCR

6.1 Introduction

In this chapter we summarize the program developed by Petrobras to monitor the steel catenary riser installed on the P18 platform in terms of loads, displacements and forces. The goal of such a monitoring system is to give the design team more confidence on the design premises and hence, reduce the uncertainties. The calibration based on the comparison between the measured data and the predicted values will help in the consolidation of the SCR technology. Some results from the measurements are presented and then some conclusions are drawn from these results. This is a preliminary analysis since the amount of data is huge and the data base where measurements will be stored is still being organized. In the end we make a comparison between the experimental data and the prediction from Shear7 and WBFEM.

6.2 Monitoring System

In 1995 Petrobras started a project to build and install a steel catenary riser prototype on the P18 semi-submersible platform, located at 910m water depth. It was conceived to be a dummy riser with a comprehensive monitoring system. Three very important areas regarding the SCR project were assigned as the main objects of monitoring:

- Stresses at the touch down point, at first welding and at the wave zone.
- Platform motions, including offsets, first and second order motions.
- VIV along the riser.

Other quantities like environmental loads were also measured. The system encompasses all the aspects that are important in the design methodology.

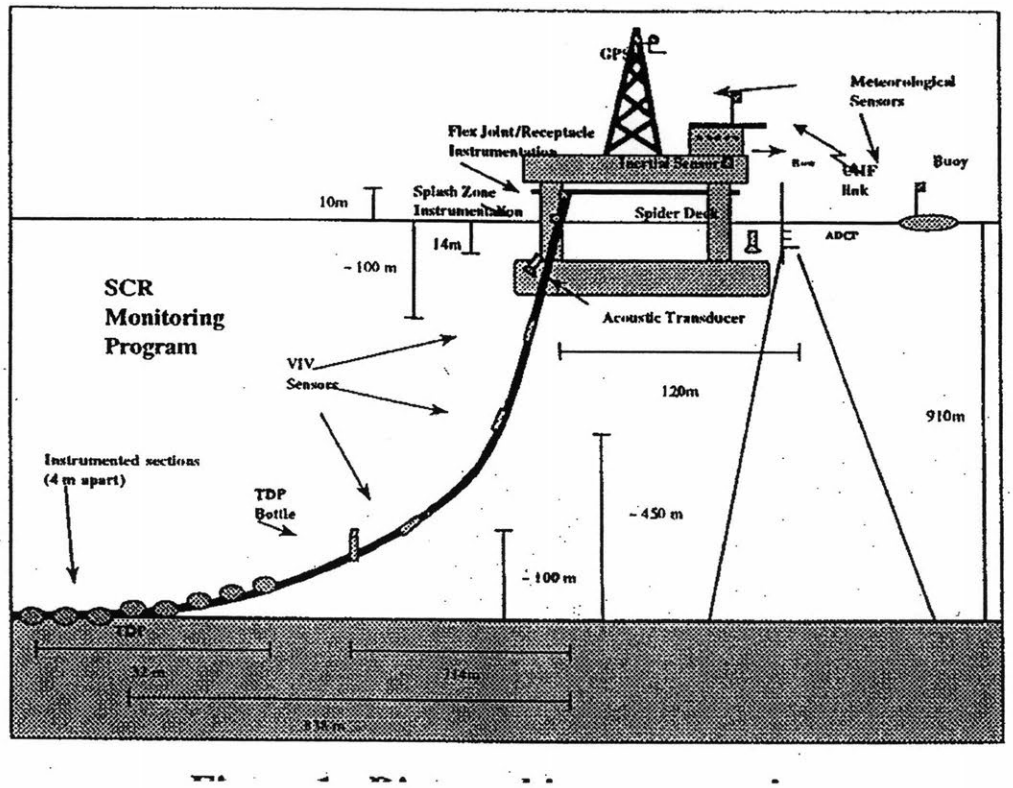

Figure 6-1: Monitoring system installed in the P18 steel catenary riser.

Figure 6-1 gives an idea of the instrumentation used in the implementation of the monitoring system. The parameters of interest are defined as:

- Environmental loads: current profile, wave directional spectra and wind
- Platform position and motions
- Mooring line tension
- Forces at the touch down point, wave zone and riser top
- VIV

The monitoring activities were distributed in 5 monitoring sub systems:

- Meteo-Oceanographic
- Platform position and motions
- Top loads

- TDP loads
- Riser position and motions

Some of the main characteristics of the monitoring system are:

- Internal clocks synchronized by GPS
- Unattended operations
- Operational configuration can be changed remotely
- Executable programs can be loaded remotely
- Local data storage in the subsea equipment
- Data transmitted to the surface by acoustic telemetry
- Redundancy on the permanently installed subsea equipment

Because of the low probability of survival during the pipe-laying operation, it was required that the transmission of the data from the subsea sensor packages to the surface should be made acoustically.

6.2.1 Environmental Loads

Sismo is the meteo-oceanographic monitoring system that controls and collect data from

- Local sensors for measuring wind speed and direction, temperature, barometric pressure and relative humidity.
- The surface meteo-oceanographic buoy. With 2.76m diameter, it is moored around 1000m away from the P18. The buoy measures its heave, roll, pitch and heading, meteorological parameters, sea surface temperature and surface current.
- The two high power units Acoustic Doppler Current Profilers (ADCP) for measuring current profile along the water depth in terms of intensity and direction. One is installed at the sea floor looking up and with internal data recording, retrieved every three months for battery change and data collection. The other is suspended at the platform looking downward and is connected by cable to the Sismo system.

These measurements are important because, among other reasons, the current is one of the main sources of VIV.

6.2.2 TDP Monitoring System

Strain gages were installed in the touch down point region in order to measure tension, in-plane and out-of-plane bending moments. Time series of 900s, every 3 hours would be recorded. The strain gages had to be protected by a polymer collar which, in turn, had to be protected against damage during handling and soil contact by a steel blister cover. Four TDP bottles were used to monitor the forces in the region near the sea bottom. They were numbered from 1 to 4 in the anchor direction. The sampling rate was $1Hz$ in the measurements.

The main objective of the measurements in this region was the study of the interaction between the soil and the riser but they can be also very useful for assessment of intermittent VIV. As we have seen in section 4.2.3, the region just above the touch down point is where the highest KC number occurs when there is a heave motion applied on top of the riser.

6.2.3 Top Monitoring System

The main top quantities measured are the following: inclinations, in-plane bending moments, out-of-plane bending moments and tension. The system has the strain sensors connected to a remote electronic unit installed at the platform spider deck. Until 1999 November 10^{th}, the sampling rate was 1Hz. After this day, it was changed to 2Hz.

6.2.4 Riser Motions Monitoring System

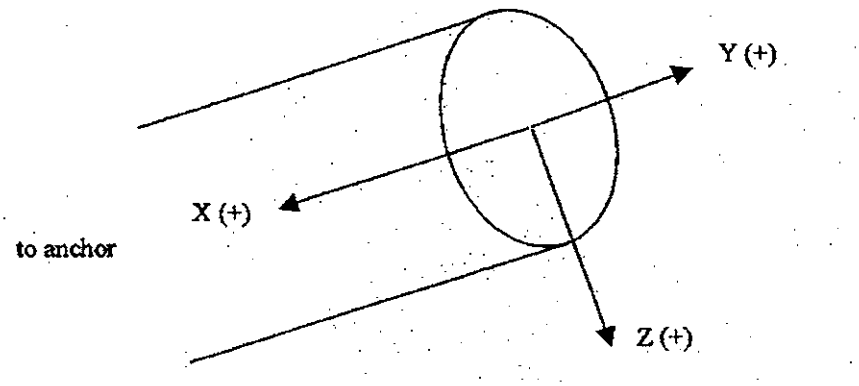

Figure 6-2: System of reference for the quantities measured by the VIV bottles.

This monitoring system of the riser motions is designed to measure quantities according to the riser coordinate system shown in Figure 6-2 above. The X direction is coincident with the longitudinal axis of the riser. The Y and Z axes define a cross sectional plane perpendicular to X, while the X and Z axes define a vertical plane. The main quantities measured in the VIV bottles are the following: X, Y and Z accelerations, Y and Z angular velocities. The corresponding linear and angular displacements are obtained by double integration. Three bottles, numbered from 1 to 3 in the anchor direction, were installed at depths equal to $221m$, $306m$ and $535m$, respectively. The data was measured and recorded at a rate of 2Hz for 5 minutes every 3 hours and the signal was lowpass filtered at 0.5 Hz. This value was chosen based on the prediction of VIV frequencies excited by the current profiles in Campos Basin.
Figure 6-3 shows the position of P18 together with the SCR. The longitudinal platform axis makes an angle of 23° with the North direction and the plane of the scr makes an angle of 192.11° with the North.

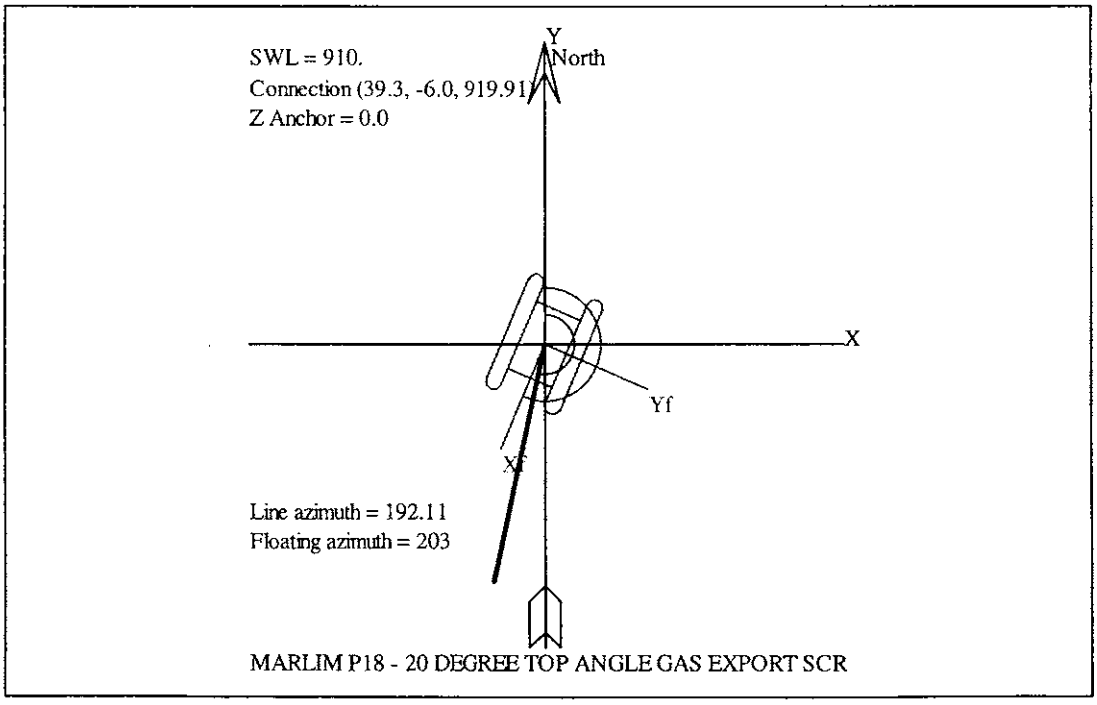

Figure 6-3: Position of platform P18 and the steel catenary riser installed on it with respect to the North direction

The X and Y axis shown in Figure 6-3 correspond to the East and North directions, respectively while Xf and Yf are the global axis used by Anflex to define the structural system of the scr.

6.3 Analysis of Measurements

The main characteristics of the scr are

Water depth: 910m

Angle of catenary plane with North direction: 192.11°

Outside diameter: 0.273m

Inside diameter: 0.232

Top angle with the vertical direction: 20.5°

Total length: 2066.5m

Bending stiffness: 27269kNm2

Axial stiffness: 3400000kN

Density: 77kN/m3

Suspended length: 1345m

Table 6.1 shows the first 25 natural frequencies (in Hz) associated with both the in-plane and out-of-plane mode shapes. They were calculated by Anflex and compared with the values obtained through WBFEM. They are in the range of frequencies obtained in the measurements of the riser motions by the VIV bottles 1, 2 and 3. The average difference between the natural frequencies by Anflex and those calculated through WBFEM is 2%.

The calculations of the out-of-plane mode shapes using the WBFEM were made assuming an equivalent straight riser with the static distribution of tension along it. The natural frequencies obtained are close to the values calculated by Anflex, where a tri-dimensional model was employed. Hence, the behavior of the riser in the out-of-plane direction, with only the weight and buoyancy forces applied, is similar to the straightened riser with the same tension distribution.

Frequency Number	WBFEM In-plane	WBFEM Out-of-plane	FEM In-plane	FEM Out-of-plane
1	0.036	0.021	0.037	0.021
2	0.057	0.042	0.058	0.042
3	0.080	0.062	0.082	0.063
4	0.101	0.083	0.103	0.084
5	0.123	0.104	0.126	0.106
6	0.144	0.125	0.147	0.127
7	0.166	0.146	0.169	0.148
8	0.187	0.167	0.190	0.170
9	0.209	0.188	0.213	0.191
10	0.230	0.210	0.235	0.213
11	0.253	0.232	0.258	0.235
12	0.274	0.253	0.280	0.257
13	0.297	0.276	0.303	0.280
14	0.319	0.298	0.326	0.302
15	0.342	0.320	0.350	0.326
16	0.364	0.343	0.373	0.349
17	0.388	0.366	0.397	0.372
18	0.411	0.389	0.421	0.396
19	0.435	0.413	0.445	0.420
20	0.459	0.437	0.469	0.444
21	0.484	0.461	0.495	0.468
22	0.507	0.485	0.518	0.493
23	0.531	0.510	0.543	0.516
24	0.542	0.535	0.555	0.544
25	0.563	0.561	0.576	0.570

Table 6.1: The first 25 natural frequencies (in Hz) corresponding to the in-plane and out-of-plane mode shapes of the P18 SCR.

There are basically three types of VIV excitations on a riser: ocean current, ocean waves and the riser motion itself. This last excitation was studied in chapter 4. Now we are going to try and identify the influence of each type of excitation for the present P18 scr when subjected to the environmental loads.

6.3.1 Intermittent VIV

We are going to select the month of August/1999 because it is one of the few months that present trustable data so far stored in the data base. The TDP bottles ended up being useful in the subject of intermittent VIV caused by the riser response to some excitationbecause we discovered that in August these bottles were above the sea floor. A negative aspect is that only number 4 bottle was working well.

After examining the variation of P18 heave along the month of August 1999, two days were selected to be studied in more detail: 13 at 12:00h and 16 at 00:00h. They correspond to the days with the lowest and the highest heave, respectively. All the power spectra densities shown in this chapter were obtained through Matlab, except those related to the accelerations measured by the VIV bottles in which case we used an independent computer program provided by SMS.

1. August 13, 1999 at 12:00 o'clock

An important source of VIV excitation is the current acting along the riser. In this case the difficulty is the lack of data about the current since the ADCP presented problems all the time. Thus, we had to resort to surface measurements of the ocean current made by a vessel or another platform near P18 and assume a typical current profile based on these surface measurements.

The main excitations measured for this date and time are the following:

- The zero crossing period of the wave was $6.77s$, the significant wave height was $1.95m$ and its direction was 205° with respect to the North direction. It has almost the same direction as the steel catenary riser plane.
- The measured surface current magnitude and direction are 0.53m/s and 202.5° with respect to the North direction, respectively. Based on this pair of values, the typical current profile is assumed to be the one shown on table 6.2 below. It shows one general characteristic of the currents in Campos Basin: they change the direction along the depth. We see that near the surface it is approximately aligned with the scr plane.

Depth (m)	Magnitude (m/s)	Angle (degree)
50	0.55	217
100	0.50	201
150	0.49	202
250	0.28	189
350	0.14	177
450	0.10	142
550	0.13	83
650	0.18	47
750	0.18	52
900	0.24	46

Table 6.2: Typical current profile estimated for August 13, 1999 at 12:00 o'clock.

- The average heave amplitude on top of the riser is 0.33m

These excitations were applied on the FEM model of the P18 scr through a deterministic dynamic analysis in Anflex. Many quantities were calculated, such as KC number, normal velocity along the riser and shedding frequency. The results are shown in Figures 6-4 and 6-5.
The upper part of Figure 6-4 shows the maximum normal velocity along the scr, when subjected to the current and wave described previously, and the heave measured on top of the riser (0.33m) applied by the vessel. In the lower part of the same figure we see the corresponding shedding frequency calculated through equation 4.1. The region of zero normal velocity corresponds to the riser region that always lies on the sea bed.
To understand the effect of each excitation on the riser we made the same dynamic analysis with Anflex excluding the current. Figure 6-5 shows the predicted KC number (upper part) and the corresponding shedding frequency (lower part) for the riser subjected to two types of excitation:

- Heave and wave (solid line)
- Only heave (dotted line)

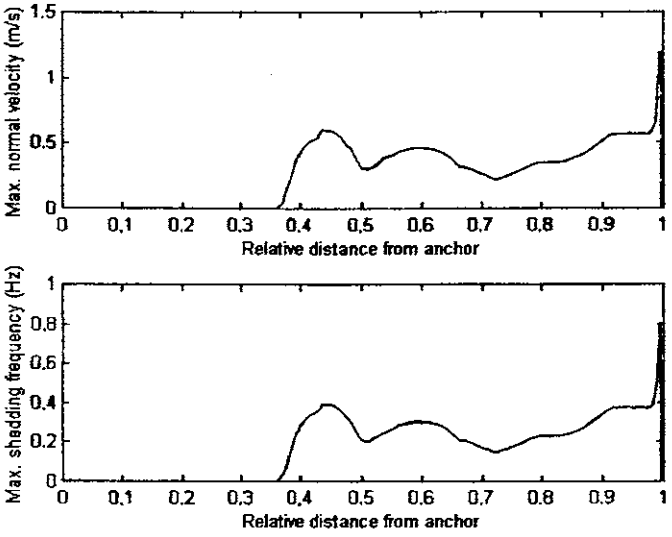

Figure 6-4: Maximum predicted normal velocity (upper part) and shedding frequency (lower part) along the P18 scr for the environmental conditions measured on August 13, 1999 at noon.

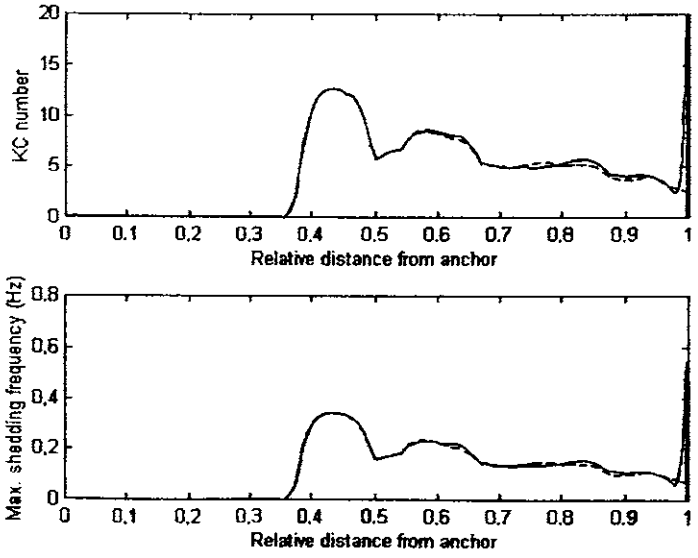

Figure 6-5: Predicted KC number (upper part) and maximum shedding frequency (lower part) along the P18 scr without the current. The solid line refers to the application of heave plus wave and the dotted line refers to application of heave only. Heave and wave were measured on August 13, 1999 at 12:00 o'clock.

Comparing the lower parts of Figures 6-4 and 6-5, we see that in the riser region near the tdp the shedding frequency can go up to 0.4 Hz and it is dominated mainly by the riser response to the heave. As we go up along the riser the influence of the current on the shedding frequency increases while the influence of the riser motion decreases. In addition to the current, in the wave zone (upper 70 m of the sea depth) the influence of the wave makes the shedding frequency increase sharply up to 0.8Hz.

Figure 6-5 indicates that neglecting the effect of current, the highest values of KC number occur in the lower region of the suspended riser and in the wave zone. The predicted KC number is below 15 along the riser except at the wave influence zone, where it can reach 20. When the current is taken into account, the distribution of shedding frequency changes (see Figure 6-4) but we see that the riser motion is still dominant in the lower part of the riser.

Figures 6-6 and 6-7 show the power spectral density of the in-plane and out-of-plane bending moments in the TDP bottle 4 on August 13 at 12:00 o'clock, respectively. The ocean wave period in Campos Basin varies, in general, between 7 and 12 seconds and the second order motion period, in surge or sway, is around 180 s. These two excitations are present in the response spectra at the TDP bottle 4. It can explain the big amount of energy seen in the frequency range up to 0.18 Hz. It indicates that the waves generated at the top of the riser managed to reach the touch down point (tdp) region. Both response spectra show little energy between 0.2 Hz and 0.3 Hz when compared to the response at the wave frequency band, for instance. However, above 0.3 Hz the response spectra indicates an increase of energy.

The rms of the bending moments shown in Figures 6-4 and 6-5 were calculated for 3 different ranges of frequencies. They are shown in the table 6.3 below:

Frequency Range	In-plane bending moment	Out-of-plane bending moment
0.05 to 0.15	0.85	0.46
0.15 to 0.25	0.53	0.32
0.35 to 0.50	0.65	0.45

Table 6.3: Rms of bending moments (in kNm) for different ranges of frequencies (in Hz) at TDP bottle 4.

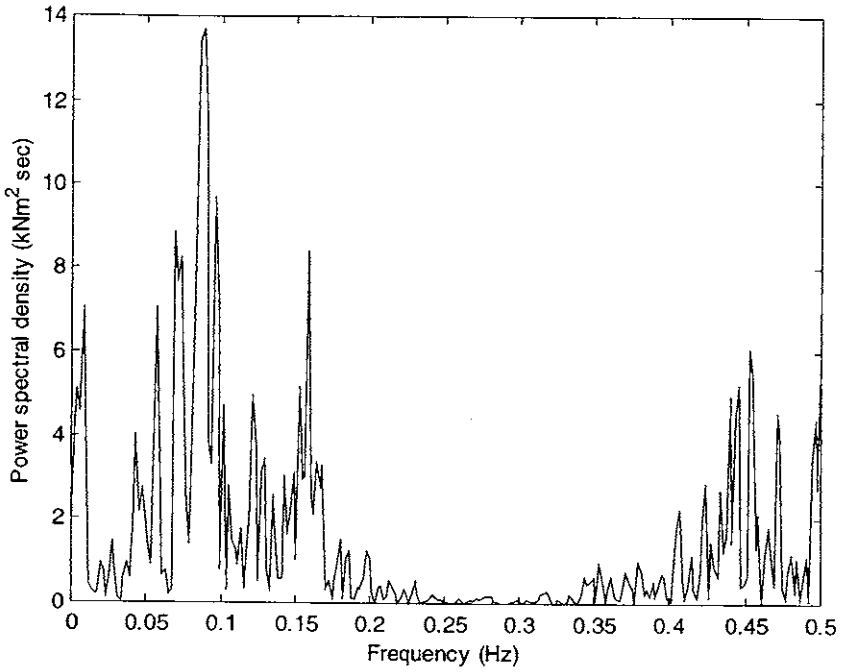

Figure 6-6: Power spectral density of the in-plane bending moment at number 4 TDP bottle of the P18 scr measured on August 13, 1999 at 12:00 o'clock.

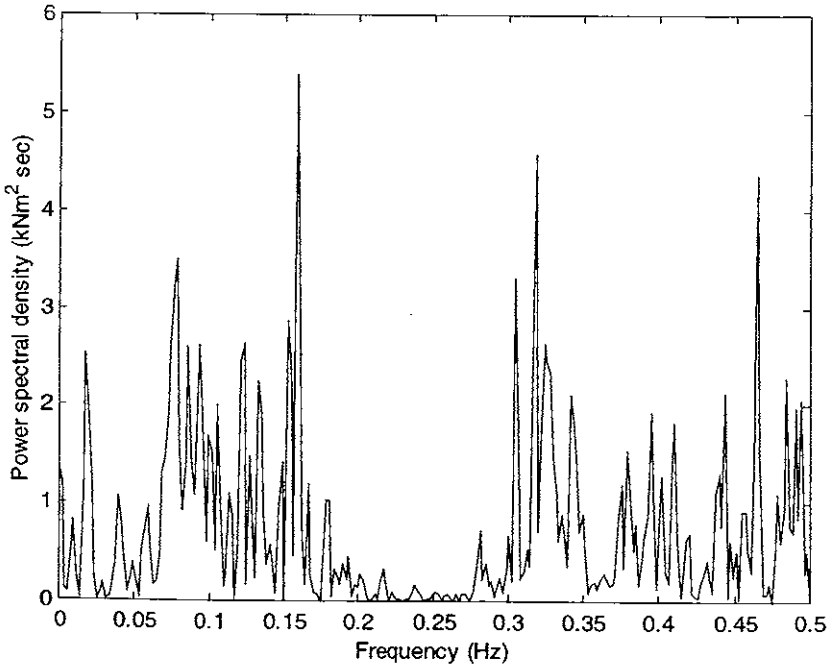

Figure 6-7: Power spectral density of the out-of-plane bending moment at number 4 TDP bottle of the P18 scr measured on August 13, 1999 at 12:00 o'clock.

2. *August 16, 1999 at 00:00 o'clock*

In the present case, the platform heave was much larger than in the previous case and we are going to investigate the main consequences of this effect. The power spectra densities of the in-plane and out-of-plane bending moments measured by the tdp bottle 4 are shown in Figures 6-8 and 6-9, respectively.

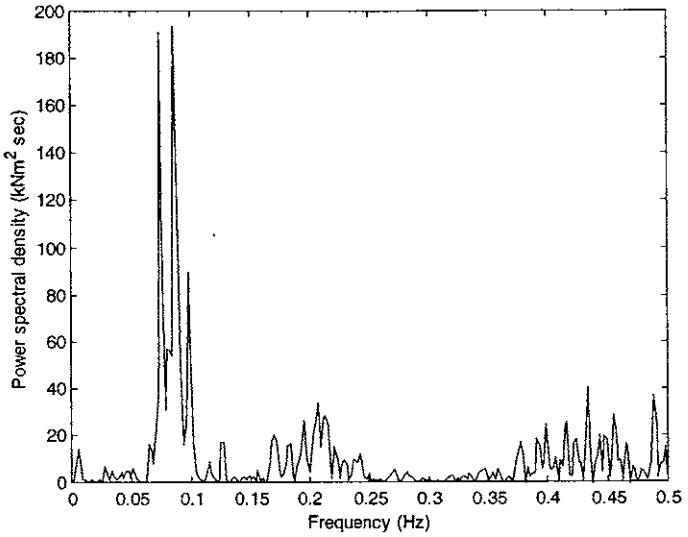

Figure 6-8: Power spectral density of the in-plane bending moment at the tdp bottle 4 measured on August 16, 1999 at 0:00 o'clock.

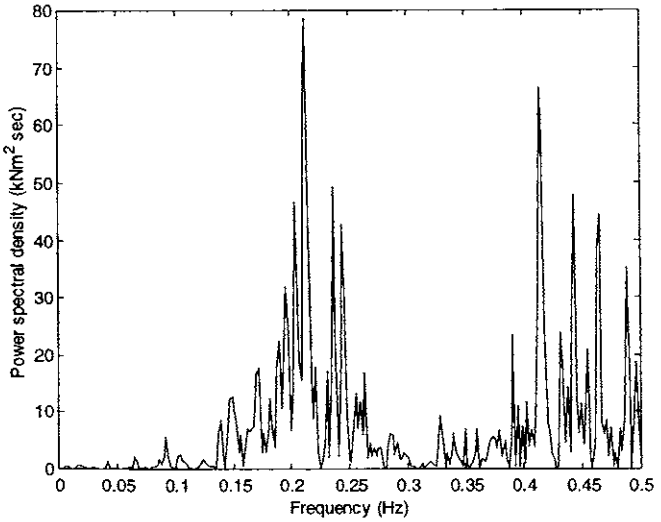

Figure 6-9: Power spectral density of the out-of-plane bending moment at the tdp bottle 4 measured on August 16, 1999 at 0:00 o'clock.

Again, we see that the riser response near the tdp have many different frequency components, going up to 0.5Hz. In the plane of the catenary the response of the riser at the wave frequency is dominant. However, in the out-of-plane direction the response above 0.2Hz is dominant.
The environmental conditions measured at this date and time are:

- The period of the wave was 12.34 s, its height was 4.6m with an angle of 32° with the North direction. The wave has a similar alignment when compared to the wave in the previous case but an opposite direction.
- The surface current magnitude and direction are 0.38m/s and 291.4° with respect to the North direction. It is almost perpendicular to the catenary plane. Based on this pair of values, the typical current profile is assumed to be the one shown on table 6.4 below.

Depth (m)	Magnitude (m/s)	Angle (degree)
50	0.35	262
100	0.31	251
150	0.29	238
250	0.16	219
350	0.11	208
450	0.10	113
550	0.14	60
650	0.18	46
750	0.26	27
900	0.26	41

Table 6.4: Typical current profile for the surface current (0.38m/s and 291.4° with North) measured on August 16, 1999 at 0:00 o'clock.

- The average heave on top of the riser is 1.45m

In order to understand this point, the rms of the in-plane and out-of plane bending moments shown in these figures were calculated for 3 different ranges of frequencies, the same as those used at August 13, at 12:00 o'clock. They are shown in the table below:

Frequency Range	In-plane bending moment	Out-of-plane bending moment
0.05 to 0.15	2.11 (2.5)	0.63 (1.4)
0.15 to 0.25	1.51 (2.8)	1.67 (5.2)
0.35 to 0.50	1.70 (2.6)	1.7 (3.8)

Table 6.5: Rms of bending moments (in kNm) near the tdp region for different ranges of frequencies (in Hz). The number between brackets represents how many times the rms is bigger than the values shown in table 6.3.

Comparing the values presented in table 6.5 with those presented in table 6.3, we see an increase of bending moment rms, specially of the out-of-plane bending moment with frequency above the wave frequency range. Perhaps the best explanation for it is the fact that while the platform heave on 16 at 00:00h was approximately 5 times the platform heave on 13 at 12:00 o'clock the wave period on August 16 is approximately twice the wave period on August 13. Hence, the vertical velocity amplitude on top of the riser (proportional to the product of heave amplitude and heave frequency) on August 16 should be larger than on August 13, assuming that the heave period is close to the wave period. As a consequence, it is likely that the riser normal velocities near the tdp caused by the vessel motion should be higher on August 16 than on August 13, causing the VIV frequencies and lift forces to be larger too. Furthermore, comparing the ocean current magnitudes shown in tables 6.4 and 6.2, we see that on August 16 the current magnitude was smaller than on August 13. Hence, the average shedding frequency caused by the current on August 16 should be smaller. It is a situation similar to what happened with the scr large model studied in chapter 4 when a heave motion was applied on its top. All these considerations point out the importance of the riser motion in generating intermittent VIV.

To verify these ideas, the three excitations described previously were applied to the riser through a deterministic analysis in Anflex and quantities like KC number and shedding frequency were calculated. The results are shown in Figures 6-10 and 6-11.

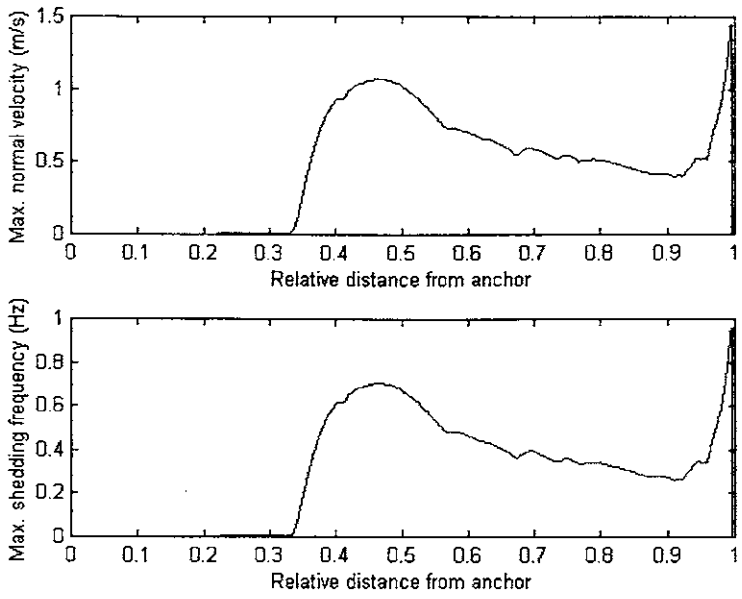

Figure 6-10: Maximum predicted normal velocity (upper part) and shedding frequency (lower part) along the P18 scr for the environmental conditions measured on August 16, 1999 at 0:00 o'clock.

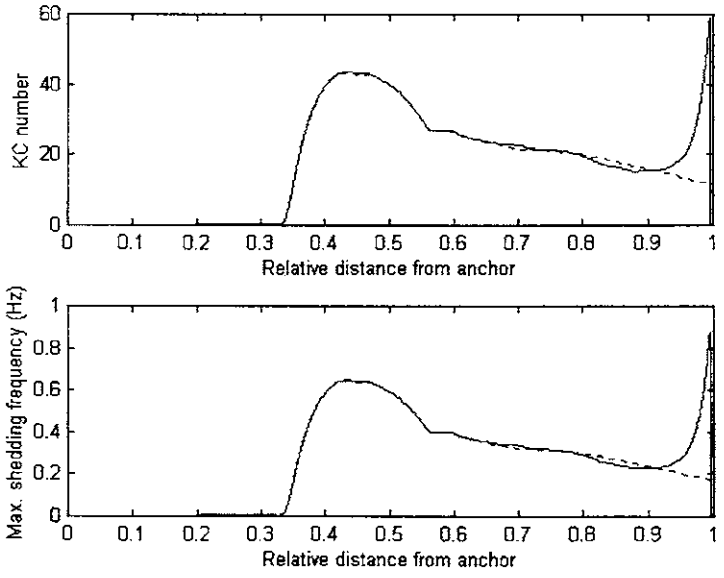

Figure 6-11: Predicted KC number (upper part) and maximum shedding frequency (lower part) along the P18 scr without the current. The solid line refers to the application of heave plus wave and the dotted line refers to application of heave only. Heave and wave were measured on August 16, 1999 at 0:00 o'clock.

The upper part of Figure 6-10 shows the maximum normal velocity along the scr, when subjected to the current and wave described previously, and the heave measured on top of the riser (1.45m) applied by the vessel. In the lower part of the same figure we see the corresponding shedding frequency calculated through equation 4.1. The region of zero normal velocity corresponds to the riser region that always lies on the sea bed.

We see that because of the increase in heave, when compared to the previous case, both the shedding frequency and the normal velocity are higher despite the fact that there was a decrease in the magnitude of the ocean current. There are two main regions of VIV excitation: one on the bottom of the suspended part of the riser, due to the riser response to the heave, and another on the top, due to the action of the ocean wave.

Figure 6-11 shows the predicted KC number (upper part) and the corresponding shedding frequency (lower part) for the riser subjected to two types of excitation:

- Heave applied by P18 and wave (solid line)
- Only heave applied by P18 (dotted line)

Comparing the lower parts of Figures 6-10 and 6-11, we see that in the riser region near the tdp the shedding frequency can go up to 0.6 Hz (Figures 6-8 and 6-9 indicate it too) and it is dominated mainly by the riser response to the heave. As we go up along the riser the influence of the current on the shedding frequency increases while the influence of the riser motion decreases. The influence of the ocean current is smaller than in the previous case because of its lower magnitude. In addition to the current, in the wave zone the influence of the wave makes the shedding frequency increase sharply up to 0.9Hz.

Figure 6-11 indicates that neglecting the effect of current, the highest values of KC number occur in the lower region of the suspended riser and in the wave zone. The predicted KC number is below 45 along the riser except at the wave influence zone, where it can reach 60.

Figure 6-12 shows a comparison between the current profile acting on the riser and the magnitude of the oscillatory flow acting on the riser due to the heave motion only. The upper part refers to August 13 and the lower part to August 16. We see that on August 13 the current velocities had magnitudes a little larger than the magnitudes caused by the heave. However, on August 16 the oscillatory flow caused by the heave was predominant on the VIV excitation.

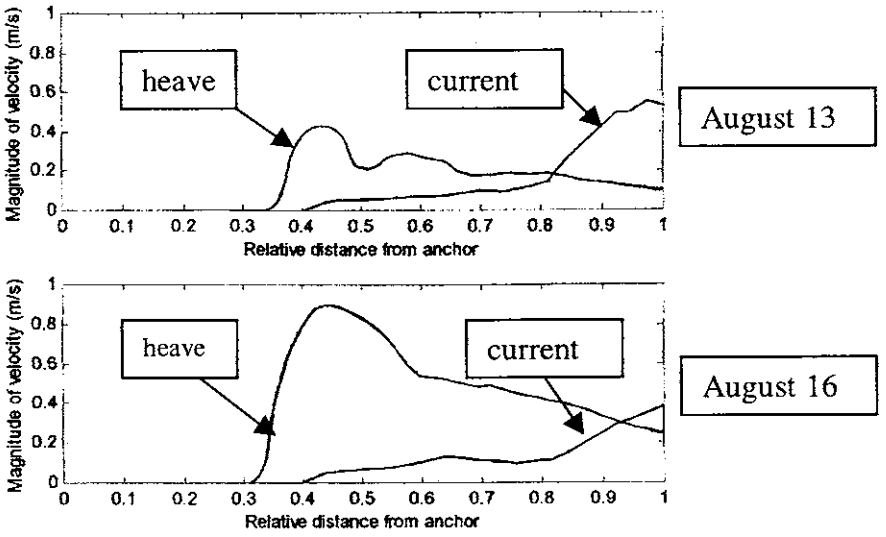

Figure 6-12: Comparison between the velocity magnitudes caused by current and heave only.

The power spectra density plots of the in-plane and out-of-plane bending moments at the top of the riser are shown in Figures 6-13 and 6-14, respectively. We see that the response at that location is dominated by the second order motion frequency and the wave frequency.

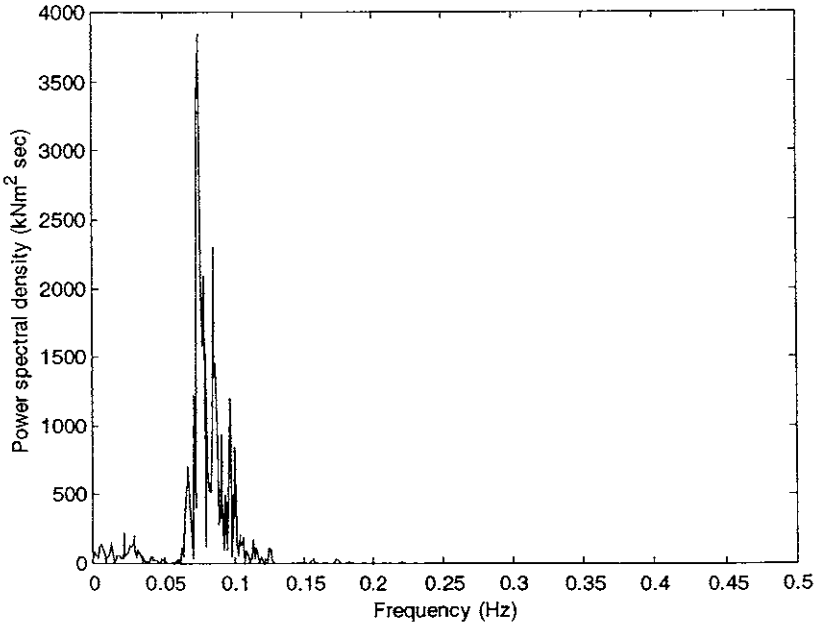

Figure 6-13: Power spectral density of the in-plane bending moment at the top of the scr measured on August 16, 1999 at 0:00 o'clock.

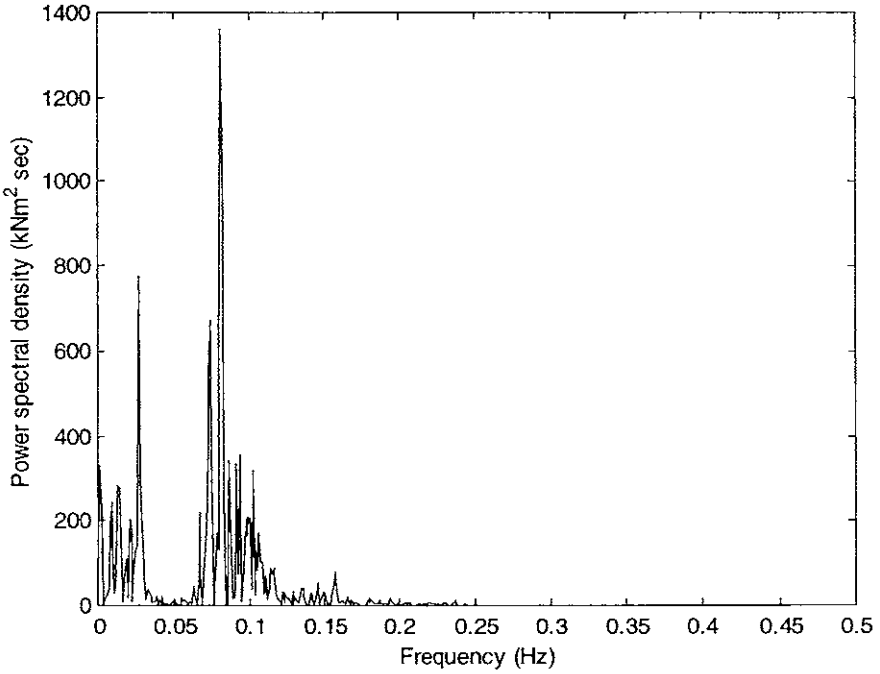

Figure 6-14: Power spectral density of the out-of-plane bending moment at the top of the scr measured on August 16, 1999 at 0:00 o'clock.

- *Estimate of damping ratio at the wave frequency*

We can use Figures 6-8 and 6-13 to have an idea of the total damping acting on the riser. By total damping we mean the structural plus the hydrodynamic. We know that waves created in the riser by VIV are attenuated as they travel along the riser. Assuming a linear damping model, then the waves are attenuated exponentially with distance traveled by the factor $\exp(-\zeta \cdot \gamma \cdot \Delta s)$, where ζ is an equivalent linear damping ratio and Δs is the distance traveled along the riser. In other words, suppose we have a travelling decaying wave along the riser. The ratio of two consecutive displacement amplitudes at two different locations separated by a distance Δs is given by $\exp(-\zeta \cdot \gamma \cdot \Delta s)$. Since the response spectra is proportional to response amplitude squared, we have that if S_1 and S_2 are the spectral areas between two different frequencies, then the effective damping can be calculated as

$$\frac{S_2}{S_1} = \exp(-2\zeta \cdot \gamma \cdot \Delta s) \quad \Rightarrow \quad \zeta = \frac{1}{-2 \cdot \gamma \cdot \Delta s} \ln\left(\frac{S_2}{S_1}\right) \tag{6.1}$$

The areas under the two spectra shown in Figures 6-8 and 6-13, between 0.06 and 012 Hz differ by a ratio of approximately 12.2 to 1. If we choose an average frequency of 0.08 Hz and an average wavenumber of $0.01035m^{-1}$ the formula above yields a value of 8.9% for the effective damping. In general, the structural damping adopted for scr is around 0.3%. The difference between the values refers to the hydrodynamic damping. Furthermore, the wave propagation parameter can be estimated as $3 \cdot 0.089 = 0.267$. This value indicates that the propagating waves can reach the ends of the riser but with decaying amplitudes due to the effect of the damping. It indicates that the waves generated by the ocean waves on top of the riser can reach the bottom of the riser and this fact is shown in Figures 6-8 and 6-13.

6.3.2 VIV along the SCR

The VIV bottles started measuring the accelerations on February 2000 and stopped on July of the same year to exchange the batteries. The problem related with this period of time is the lack of environmental load data. Concerning the current data, we do not have a measured current profile since the ADCP never worked. The best we can do is to use a typical profile for the current based on the measured surface current magnitude and direction (always with respect to the North direction). Concerning the waves, the buoy presented many problems during this period too. Furthermore, because of the huge amount of data, the environmental load data and the platform motion data related to this period are not in the data base yet. However, some interesting conclusions can be drawn.

As for the VIV bottles, only bottles 1 and 3 worked. Unfortunately, the measurements were not always at the same time. The sampling rate is 2Hz but the data was high filtered at 0.5 Hz.

The data of measurements are designated by *ymmddhh.vfn,* where *y* means the year (it is always equal to 0 because they refer to 2000), *mm* stands for the month (from 1 to 12), *dd* means the day of the month, *hh* means the full hour of the day (from 0 to 23) and the extension *vfn* means VIV bottle number *n*. Two days were selected to be studied in more detail.

1. June 07, 2000 at 14:00 o'clock

Figures 6-15 and 6-16 show the power spectral densities of the 0060714.vf1 data file (i.e., June 7, 2000 at 14:00 o'clock) of the Y and Z accelerations at bottle 1, respectively. By inspecting these plots we see a strong concentration of energy around 0.35 Hz. Unfortunately we have no data for the same time at VIV bottle 3.

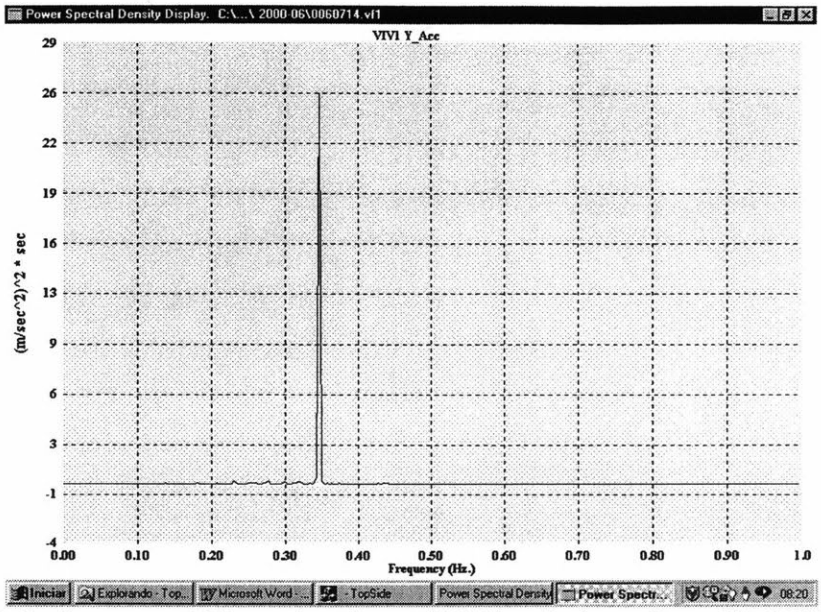

Figure 6-15: Psd of measured Y acceleration at VIV bottle 1, on June 07, 2000 at 14:00 o'clock.

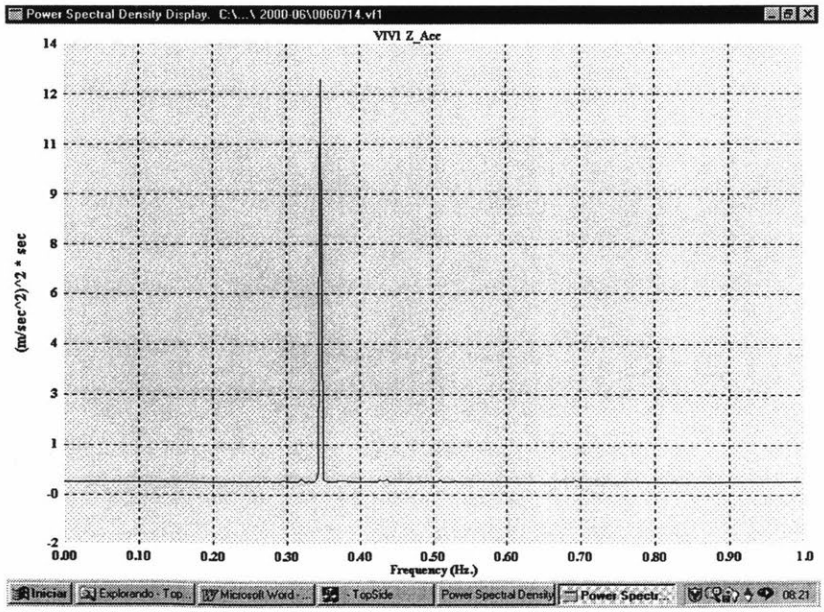

Figure 6-16: Psd of measured Z acceleration at VIV bottle 1 on June 07, 2000 at 14:00 o'clock.

The measured environmental conditions are:

- The wave characteristics are: period of 7.78s, height of 2.33m and direction of 65 with North direction.
- The surface current magnitude and direction are $0.54m/s$ and 236°, respectively. Based on these values, the typical current is the same as the one given in table 6.6.

Depth (m)	Magnitude (m/s)	Angle (degree)
50	0.55	217
100	0.50	201
150	0.49	202
250	0.28	189
350	0.14	177
450	0.10	142
550	0.13	83
650	0.18	47
750	0.18	52
900	0.24	46

Table 6.6: Typical current profile for the surface current (0.53m/s and 202.5° with North) measured on August 13, 1999 at 12:00 o'clock.

- Average heave applied on top of the riser: 0.3m

All these excitations were applied to the riser through a deterministic analysis in Anflex and quantities like KC number and corresponding maximum shedding frequency were calculated. The results are shown in Figure 6-17. The symbols '*' indicate the position of VIV bottles 1 and 3 on the riser.

In order to study the effect of the periodic excitations on the scr, two dynamic analyses were carried out using Anflex:

- The scr subjected to the wave and the heave applied by P18 (solid line in Figure 6-18)
- Only heave applied by P18 (dotted line in Figure 6-18)

The results are shown in Figure 6-18.

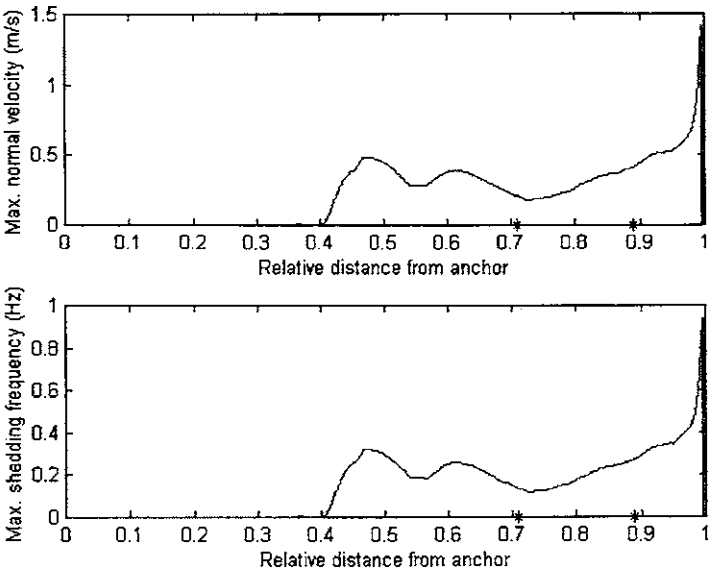

Figure 6-17: Maximum predicted normal velocity (upper part) and shedding frequency (lower part) along the P18 scr for the environmental conditions measured on June 07, 2000 at 14:00 o'clock.

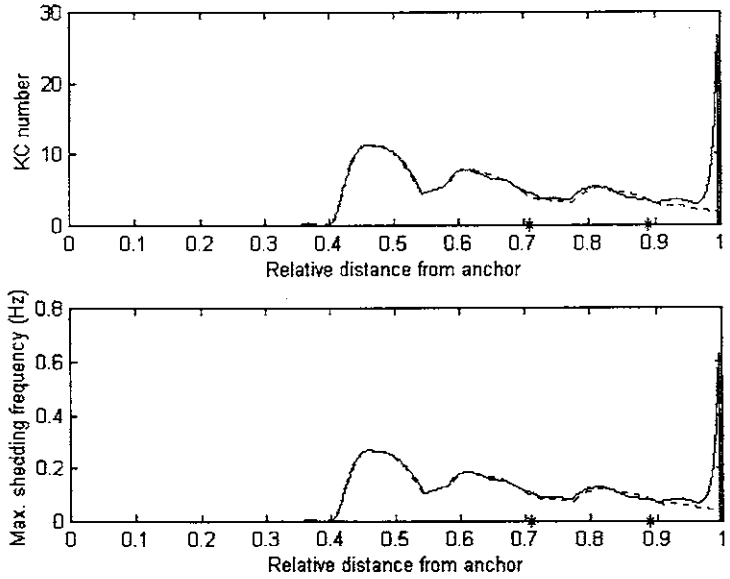

Figure 6-18: Predicted KC number (upper part) and maximum shedding frequency (lower part) along the P18 scr without the current. The solid line refers to the application of heave plus wave and the dotted line refers to application of heave only. Heave and wave were measured on June 07, 2000 at 14:00 o'clock.

The distribution of KC and shedding frequency is similar to those obtained in the two previous cases. Near the tdp the riser motion drives the VIV formation. As we go up, this influence decreases and the current influence becomes greater and greater. Near the surface we have also the influence of waves. VIV bottle 1 shows a spike at 0.35 Hz. The lower part of Figure 6-17 indicates that it must come from the riser region above this bottle because this region presents shedding frequency above 0.35 Hz. Hence, in the upper part of the riser the VIV frequency is being driven by ocean current plus wave.

Passing a high filter on the Y displacement time series (obtained by double integration of the corresponding Y accelerations) with cutoff equal to 0.3Hz and calculating the corresponding rms value, we obtain 0.0634 m. In this case, the ratio A/D is 0.25. Passing the same high filter at 0.3Hz at the Z displacement time series, the rms is 0.0415 with A/d equal to 0.16.

Figures 6-19 and 6-20 show the power spectra density of the in-plane and out-of-plane bending moments at the top end of the riser. This data was measured on the same day at 15:00 o'clock. It was the closest to the corresponding VIV data time at bottle 1. We see that the second order platform motion and the wave are predominant in the riser top motion. However, there is some energy a little bit above 0.3 Hz, especially at the out-of-plane bending moment data, which must come from the VIV excitation. A curious feature is the appearance of a spike a little above 0.6Hz, especially at the in-plane bending moment data. The most probable explanation for this spike at a so high frequency is the drag force caused by VIV. We know that the unsteady drag forces (in-line direction) occur at approximately twice the frequency of the corresponding lift forces (out-of-plane direction).

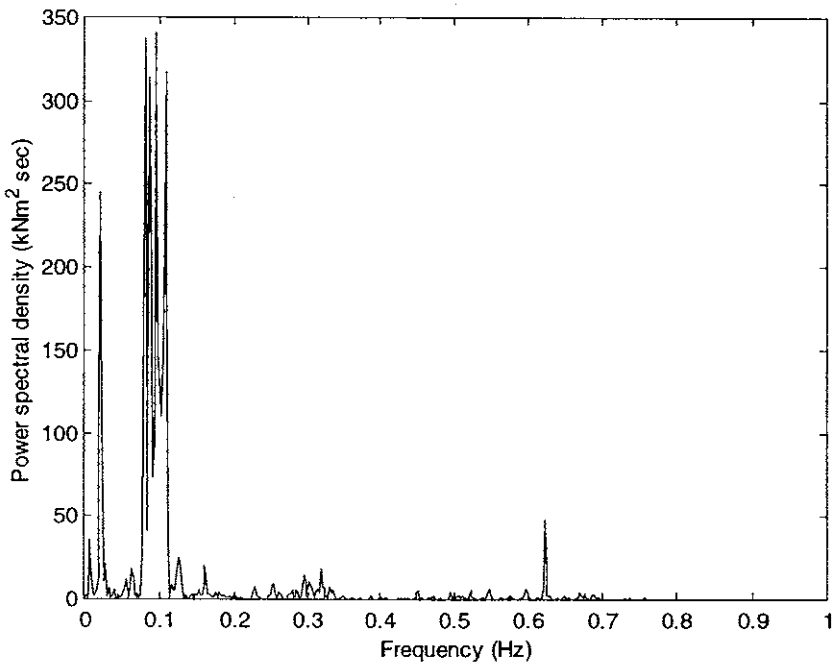

Figure 6-19: Psd of the in-plane bending moment at the top region of the riser, measured on June 07, 2000 at 14:00 o'clock.

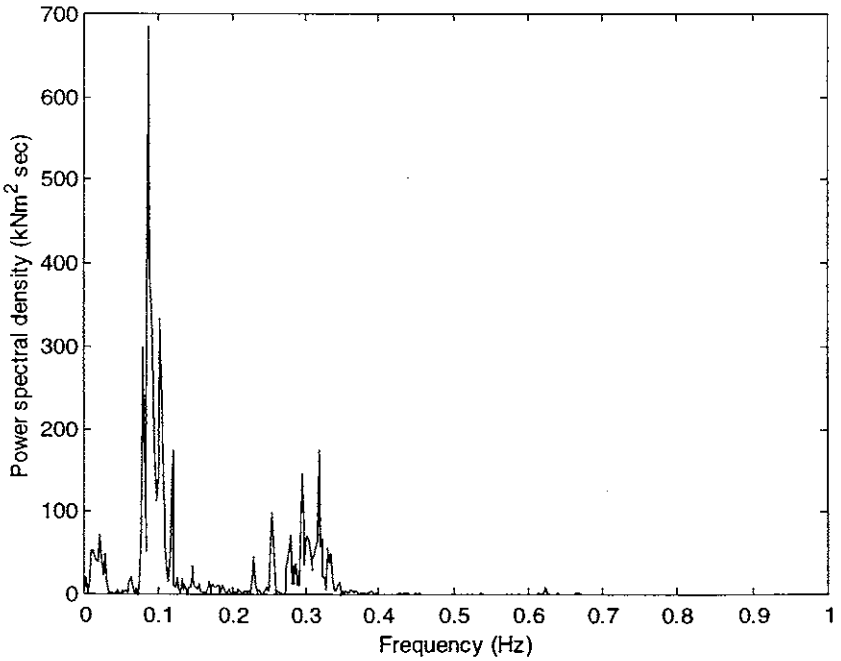

Figure 6-20: Psd of the out-of-plane bending moment at the top region of the riser, measured on June 07, 2000 at 14:00 o'clock.

2. *July 01, 2000 at 02:00 o'clock*

Figures 6-21 and 6-22 show the 0070102.vf1 data for the Y and Z accelerations for bottle 1, respectively. Figures 6-23 and 6-24 show the 0070103.vf3 data for the Y and Z accelerations for bottle 3, respectively. These measurements were made at the same time. We see a strong concentration of energy around 0.4 Hz in both bottles, especially for the Y displacements.

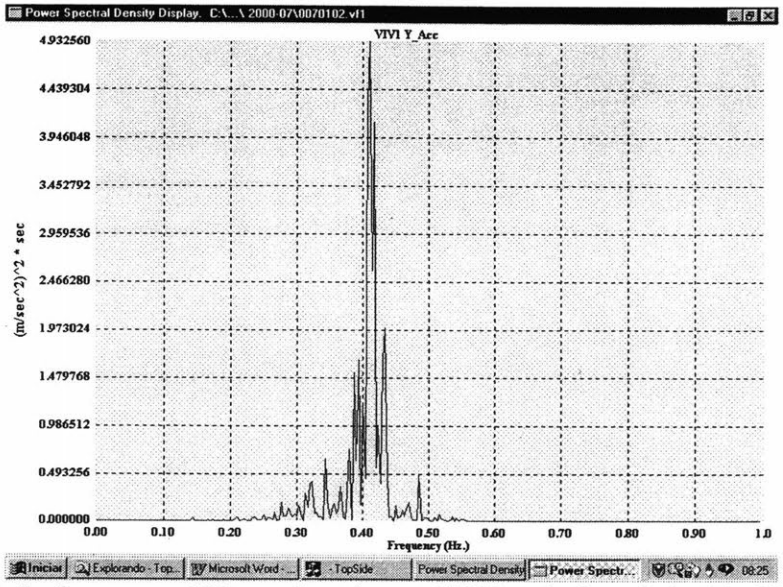

Figure 6-21: Psd of measured Y acceleration at VIV bottle 1 on July 01, 2000 at 02:00 o'clock.

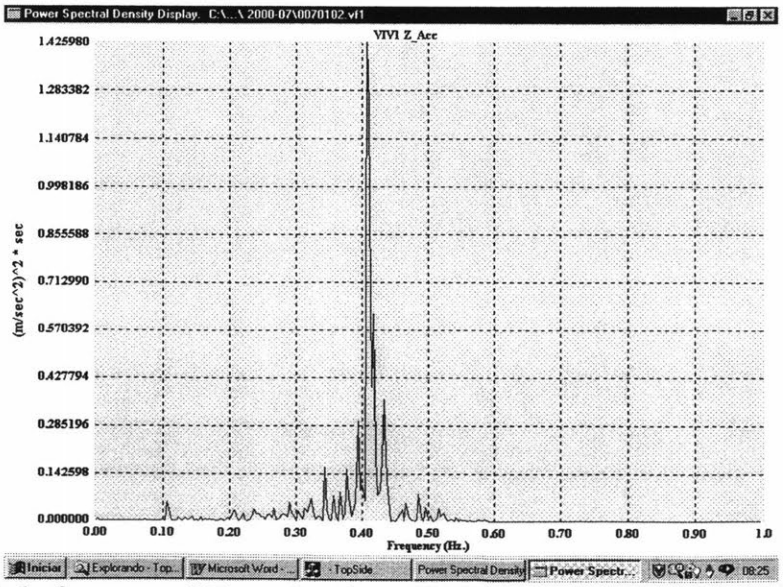

Figure 6-22: Psd of measured Z acceleration at VIV bottle 1 on July 01, 2000 at 02:00 o'clock.

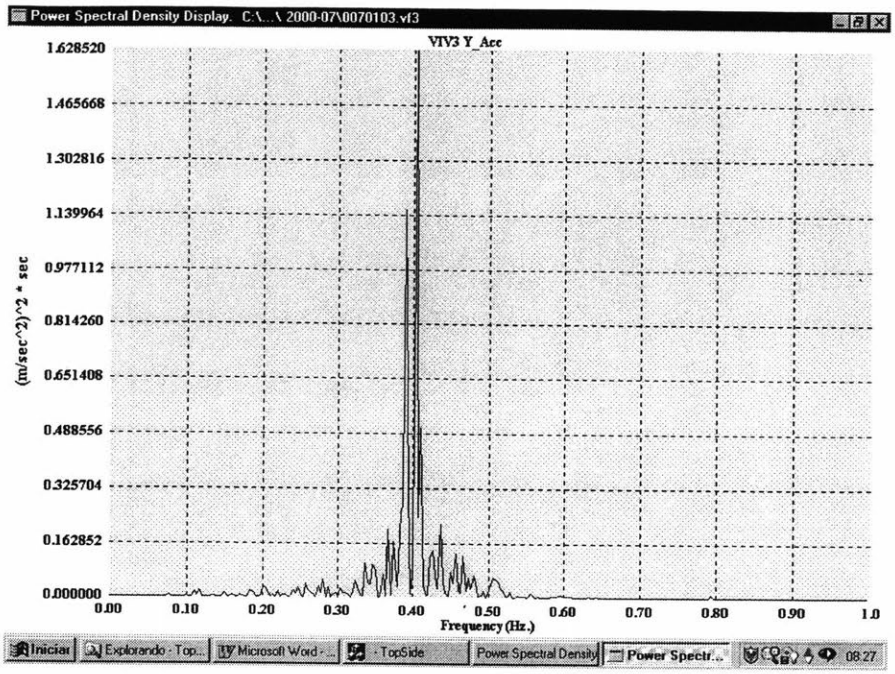

Figure 6-23: Psd of measured Y acceleration at VIV bottle 3 on July 01, 2000 at 02:00 o'clock.

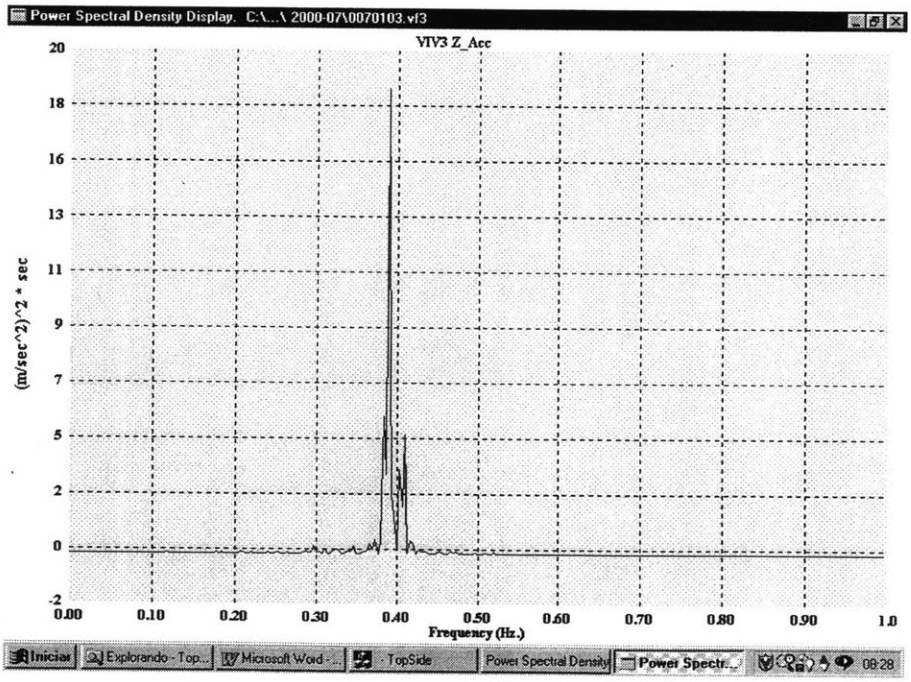

Figure 6-24: Psd of measured Z acceleration at VIV bottle 3 on July 01, 2000 at 02:00 o'clock.

The environmental conditions are:

- The wave characteristics are: period of 7.04s, height of 2.1m and direction of 61 with respect to the North
- The surface current is defined by $0.67m/s$ with 214° with respect to North direction. Typically this current is defined by the following table:

Depth (m)	Magnitude (m/s)	Angle (degree)
50	0.65	215
100	0.54	190
150	0.53	198
250	0.28	185
350	0.15	184
450	0.09	149
550	0.11	79
650	0.15	52
750	0.16	53
900	0.20	49

Table 6.7: Typical current profile for the surface current (0.67m/s and 214° with North) measured on July 01, 2000 at 02:00 o'clock.

- Average heave on top of the riser is 0.36m

All these excitations were applied to the riser through a deterministic analysis in Anflex and quantities like KC number and shedding frequency were calculated. The results are shown in Figures 6-25. The symbols '*' indicate the position of VIV bottles 1 and 3 on the riser.

In order to study the effect of the periodic excitations on the scr, two dynamic analyses were carried out using Anflex:

- The scr subjected to the wave and the heave applied by P18 (solid line in Figure 6-26)
- Only heave applied by P18 (dotted line in Figure 6-26)

The results are shown in Figure 6-26.

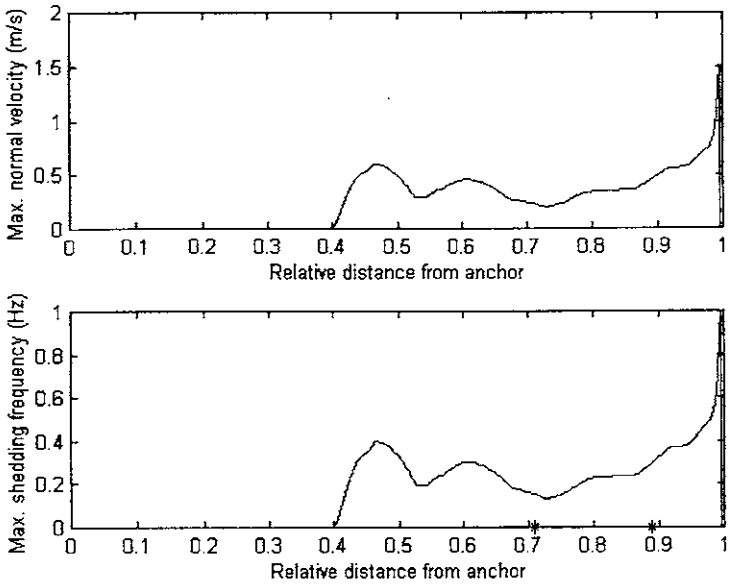

Figure 6-25: Maximum predicted normal velocity (upper part) and shedding frequency (lower part) along the P18 scr for the environmental conditions measured on July 01, 2000 at 02:00 o'clock.

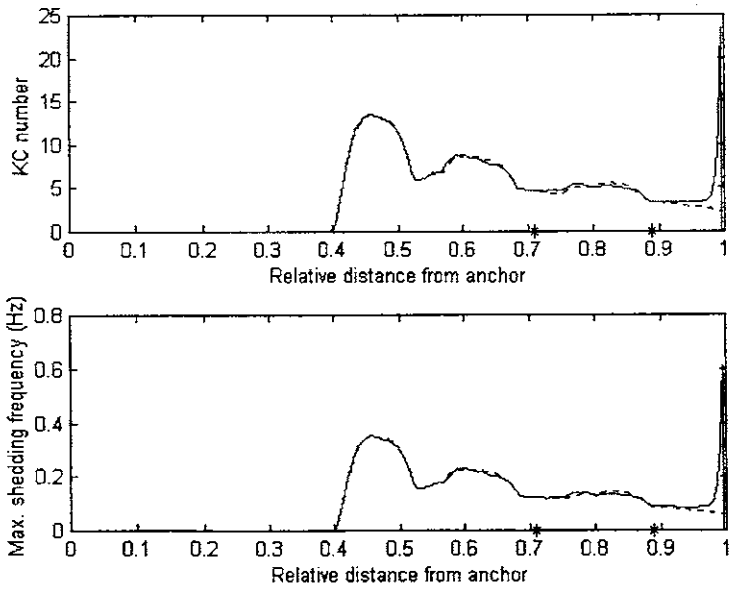

Figure 6-26: Predicted KC number (upper part) and maximum shedding frequency (lower part) along the P18 scr without the current. The solid line refers to the application of heave plus wave and the dotted line refers to application of heave only. Heave and wave were measured on July 01, 2000 at 02:00 o'clock.

The distribution of KC and shedding frequency is similar to those obtained previously. Near the tdp the riser motion drives the VIV formation. As we go up, this influence decreases and the current influence becomes greater and greater. Near the surface we have also the influence of waves. VIV bottles 1 and 3 show a spike at 0.4 Hz. According to Figure 6-25 there are only two regions where structural waves could be generated with this frequency: near the tdp (a very short portion) and near the top region.

Passing a high filter to the Y displacement time series derived by double integration of the corresponding acceleration time series, with cutoff at 0.35 Hz and calculating the rms of the resultant series, we obtain 0.0475 or A/D ratio of 0.19. Doing the same thing for the Z displacements, we obtain rms of 0.0237 or A/D equal to 0.093.

Figures 6-27 and 6-28 show the power spectra density of the in-plane and out-of-plane bending moment, respectively, on top of the riser. This data was measured on the same day at 3:00 o'clock, which was the closest time to the one under consideration. In Figure 6-27 the riser response is dominated by the wave and second order motion. In the out-of-plane direction, we see a strong contribution at 0.4 Hz from the VIV to the riser response, which is bigger than the contributions from waves and second order motion. This value is close to the maximum shedding frequency calculated previously. The interesting thing is the appearance of a spike for the in-plane bending moment power spectra density at a frequency twice the VIV frequency of the main contribution for the out-of-plane bending moment response. It is the second time we verify it. Again, the best explanation for it is the unsteady drag force. If we look at the directions that the ocean wave and surface current are acting, we see that the in-plane component is bigger than the out-of-plane component. From Figures 6-25 and 6-26 we see that the predicted shedding frequency can reach values up to 1 Hz. Hence, it indicates that there is VIV in the out-of-plane direction at 0.4 Hz with in-line vibration at 0.8 Hz.

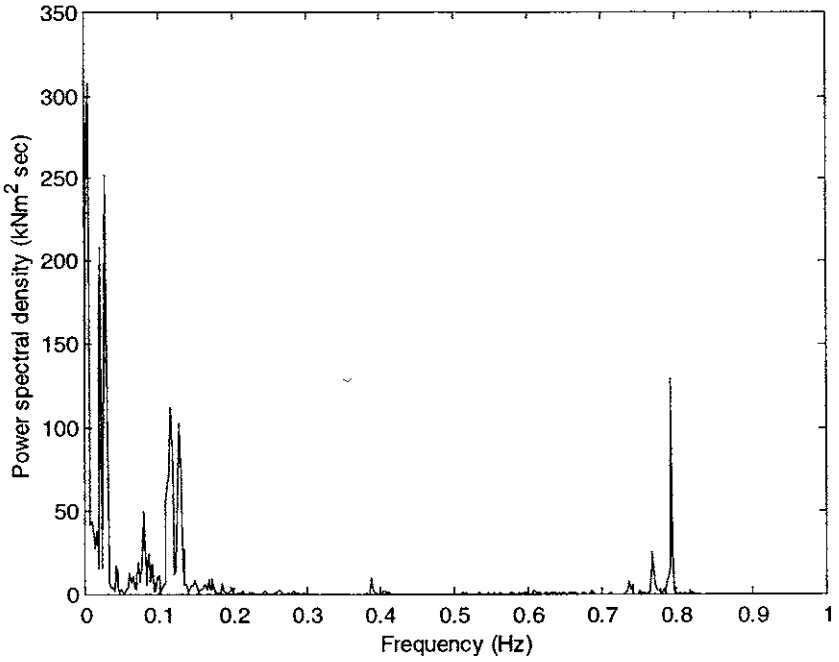

Figure 6-27: Psd of in-plane bending moment in the top region of the riser measured on July 01, 2000 at 02:00 o'clock.

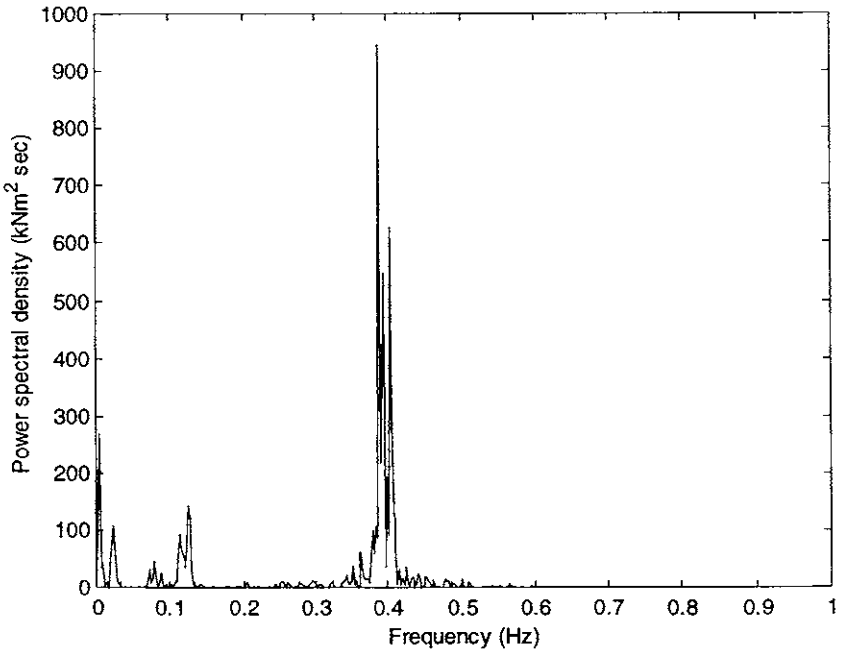

Figure 6-28: Psd of out-of-plane-plane bending moment in the top region of the riser measured on July 01, 2000 at 02:00 o'clock.

- *Estimate of damping ratio*

Using the plots shown in Figures 6-21 and 6-23 of the out-of-plane Y accelerations can be used to estimate the damping ratio of the P18 scr through equation 6.1. The area under psd curves between the frequencies 0.38 Hz and 0.43 Hz are $0.24(m/s^2)^2$ and $0.13(m/s^2)^2$, respectively. The average wavenumber for the chosen frequency of 0.4Hz is $0.039m^{-1}$ calculated from the wave dispersion relation. The distance between VIV bottles 1 and 3 is approximately 360m. Substituting these values in equation 6.1 we obtain a damping ratio of 2.2%. Natural frequency number 18 is the closest to the average frequency of 0.4 Hz. Hence, the wave propagation parameter (described is chapter 4) is given by $18 \cdot 0.022 = 0.396$. This value suggests that spatial attenuation is important but the propagating waves can reach and be reflected at the ends of the riser, creating like a pattern of standing waves with spatial attenuation.

This scr subjected to the action of the ocean current was simulated through Shear7. It predicted a total damping of 1.6%. One explanation for this difference is the fact that Shear7 did not take into account the effects of the riser motion nor the wave.

6.4 Comparison between Measured and Predicted Values.

As stated before, there are two basic objectives to be achieved with this campaign of measurements on P18 steel catenary riser:

- Evaluation of design methodology that is employed today for the calculation of fatigue life.
- Check the predictions of numerical codes.

Both objectives are intimately related as the predictions of numerical codes are embedded in the design methodology. There are also other aspects to be considered in the design of a steel catenary riser such as maximum stresses. However, fatigue life was always closely related to the technical feasibility of the riser. In terms of fatigue life, we have Shear7 code whose predictions will be used for the comparison with the measurements.

According to preliminary VIV analysis of the P18 scr made with the typical current profiles that occur in Campos Basin, the worst cases in terms of damage rate are the currents going to the South or South-West direction with magnitude at the surface between 0.9 and 1.0 m/s. Looking

at the surface measurements we noticed that on June 30th of 2000, at 19:00 o'clock a surface current with magnitude 0.91 m/s and direction 212° with respect to the North direction was measured. Thus, we picked the typical current profile described by the table 6.8 below and used it to calculate fatigue life of the P18 scr through Shear7. It predicted that only the out-of-plane mode shape number 23, associated with the natural frequency of 0.516 Hz, is potentially excited. Shear7 calculated a rms of amplitude equal to 0.21m at relative position $\frac{s}{L}=0.92$, which corresponds to the location of VIV bottle 1.

Depth (m)	Magnitude (m/s)	Angle (degree)
50	0.93	214
100	0.41	172
150	0.49	201
250	0.24	163
350	0.10	208
450	0.10	127
550	0.16	83
650	0.15	58
750	0.18	45
900	0.15	53

Table 6.8: Typical current profile for the surface current (0.91m/s and 212° with North) measured on June 30, 2000 at 19:00 o'clock.

Figure 6-29 shows the psd of the Y displacement at VIV bottle 1 measured on June 30 at 19:00h. when a surface current with 0.91m/s of magnitude and 212 of direction with respect to the North direction was measured. We see a big spike in the riser response at 0.49Hz, which is close to the Shear7 prediction of potentially excited frequency, and another at 0.464 Hz in the high frequency domain. Unfortunately there is no measurement of displacement of bottle 3 near this time.

Applying a high filter to the Y displacement time series with cutoff at 0.48Hz, we find the rms amplitude equal to 0.0374m which is 5.6 times smaller than 0.21m.

As we can see, Shear7 predicted the dominance of only one frequency (0.516Hz) which is confirmed by the power spectral density shown in Figure 6-29. However, because of conservatism embedded in the program and also due to the fact that it does not take into account oscillatory flow acting on a riser caused by waves or top heave, Shear7 predicted a much higher value for the displacement at the location of VIV bottle 1.

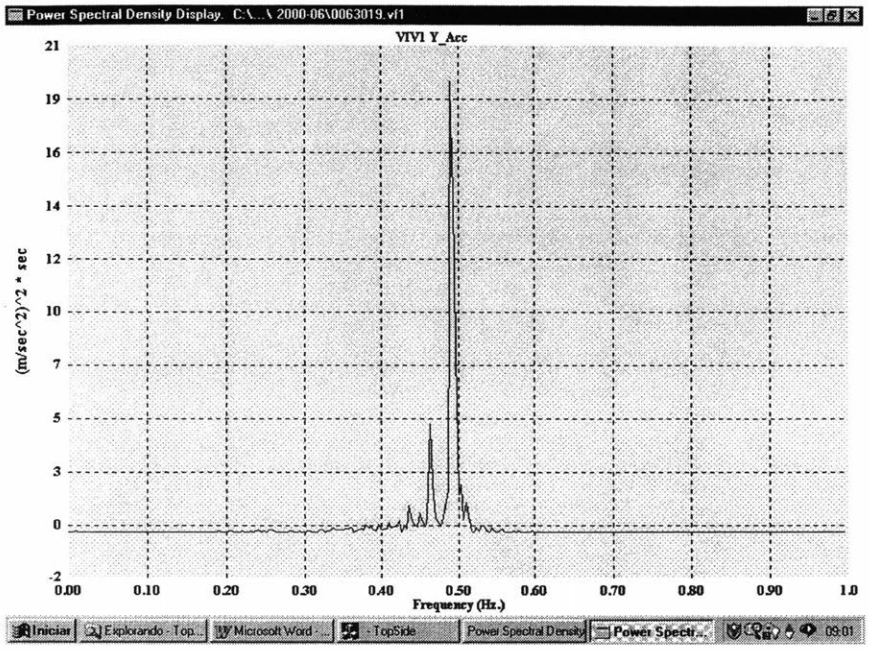

Figure 6-29: Psd of the measured Y accelerations at the VIV bottle 1 measured on June 30, 2000 at 19:00 o'clock.

Chapter 7

Conclusions

7.1 Introduction

The contributions of this dissertation fall into two main areas. On one hand, a numerical model that describes the dynamics of straight and curved beam elements subjected to a slowly varying tension distribution was developed. On the other hand, new insights about VIV were achieved through experimental observation and analysis of measurements. The main conclusions concerning these topics and some suggestions for future work are discussed in the following sections.

7.2 Numerical Model

In this study, we used the wave-based finite element method to develop different types of beam elements that would allow us to study the dynamic behavior of risers at high frequencies with some advantages over the conventional FEM.

The first element to be developed was the straight beam element with distributed spring and damping acting transversely in order to simulate a foundation. All the properties and the static tension distribution were constant along the element. This way, it was possible to obtain an exact solution for the governing dynamic differential equation. This solution was then used not only to describe the displacements inside the element but also to develop the dynamic stiffness matrix of this element. Some interesting characteristics of the wave dispersion relation of beams on elastic foundation were studied.

Then the influence of both shear deformation and rotary inertia were considered in the formulation of the dynamic stiffness matrix of an element under the same conditions. Furthermore, the procedure adopted here was very similar to the one that would be used for the curved beam element.

Then we considered that the beam element could be subjected to a slowly varying tension distribution. This complicated our obtaining of the solution because now we ended up with a varying coefficient in the dynamic governing equation. WKB method was employed to obtain an approximation for the solution which, in turn, was used to formulate the dynamic stiffness matrix of an element subjected to slowly varying tension the same way as we did for the constant tension case.

The next step was to use the same procedure for a curved beam element because our objective was to model marine risers and in these type of structures the radius of curvature varies along the longitudinal distance. So we started with a curved beam element with constant properties and constant tension distribution. This time we ended up with two dynamic differential equations, both of them with axial and transverse components. This means that the axial and transverse displacements were now coupled, which happened due to the appearance of a curvature in the element. In this case we obtained an exact solution for the governing equation and formulated the element dynamic stiffness matrix.

Then we considered that the tension distribution was slowly varying along the element and, again, using WKB method, we managed to obtain an approximate solution for the governing equation and formulated the dynamic stiffness matrix for the element.

The next step was to couple both straight and curved elements to allow the analysis of a riser configuration considering the length on the soil. The coupling was performed and the natural frequencies and mode shapes of some structures were compared to those obtained by conventional FEM, and good agreement was obtained.

To complete the numerical model, we developed a procedure to consider the response of a beam element, curved or not, to a distributed load of any shape acting along the element and to obtain the displacements inside the element in the context of wave-based finite element method.

The application of this numerical model was shown in many different examples involving simple structures like straight beams up to more complex ones like steel catenary risers and lazy

waves risers. Comparisons with results from theory and other codes that employ conventional finite element method were made and good agreement was obtained.

The benefit of employing this method is that it is very well suited for a high frequency dynamic model (which happens to be the case of a riser when subjected to VIV), without the need to refine the riser mesh too much as we have to do with the conventional FEM. Furthermore, spatial attenuation of travelling waves can also be taken into account.

7.3 Experiments

The measurements of three different sets of experiments were analyzed in this dissertation. The first was the Highly Compliant Riser experiment, conducted by PMB, where different configurations of risers (CVAR, Lazywave and a steel catenary riser) were subjected to harmonic top motions simulating vessel motion. Accelerations and bending moments were then measured at 8 different points along the riser. It was verified that despite the fact that there was no current or wave acting on the riser, it showed intermittent VIV. We obtained some insights about the riser behavior when subjected to VIV, about the indication of existence of a Keulegan-Carpenter number threshold and about reflection of propagating waves when they encounter bottom boundary conditions.

Another experiment with steel catenary riser was performed by the author. A small model representing the steel catenary riser on Petrobras P18 semi-submersible was placed in a towing tank and 48 out-of-plane displacements were applied on its top end with different amplitudes and frequencies. Interesting cases of riser response resonance were obtained when there was a match between at least two of the following frequencies: riser natural frequency, average shedding frequency and multiple of input frequency.

Finally there was the full scale experiment with the steel catenary riser on Petrobras P18. In this project we tried to measure the most important quantities involved in the design of a riser, such as ocean current, waves, vessel motions, bending moments and acceleration at some points along the riser. This type of project is important because it can provide information for real risers at full scale Reynolds number and mode shapes. On the other hand, this is a very long project whose data are just beginning to be analyzed. It will take many more months until some

definitive conclusions can be drawn. However, some ideas could be extracted from this initial investigation. First, it indicated that the intermittent VIV caused by the riser response to the vessel motion can be an issue. Frequencies much higher than the wave or vessel motion frequency appeared on the bottom part of the riser. If we are going to compare the measurements with the predictions from some program, these high frequencies should be considered. Second, a quick comparison between measured displacement with Shear7 prediction showed that Shear7 is very conservative. The decrease of this conservatism is a key issue in the design of a riser.

The experience gained with this type of project indicates that there are several problems that we have to face, such as the difficulty in making all the equipment work at the same time during measurements and the difficulty in interpreting the results due to uncertainties in measurements.

7.4 Contributions

The original contributions presented in this dissertation can be summarized as the following:

1. Development of a straight beam element in the context of wave based finite element method, considering shear deformation and rotary inertia effects plus the effect of distributed stiffness and damping acting transversely on the straight beam element. All properties inside the element are constant and the tension distribution can be constant or slowly varying.
2. Development of a uniform curved beam element, subjected to a constant or slowly varying tension.
3. Coupling of both straight and curved beam elements in order to allow the analysis of a whole riser configuration, including the effect of soil.
4. New insights about VIV based on experimental observations, such as: 1) existence of a KC threshold; 2) Interactions with bottom boundary conditions; 3) VIV resonance in scr and 4) full scale confirmation of unsteady heave-induced VIV..

7.5 Recommendations for Further Research

Some suggestions on the future research related to the present work are given in this section.

1. Consideration of some kind of variation of the curvature radius along the curved beam element in the dynamic model. This could improve the results obtained in this dissertation and probably decrease even more the number of elements necessary to represent the marine riser.
2. Repetition of the laboratory test with the small steel catenary model under the action of waves to see the influence in the resonance issue.
3. More high Reynolds number data from laboratory tests to improve the hydrodynamic coefficients used in the prediction codes. This way we can improve the match between what is predicted and what is measured.

Bibliography

[1] D. W. Allen. Vortex-Induced Vibration of Deepwater Risers. *Offshore Technology Conference*, pp. 209-215, 1998.

[2] K. J. Bathe. *Finite Element Procedures in Engineering Analysis*. Prentice-Hall, New Jersey, 1988.

[3] P. W. Bearman, E. D. Obasaju and J. M. R. Graham. A Model Equation for the Transverse Forces on Cylinders in Oscillatory Flows. *Applied Ocean Research*, vol. 6 pp. 166-172, 1984.

[4] P. W. Bearman and E. D. Obasaju. Transverse Forces on a Circular Cylinder Oscillating In-line with a Steady Current. Eighth Int. Conference on Offshore Mechanics and Artic Engineering, pp. 253-258, 1989.

[5] P. W. Bearman, X. W. Lin and P. R. Mackwood. Measurements and Prediction of Response of Circular Cylinders in Oscillating Flow. *Proceedings of the Sixth International* BOSS *Conference*, vol. 1 pp. 297-307, 1992.

[6] C. M. Bender and S. A. Orszag. *Advanced Mathematical Methods for Scientists and Engineers*, McGraw Hill, 1978.

[7] R. D. Blevins. *Flow-Induced Vibration*. Van Nostrand Reinhold Co., 2nd ed., 1990.

[8] R. D. Blevins. *Formulas for Natural Frequency and Mode Shape*. 1979

[9] J. J. Burgess and M. S. Triantafyllou. The Elastic Frequencies of Cables. *Journal of Sound and Vibration*, 120(1), pp. 153-165, 1988.

[10] R. D. Clough and J. Penzien. *Dynamics of Structures*. McGraw-Hill Book Co., 1975.

[11] S. F. A. Cornut and J. K. Vandiver. Offshore VIV monitoring at Schiehallion – Analysis of Riser VIV Response. *Proceedings of ETCE/OMAE 2000*, pp. 1-9, 2000.

[12] D. L. Garrett. Dynamic Analysis of Slender Rods. *Journal Of Energy Resources Technology*, ASME, 104,pp. 302-306, December, 1982.

[13] D. L. Garrett. *Riser Development*. Technical Note, Mobil Research & Development Company, 1995.

[14] Gopalkrishnan. *Vortex-Induced Forces on Oscillating Bluff Cylinders.* Ph.D. thesis, Massachusetts Institute of Technology, Cambridge, MA, 1993.

[15] K. F. Graff. Elastic Wave Propagation in a Curved Sonic Transmission Line. IEEE *Trans., Sonics and Ultrasonics*, 1970.

[16] K. F. Graff. *Wave Motion in Elastic Solids.* Dover Publication, New York, 1991.

[17] M. A. Hayner. *Wave-based Finite Element Method applied to Thick, In-vacuo, Cylindrical Shells with Keel or Bulkhead Plate Attachments at Middle to High Frequency.* PhD thesis, Massachusetts Institute of Technology, Cambridge, MA, 1998.

[18] F. B. Hildebrand. *Advanced Calculus for Applications.* Prentice-Hall, Englewood Cliffs, New Jersey, 1976.

[19] C. T. Howell. *Investigation of the Dynamics of Low-Tension Cables.* Ph.D. thesis, Massachusetts Institute of Technology, Cambridge, MA, 1992.

[20] E. Huse, G. Kleiven and F. G. Nielsen. Large Scale Model Testing of Deep Sea Risers. *Offshore Technology Conference*, pp. 189-197, 1998.

[21] H. M. Irvine. *Cable Structures.* MIT Press, Cambridge, MA, 1981.

[22] H. M. Irvine and T. K. Caughey. The Linear Theory of Free Vibrations of a Suspended Cable. *Proceedings of the Royal Society Series*, vol. 341 pp. 299-315, 1974

[23] J. A. F. Junior. *Hydrodynamic Loading and Response of Offshore Risers.* Ph.D. thesis. University of London, 1998.

[24] Y. C. Kim. *Nonlinear Vibration of Long Slender Beams.* Ph.D. thesis, Massachusetts Institute of Technology, Cambridge, MA, 1983.

[25] Y. H. Kim, J. K. Vandiver and R. Holler. Vortex-Induced Vibration and Drag Coefficients of Long Cables Subjected to Sheared Flows. Journal of Energy Resources Technology. Vol. 108, pp. 77-83, 1986.

[26] R. King. A Review of Vortex Shedding Research and its Application. *Ocean Engineering* vol. 4 pp. 141-171, 1977.

[27] Li Li. *The Dynamics of Strings with Rigid Lumps.* Ph.D. thesis, Massachusetts Institute of Technology, Cambridge, MA, 1993.

[28] H. Lie, K. Mo and J. K. Vandiver. VIV Model Test of a Bare and Staggered Buoyancy Riser in a Rotating Rig. *Offshore Technology Conference*, pp. 177-187, 1998.

[29] B. R. Mace. Wave Reflection and Transmission in Beams. *Journal of Sound and Vibration*, 97(2), pp. 237-246, 1984.

[30] L. S. D. Morley. Elastic Waves in a Naturally Curved Rod. *Quart. Jl Mech. Appl. Math.*, vol. XIV, pp. 152-172.

[31] E. D. Obasaju, P. W. Bearman and J. M. R. Graham. A Study of forces, circulation and vortex patterns around a circular cylinder in oscillating flow. *Journal of Fluid Mech.* vol. 196 pp. 467-494, 1988.

[32] M. S. Pantazopoulos. Vortex-Induced Vibration Parameters: Critical Review. OMAE vol. 1 pp. 199-255, 1994

[33] V. J. Papazoglou and S. Mavrakos. Non-linear Cable Response and Model Testing in Water. *Journal of Sound and Vibration*, 140(1), pp. 103-115, 1990.

[34] W. Press, S. Teukolsky, W. Vetterling and B. Flannery. *Numerical Recipes in* FORTRAN. Cambridge University Press, 1986.

[35] S. E. Rambert. Vibrations of Inclined Slack Cables. *Journal of Structural Division*, ASCE vol. 108 pp. 1662-1664, 1982.

[36] S. S. Rao. *Mechanical Vibrations*. Addison-Wesley Publishing Company, Third Edition, 1995.

[37] M. Reis. *Wave Propagation in Elastic Beams and Rods*. Ph.D. thesis, Massachusetts Institute of Technology, Cambridge, MA, 1978

[38] R. J. Roark. *Formulas for Stress and Strain*. 1975

[39] T. Sarpkaya. Hydrodynamic Damping, Flow-Induced Oscillations and Biharmonic Response. Transactions of the ASME, vol. 117 pp. 231-238, 1995.

[40] J. Schifter. *The effects of Bending Stiffness on the Dynamics of Catenary Cables*. MSc thesis, Massachusetts Institute of Technology, Cambridge, MA, 1996.

[41] R. M. C. Silva, D. Oliveira, R. Z. M. Filho and M. M. Mourelle. The Comprehensive Monitoring Program for the First Steel Catenary Riser Installed in the Semi-submersible P-18. Deep Offshore Technology, 1999.

[42] Sumer. Hydrodynamics Around Cylindrical Structures.

[43] A. H. Techet. *Vortical Patterns Behind a Tapered Cylinder*. MSc thesis, Massachusetts Institute of Technology, Cambridge, MA, 1998.

[44] A.A. Tjavaras. *The Dynamics of Highly Extensible Cables*. PhD thesis, Massachusetts

Institute of Technology, Cambridge, MA, 1996.

[45] M. S. Triantafyllou. *Cable Mechanics with Marine Applications*. Dept. Ocean Eng., MIT, Cambridge, MA 1990.

[46] M. S. Triantafyllou. The Dynamics of Taut Inclined Cables. *Quart. Jl Mech. Appl. Math.*, vol. 37, pp. 423-439.

[47] M. S. Triantafyllou, A Bliek and H. Shin. Dynamic Analysis as Tool for Open-Sea Mooring System Design. SNAME Transactions, vol. 93, pp. 303-324, 1985

[48] K. Vandiver. Dimensionless Parameters Important to the Prediction of Vortex-Induced Vibration of Long, Flexible Cylinders in Ocean Currents. *Journal of Fluids and Structures* vol. 7 pp. 423-455, 1993.

[49] J. K. Vandiver and J. Y. Jong. The Relationship between In-line and Cross-flow vortex-Induced Vibration of Cylinders. *Journal of Fluids and Structures*. Vol. 1, pp. 381-399, 1987

[50] M. Venugopal. *Damping and Response Prediction of a Flexible Cylinder in a Current.* Ph.D. thesis, Massachusetts Institute of Technology, Cambridge, MA, 1996.

[51] K. Vikestad. *Multi-Frequency Response of a Cylinder Subjected to Vortex Shedding and Support Motions*. Ph.D. thesis, Norwegian University of Science and Technology, Trondheim, Norway, 1998.

[52] K. Vikestad and K. H. Halse. Effect of Variable Current on Vortex-Induced Vibrations. *Proceedings of the Tenth International Offshore and Polar Engineering Conference.* Vol 3 pp. 493-498, 2000.

[53] K. Vikestad and K. H. Halse. VIV Lift Coefficients Found from Response Build-up of na Elastically Mounted Dense Cylinder. *Proceedings of the Tenth International Offshore and Polar Engineering Conference.* Vol. 3 pp. 455-460, 2000.